Physical Chemistry of Limonene Microemulsions and their Interaction with Oil

MATTHEW ROYLE

Physical Chemistry of Limonene Microemulsions and their Interaction with Oil

Matthew Royle

A thesis submitted for the degree of Doctor of Philosophy

Supervisor: Prof. Colin Bain
Industrial supervisor: James Silas
Department of Chemistry
Durham University
2023

Dedication

I dedicate this work to my parents, Colette and Charles Royle.

Declaration

The work described herein was undertaken at the Department of Chemistry, Durham University between February 2018 and February 2023. All of the work is my own, except where specifically stated otherwise. No part has previously been submitted for a degree at this or any other university.

Acknowledgements

I would first like to thank my industrial sponsors Flotek for their continued support and opportunity to visit their laboratories in Houston. It was unfortunate there were not more chances to meet in person, but circumstances dictated otherwise.

I am grateful to Colin Bain for his guidance and seemingly endless patience throughout the project. It has been a privilege to work for you and to get to know you over the years.

I would like to thank the Bain group for creating such a welcoming and warm environment. I would like to thank Lisong Yang for being a wonderful friend and mentor to me, without her help and contagious positivity I would not have been able to get this far. I would also like to thank Walter Hama for the enthusiastic discussions on all sorts of topics (mainly tennis and man united) and apologies to Jing for having to sit between the two of us during the discussions…

I'd like to thank a number of friends, particularly the guys at staff badminton and staff volleyball! A special mention must go to Jack Fradgley for taking me on so many therapeutic runs and being a wonderful friend, I'm glad we both decided to turn up to elvet striders that night!

I would like to thank my family for their love and support throughout my time at Durham. They do not need to read the words on this page to know how much I cherish the ever-growing Royle clan.

Many thanks to Tim and Claudia for countless fun evenings, shared experiences (there are too many to list) and companionship. You made my time in Durham a much happier one and provided a peaceful home environment during the uncertainty of the pandemic, thanks bent coppers!

Finally, I would like to thank my partner Ioana for improving my life as soon as she entered it. You continue to make me want to be a better person with your love and support, even during my grey days. Ești soarele vieții mele.

Abstract

This thesis aims to study the phase behaviour of limonene microemulsions using a formulation used in industry for enhanced oil recovery. The use of a stopped-flow FRET technique was able to elucidate a mechanistic study of micelle fusion kinetics with respect to limonene microemulsions.

The first part of the project used several phase measurement methods and spectroscopic techniques to determine the physical properties of a limonene microemulsion using a commercial surfactant and the phase behaviour of its components. The various techniques employed are useful tools for future formulators when studying limonene microemulsions. The commercial surfactant, despite showing branching was deemed suitable as an alternative to pure $C_{12}E_7$, exhibiting behaviour expected of pure $C_{12}E_7$. The phase measurements also gave insight to the kinetic mechanistic studies that followed.

The second part of the project investigated a suitable method to observe micelle exchange kinetics for limonene microemulsions and derive quantifiable kinetic data. A stopped-flow FRET technique was used to observe the exchange and Target Factor Analysis was used for quantitative analysis. Initial trials using pyrene as a fluorescent dye was not suitable due to insufficient solubility of the fluorescent probe within the micelles. The use of FRET probes was successful in observing micellar exchange on a timescale that was detectable (>8 ms). Target Factor Analysis gave significantly improved clarity to the data obtained and allowed me to deduce micelle fusion kinetics from the observed data. The stopped-flow FRET technique combined with Target Factor Analysis is a novel approach to the study of micelle fusion kinetics.

The final part of the project used the stopped-flow FRET technique to compare micelle exchange kinetics with similar microemulsion systems, determine the effect of temperature, concentration, and introduction of salt on micelle exchange. This was taken further, observing the interaction of limonene microemulsions with a crude oil mimic. By comparing several microemulsion systems and changes in environment, a greater understanding of the kinetic pathways micelles can take in

fusion processes was garnered. The use of the stopped-flow FRET technique using a crude oil mimic demonstrates the capability of the technique for future use on oil surfaces.

Contents

List of abbreviations

BTEX – Benzene, toluene, ethyl benzene and xylene

$C_{12}E_7$ - Heptaethylene Glycol Monododecyl Ether

IPA – Iso-propyl alcohol

CMC – Critical micelle concentration

FRET – Förster resonance energy transfer

EOR – Enhanced oil recovery

ULIFT – Ultra low interfacial tension

IFT – Interfacial tension

PIT – Phase inversion temperature

SDS – Sodium dodecyl sulphate

NBD-PE - (N-(7-Nitrobenz-2-oxa-1,3-diazol-4-yl)-1,2-dihexadecanoyl-snglycero-3-phosphoethanolamine, triethylammonium salt)

Rh-PE – 1,2-dioleoyl-sn-glycero-3-phosphoethanolamine-N-(lissamine rhodamine B sulfonyl) (ammonium salt)

PCA - Principal component analysis

TFA – Target factor analysis

AFA – Abstract factor analysis

SFA – Significant factor analysis

LFA – Loading factor analysis

SVD – Singular value decomposition

REP – Error in refined spectrum

RET – Error in the target spectrum

$\bar{n}$ – Average number of solubilised SDS molecules per micelle

NaCl – Sodium Chloride

NMR – Nuclear magnetic resonance

Introduction

I1 Motivation and aims

Microemulsions have two defining characteristics that make them appealing to the petroleum industry: first, they are thermodynamically stable; second, they possess ultra-low interfacial tension at the water-oil interface. The theory of microemulsion formation and their characteristic behaviour is described in more detail in §1.2. Microemulsions are used in enhanced oil recovery to increase oil recovery rates where after primary and secondary oil recovery processes, 40–70% of oil can still be trapped by capillary forces [1]. The global pandemic has shaken the energy sector, with a 5% drop in global energy demand reported for 2020 and 18% drop in energy investment [2]. Global energy demand is expected to reach pre-crisis levels by 2023 and will continue to rise as countries develop. Fossil fuels still hold the largest share of demand for energy. Renewable energy has grown strongly over recent years, with a move away from coal-fired power stations, towards existing renewable energy sources and newly developing technology such as carbon capture utilisation and storage. Despite established renewable technologies and new technologies emerging, crisis events such as the ongoing Russia-Ukraine war caused a great strain on the supply chain. The global demand for alternative sources of energy to replace Russian oil and gas was too great for renewable sources to respond to in such a short time frame. Natural gas supplies were rapidly acquired by developed countries in Europe. Exploring new reservoirs for traditional oil recovery was also not viable, leaving fracking as the most suitable alternative to respond quickly enough to the oil crisis.

It is important for the petroleum industry to move towards more sustainable ways of recovering oil. BTEX chemicals – short for benzene, toluene, ethyl benzene and xylene – are extensively used in the oil industry for enhanced oil recovery. BTEX chemicals dissolve paraffin waxes and asphaltene, which are known to reduce oil recovery by altering wettability and restricting flow. BTEX chemicals cause risk to human health and damage the environment. Evidently, a more environmentally friendly alternative is required. Limonene, a cyclic monoterpene, is the major

constituent in the oil of citrus fruit and can be used in a variety of oil-field applications, such as hydraulic fracturing stimulation, degreasing offshore vessels, cementing operations, and well-bore cleanouts [3][4]. Flotek Industries, the industry partner on this project, have shown that limonene performs as well as xylene and toluene at dissolving paraffin waxes and asphaltene deposits [4]. When paraffin and asphaltene deposits are left untreated can accumulate to form unwanted sludges in oil wells. Flotek have incorporated limonene to create a more environmentally friendly microemulsion system through their patented Complex Nano Fluid (CNF) technology systems and continue to work on other systems. Limonene has not been found to have significant negative impacts on the environment or present a major risk to human life. Limonene provides a safer alternative to BTEX-based chemicals and providing microemulsions able to produce more sustainable enhanced oil recovery.

My project aims to improve our understanding of limonene microemulsions and how they interact with oil on surfaces. An improved understanding of the mode of action of limonene-based microemulsions, would assist formulators to tailor their formulation to the conditions of a particular oil well, improving oil recovery at new and existing sites throughout the oil industry. The microemulsion system used for this study consists of limonene (oleic phase), isopropyl alcohol (IPA, cosurfactant), heptaethylene-glycol monododecylether ($C_{12}E_7$, non-ionic surfactant) and water (aqueous phase). To achieve this aim for the microemulsion system mentioned, an extensive experimental study has been undertaken on model systems to determine the behaviour of the microemulsion system in solution at the bulk oil-water interface.

I2 Limonene

Limonene is a cyclic monoterpene with the molecular formula $C_{10}H_{16}$ and is an essential oil found in citrus fruits such as lemons, limes, and oranges. Limonene has two optical isomers, with identical chemical properties but differing odours. (+)-limonene or D-limonene has an orange aroma, whereas (-)-limonene or L-limonene has a piney odour. The two isomers of limonene have been depicted below.

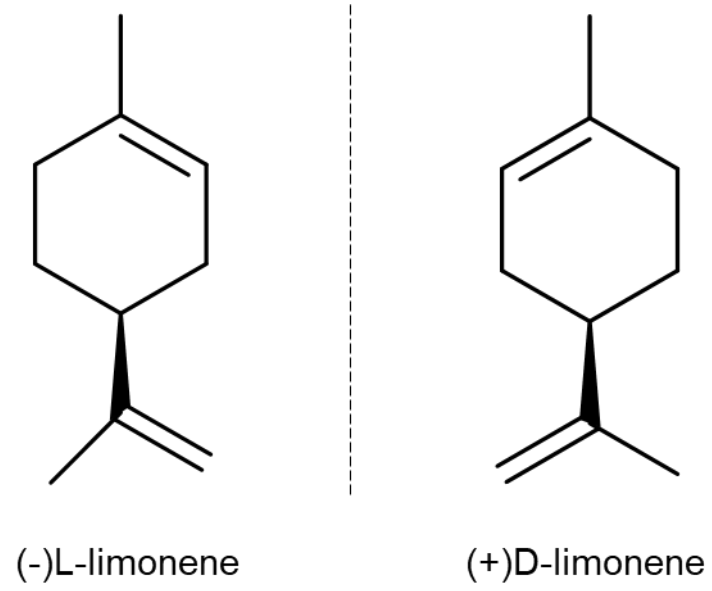

Figure i1: Two optical isomers of limonene.

Limonene is used in several ways: as a solvent in industrial cleaning products, flavouring in medicine, and as a fragrance in most household cleaning products. As a naturally occurring oil, limonene is being used more and more frequently to replace more harmful solvents.

The main extraction method for D-limonene is through the by-product of citrus juicing. Lower purity (food grade) limonene is collected when the oil is pressed from the peel and separated from the juice. To obtain higher grade D-limonene (used for the purpose of this study) the peels undergo steam distillation, providing companies with the ability to recycle waste citrus peels with little toxic waste.

Terpenes, particularly limonene, are attractive to the oil industry due to their green properties: limonene is a natural product, biodegradable, and has low toxicity, whilst

being a suitable solvent for organic deposits in oil wells. Limonene can also be blended with surfactants and co-surfactants to enhance their performance in enhanced oil recovery. Flotek provides oilfield specialty solutions to drilling, cementing, stimulation and production challenges using their patented Complex Nano Fluid (CNF) technology systems and various other patented systems.

I3 Oil recovery methods

Oil extraction is divided into three phases: primary, secondary, and tertiary or enhanced oil recovery (EOR). Primary oil recovery is the first phase, a wellbore is created by drilling a hole through the soil. Gravity and pressure inside the reservoir force the oil into the wellbore. Once the pressure has equalised the oil can be extracted by installing an artificial lift mechanism such as a beam-pumping unit. Primary oil recovery typically extracts ~10% of the available oil in a particular reservoir. Secondary oil recovery uses an injection of either gas or water to increase the pressure in the reservoir, displacing additional oil from the reservoir and forcing the oil to the surface. Waterflooding is typically favoured for secondary recovery and can double the amount of oil recovered from primary oil recovery. When secondary oil recovery does not recover a suitable amount of oil tertiary methods are often used.

There are three main types of EOR:

- Chemical flooding, a surfactant system or polymer system is pumped through injection wells to mobilise oil left behind from primary and secondary oil recovery.
- Thermal recovery, the reservoir is heated using steam to reduce the interfacial tension and viscosity of the crude oil, allowing the oil to then flow to the wellbore.
- Gas injection, gas (usually CO_2) is injected through a gas cap to increase the pressure of the reservoir, the gas effectively sweeps the remaining oil to the surface.

EOR methods, including hydraulic fracturing will typically target a yield of 70% of oil from a reservoir, returning a much more efficient recovery method for oil [5].

For primary oil recovery, the low yield stems from reservoir pressure gradually lowering over time, even with an artificial lift being used. When the reservoir pressure falls below the oil bubble point, gas will escape from the oil and will flow to the surface

in place of oil. This also results in the viscosity of oil increasing, thus having less mobility, lowering recovery rate further. Injecting water to the reservoir can help maintain a high enough pressure for recovery, however, addition of water can block rock pores and reduce rock permeability.

Capillary forces are described by the Young-Laplace equations and are responsible for effectively blocking oil in the rock pores. Blocking of rock pores is dependent on the pore sizes of the rock and capillary pressure inside the pore. If the rock is water wet, then the small pores will generally have more water than large pores [6]. Capillary forces can be quantified by the capillary number given in equation i1. The capillary number is a dimensionless quantity that relates the viscous forces to interfacial tension forces,

$$Ca = \frac{v\mu}{\gamma} \tag{i1}$$

Here v is velocity, μ is the fluid viscosity and γ is the interfacial tension between displaced and displacing fluid. For mobilisation of oil there is a critical capillary number found at ~ 10^{-5}–10^{-3}, determined from multiple core-flood experiments [7]. A reduction in rock permeability is explained in detail by Muggeridge et al. [8]. The rock's natural geological heterogeneity can form high permeability channels which the water can preferentially flow through. As a result, the water can bypass large volumes of oil that are held in the lower permeable portions of the reservoir and so giving a reduced recovery rate of oil. Referring to equation i1, a diluted microemulsion can change the capillary forces between the rock pores in the reservoir and injecting fluid by reducing the interfacial tension.

Figure i3 is a schematic giving an example of chemical flooding, in this case microemulsion flooding of an oil well in enhanced oil recovery. After primary and secondary methods, dilute microemulsions are driven down the injection well. The dilute microemulsions lower the interfacial tension at the oil-water interface, giving better mobility and viscosity control of the well. This system is not limited to microemulsions alone, surfactant and polymer floods are also used to mobilise oil.

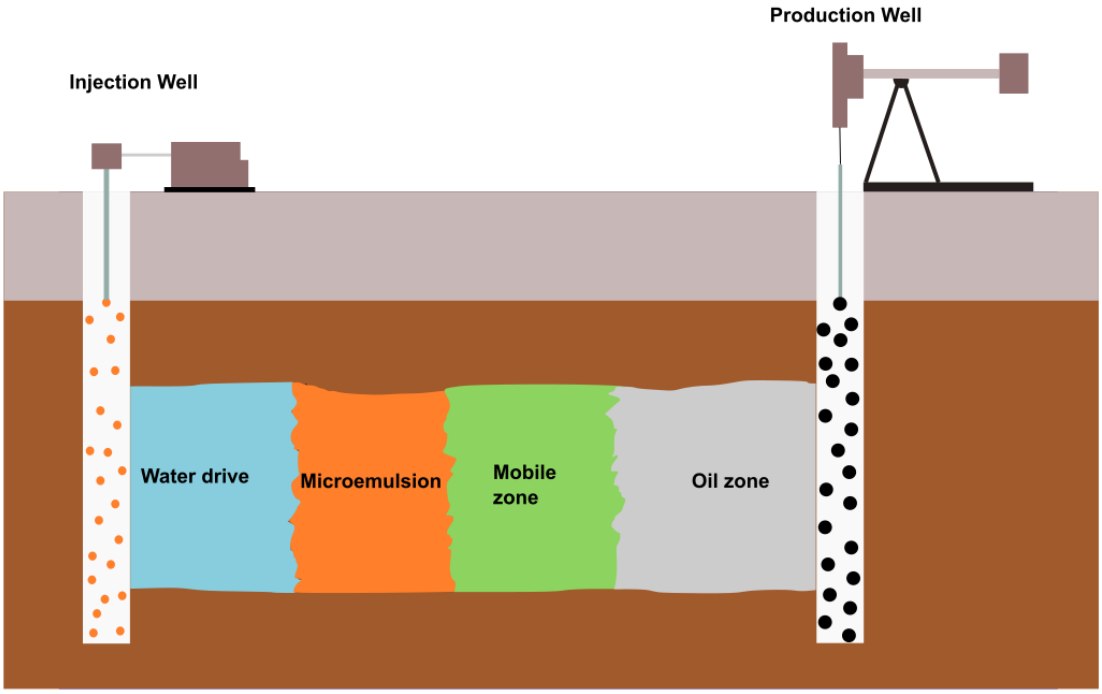

Figure i2: Schematic of microemulsion flood of an oil well.

I4 Microemulsions in enhanced oil recovery

Microemulsions have been used for EOR since the early 1960s, the earliest being the Maraflood process, created by Marathon Oil in 1963. In the 1970's, Healy and Reed conducted further work on microemulsion flooding and formed an excellent review on the physiochemical aspects of microemulsion flooding [9]. The microemulsion system used was monoethanolamine salt of C_N o-xylene sulfonic acid (surfactant), tertiary amyl alcohol (cosolvent), 90% Isopar-M plus 10% heavy aromatic naphtha (oil) and brine, with over 100 compositions evaluated for the system. An extensive study of the multiphase region was undertaken to determine which conditions such as salinity, temperature, flooding effects and the role of the co solvent are needed for optimum oil recovery.

There was a clear trend found between solubilisation parameter and interfacial tension as a function of salinity. Lowering of interfacial tension increases the solubilisation capacity of the microemulsion, thus low interfacial tensions represent micelles swelled with the internal phase.

When determining the ideal conditions by changing parameters such as temperature, salinity, etc., Healy and Reed found that simple solubilisation parameter experiments worked well for the parameter in question. Once a parameter was optimised in the solubilisation parameter experiments, core flood experiments were undertaken to determine the oil recovery as a function of that parameter.

The core flood experiments found the best oil recovery is established when microemulsions are equilibrated at high water-oil ratios in the mixture. It was also found that the microemulsion-oil interfacial tension determines the effectiveness of the displacement of oil at the front of the microemulsion slug. Whereas microemulsion-water interfacial tension dictates the displacement at the rear, the least effective of the two determines the outcome.

Since the work by Healy and Reed, there have been new trends using microemulsions in conventional and unconventional EOR recovery methods [10]–[15]. The addition of nanoparticles has been recently studied to stabilise microemulsions in harsh conditions so that microemulsions can be deployed in a wider variety of oil wells successfully [10],[16],[17]. Qin et al. synthesised silicon oxide in-situ in a microemulsion to promote the formation of Pickering emulsions [10]. The microemulsions stabilised by nanoparticles were compared with microemulsions ability to mobilise oil through reducing the interfacial tension and enhancing emulsification. Qin et al. found that microemulsions stabilised by nanoparticles were able to recover more oil than microemulsions without nanoparticles due to the emulsification of oil into even smaller droplets where nanoparticles and surfactants would interact at the interface. The smaller oil droplets could penetrate smaller capillaries elements of the rock than microemulsions could, giving greater wettability change.

I5 Flotek case studies of microemulsions for oil recovery

Flotek have conducted much research into the use of microemulsions to aid oil recovery. Their focus is to use their patented microemulsion formula, which utilises D-limonene to create a biodegradable fracking fluid and alternative chemical solution to microemulsions using BTEX solvents in enhanced oil recovery.

Kutty et al. present the benefits of using limonene microemulsions in an acid recipe on well performance [18]. An acid recipe is typically formulated to clean a carbonate reservoir and allow for better injection fluid rates [19]. Kutty et al. give a more detailed description of their acid recipe formulation in their study. Kutty et al. list the benefits of using what they term complex nano fluids, including reducing interfacial tension and capillary pressure to penetrate deeper into rock formations, thus leading to longer and better production rates. They also suggest that by using the nano fluid, the need for the use of BTEX oils in drilling fluids is reduced, which are hazardous to marine environments.

Zelenev et al. investigated the use of microemulsions to improve fluid recoveries from columns of shale/sand mixtures [20]. They found microemulsions significantly improved the extent of fluid recovery when compared with simple brine recoveries. Brine recoveries only managed a maximum 30% fluid recovery in a horizontal column whereas the microemulsion system reached a maximum of 60% fluid recovery.

Penny et al. discussed the use of nanofluid systems using a variety of surfactants and their impact on oil recovery when injected through sand columns [21]. This study also tried to identify which test method by measuring adsorption, contact angles, wettability and flow best identifies the most effective surfactant system for improving oil recovery.

Bui et al. have also investigated the mechanism of action of limonene microemulsions penetrating into shale nanopores [22]. Bui et al. mention that, despite it being well known that microemulsions are effective for oil recovery, much about the mechanism is not known. They have used molecular dynamics simulation to simulate oil-wet and water-wet surfaces found in shale. Their results show that wettability of the solid surface plays a key role when capillaries are less than 10 nm. For oil-wet surfaces the microemulsion droplets adsorb on the surface, whereas in water-wet surfaces the

droplets can penetrate into nanocapillaries. For both cases, the limonene and $C_{12}E_7$ penetrate into the capillaries where they can then solubilise the crude oil.

Zelenev et al. conducted similar work to Bui et al. through investigating the interactions of microemulsions with shale rock [23]. Wettability and adsorption measurements were taken with Marcellus shale rock and limonene microemulsions, using the same microemulsion formulation as in my research. The adsorption experiments were completed through surface tension measurements of the microemulsions before and after equilibrium with shale. The wettability data was obtained through contact angle measurements of dilute microemulsions on a shale surface. Their results show that dilute microemulsions adsorb to the shale in a different way to a surfactant solution due to a change in the net distribution of the surfactant in the system. The study suggests that limonene adsorbs onto the surface along with the surfactant with the degree of adsorption dependent on the surfactant concentration in the microemulsion. The mechanism of adsorption has been found to have some distinct features.

1. The surfactant adsorbs with hydrocarbon chains facing the shale surface via Lifshitz-van der Waals forces. Shale is an oil-wet surface in the presence of air [24].
2. Hydrogen bonding between ethoxylate groups in the surfactant and shale is very unlikely.
3. It is assumed that ethoxylated alcohol adsorbs through a “tail down” system with limonene present in the adsorption layer.

Hernandez, Ehler and Trabelsi demonstrated the efficacy of crude oil removal from sand using microemulsions [26]. A new experimental technique named the Shaken Bottle test in combination with UV-Vis spectroscopy was used to quantify crude oil residue removal. A comparative study with a surfactant package showed limonene microemulsions remove a much larger amount of crude oil residue from sand surfaces than the equivalent surfactant package. They propose a removal mechanism of crude oil from sand using a microemulsion. The diluted microemulsion comes into contact with sand, the D-limonene and surfactant adsorb onto the surface of the sand. D-limonene then diffuses into the crude oil layer, softening the crude oil and then removing the crude oil within the micelles in the aqueous phase. The removal mechanism suggested by Hernandez et al. can be seen in figure i4 below.

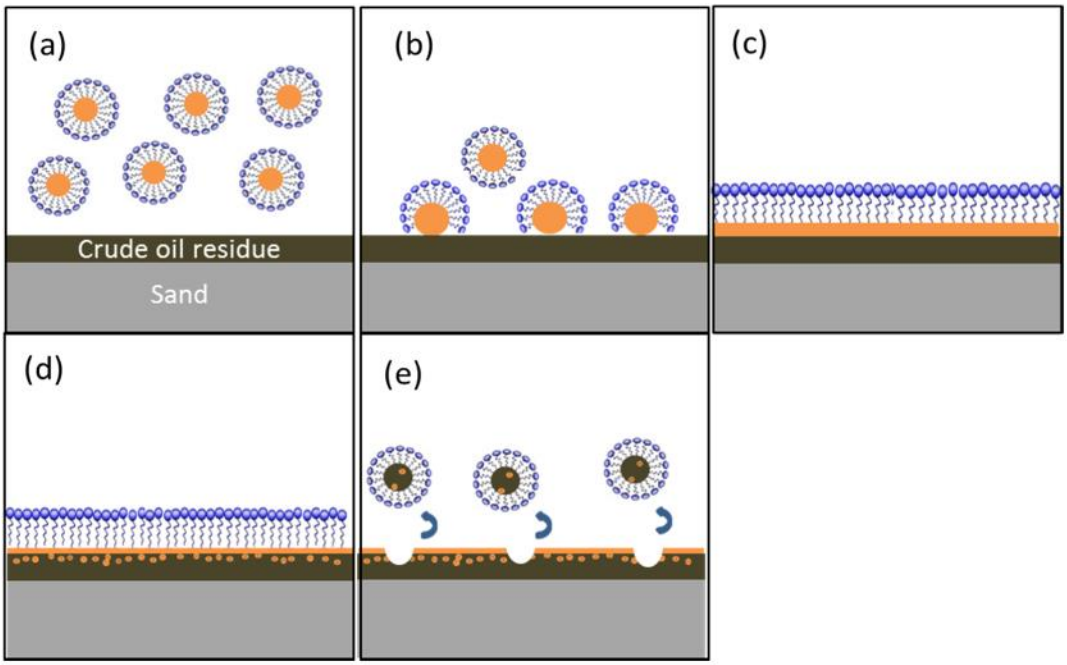

Figure i3 : Hernandez et al. scheme showing the removal mechanism of crude oil from sand using d-limonene microemulsions [26] with permission. (a) the microemulsion comes into contact with the sand surface, (b) and (c) surfactant and d-limonene adsorbs onto the sand surface, (d) d-limonene softens crude oil, (e) crude oil residue is incorporated into the micelles and removed from the crude oil layer.

Whilst this model may be valid for a system where the quantities of limonene and crude oil are similar, as shown in i4c, the microemulsions in this study and typical microemulsion flooding methods use a dilute microemulsion which will have a much lower concentration of limonene to crude oil.

References

[1] M. A. K. M. F. Nazar. S. S. Shah, “Microemulsions in Enhanced Oil Recovery: A Review,” *Journal Pet Sci Technol*, vol. 29, no. 13, pp. 1353–1365, 2011.

[2] IEA, “World Energy Outlook 2020,” Oct. 2020. https://www.iea.org/reports/world-energy-outlook-2020 (accessed Dec. 13, 2021).

[3] R. Ciriminna, M. Lomeli-Rodriguez, P. Demma Carà, J. A. Lopez-Sanchez, and M. Pagliaro, “Limonene: A versatile chemical of the bioeconomy,” *Chemical Communications*, vol. 50, no. 97, pp. 15288–15296, 2014, doi: 10.1039/c4cc06147k.

[4] K. Fisher, “Terpenes replacing BTEX in oilfields.” American Gas and Oil Reporter, p. editor’s choice September, 2013.

[5] F. D. S. Curbelo *et al.*., “Adsorption of non-ionic surfactants in sandstones,” *Colloids Surf A Physicochem Eng Asp*, vol. 293, no. 1–3, pp. 1–4, 2007, doi: 10.1016/j.colsurfa.2006.06.038.

[6] N. J. Clark, *Elements of petroleum reservoirs*. Dallas: Society of Petroleum Engineers of AIME, 1969.

[7] M.-C. C. A. Pope, “A multi-scale approach to dynamic processes at the oil-water interface in surfactant enhanced oil recovery,” no. September, 2017.

[8] A. Muggeridge *et al.*., “Recovery rates, enhanced oil recovery and technological limits,” *Philosophical Transactions of the Royal Society A: Mathematical, Physical and Engineering Sciences*, vol. 372, no. 2006, 2014, doi: 10.1098/rsta.2012.0320.

[9] R. L. Reed and R. N. Healy, “SOME PHYSICOCHEMICAL ASPECTS OF MICROEMULSION FLOODING: A REVIEW,” *Improved Oil Recovery by Surfactant and Polymer Flooding*, pp. 383–437, Jan. 1977, doi: 10.1016/B978-0-12-641750-0.50017-7.

[10] T. Qin, L. Goual, M. Piri, Z. Hu, and D. Wen, “Nanoparticle-stabilized microemulsions for enhanced oil recovery from heterogeneous rocks,” *Fuel*, vol. 274, p. 117830, Aug. 2020, doi: 10.1016/J.FUEL.2020.117830.

[11] M. Tagavifar, S. Herath, U. P. Weerasooriya, K. Sepehrnoori, and G. Pope, “Measurement of Microemulsion Viscosity and Its Implications for Chemical Enhanced Oil Recovery,” *SPE Journal*, vol. 23, no. 01, pp. 66–83, Aug. 2017, doi: 10.2118/179672-PA.

[12] Z. Hu, E. Nourafkan, H. Gao, and D. Wen, “Microemulsions stabilized by in-situ synthesized nanoparticles for enhanced oil recovery,” 2017, doi: 10.1016/j.fuel.2017.08.004.

[13] Z. Jeirani, B. M. Jan, B. S. Ali, I. M. Noor, C. H. See, and W. Saphanuchart, “Formulation, optimization and application of triglyceride microemulsion in enhanced oil recovery,” *Ind Crops Prod*, vol. 43, pp. 6–14, 2013, doi: 10.1016/j.indcrop.2012.07.002.

[14] V. C. Santanna, F. D. S. Curbelo, T. N. Castro Dantas, A. A. Dantas Neto, H. S. Albuquerque, and A. I. C. Garnica, “Microemulsion flooding for enhanced oil recovery,” *Journal Pet Sci Eng*, vol. 66, no. 3–4, pp. 117–120, 2009, doi: 10.1016/j.petrol.2009.01.009.

[15] T. Qin, G. Javanbakht, L. Goual, M. Piri, and B. Towler, “Microemulsion-enhanced displacement of oil in porous media containing carbonate cements,” *Colloids Surf A Physicochem Eng Asp*, vol. 530, no. July, pp. 60–71, 2017, doi: 10.1016/j.colsurfa.2017.07.017.

[16] R. Aveyard, “Can Janus particles give thermodynamically stable Pickering emulsions?,” *Soft Matter*, vol. 8, no. 19, pp. 5233–5240, 2012, doi: 10.1039/C2SM07230K.

[17] C. Schulreich *et al.*., “Bicontinuous microemulsions with extremely high temperature stability based on skin friendly oil and sugar surfactant,” *Physicochem. Eng. Aspects*, vol. 418, pp. 39–46, 2013, doi: 10.1016/journal.colsurfa.2012.10.039.

[18] S. M. Kutty *et al.*., “Well Performance Improvement Using Complex Nano Fluids,” *Abu Dhabi International Petroleum Exhibition and Conference*, 2015, doi: 10.2118/177831-MS.

[19] Environment Agency, “Use of acid at oil and gas exploration and production sites,” 2018. Webpage. date accessed 20/9/2023. Doi: https://consult.environment-agency.gov.uk/onshore-oil-and-gas/onshore-oil-and-gas-regulation-information-page/supporting_documents/Acidisation%20FAQs%20January%202018.pdf

[20] A. S. Zelenev, H. Zhou, L. B. Ellena, G. S. Penny, C. Chemical, and I. Company, “Microemulsion-Assisted Fluid Recovery and Improved Permeability to Gas in Shale Formations,” *Society of Petroleum Engineers Journal*, pp. 1–7, 2010, doi: 10.2118/127922-MS.

[21] G. Penny *et al.*., “Nanofluid System Improves Post Frac Oil and Gas Recovery in Hydrocarbon Rich Gas Reservoirs,” *Society of Petroleum Engineers Journal*, 2012.

[22] K. Bui, I. Y. Akkutlu, A. S. Zelenev, and J. Silas, “Understanding Penetration Behavior of Microemulsions Into Shale Nanopores,” *SPE Europec featured at 79th EAGE Conference and Exhibition*. Society of Petroleum Engineers, Paris, France, p. 12, 2017. doi: 10.2118/185787-MS.

[23] A. S. Zelenev, L. M. Champagne, and M. Hamilton, “Investigation of interactions of diluted microemulsions with shale rock and sand by adsorption and wettability measurements,” *Colloids Surf A Physicochem Eng Asp*, vol. 391, no. 1–3, pp. 201–207, Nov. 2011, doi: 10.1016/j.colsurfa.2011.07.007.

[24] M. A. Q. Siddiqui, S. Ali, H. Fei, and H. Roshan, “Current understanding of shale wettability: A review on contact angle measurements,” *Earth Sci Rev*, vol. 181, pp. 1–11, Jun. 2018, doi: 10.1016/J.EARSCIREV.2018.04.002.

[25] L. Zhang *et al.*., “Wettability of a quartz surface in the presence of four cationic surfactants,” *Langmuir*, vol. 26, no. 24, pp. 18834–18840, Dec. 2010, doi: 10.1021/LA1036822/ASSET/IMAGES/MEDIUM/LA-2010-036822_0005.GIF.

[26] H. W. Hernandez, W. Ehlert, and S. Trabelsi, “Removal of crude oil residue from solid surfaces using microemulsions,” *Fuel*, vol. 237, no. July 2018, pp. 398–404, 2019, doi: 10.1016/journal.fuel.2018.10.035.

Chapter Guide

Within this thesis, the fundamental concepts for the project are introduced in chapter 1. Chapter 2 contains the experimental work to characterise and determine the phase behaviour of our limonene microemulsion. A number of techniques were used including, mass spectrometry, tensiometry, and phase tube measurements. Chapter 3 describes the theory of micellar interaction kinetics and introduces the stopped-flow fluorescent technique developed to observe the exchange processes between micelles. The first stopped-flow fluorescent experimental technique proposed was fluorescence quenching using pyrene as a fluorescent dye. The fluorescence quenching technique was not able to observe the exchange kinetics on a fast enough timescale. Calculations showed that pyrene can diffuse through the bulk aqueous phase between micelles faster than could be measured. Therefore, a new experiment was introduced using the stopped-flow apparatus with Förster Resonance Energy Transfer (FRET). The stopped-flow FRET experiment utilises a common FRET pair to observe the exchange process arising from micelle fusion. When the micelles collide and exchange contents, excited donor probes transfer energy to the acceptor probes.

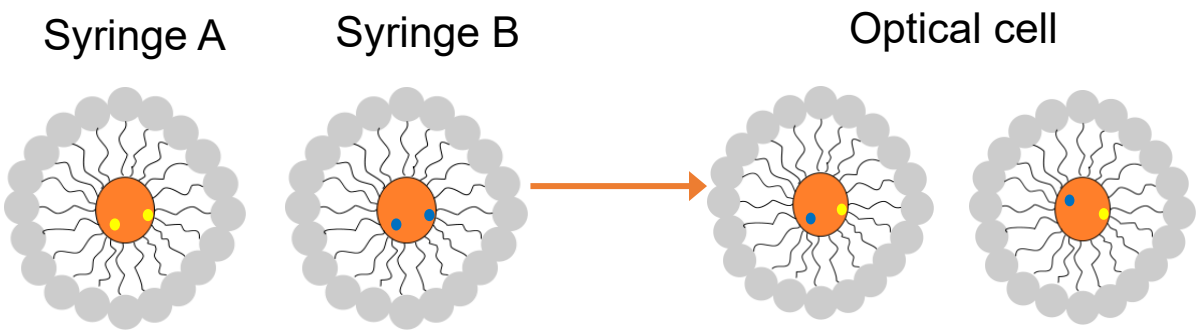

Figure i4: Illustration of micelles inside syringes A and B in the stopped-flow device. The final state is a representation of the micelles in the optical cell after equilibration of contents. The yellow dots indicate donor dye molecules, the blue dots indicate acceptor dye molecules.

Chapter 4 explains the quantitative analysis method (target factor analysis) for the FRET experiments. The theory of target factor analysis is explained in the context of this study. A complete exemplar for each step of the analysis process is presented with issues found during experimentation also discussed. Chapters 5-7 present the

FRET studies with quantitative analysis for our microemulsion with comparisons to other solvents, changes in conditions and exploring the effects of charge on the kinetics of micelle exchange. Chapter 8 presents the results of micellar kinetic exchange of our limonene microemulsion with a crude oil mimic using the stopped-flow FRET method.

Chapter 1 - Fundamental concepts and microemulsion theory

1.1 Fundamental Concepts

There are some fundamental principles of surface chemistry which have underpinned my project. The concepts covered in this chapter help to understand how microemulsions phase behaviour can change with different conditions and the kinetic processes in micellar systems.

1.1.1 Critical micelle concentration

Micelles are of great importance to this project as the solubilisation of crude oil using limonene microemulsions would not be possible without the formation of micelles and thus a knowledge of the critical micelle concentration.

The critical micelle concentration (CMC) is the concentration of surfactants required to form thermodynamically stable, microscopic aggregates in bulk solution. At the critical micelle concentration, the chemical potential of surfactant molecules in micelles is the same as the chemical potential of monomers in solution.

The critical micelle concentration can affect, and is directly related to, changes in many physical properties such as surface tension, conductivity, refractive index, and other optical properties. As a result, there are a number of methods that can be used to determine the CMC such as tensiometry, conductivity measurements, UV-Vis spectroscopy and dynamic light scattering. The nature of the surfactant can affect the suitability of a particular method to determine the CMC and it is often commonplace to use complementary methods to validate CMC results. The typical relationship between surfactant concentration and surface tension is depicted in figure 1.1. Perinelli et al. highlight the strengths and weaknesses of several techniques to provide CMC values for both non-ionic and ionic surfactants [1]. Perinelli et al. found tensiometry and fluorescence spectroscopy to be most reliable to determine the CMC for both anionic and non-ionic surfactants. Perinelli et al. also provide an overview of the mathematical treatment of the raw data obtained from various techniques including tensiometry,

conductimetry, fluorescence spectroscopy, densimetry and ultrasound spectroscopy. They propose a ‘second-derivate’ approach to analyse raw data taken and found it gave reliable determination of the CMC, when compared to traditional methods.

Mukerjee and Mysels give an extensive report on methods available to measure the CMC and have also compiled a large data set of critical micelle concentrations for aqueous surfactant systems providing a great point of reference for formulators of surfactant systems [2].

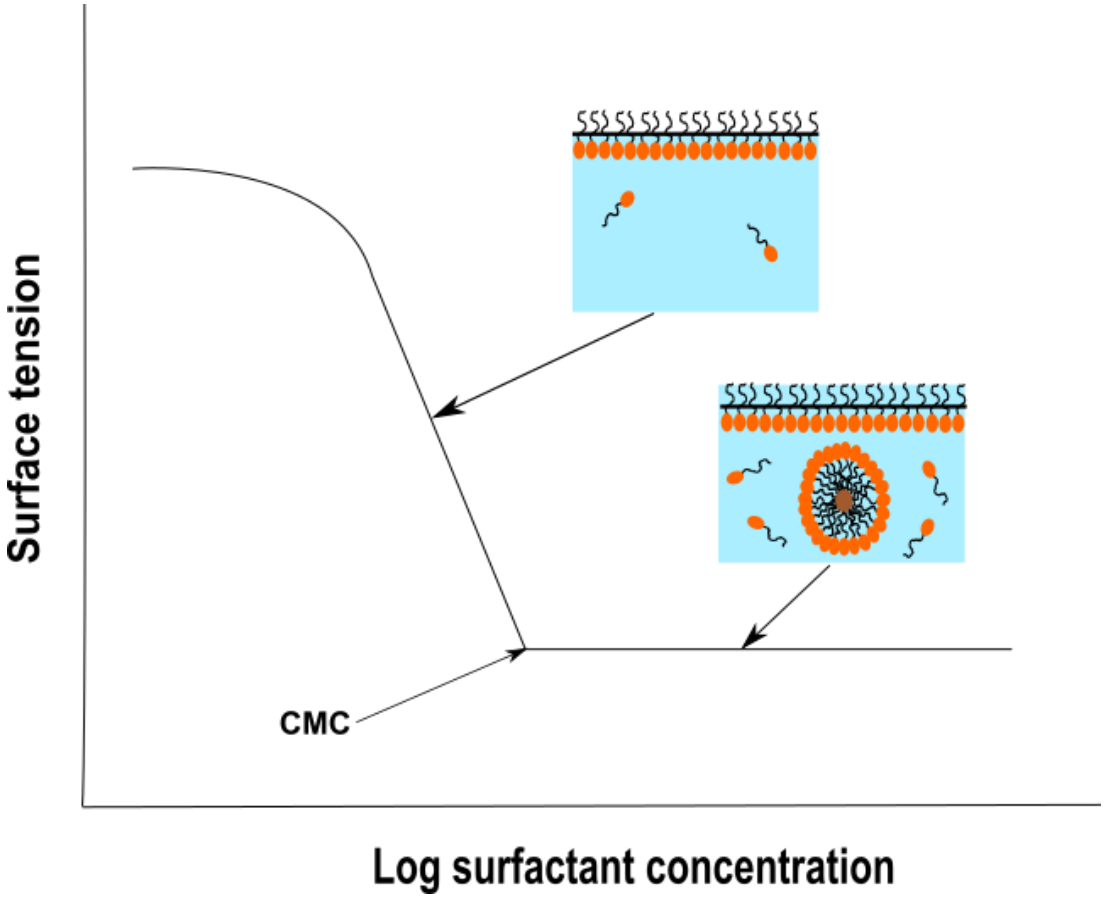

Figure 1.1: Schematic of surface tension vs the surfactant concentration of the system.

Micellisation minimises the free energy of the system by reducing the contact of the hydrophobic tails with water, explored by Tanford extensively and known as the hydrophobic effect [3]. It is energetically unfavourable to solvate hydrocarbon tails of surfactants in an aqueous solution. Therefore, the tails of the surfactants in the bulk arrange themselves into aggregates via the hydrophobic effect. This produces the oily

cores in micelles or the reverse situation if the bulk solution is oil. It should be noted that as the surfactant concentration increases past the CMC the chemical potential no longer changes and as a result, as can be seen in figure 1.1, the surface tension remains constant.

1.1.2 Solubilisation capacity

Knowledge of the solubilisation capacity of a microemulsion for model oils and crude oils gives indication of the efficacy of the microemulsion systems ability to mobilise oil for enhanced oil recovery. Solubilisation can be defined in our case as the dissolving of crude oil through interactions with micelles of the microemulsion system to create a thermodynamically stable isotropic solution with reduced thermodynamic activity of the crude oil. Importantly, it means a substance, such as crude oil, usually insoluble in water, can be dissolved in water when a microemulsion is formed whilst remaining thermodynamically stable.

Solubility of an insoluble substance in a surfactant solution such as our limonene microemulsion is negligible at concentrations below the critical micelle concentration. Once the critical micelle concentration is reached, the solubility of a substance increases linearly with increased surfactant concentration, showing that solubility is reliant upon micelle formation [4].

The solubilisation capacity can be influenced by many factors. The geometry of the micelle plays a key role. Mukerjee comments that if the Laplace pressure arising from a curved surface is lowered, then the interfacial tension also decreases and so solubilisation capacity will increase [5].

The surfactant structure impacts the solubilisation capacity of a microemulsion. As crude oil will be solubilised in the interior of an oil-in-water micelle, it is logical to expect that factors that increase the size of the micelle - such as surfactant head group size or chain length - increase the solubilisation capacity. Saito and Shinoda investigated the effects of several parameters for the solubilisation of heptane with non-ionic surfactants [6]. Saito and Shinoda found that although the hydrocarbon chain length

is an important factor for solubilisation, there needs to be a balance struck between the hydrocarbon chain length and oxyethylene chain length for a given temperature.

The temperature in the system for non-ionic surfactants effects the solubilisation power of the micelle in a microemulsion system. As the temperature is raised, the solubilisation capacity increases, increasing more dramatically the closer to the cloud point of the surfactant [6]. The increase in solubilisation capacity with temperature due to a change in the preferred curvature of the interface. As temperature increases, the headgroups become less strongly hydrated, reducing the preferred curvature and increases the micelle size. When the cloud point is reached, the preferred curvature is zero. The surfactants will no longer form micelles and instead form lamellar phases, which separate out of solution as large aggregates. The degree of hydration for the hydrophilic head is insufficient to solubilise the hydrocarbon chain and leads to a cloudy appearance [7].

1.1.3 Micelle fusion process

The kinetics processes in micellar systems have been studied extensively [8]– [12]. Rharbi and Winnik used stopped-flow fluorescence to determine the solute exchange between Triton X-100 (TX100) micelles using a pyrene probe [13], [14]. Rharbi and Winnick propose three distinct mechanisms for the exchange of solute molecules between micelles in aqueous solution. The first mechanism involves rapid exchange of monomers between the micelles and water phase, first theorised by Aniansson and Wall [11], [12]. The second mechanism involves the fragmentation of micelles into ‘sub micelles’. The sub-micelles can either grow through monomer uptake or fuse with other sub-micelles. The third mechanism describes a ‘super micelle’ formation in which two micelles approach one another, fuse to form a ‘super micelle’ and exchange their contents, then fragment to normal micelles.

In microemulsions, these ‘super micelles’ are often known as ‘transient dimers’. Microemulsions can solubilise additional oil through transient dimer formation. The existence of transient dimers has been inferred from experiments in which a pyrene-labelled triglyceride is incorporated into micelles of Triton X-100 [6]. Micelles collide

on a regular basis and dimers are stable long enough to exchange the pyrene molecule.

Griffiths et al. produced a series of papers to describe the possible pathways for the kinetics of C_nE_m micelle formation and breakdown after dilution [16]– [18]. Griffiths et al. found a discrepancy between their experimental results and predictions of the traditional Becker-Döring model of stepwise monomer loss. Griffiths et al. proposed a new pathway, similar to Rharbi and Winnick, for re-equilibration of micelles on timescales which have been observed with a stopped-flow fluorescence relaxation technique. Micelles will form at different stages on distinct timescales. The initial pathway involves a conventional nucleation of monomers to form aggregates. Once micelles are formed, additional micelle formation is catalysed by existing micelles. A micelle will swell through monomer addition and break up into smaller micelles. The smaller micelles will add monomers to reach equilibrium. The mechanism of micelle swelling, breaking and subsequent monomer addition has a lower energy barrier than the aggregation of monomers.

Fletcher et al. describes the steps involved in the exchange of contents between micelles [19]. The observed time constant for the process is described as the sum of each step and the collision between the two micelles is governed by diffusion. The coalescence process is broken into formulation of a droplet encounter pair, which coalesces to form a transient dimer. The coalescence of the encounter pair is proposed to proceed via an “hourglass” transition state. A schematic of the proposed interaction between two droplet encounter pairs by Fletcher et al. has been redrawn for a possible case for two limonene microemulsion droplets colliding in figure 1.2.

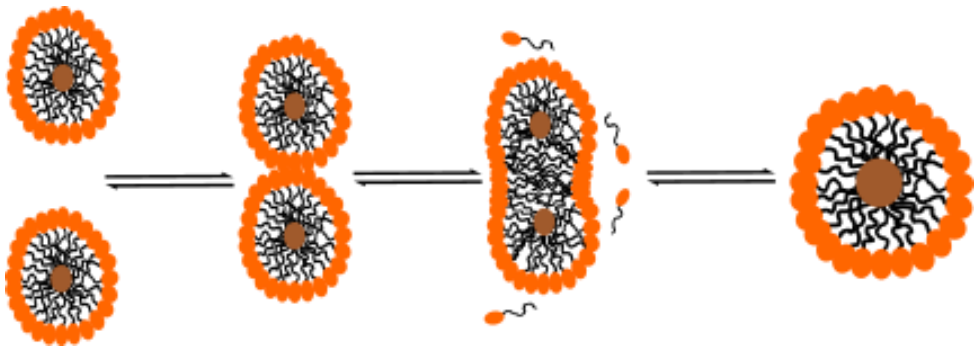

Figure 1.2: Schematic described by Fletcher et al. redrawn for two microemulsion droplets colliding, forming transient super micelles, exchanging contents and subsequent separation.

Second-order rate constant increases with increasing “stickiness” of collisions, which enhances the formation of an encounter pair, and for factors which reduce the energy cost of the transition state.

Fletcher et al. proposed that the inter-droplet interactions are weakest at the solubilisation phase boundary and become more attractive as the cloud point is approached, explaining some part for the temperature dependence of the rate of dimer formation. Another explanation proposed by Fletcher et al. for the rate increase when moving away from the solubilisation phase boundary may be the energy penalty when forming the transition state. The energy penalty originates from the deformation of the surfactant film from shear, bending or surface area changes. Fletcher explains that the monolayer bends to form regions of highly curved films when transitioning to a dimer. The magnitude depends on the spontaneous curvature and rigidity of the surfactant monolayer. At the solubilisation phase boundary, the curvature is close to spontaneous curvature and the energy required to bend the interface to the transition state is at maximum. Whereas, at temperatures away from the solubilisation phase boundary spontaneous curvature is less than the actual curvature and so the energy penalty decreases when forming the transition state.

When the transient dimer is formed, the interfacial area of the transient dimer will be lower than the interfacial area of the two separate droplets. As the surfactant monolayer is in a close-packed formation, desorption of surfactant from the interface can accommodate the lower interfacial area. This will cause an increase in the overall energy barrier to form a transient dimer, justifying the assumption that coalescence is easier if the surfactant is able to desorb from the surface more easily.

The rate of exchange for droplets of a water-in-oil microemulsion has been measured by Fletcher et al. [20]. The rate of exchange could be characterised by a second-order rate constant occurring on a millisecond timescale. Fletcher et al. inferred that the rate-limiting step in the process was the opening of the surfactant layer through activation enthalpies and entropies derived from Arrhenius plots. The kinetic measurements made by Fletcher et al. used a custom built stopped-flow instrument similar to the experiments we employ.

1.2 Microemulsions

A microemulsion is a liquid dispersion of an aqueous phase and oil phase, combined with a surfactant and often a cosurfactant. They could be considered as small emulsions: they have droplet dispersions of either oil-in-water or water-in-oil, much like emulsions, with a droplet size of typically 10–100 nm. However, unlike emulsions, microemulsions if left over time, will not undergo phase separation as they are thermodynamically stable. Emulsions also tend to have a milky dispersed phase with more work required to form than the more translucent microemulsion, which in the right conditions can form spontaneously [4]. There were some authors that believed a solution must be transparent in appearance to qualify as a microemulsion [21], [22]. However, Winsor deduced that transparency was not needed with stable translucent micellar solution. Winsor went onto describe that the degree of translucency of a microemulsion is a result of the size and configuration of the micelles [23].

Microemulsions should not be confused with nanoemulsions, despite their namesake suggesting micron size, the particles in microemulsions tend to range from 10–100 nm. Nanoemulsions particle size typically range from 30–1000 nm [24]. Unlike microemulsions, nanoemulsions are thermodynamically unstable and should be considered as conventional emulsions that contain very small particles.

1.2.1 Winsor phase studies of microemulsions

Microemulsions have differing phase behaviours depending on a number of factors e.g., temperature/type of surfactant. Microemulsion phase behaviour can be classified using the Winsor system. The Winsor classification system identifies four general types of phase equilibria in microemulsions:

Winsor I: An oil-in-water (O/W) microemulsion is formed as the surfactant is preferentially soluble in water. There is a surfactant-rich aqueous phase which is in equilibrium with an oil phase where surfactant concentration is low. The aqueous phase exists as the continuous phase.

Winsor II: A water-in-oil (W/O) microemulsion is formed as the surfactant is preferentially soluble in oil. There is a surfactant-rich oil phase in equilibrium with the aqueous phase where surfactant concentration is low. The oil phase exists as the continuous phase.

Winsor III: This can also be called a middle-phase microemulsion. A Winsor III microemulsion consists of three discrete phases. There is an excess water and oil phase with low surfactant concentration and a surfactant-rich middle-phase in equilibrium. The middle phase is bicontinuous.

Winsor IV: Exists as a single phase when the surfactant concentration is high, thus there is no excess phase present.

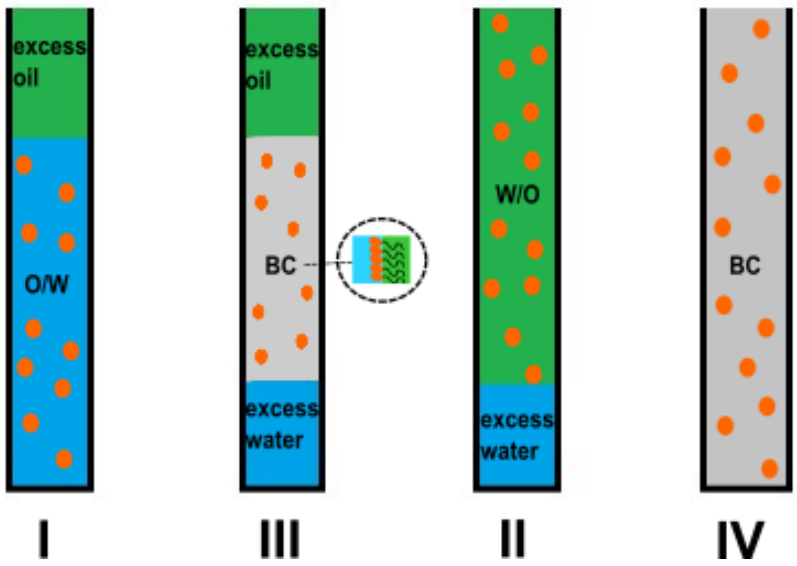

Figure 1.3: Schematic diagram of Winsor-type phase behaviour of microemulsions, *BC* is the bicontinuous phase.

Winsor formed much of the early work in defining the conditions required for microemulsion formation, originally describing three kinds, spherical water external, spherical oil external and lamellar [23].

Winsor later described spherical micelles can arrange themselves in equilibrium to form cubic phases and cylindrical micelles can arrange into a hexagonal lattice structure [25]. There have been advancements since to give further classification of discrete microemulsion structures, such as the sponge phases reported by Hellweg [26], further exploration of cubic structures [27], and a greater understanding of bicontinuous microemulsion phases [28] [29].

1.2.2 Ultra-low interfacial tension in microemulsions

A fundamental property of microemulsions is their ultra-low interfacial tension between the oil and aqueous phase, referred to as ULIFT. Sometimes, there is a middle phase between the excess oil and excess aqueous phase, which is a bicontinuous structure of interconnected aqueous and oleic phases. The interfacial tension (IFT) can be defined as the work required to increase the size of the interface between two immiscible phases, specifically at the boundary of two immiscible liquids. At the interface, the oil interacts through dispersion forces both with other oil molecules and with water. The oil-water interfacial tension arises from hydrogen bonding and can be both an entropic and an enthalpic effect depending on the curvature of the interface.

The interface will tend to become more spherical to make its surface energy as low as possible. The surfactant acts to lower the surface tension at the interface; the amphiphilic nature of surfactants lowers the free energy of the system it is dissolved in. In aqueous solution, the hydrophobic group of the surfactant causes repulsion of the surfactant with water and so reduces the work required for a surfactant to be transferred from the bulk to the surface. The free energy will continue to decrease until the chemical potentials of the surfactant in the bulk and surface are equal and no more surfactant adsorbs. The presence of the hydrophilic group interacts with the water, which can prevent the formation of separate phases to give micelles, though some hydrophilic groups such as alcohols form separate phases over micelles. For C_nE_m surfactants the chain length and temperature determine whether micelles form or phase separation occurs.

Chun Huh developed the relationship of solubilisation power of the surfactant with IFT [30]. Huh predicts the IFT between the microemulsion phase and excess phase is inversely proportional to the square of solubilisation ratio. The Chun Huh equation can be used to estimate the interfacial tension between the microemulsion phase and excess phase, therefore being able to determine quickly if a microemulsion system is suitable for enhanced oil recovery.

To recover residual oil from microemulsion injection, the interfacial tension must be below 10^{-2} mN m^{-1} [31]. Rosen et al. go into an in-depth description of the fundamental properties required to obtain ultralow interfacial tension [32]. They measured the

interfacial tension using a spinning-drop tensiometer on a range of surfactants, with three oil phases of decane, dodecane and tetradecane. The results from Rosen et al. prove that ULIFT can be achieved at very low surfactant concentrations when certain mixtures of surfactants are used. The structure of the micelles has an impact on the IFT, notably the packing parameter. The packing parameter is defined as $v_o/a_o l_c$, where v_o is the surfactant tail volume, a_o is the surface area of the head group at the micelle-solution interface and l_c is the fully extended tail length. When the packing parameter was close to 1, the micelle structures were found to be lamellar, allowing a maximum amount of the oil phase to be incorporated and as a result reduces the IFT close to zero [32].

At very low surface tension, the shape of the interface is dictated by the bending energy. A curved surface is described by two principal radii of curvature, R_1 and R_2, with the planes intersecting each other at right angles. The curvatures are defined as $c_1 = 1/R_1$ *and* $c_2 = 1/R_2$ [33]. If there are no constraints placed on an interface, then the curvature that minimises the free energy is called the spontaneous curvature c_0. The type of microemulsion that is formed is dictated by the spontaneous curvature of the interface. When c_0 is positive an oil-in-water microemulsion forms. When c_0 is negative a water-in-oil microemulsion is formed. For bicontinuous microemulsions $c_0 = 0$. Zero mean curvature does not mean that the interface must be planar: c_1 and c_2 can have equal magnitudes but opposite signs. Surfaces with zero mean curvature are called minimal surfaces. Since $R_1 = -R_2$ there is no Laplace pressure difference across the interface and the oil and water in the middle phase are at ambient pressure.

To bend the surface, there is an energy penalty to pay, described by two elastic moduli: the bending modulus *(k)* and the Gaussian modulus *($\bar{k}$).* The bending modulus represents the energy required to bend a unit area of surface area by a unit amount. The Gaussian modulus accounts for film topology. The surface will adopt a shape to minimise the bending free energy defined by equation 1.1 below [33].

$$F = \int \left[\frac{k}{2}(c_1 + c_2 - 2c_0)^2 + \bar{k}c_1c_2\right] dA \qquad (1.1)$$

Co-solvents are often needed to make a surfactant soluble enough for chemical flooding in enhanced oil recovery. A particular molecule chosen as a co-solvent may also have the complementary effect of lowering the surfactants IFT, therefore also

working as a co-surfactant. Sahni et al. discuss the need for co-solvents to make the surfactant solution stable, stressing the most important requirement for successful oil recovery is to have a “clear, stable single phase to transport in a reservoir over long distances” [34]. The co-solvent will preferentially partition between the hydrophobic tails of surfactants at the interface; this reduces the formation of viscous structures which are poor for mobility, such as gels or liquid crystals. Sahni et al. also suggest that trends in physical behaviour of a particular microemulsion is unique to a particular crude oil; therefore, microemulsion phase behaviour measurements should be made to determine the optimum formulation for a particular reservoir.

1.2.3 Shape and geometry of micellar aggregates

As my project aims to characterise the limonene microemulsions formed, it is important to understand the properties that determine the geometry of micelles. The shape a particular micelle favours, whether it is spherical, rod-like, or lamellar, depends on packing parameters. Israelachvili introduced a simple theoretical model to predict the structure amphiphiles take in self-assembly, accounting for thermodynamics, free energies, and geometrical constraints [35].

Israelachvili first set out to describe the thermodynamics of self-assembly by referring to work by Tanford [36], which considers each aggregate to be a distinct species with its own free energy given by $N\mu_N^0$, where *N* is the aggregation number and μ_N^0 is the standard chemical potential of the aggregate. It is shown that if aggregates are energetically favoured, then the transition from disaggregated to aggregated state is dependent on a balance of entropy and energy, and there are two cases where large aggregates can be formed with respect to μ_N^0.

1. The standard chemical potential of the aggregate has a minimum value at an aggregation number denoted as *M* by Israelachvili. This minimum value arises from competition between the hydrophobic free energy of the hydrocarbon tails and the head group interactions from electrostatic or geometric constraints. When the distribution of micelle size is small then an assumption of the mean micelle aggregation number being equal to *M* can

be made, allowing the critical micelle concentration to be approximated neglecting polydispersity.

2. The other case for chemical potential of the aggregate is when the chemical potential decreases monotonically towards a limiting value, the aggregation number moves towards infinity. It is noted that this form arises as a result of end effects contributing to μ_N^0 for certain micelle shapes such as rod-like micelles where the energy per monomer decreases.

Israelachvili also formulated a model for the free energy contributions in the aggregated and dispersed states of micelles. The aggregated state was considered first. The contributions of the free energy in the aggregate state are divided into two terms, the bulk and surface terms. The bulk free energy per amphiphile is succinctly reduced to be a function of temperature and number of carbon atoms. The surface contributions are then subdivided into two contributions: 1) attractive forces from the hydrocarbon tail or surface tension forces; 2) Repulsive electrostatic forces working against each other.

The driving force behind considering geometric constraints is a packing parameter for self-assembly, as otherwise the spherical micelle shape would always be favoured based on thermodynamic arguments (which is known to not always be the case). Israelachvili deduced that, assuming the system has little polydispersity, a micelle will form the smallest shape and size, also assuming that the mean area per amphiphile will always be close to the optimum area per head group at the micelle–water interface (termed the critical packing shape). A balance is needed for the optimum area per head group, as with a smaller area the less the water can interact with the oil core; however, as the area decreases the more likely head groups are to repel each other. It is also noted that for other shapes other than spherical micelles to be considered, there must be a critical aggregation number where a spherical shape would be forbidden.

With these assumptions made, Israelachvili formed two criteria for allowed aggregates:

1. “No point in the structure can be farther from the hydrocarbon water surface than l_c”. l_c refers to the fully extended length of the hydrocarbon chain.
2. “The total hydrocarbon core volume of the structure V and the total surface area A must satisfy $V/v = A/a_0 = N$.” v is the hydrocarbon core volume, a_0 is the optimum area and N is the critical aggregation number.

Local packing criteria need to be applied to deduce if amphiphiles are packing energetically favourably across the whole of the aggregate and not just on average. Therefore, a packing equation can be derived given in equation 1.2. v is the volume of the micelle hydrocarbon core, a is the surface area, l_c is the length of the hydrocarbon tail and R_1 and R_2 are the local radii of curvature in the micelle [35].

$$\frac{v}{a} = l_c \left[1 - \frac{l_c}{2}\left(\frac{1}{R_1} + \frac{1}{R_2}\right) + \frac{{l_c}^2}{3R_1R_2}\right] \tag{1.2}$$

Israelachvili then goes on to describe a shape that satisfies all the criteria just mentioned as an ellipse of revolution, the properties of which have transitional shapes, from spheres to infinite cylinders. Although ellipsoids are quite a common shape for micelles ($v/l_c a_0$ between 1/3 and ½), when oil is introduced to the micelle, R is no longer required to be less than l_c, meaning spheres are then favoured.

Tanford proposed a relationship between the volume of the hydrocarbon core, v, the number of carbon atoms in a (linear) hydrocarbon tail, n, and the length, l_c, of the hydrocarbon chain, [27].

$$v = (27.4 + 26.9n)\ \text{Å}^3\ per\ hydrocarbon\ chain$$

$$l_c = (1.5 + 1.265n)\ \text{Å}\ per\ hydrocarbon\ chain$$

The calculation of the volume occupied by the alkyl chain tail in the hydrocarbon core was derived by Tanford from previous data taken by Reiss-Husson and Luzzati [38]. The length of the hydrocarbon chain equation is based on the maximum extension of the hydrocarbon chain. Firstly, the distance between alternate carbon atoms (given as

2.53 Å) in the chain is considered, the Van der Waals radius of the terminal methyl group is also added (given as 2.1 Å), and then half of the bond length to the atom that is not in the hydrocarbon core (given as roughly equal to 0.6 Å).

This early work undertaken by Tanford and Israelachvili was taken a step further by Mitchell and Ninham to include vesicle and microemulsions, with an observation of trends through changing parameters such as temperature, oil type and addition of cosurfactants [39].

In a dilute solution, the aggregates are considered not to interact with each other, allowing the distribution of aggregates to be determined by the law of mass action. For any aggregation number, the shape that occurs with minimum energy is much more favoured than other shapes possible and the idea of infinite aggregates, introduced by Tanford and Israelachvili previously, is also possible. Mitchell and Ninham provide mathematical justification for this theory for one, two- and three-dimensional cases.

In the simplest case, μ_N^o is described as the sum parts of the bulk contributions, surface contributions, curvature contributions and packing constraints. To obtain an overall prediction for the shape an aggregate will take, Ninham and Mitchell refer to their work with Israelachvili [35]:

Spherical micelles	$v/a_0 l_c < 1/3$
Cylindrical micelles	$1/3 < v/a_0 l_c < 1/2$
Bilayers and vesicles	$½ < v/a_0 l_c < 1$
Inverted structures	$v/a_0 l_c > 1$

Ninham and Mitchell point to several problems with this expression, particularly in the case of vesicles. The first issue is the assumption that curvature effects, due to head-group interactions are small, if they are not then this theory breaks down. It is also not certain that curvature effects have only head-group contributions, there could be hydrocarbon tail effects which could be having an equal impact.

A molecular thermodynamic model can also be used to give a more in-depth account of the different contributions that sum to give the total free energy of aggregation. Nagarajan and Ruckenstein produced a model that predicts the aggregation behaviour of C_nE_m non-ionic surfactants [37]. Nagarajan and Ruckenstein first establish an aggregate size distribution equation given in equation 1.3. *Yg* is the mole fraction of

aggregates in solution and $\Delta\mu_g^{\ominus}$ is the difference in standard chemical potential between a surfactant molecule in an aggregate and a singly dispersed molecule in water.

$$Y_g = Y_1^g exp\left(-\frac{g\Delta\mu_g^{\ominus}}{kT}\right) \tag{1.3}$$

The shape of the aggregate size distribution is determined by the term $\mu_g^{\ominus}$(g). Nagarajan and Ruckenstein then identify six contributions to $\Delta\mu_g^{\ominus}$ which affect the shape of the aggregate size distribution. These are the free energy of tail transfer; the free energy of surfactant tail deformation; solvent mixing free energy; head group deformation free energy; head group steric interaction free energy; the aggregate core-water interfacial free energy.

1.2.4 Geometry of microemulsions

The classic theory for micellar aggregate shape and size has been discussed in §1.2.3. This can be extended to the case of microemulsions. Ninham and Mitchell consider most microemulsions to be monodisperse, with the size of the drops not just determined by amount of oil, but a consideration of the ratios of oil:water:surfactant.

It gets more complicated to determine which aggregate forms, as the microemulsion is a multicomponent system and so the overall composition of the mixture needs to be considered. The most likely aggregate to form is one that works to have a minimum free energy per molecule of surfactant and minimum free energy per molecule of oil $\mu_{M,N}^{o}$. The case for an oil-in-water microemulsion, where the oil is in excess, is a simple one as the chemical potential of the oil is equal to that in the bulk phase. To determine the composition of the system, Ninham and Mitchell describe the possible compositions an aggregate can take [39]. Determining the composition of aggregates is a difficult task as the chemical potential of the monomers needs to be determined. Ninham and Mitchell propose an indirect method by assuming the chemical potential of one species. The composition of the corresponding aggregate can then be determined. This is iterated until the overall composition of the system is calculated.

They give proof of this by using an example of a microemulsion with excess oil. The known chemical potential of the oil is used; therefore the aggregates must take the form which minimises the free energy of the system. The corresponding chemical potential of the surfactant is then equal to this minimum free energy value calculated found for the oil.

Ninham and Mitchell also discuss packing constraints in microemulsion drops to create an expression for the chemical potential of both molecules of oil and surfactant. They use the simplest geometry for a microemulsion aggregate with respect to oil-in-water and water-in-oil aggregates which has been redrawn in figure 1.4 [39].

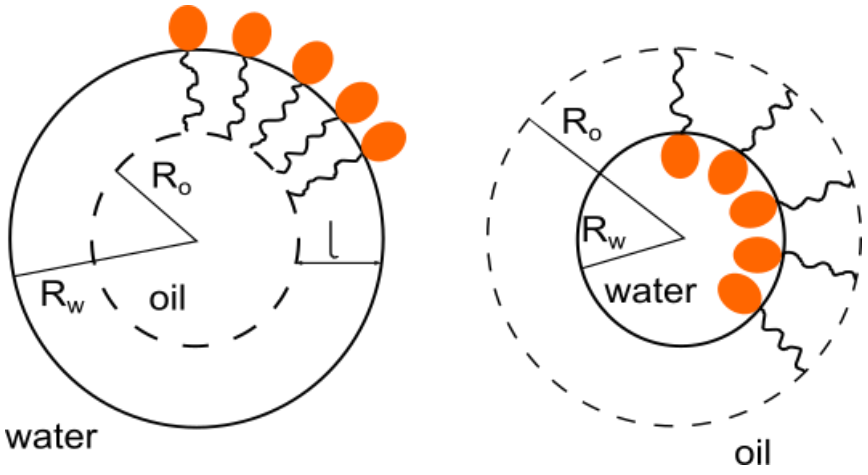

Figure 1.4: A simple depiction of the geometry of an oil-in-water and water-in-oil microemulsion reproduced with from Ninham and Mitchell [39] . Details of permission can be found at the end of the thesis in permission table.

Curvature plays a key role in determining the dimensions of microemulsion drops. Curvature can affect the allowed optimal structures in some circumstances. Ninham and Mitchell go on to give a thorough mathematical argument to characterise curvature for ionic and non-ionic drops. When curvature is considered, normal drops are found where inverted drops are expected, and larger drops are found when zeroth – order theory gives micelles. Ninham and Mitchell compare curvature effects for microemulsion drops and vesicles, they found that curvature effects play a much larger role for microemulsions than for vesicles.

A more modern approach to shapes of microemulsions and their phases use an extension of the work by Helfrich which determined the curvature free energy of fluid membranes, focusing on vesicles [40]. One form of the Helfrich Hamiltonian equation for spherical objects can be seen in equation 1.4 below to describe the curvature

energy derived by Jung [41]. *k* is the bending modulus, R_0 is the spontaneous radius of curvature.

$$G(R) = 4\pi R^2 \left[\frac{k}{2}\left(\frac{2}{R} - \frac{2}{R_0}\right)^2 + \frac{\bar{k}}{R^2} \right] \quad (1.4)$$

Lade and Krawietz explain that whilst Helfrich's theory of the curvature energy allows for many microemulsion structures, it does not describe a middle phase microemulsion in equilibrium of excess oil and water phases [42]. Lade and Krawietz introduce a new bending energy function to describe the coexistence of the bicontinuous microemulsion with both water and oil.

Nagarajan and Ruckenstein's molecular thermodynamic approach built on their previous work mentioned earlier for aggregates of C_nE_m, predicting structural and compositional characteristics of microemulsions which can be used for oil-in-water, water-in-oil and bicontinuous microemulsions [43].

They describe their model as follows:

"We take into account chain packing, which depends on the curvature of the aggregates, the self-association of alcohol in the oil, the penetration of the interfacial layer region of the microemulsion by the oil molecules, their effects on chain packing and interfacial energies, and the hard-core interactions among the droplets."

Their model was able to determine many microstructural features such as droplet radius, thickness of interfacial layer and distribution of the components of the microemulsion system in differing micro domains.

More recent studies introduce approaches to account for lipophilic contributions to the free energy of solubilization in micelles using a microscopic approach of Hamaker [34]. The lipophilic terms are defined in terms of molecular interactions and molecular properties and are consistent with the Hydrophilic-Lipophilic-Difference equations often employed by formulators to predict the phase behaviour of microemulsions. Acosta et al. use this model to determine the solubilisation of oil in micelles but also note that although the work of Ninham and Mitchell, and Nagarajan and Ruckenstein to attempt to address intramicellar interactions at low aggregate concentration, lipophilic interactions are one of the most important driving forces for self-assembly. They also state that to calculate intramicellar interactions for a spherical micelle, the

Van der Waals interactions between a spherical core and the tail shell must be accounted for. Van der Waals integration configurations were made to calculate these intramicellar interactions [45].

As discussed throughout this section, the most common microemulsion structures consist of spherical droplets with either excess oil or excess water. Langevin notes that there is also a rare case whereby the structure is made of elongated cylinders or sponge-like lamellae [46]. These structures are found when the spontaneous curvature of the surfactant layer is near zero. The cylinder structures are found when the system is oil continuous, when the cylinders are swollen with water they deform into droplets. Sponge-like lamellae can be found in oil continuous or water continuous systems and swollen to a large degree.

1.2.5 Thermodynamic stability of microemulsions

A key characteristic of microemulsions is their thermodynamic stability. It is important to consider the Gibbs free energy for spontaneous microemulsion formation. Ruckenstein et al. investigated the origin of the stability of microemulsions using a thermodynamic approach, studying the free energy of formation of the double layers, Van der Waals and double layer interaction potentials and the entropy of formation of the microemulsion [47]. Ruckenstein detailed further work on the thermodynamic stability of microemulsions, to prove that the dilution effect is the main factor for the thermodynamic stability of microemulsions [48]. Ruckenstein explains that whilst the accumulation of the surfactant and cosurfactant at the interface reduces the interfacial tension; it also means there is a large decrease in the concentration of surfactant and cosurfactant in the two bulk phases. The chemical potential of the surfactant and cosurfactant also lowers both at the interface and the bulk phases, decreasing the free energy of the system. If the decrease of free energy is large enough to overcome the positive free energy from surface tension, then spontaneous formation of microemulsions occurs. Ruckenstein described this as the dilution effect. Most investigators do not apply as rigorous an investigation as Ruckenstein to determine if their microemulsion system is thermodynamically stable, instead associating stable with stable equilibrium. Fay et al. succinctly noted that an isolated system has reached

equilibrium when no further macroscopic changes occur [49]. Thus, if the microemulsion system does not appear to undergo further chemical reaction or indicate a phase change over a long period of time, it can be assumed the microemulsion is thermodynamically stable.

References

[1] D. R. Perinelli, M. Cespi, N. Lorusso, G. F. Palmieri, G. Bonacucina, and P. Blasi, "Surfactant Self-Assembling and Critical Micelle Concentration: One Approach Fits All?," *Langmuir*, vol. 36, no. 21, pp. 5745–5753, Jun. 2020, doi: 10.1021/ACS.LANGMUIR.0C00420/SUPPL_FILE/LA0C00420_SI_001.PDF.

[2] P. Mukerjee and K. J. Mysels, "Critical micelle concentrations of aqueous surfactant systems," National Standard reference data system, 1971.

[3] C. Tanford, *The hydrophobic effect: formation of micelles and biological membranes 2d ed*. J. Wiley., 1980.

[4] M. J. Rosen, *Surfactants and interfacial phenomena*, vol. 40. 1989. doi: 10.1016/0166-6622(89)80030-7.

[5] P. Mukerjee, "Solubilization in Aqueous Micellar Systems," in *Solution Chemistry of Surfactants: Volume 1*, K. L. Mittal, Ed. Boston, MA: Springer New York, 1979, pp. 153–174. doi: 10.1007/978-1-4615-7880-2_6.

[6] H. Saito and K. Shinoda, "The solubilization of hydrocarbons in aqueous solutions of non-ionic surfactants," *Journal Colloid Interface Sci*, vol. 24, no. 1, pp. 10–15, May 1967, doi: 10.1016/0021-9797(67)90271-8.

[7] W. N. Maclay, "Factors affecting the solubility of non-ionic emulsifiers," *J Colloid Sci*, vol. 11, no. 3, pp. 272–285, Jun. 1956, doi: 10.1016/0095-8522(56)90052-6.

[8] R. Pool and P. G. Bolhuis, "Sampling the kinetic pathways of a micelle fusion and fission transition," *Journal Chem Phys*, vol. 126, no. 24, p. 244703, Jun. 2007, doi: 10.1063/1.2741513.

[9] M. Chen, X. Zhang, and H. Zhang, "Fusion and clustering of spherical micelles by extruding through a cylindrical channel," *RSC Adv*, vol. 9, no. 42, pp. 24394–24400, Aug. 2019, doi: 10.1039/C9RA05146E.

[10] L. R. Parent *et al.*, "Directly Observing Micelle Fusion and Growth in Solution by Liquid-Cell Transmission Electron Microscopy," *Journal Am Chem Soc*, vol. 139, no. 47, pp. 17140–17151, Nov. 2017, doi: 10.1021/JACS.7B09060/SUPPL_FILE/JA7B09060_SI_012.MOV.

[11] E. A. G. Aniansson and S. N. Wall, "On the kinetics of step-wise micelle association," *Journal of Physical Chemistry*, vol. 78, no. 10, pp. 1024–1030, 1974, doi: 10.1021/j100603a016.

[12] E. A. G. Aniansson *et al.*, "Theory of the kinetics of micellar equilibria and quantitative interpretation of chemical relaxation studies of micellar solutions of ionic surfactants," *Journal of Physical Chemistry*, vol. 80, no. 9, pp. 905–922, 1976, doi: 10.1021/j100550a001.

[13] Y. Rharbi and M. A. Winnik, "Solute exchange between surfactant micelles by micelle fragmentation and fusion," *Adv Colloid Interface Sci*, vol. 89–90, pp. 25–46, Jan. 2001, doi: 10.1016/S0001-8686(00)00054-3.

[14] Y. Rharbi, M. Li, M. A. Winnik, and K. G. Hahn, "Temperature Dependence of Fusion and Fragmentation Kinetics of Triton X-100 Micelles," 2000, doi: 10.1021/ja9942585.

[15] Y. Rharbi and M. A. Winnik, “Solute exchange between surfactant micelles by micelle fragmentation and fusion,” *Adv Colloid Interface Sci*, vol. 89–90, pp. 25–46, 2001, doi: 10.1016/S0001-8686(00)00054-3.

[16] I. M. Griffiths, C. J. W. Breward, D. M. Colegate, P. J. Dellar, P. D. Howell, and C. D. Bain, “A new pathway for the re-equilibration of micellar surfactant solutions,” *Soft Matter*, vol. 9, no. 3, pp. 853–863, 2013, doi: 10.1039/c2sm27154k.

[17] A. I. M. Griffiths, C. D. Bain, C. J. W. Breward, S. J. Chapman, and S. L. Waters, “AN ASYMPTOTIC THEORY FOR THE RE-EQUILIBRATION OF A MICELLAR SURFACTANT SOLUTION,” vol. 72, no. 1, pp. 201–215, 2012.

[18] I. M. Griffiths, C. D. Bain, C. J. W. Breward, D. M. Colegate, P. D. Howell, and S. L. Waters, “On the predictions and limitations of the Becker-Döring model for reaction kinetics in micellar surfactant solutions,” *J Colloid Interface Sci*, vol. 360, no. 2, pp. 662–671, 2011, doi: 10.1016/j.jcis.2011.04.074.

[19] S. Clark, P. D. I. Fletcher, and X. Ye, “Interdroplet exchange rates of water-in-oil and oil-in-water microemulsion droplets stabilized by pentaoxyethylene monododecyl ether,” *Langmuir*, vol. 6, no. 7, pp. 1301–1309, 1990, doi: 10.1021/la00097a019.

[20] P. D. I. Fletcher and J. F. Holzwarth, “Aggregation kinetics of oil-in-water microemulsion droplets stabilized by C12E5,” *Journal of Physical Chemistry*, vol. 95, no. 6, pp. 2550–2555, 1991, doi: 10.1021/j100159a082.

[21] D. O. Shah, A. Tamjeedi, J. W. Falco, and R. D. Walker, “Interfacial instability and spontaneous formation of microemulsions,” *AIChE Journal*, vol. 18, no. 6, pp. 1116–1120, Sep. 2018, doi: 10.1002/aic.690180605.

[22] J. H. Schulman, W. Stoeckenius, and L. M. Prince, “Mechanism of Formation and Structure of Micro Emulsions by Electron Microscopy,” *Journal Phys Chem*, vol. 63, no. 10, pp. 1677–1680, Oct. 1959, doi: 10.1021/j150580a027.

[23] P. A. Winsor, *Solvent properties of amphiphilic compounds.* London: Butterworths, 1954.

[24] D. J. McClements, “Nanoemulsions versus microemulsions: Terminology, differences, and similarities,” *Soft Matter*, vol. 8, no. 6. pp. 1719–1729, Feb. 14, 2012. doi: 10.1039/c2sm06903b.

[25] P. A. Winsor, “Liquid Crystallinity in Relation to Composition and Temperature in Amphiphilic Systems,” *Molecular Crystals and Liquid Crystals*, vol. 12, no. 2, pp. 141–178, Jan. 1971, doi: 10.1080/15421407108082769.

[26] T. Hellweg, “Phase structures of microemulsions,” *Curr Opin Colloid Interface Sci*, vol. 7, no. 1–2, pp. 50–56, 2002, doi: 10.1016/S1359-0294(02)00004-3.

[27] J. Tabony, “Formation of cubic structures in microemulsions containing equal volumes of oil and water,” *Nature*, vol. 319, p. 400, Jan. 1986.

[28] B. Lindman, K. Shinoda, U. Olsson, D. Anderson, G. Karlström, and H. Wennerström, “On the demonstration of bicontinuous structures in microemulsions,” *Colloids and Surfaces*, vol. 38, no. 1, pp. 205–224, Jan. 1989, doi: 10.1016/0166-6622(89)80154-4.

[29] C. G. Vonk, J. F. Billman, and E. W. Kaler, “Small angle scattering of bicontinuous structures in microemulsions,” *Journal Chem Phys*, vol. 88, no. 6, pp. 3970–3975, Mar. 1988, doi: 10.1063/1.453846.

[30] C. Huh, “Interfacial tensions and solubilizing ability of a microemulsion phase that coexists with oil and brine,” *Journal Colloid Interface Sci*, vol. 71, no. 2, pp. 408–426, Sep. 1979, doi: 10.1016/0021-9797(79)90249-2.

[31] W. R. Foster, “A Low-Tension Waterflooding Process,” *Journal of Petroleum Technology*, vol. 25, no. 02, pp. 205–210, 1973, doi: 10.2118/3803-PA.

[32] M. J. Rosen, H. Wang, P. Shen, and Y. Zhu, “Ultralow interfacial tension for enhanced oil recovery at very low surfactant concentrations,” *Langmuir*, vol. 21, no. 9, pp. 3749–3756, 2005, doi: 10.1021/la0400959.

[33] S. HYDE *et al.*, “Chapter 1 - The Mathematics of Curvature,” S. HYDE, B. W. NINHAM, S. ANDERSSON, K. LARSSON, T. LANDH, Z. BLUM, and S. B. T.-T. L. of S. LIDIN, Eds. Amsterdam: Elsevier Science B.V., 1997, pp. 1–42. doi: https://doi.org/10.1016/B978-044481538-5/50002-2.

[34] V. Sahni, R. M. Dean, C. Britton, D. H. Kim, U. Weerasooriya, and G. A. Pope, “The role of co-solvents and co-surfactants in making chemical floods robust,” *Spe 130007*, no. 1976, 2010, doi: 10.2118/130007-MS.

[35] J. N. Israelachvili, D. J. Mitchell, and B. W. Ninham, “Theory of self-assembly of hydrocarbon amphiphiles into micelles and bilayers,” *Journal of the Chemical Society, Faraday Transactions 2: Molecular and Chemical Physics*, vol. 72, no. 0, pp. 1525–1568, 1976, doi: 10.1039/F29767201525.

[36] C. Tanford, “Micelle shape and size,” *Journal of Physical Chemistry*, vol. 76, no. 21, pp. 3020–3024, 1972, doi: 10.1021/j100665a018.

[37] R. Nagarajan and E. Ruckenstein, “Theory of surfactant self-assembly: a predictive molecular thermodynamic approach,” *Langmuir*, vol. 7, no. 12, pp. 2934–2969, Dec. 1991, doi: 10.1021/la00060a012.

[38] F. Reiss-Husson and V. Luzzati, “The structure of the micellar solutions of some amphiphilic compounds in pure water as determined by absolute small-angle X-ray scattering techniques,” *Journal of Physical Chemistry*, vol. 68, no. 12, pp. 3504–3511, 1964, doi: 10.1021/j100794a011.

[39] D. J. Mitchell and B. W. Ninham, “Micelles, vesicles and microemulsions,” *Journal of the Chemical Society, Faraday Transactions 2: Molecular and Chemical Physics*, vol. 77, no. 4, pp. 601–629, 1981, doi: 10.1039/F29817700601.

[40] W. Helfrich, “Elastic properties of lipid bilayers: theory and possible experiments,” *Z Naturforsch C*, vol. 28, no. 11, p. 693, 1973.

[41] H.-T. Jung, S. Y. Lee, E. W. Kaler, B. Coldren, and J. a Zasadzinski, “Gaussian curvature and the equilibrium among bilayer cylinders, spheres, and discs.,” *P. Natl. Acad. Sci. USA*, vol. 99, no. 24, pp. 15318–22, 2002, doi: 10.1073/pnas.242374499.

[42] O. Lade and A. Krawietz, “A bending elasticity approach to the three-phase coexistence of microemulsions,” *Journal Chem Phys*, vol. 115, no. 23, pp. 10986–10997, 2001, doi: 10.1063/1.1418730.

[43] R. Nagarajan and E. Ruckenstein, “Molecular Theory of Microemulsions,” *Langmuir*, vol. 16, no. 16, pp. 6400–6415, Aug. 2000, doi: 10.1021/la991578t.

[44] A. B. Troncoso and E. Acosta, “Van der Waals free energy model for solubilization of oil in micelles,” *Soft Matter*, vol. 11, no. 3, pp. 516–531, Dec. 2014, doi: 10.1039/C4SM02197E.

[45] A. B. Troncoso and E. Acosta, “The van der Waals Interactions in Sphere-Shell and Cone-Shell Configurations,” *Journal of Physical Chemistry B*, vol. 116, no. 48, pp. 14051–14061, Dec. 2012, doi: 10.1021/JP305534D.

[46] D. Langevin, “Microemulsions,” *Acc Chem Res*, vol. 21, no. 7, pp. 255–260, Jul. 1988, doi: 10.1021/ar00151a001.

[47] J. C. Chi. Eli Ruckenstein, “Microemulsions Stability of Microemulsions,” 1974.

[48] E. Ruckenstein, “The origin of thermodynamic stability of microemulsions,” *Chem Phys Lett*, vol. 57, no. 4, pp. 517–521, Aug. 1978, doi: 10.1016/0009-2614(78)85311-1.

[49] J. A. Fay, *Molecular thermodynamics.* Reading, MA: Addison-Wesley, 1965.

Chapter 2 Characterisation and phase behaviour of limonene microemulsions

2.1 Formulation of limonene microemulsion

2.1.1 Materials

Flotek provided the ultra-high purity D-limonene and a commercial linear alcohol ethoxylate (BIO-SOFT EC-600) $C_{12}E_7$. Isopropyl alcohol (IPA) was bought from Fischer Scientific UK (lab reagent grade). High-purity water was from an Elga Purelab Chorus 1 system.

Mass spectrometry and ^{1}H NMR experiments of the linear alcohol ethoxylate were undertaken to determine the suitability of the surfactant for further study. Despite a broad distribution of head groups and chain length, an average distribution of $C_{12}E_7$ was found. A measurement for pure $C_{12}E_7$ was also taken to see if the phase behaviour was the same as bio-soft EC-600. The pure $C_{12}E_7$ did also show a distribution of head groups and chain lengths, but in much lower abundance. The results of the spectroscopic studies can be found in Appendix A.

2.1.2 Preparation of limonene microemulsion

A simple and repeatable procedure to form a microemulsion with mass fraction ratios of *15% limonene / 23% IPA / 23% $C_{12}E_7$ / 39% water* was developed, the mass fraction ratios used are representative of the commercial composition recommended by Flotek. Each component is weighed using an analytical mass balance and added to a phase tube. The phase tube is mixed using the inversion mixing method; after leaving to equilibrate a clear microemulsion is formed.

Figure 2.1: Image taken of Winsor IV limonene microemulsion. Mass fraction ratios of 15% limonene / 23% IPA / 23% $C_{12}E_7$ / 39% water.

2.2 Estimating the size of swollen micelles

The molar ratio of limonene to $C_{12}E_7$ in our formulation can be used to estimate the radius of the hydrophobic core in swollen micelles. The surface area to volume ratio of a sphere is,

$$\frac{S}{V} = \frac{3}{R} \tag{2.1}$$

V is the volume of a sphere, *S* is the surface area of a sphere, *R* is the radius of a sphere. If each surfactant molecule occupies an area *A* at the oil-water interface, with a total surfactant tail volume V_0, and each molecule of limonene has a volume V_l, then,

$$\frac{S}{V} = \frac{A}{V_0 + (v_l / \frac{N_s}{N_l})} \tag{2.2}$$

N_s is the number of moles of surfactant, N_l is the number of moles of limonene,. $\frac{N_s}{N_l}$ is the molar ratio of $C_{12}E_7$ to limonene and can be derived through the known mass in

the original microemulsion formula. V_l can also be derived using the measured mass of limonene and known density of limonene.

A can be estimated from literature values, for example experiments on the adsorption of pure $C_{12}E_7$ at an oil-water (or air-water) interface. From air-water measurements by Rosen et al. [1] A = 57 Å^2, or 5.7 x 10^{-15} cm^2. It should be noted that the area per molecule, *A*, taken from Rosen et al. is for a planar interface, giving only an approximation for our curved interface. This limits the accuracy of the calculation but is still sufficient to estimate the size of the swollen micelles. *A* could have been measured directly using small-angle neutron scattering or using the tensiometry data, however as this was an estimation for the size of the swollen micelles, I believed this approximation was sufficient for this study. With additional experimental time, SANS should have been used to give a precise measurement of the swollen micelles.

This calculation has been made for a one-phase microemulsion system, allowing the total mass of limonene to be used. If the oil phase was in excess, i.e. for an oil-in-water microemulsion, the micelles would only be in the aqueous phase meaning the oil phase should not be included in the calculation. Instead, molar ratio of surfactant/limonene ratio in the aqueous phase, where the micelles exist, would need to be obtained.

The formula used to create limonene microemulsions is as follows: 15% Limonene / 23% IPA / 23% $C_{12}E_7$ / 39% water. If we take the case to formulate 10 g of our limonene microemulsions we would then have: 1.5 g Limonene / 2.3 g IPA / 2.3 g $C_{12}E_7$ / 3.9 g water.

Using the density formula, $\rho = \frac{m}{V}$, we can find the volume of one limonene molecule using $V_l = \left(\frac{m}{\rho}\right)$. With ρ = 0.842 g/cm^3 and a molar mass of 136.24 g mol^{-1}, V_l = 2.69 x 10^{-22} cm^3. Using the mean molar mass of $C_{12}E_7$ of 494.71 g mol^{-1}, the molar ratio of surfactant to limonene is $\frac{N_s}{N_l} = 0.42$. V_0 can be calculated for one surfactant molecule through addition of CH_2 groups and terminal methyl group, vales for volumes of CH_2 and CH_3 is taken from the literature [2].

Eq. 2.2 then gives $\frac{S}{V} = 5.77 \times 10^6\ cm^{-1}$,

R = 5.2 x 10^{-7} cm or 5.2 nm

The estimation of the size of our swollen micelles is a useful tool to predict phase behaviour of limonene microemulsions and aid explanations of phase behaviour of comparative systems and interaction with crude oil. Knowing the radius of the micelle core R allows me to calculate important functions of micelle kinetics in micelle fusion, such as diffusion coefficients and collision rates.

As the size of limonene microemulsions is below the detection threshold of particle sizing techniques available for this study, no further experimental investigation was undertaken to determine the size of our swollen micelles.

2.3 CMC of industrial $C_{12}E_7$ compared with pure $C_{12}E_7$

The surfactant used in this study is a commercial surfactant linear ethoxylate (Biosoft EC-600) provided by Flotek, with the overall structure of $C_{12}E_7$ as shown in figure 2.2 below.

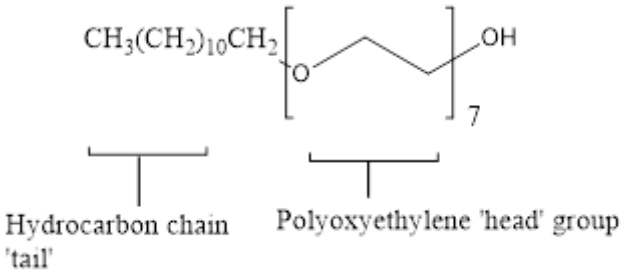

Figure 2.2: Chemical structure of $C_{12}E_7$, the hydrocarbon chain 'tail' is linear, as is the polyoxyethylene 'head' group.

Commercial non-ionic surfactants can often contain impurities or possess a large molecular weight distribution, attributed mainly to the head groups. Mass spectrometry results of our bio-soft EC-600 show a broad molecular weight distribution as discussed earlier and can be found in Appendix A.

Determining the CMC of the surfactant used for our limonene microemulsions was needed to ensure that dilutions for future experiments would not go below the CMC.

Patist et al. use a surface tension (Wilhelmy plate) and dye micellization method to compare the CMC of nine commercial surfactants with two pure surfactants [3]. Their study shows that the presence of more surface-active species within a surfactant lowers the CMC of a commercial surfactant. They found that the surface tension method was much more sensitive to the lowering of the CMC than the dye micellisation method.

Pendant-drop shape analysis has been used to use to measure the surface tension of our commercial surfactant at a range of concentrations. The FTÅ-200 fits the shape of the drop to the Young-Laplace equation using built-in software. The shape of a drop is determined by its radii of curvature, R_1 and R_2, for a spherical drop R_1 and R_2 are equal.

The Young-Laplace equation relates the shape and interfacial tension (γ) to the change in laplace pressure:

$$\Delta p = \gamma\left(\frac{1}{R_1} + \frac{1}{R_2}\right)$$
$$\Delta p = \rho g h \tag{2.3}$$

where Δp is the Laplace pressure difference across the interface, ρ is the fluid density, g is acceleration due to gravity and h is the height of the droplet.

Gravitational and interfacial forces must be of the same order of magnitude to have stable pendant drops and measure their interfacial tensions by drop-shape analysis, i.e. the Bond number B_0, must be close to 1.

$$B_0 = \frac{\rho g r_0 h_0}{\gamma} \tag{2.4}$$

Figure 2.3 shows a typical image from the software to analyse our commercial $C_{12}E_7$ in water droplet. The vertical line through the centre of the drop ensures axial symmetry. The large horizontal line running through the maximum diameter of the droplet, which if calibrated correctly, terminates on the edges of the drop. When the drop volume and surface area are computed, an additional horizontal line is drawn at the wet end of the tip, where the fluid volume and area of measurement terminate.

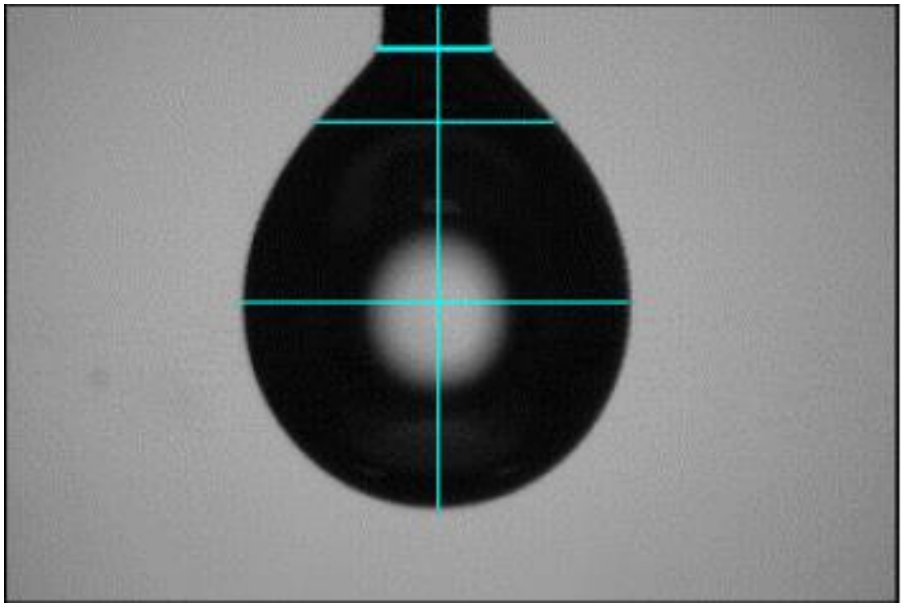

Figure 2.3 : Pendant drop image of Biosoft EC-600 $C_{12}E_7$ in water.

There are two assumptions made for this technique. First, the drop is symmetric around a vertical axis: the viewing angle bears no relevance on the measurement. Second, the drop is static. By assuming the drop is static the only forces affecting the shape of the drop are interfacial tension and gravity. The pendant drop method has a distinct advantage over the wilhelmy plate method for surface tension measurements as the wilhelmy plate method is extremely sensitive to impurities on the plate. The wetting ability of the solid surface does not have any effect on the result.

2.3.1 Method

Phase tubes of a range of concentrations above and below the estimated CMC are made with our commercial $C_{12}E_7$. The FTÅ-200 used for interfacial tension measurements can be seen in figure 2.4. A computer-controlled syringe pump is driven by a stepper motor to dispense the pendant drop. Backlit by an LED, images of the resultant droplets are captured by a camera (Watec, Wat-902B) connected to a computer and the images analysed using Fta32 v2.0 software. To obtain accurate dimensions a 3-mm calibration sphere is first used in place of the droplet. The microscope is tuned to focus on the sphere and take accurate images.

The glassware, syringe, needle, and cuvettes were all thoroughly cleaned in alkaline cleaning solutions (Decon 90), sonicated, rinsed with water and dried in an oven. Any final residue was dried using a stream of nitrogen gas.

The software runs an edge detection routine and solves the Young-Laplace equation numerically.

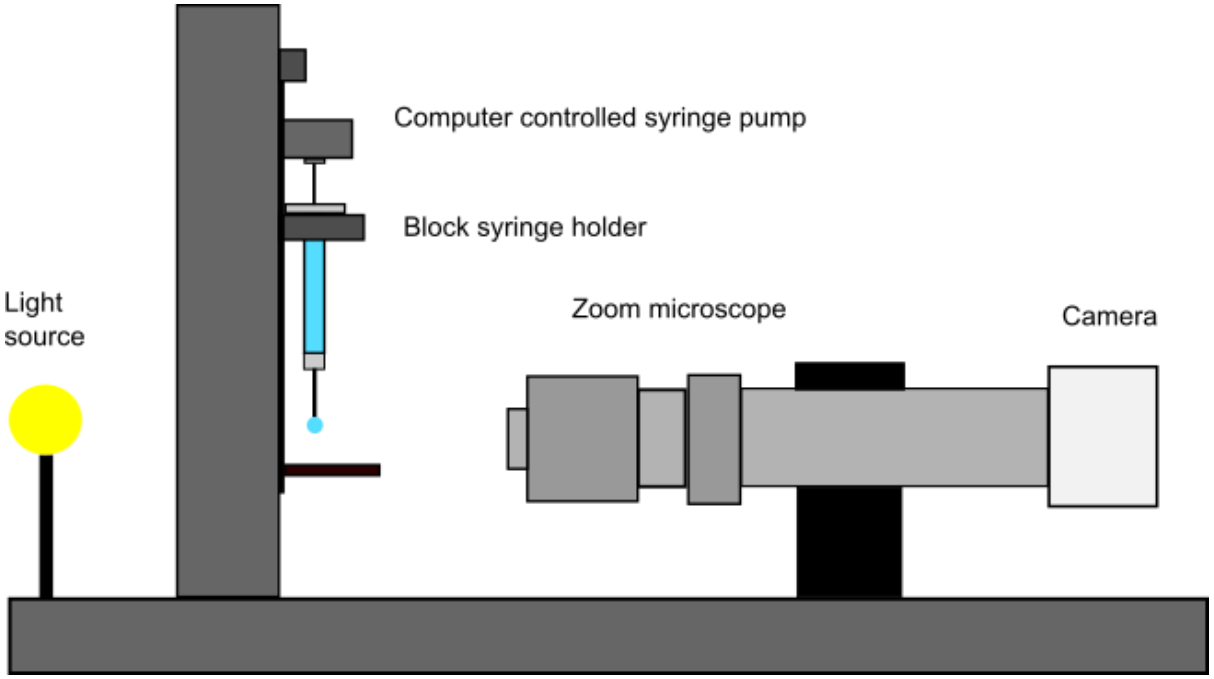

Figure 2.4: A simple experimental setup for pendant drop tensiometry to carry out interfacial tension measurements.

2.3.2 Results

A calibration test was first completed with pure water. Pure water was measured to be 72.83 mN/m at room temperature, which conforms to the literature [4]. A plot of interfacial tension vs ln[c] can be seen in figure 2.5 of our commercial $C_{12}E_7$ in pure water for a series of concentrations.

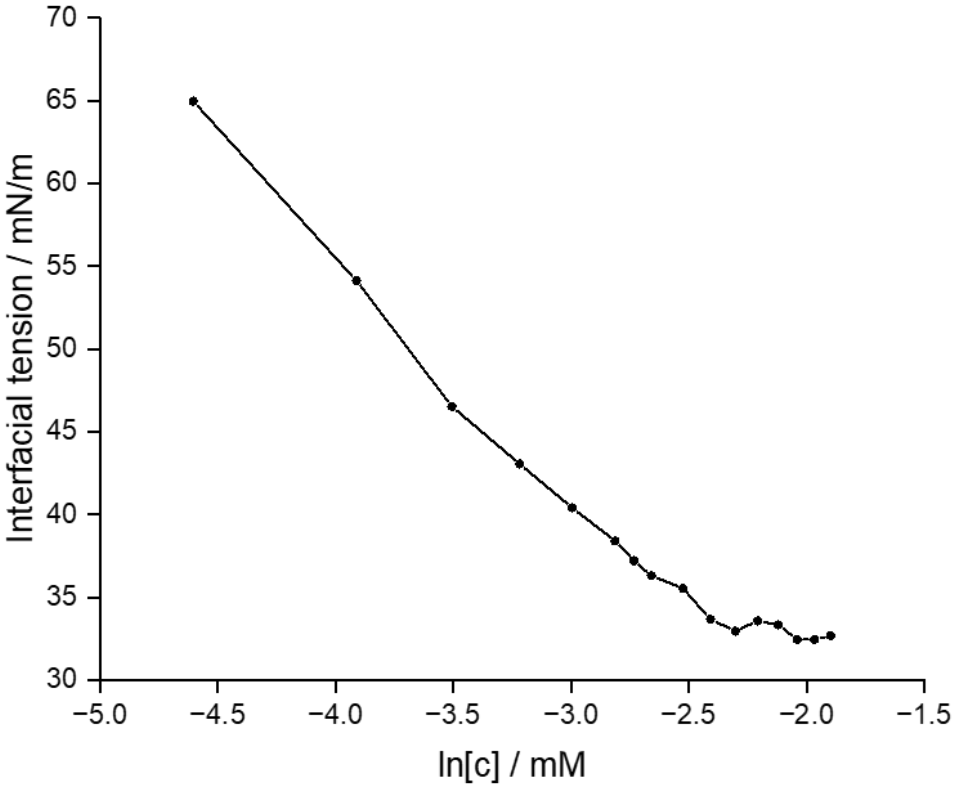

Figure 2.5: Plot of interfacial tension vs concentration of commercial $C_{12}E_7$ in pure water. The section between -3.5 to -2.4 is used to determine the CMC of $C_{12}E_7$.

The surface excess can be calculated from the slope of interfacial tension vs ln[c] using the Gibbs equation,

$$\Gamma = -\frac{d\gamma / d(\ln[c])}{nRT} \tag{2.5}$$

Γ is the surface excess, *c* is the surfactant concentration, *R* is the gas constant and *T* is temperature. For a non-ionic surfactant *n* is equal to 1. The slope of the straight section in figure 2.5 has been taken to give a linear fit (given in fig 2.6) for *(dγ/dln[c])* [5].

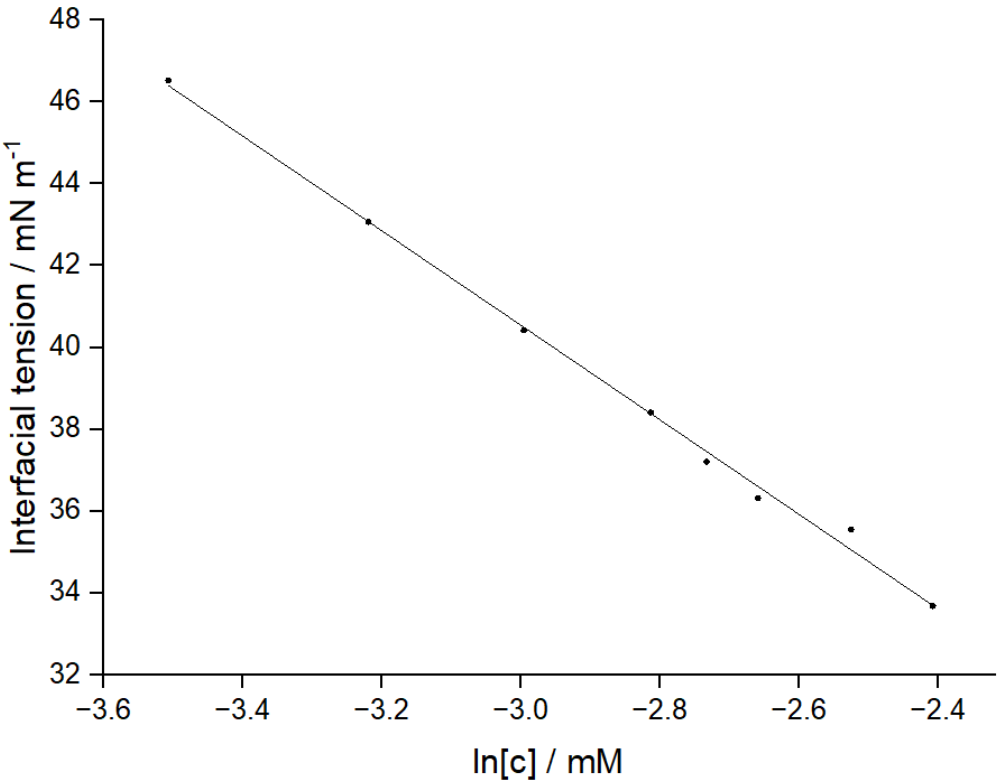

Figure 2.6: Fit to deduce the surface excess. Concentration range of straight line from -3.5 to -2.4 used.

A literature value for the surface excess of pure $C_{12}E_7$ at the CMC is 2.9 x 10^{-6} mol m^{-2} at 25 °C [6]. The surface excess of the commercial surfactant was calculated to be 4.7 x 10^{-6} mol m^{-2} at 25 °C. Using the point at which the linear trend plateaus (ln c = -2.4) the CMC is given as 0.09 mM, close to the literature value of 0.08 mM [6].

The CMC of the commercial surfactant is slightly higher than the pure surfactant due to the degree of ethoxylation and extended chain length as discussed earlier with reference to work by Patist [3]. The results of this CMC investigation allowed me to create a benchmark for a dilution limit when investigating the micelle fusion process and subsequent studies.

2.4 Solubilisation capacity of limonene microemulsions

When using limonene microemulsions for enhanced oil recovery, the concentration of the surfactant microemulsion and conditions such as temperature and the presence of salt can change depending on the type of well. It is important to study the effect temperature and concentration of surfactant has on the solubilisation capacity of our limonene microemulsions to understand their applicability to changing well conditions.

The solubilisation capacity of micelles can be affected by factors such as temperature, concentration, spontaneous curvature and interfacial tension at the spontaneous curvature. Minimising the spontaneous curvature and interfacial tension at the interface maximises the solubility of a micellar system [7]. Limonene microemulsions exhibit a low spontaneous curvature and are known for their ultralow interfacial tension at the interface. The solubilisation capacity of my limonene microemulsion was measured at two different concentrations of $C_{12}E_7$. The same has also been measured at 50 °C to determine the effect of temperature on the solubilisation capacity for our limonene microemulsion. Raising the temperature dehydrates the head groups reducing steric repulsions and lowering the spontaneous curvature. Increasing the temperature would be expected to increase the solubilisation capacity until the phase inversion point is reached.

2.4.1 Method

The limonene microemulsions were formulated as described in §2.1 with differing surfactant mass ratios to form a clear microemulsion. The phase tubes were placed in a water bath at the desired temperature. The phase tubes were left in the water bath for 30 minutes to reach thermal equilibrium. Limonene was added dropwise, stirred and allowed to equilibrate until the first signs of turbidity were visible.

2.4.2 Results

Table 2.1 shows the solubilisation capacity of limonene microemulsions at two surfactant concentrations, 25 °C and 50 °C. V_o/V_s describes the oil solubility in the microemulsion, V_o is the volume of oil and V_s is the volume of surfactant.

Table 2.1: Solubility measurements of limonene microemulsions at differing surfactant concentration and temperature.

Initial volumes (ml) of Limonene:IPA:$C_{12}E_7$:Water	Temperature °C	Maximum addition of limonene before turbidity (ml)	V_o/V_s
1.5 : 2.3 : 1.7 : 3.9	25	0.15	0.97
1.5 : 2.3 : 1.7 : 3.9	50	1.20	1.59
1.5 : 2.3 : 2.3 : 3.9	25	1.00	1.09
1.5 : 2.3 : 2.3 : 3.9	50	2.20	1.61

For both concentrations of surfactant, there is an increase in oil solubilisation when temperature is increased. There is no significant change to the solubilisation capacity when the concentration of the surfactant is lowered in relation to the other constituents. There may be a more noticeable change when the concentration of the surfactant is lowered further in relation to oil, however this may change the composition of the microemulsion away from a Winsor IV region, not desirable for our studies.

2.5 Phase diagram of limonene microemulsion

Phase diagrams can give important information regarding the phase behaviour of a microemulsion system. Much work has been undertaken by Kahlweit, Sottmann and Strey to describe phase behaviour of microemulsions using non-ionic surfactants, specifically C_iE_j; their work has been particularly informative in understanding ternary phase diagrams and fishtail diagrams [8]–[17].

The type of phase diagram used is dependent on the number of phases considered in the system. The number of phases in a given system can be derived from the Gibbs phase rule. *F* is the number of state variables that can be changed independently, *C* is the number of independent chemical constituents and *P* is the number of phases present in the system.

$$P + F = C + 2 \tag{2.6}$$

There is a degree of complication depending on the number of phases incorporated. Beyond binary and ternary systems come phase prisms, which get increasingly difficult to interpret and understand. It is often useful to control certain parameters to create a simpler diagram. The most common phase diagram used for microemulsions is a ternary phase diagram, or phase triangle. Sottman describes the differing phase triangles for C_iE_j with oil and water [15]. An idealised schematic for a $C_{12}E_7$, water and limonene ternary phase diagram at ambient temperature as discussed by Sottman can be seen in figure 2.7 [15]. For the idealised diagram in figure 2.7, it is noted that although a three-phase region can be seen, it is generally only observed at specific temperature intervals [18]. For this case, a pseudo ternary phase diagram has been used with varying concentrations of oil, water, and surfactant mixture. Temperature has been controlled to 25 °C and sealed test tubes assume constant pressure, with four components in our system there can be a maximum of three degrees of freedom. For my system, an equal ratio of IPA:EC-600 was maintained, using one degree of freedom, thus leaving a maximum of three phases. So three phases now occur at a single composition, two phases along a line in the phase diagram and one phase everywhere else. Everywhere within the three-phase region the composition of the three phases is the same, from the corners of the triangle.

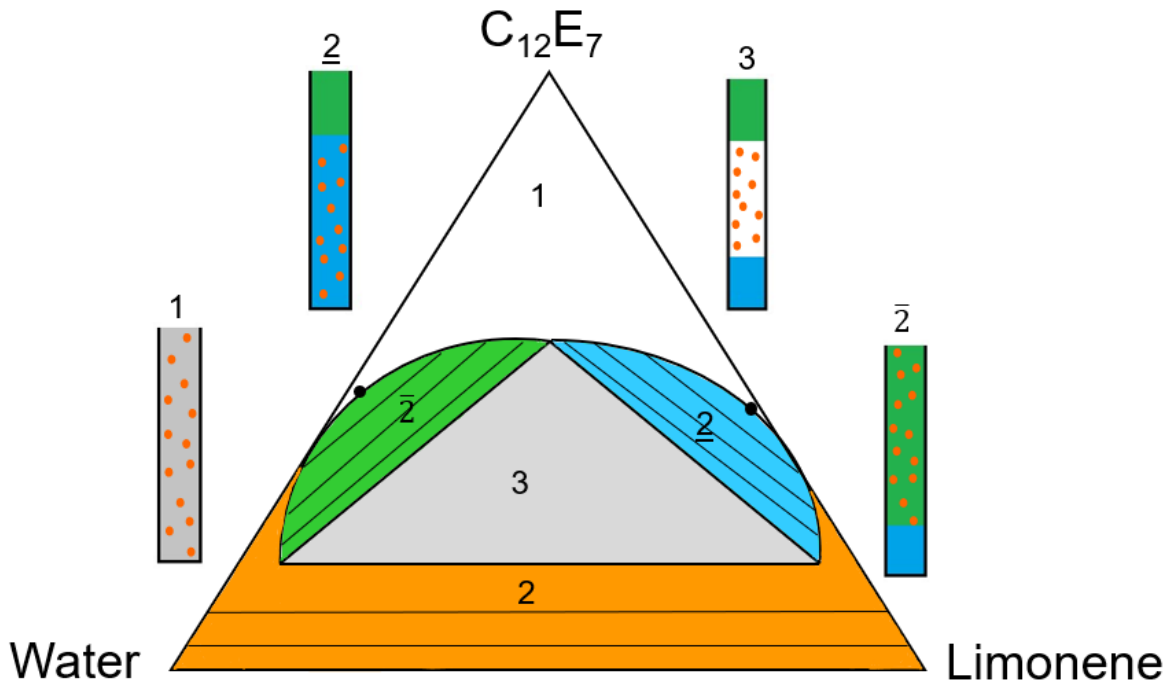

Figure 2.7: Ternary phase diagrams of a non-ionic surfactant at ambient temperature. A three phase middle region dominates the phase triangle. 1 represents a Winsor IV microemulsion, 2 represents a Winsor I oil-in-water microemulsion, $\bar{2}$ represents a Winsor II water-in-oil microemulsion, 3 is a Winsor III middle phase microemulsion.

Tie lines are observed in this phase diagram, tie lines connect two phases of equal chemical potentials. Tie lines are determined experimentally and the relative amount of the two phases at this point can be determined using the lever rule. It should also be noted that the phase diagram in figure 2.7 appears to have 'plait points.' Plait points in these circumstances are the critical points in which the miscibility gaps in the two-phase region disappears.

As this study was conducted at 25 °C, it was thought that the phase diagram would be similar to that seen in figure 2.8. A previous member of the Bain group, Alex Hargreaves, shows another depiction of an idealised phase triangle for a microemulsion system close to the phase inversion point.

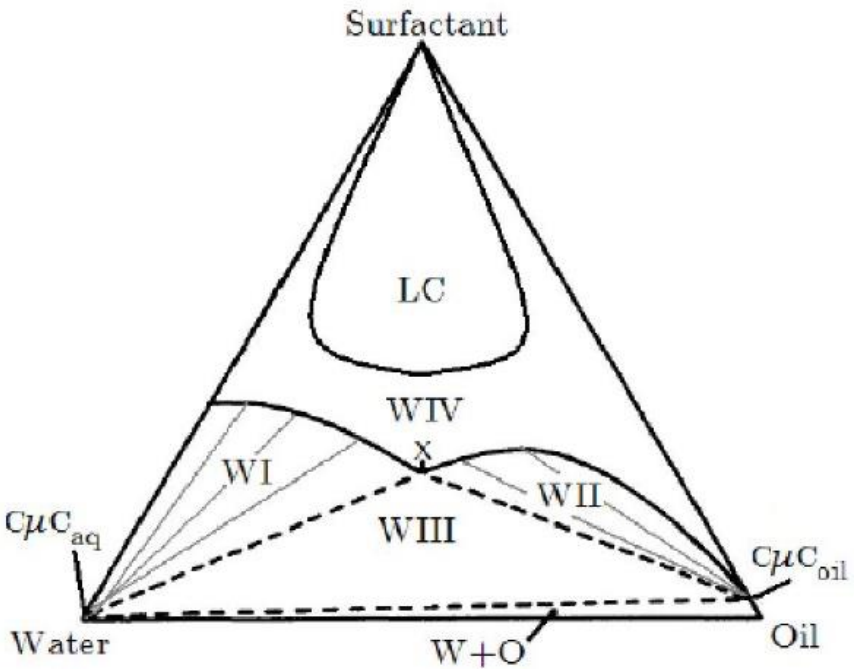

Figure 2.8: A ternary phase diagram of oil, water and surfactant. LC is the liquid crystal region and the 'X' point, which represents the smallest amount of surfactant required for a Winsor IV microemulsion.

It is interesting to note there is a liquid crystal region at quite high surfactant concentrations, but we do not need to consider this for our study as we are using much lower surfactant concentrations. The $C\mu C_{aq}$ and $C\mu C_{oil}$ points referred to in figure 2.8 are the critical microemulsion concentrations of each solvent required to form a microemulsion. Microstructures of the WIII microemulsion can be determined using NMR-self-diffusion measurements, small-angle neutron and X-ray scattering (SANS and SAXS) and many more.

2.5.1 Method

The method has been described well by Strey et al. [13]. Differing mass ratios of oil and water are made in sealed phase tubes and kept at 25 °C in a water bath. A surfactant mixture of 1:1 mass ratio of $C_{12}E_7$: IPA stock solution is made and mixed well, named surfactant blend. The surfactant mixture is then titrated into the oil-water mixture and mixed well, allowing the solution to equilibrate between each addition. Phase changes are noted until the phase tube becomes an isotropically clear one phase microemulsion. When considering the phase diagram in figure 2.9, each composition of oil and water begins on the bottom axis in the 2-phase region. When a phase boundary is crossed the mass percentage of surfactant is noted and shown as a data point in the diagram. The points collected from the indicated phase boundaries

have been connected to delineate the phases, there will be errors associated with phases change.

2.5.2 Results

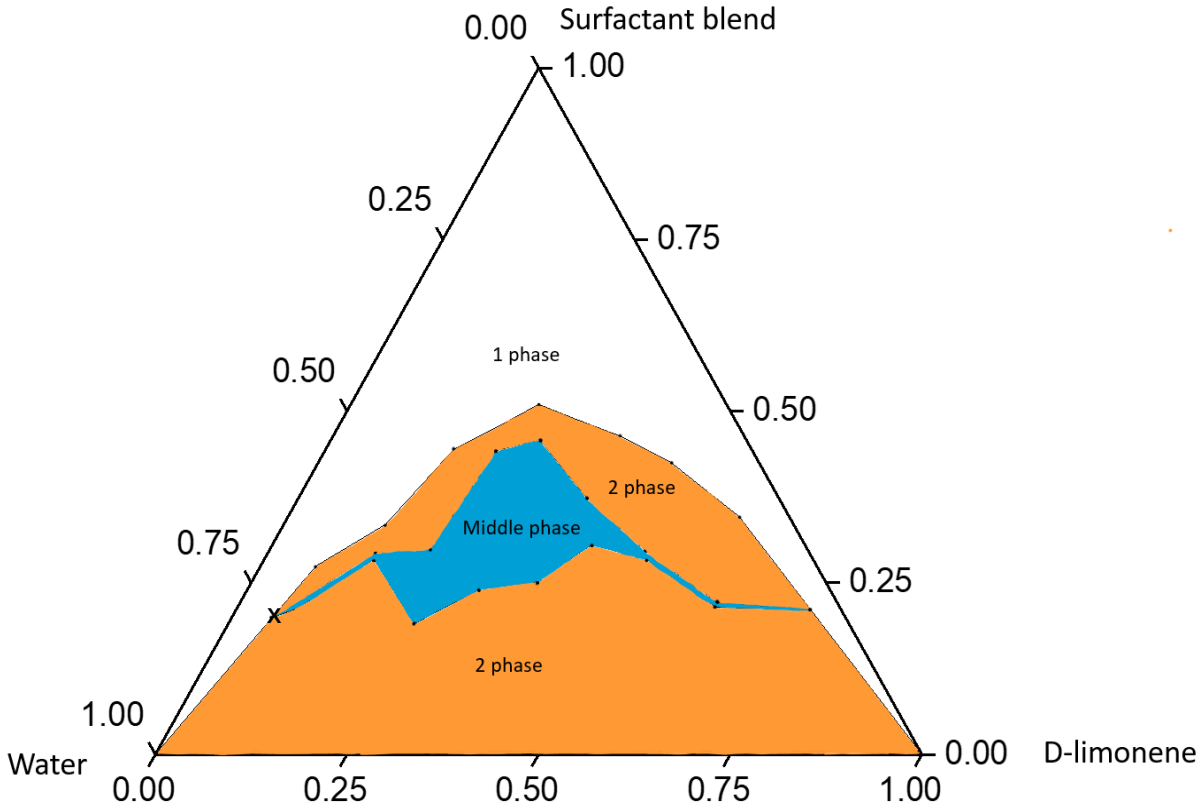

Figure 2.9: A pseudo ternary phase diagram for the microemulsion system. The surfactant blend is a 1:1 mass ratio of IPA and EC-600 ($C_{12}E_7$), the 'X' point is marked as the lowest amount of surfactant required to make a Winsor IV microemulsion.

Figure 2.9 shows a dominant two-phase region and a discrete middle phase region. The nature of the surfactant plays a key role in the phase behaviour as does the nature of the oil. The minimum concentration of surfactant needed to create a one phase region were noted for each composition of oil and water and can be seen as data points on the phase diagram.

2.6 Fish tail plots of limonene microemulsion

The fish tail diagram is another useful technique to display the phase behaviour of a microemulsion. Fish tails can be thought of as a segment of the overall phase prism in which the temperature dependence of the microemulsion is observed. By fixing the oil/water ratio, the changes in phase can be observed at different surfactant concentrations as a function of temperature. The fish tail plot can indicate the relative efficacy of a formulation for oil recovery in relation to temperature. Fish tail plots also allow the determination of the phase inversion temperature.

Sottmann et al. give a description of fish tail diagrams for non-ionic surfactants with its corresponding, and quite complicated phase prism [15]. Papers from Strey and Pedersen explain fish tail diagrams well and provides the basis for the method used for this study [10][19]. Figure 2.10 gives an idealised view of a fish tail diagram for non-ionic surfactants at a fixed oil-water ratio.

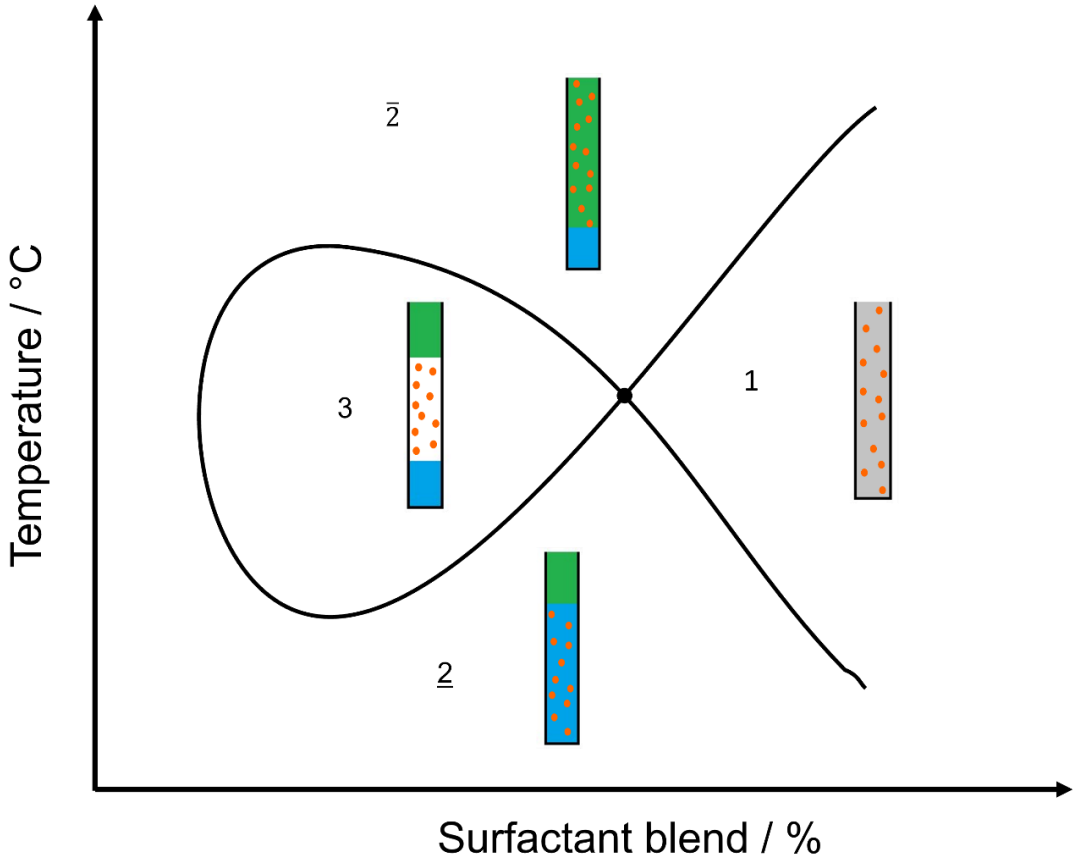

Figure 2.10: Schematic of idealised fishtail plot at a fixed oil/water ratio. 1 indicates the macroscopic single phase, Winsor IV microemulsion. $\underline{2}$ is an oil-in-water, Winsor I microemulsion region. $\bar{2}$ is a water-in-oil, Winsor II microemulsion region. 3 is the middle phase, Winsor III microemulsion region. Surfactant blend refers to a 50:50 mass fraction mix of $C_{12}E_7$ and IPA.

When the temperature is increased, for lower surfactant concentrations, the microemulsion moves from an oil-in-water microemulsion to a 3-phase middle microemulsion region, to a water-in-oil microemulsion region. At higher surfactant concentrations the microemulsion moves from an oil-in-water microemulsion to a one phase microemulsion, to eventually a water-in-oil microemulsion.

Non-ionic surfactants dissolve mainly in the aqueous phase at low temperatures, oil-swollen micelles are formed in a continuous water phase, and thus an oil-in-water microemulsion is formed. At high temperatures the surfactant dissolves mainly in the oil phase, the amphiphilic film forms water-swollen micelles in a continuous oil phase, i.e., a water-in-oil microemulsion is formed. Sottmann describes the temperature induced phase change in relation to the spontaneous mean curvature. As the temperature increases the mean curvature decreases. The mean curvature continues to decrease with temperature until the phase inversion temperature is reached, where the mean curvature equals zero. When the temperature increases beyond the phase inversion temperature the spontaneous mean curvature becomes negative.

The circular point is the state of the system where the 3-phase system meets the single-phase system. It defines both the minimum mass fraction of surfactant needed to solubilise water and oil, i.e., the efficiency of the surfactant, and the phase inversion temperature.

The single phase to water-in-oil (1 - $\bar{2}$) microemulsion phase boundary indicates the maximum amount of oil that can be solubilised in a one phase oil-in-water microemulsion at a given temperature, called the emulsification failure boundary (efb). As the temperature increases, the ability of the surfactant to solubilise oil decreases.

2.6.1 Method

The temperature and concentration of the surfactant mixture are changed at a fixed oil-water mass ratio. The phase tubes are then slowly heated at 2 °C increments and left to equilibrate for 30 minutes in a temperature-controlled water bath. This technique has been slightly adapted from the technique used at Flotek, where a heat gun is used to rapidly heat the phase tube until a phase change is observed, then allowed to cool until the phase changes again and the temperature is taken. When approaching a phase change there was often a range of temperatures (typically between a degree)

that were identified as the point of phase change. To give more precision on the determination of the phase change, a number of recordings of the observed phase change was taken. Repeated trials of the heat gun and water bath method found the water bath method was more reliable. Cooling below 0 °C was also attempted using an acetone bath with dry ice, however this method was inconsistent as the temperature would fluctuate quite a lot during cooling. Phase behaviour below 0 °C is not useful unless the microemulsion system is used in freezing conditions, such as in Antarctic oil reservoirs.

2.6.2 Results

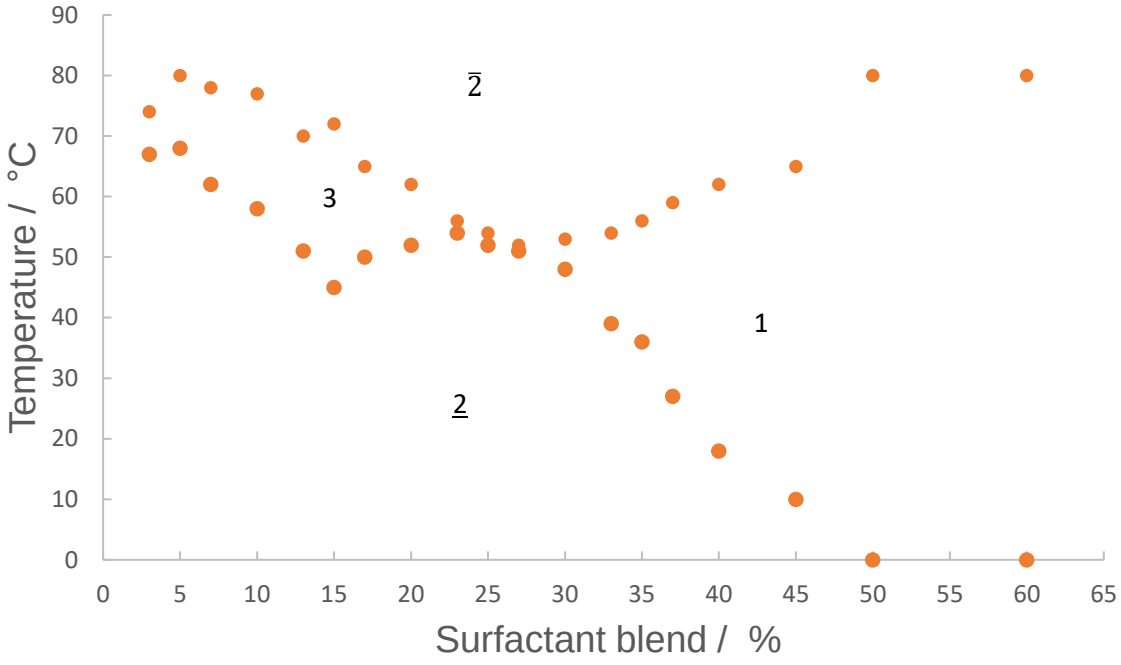

Figure 2.11: A Fishtail plot for the limonene, water, IPA and C12E7 (EC-600) microemulsion system. 1 indicates the macroscopic single phase, Winsor IV microemulsion. 2 is an oil-in-water, Winsor I microemulsion region. $\bar{2}$ is a water-in-oil, Winsor II microemulsion region. 3 is the middle phase, Winsor III microemulsion region. Orange dots represent temperatures at which a visible phase change is observed.

The results given in figure 2.11, follow a similar trend expected of the changing phase behaviour to the idealised fish-tail plot in figure 2.10. An additional note to point was at 2% and 1% surfactant blend only a two phase microemulsion was observed when heated, indicating the ‘head’ of the fish plot begins at 3% surfactant blend.

The PIT point (circular point) shown in figure 2.10 can be determined from the neck of the fish tail in figure 2.10. The PIT point in figure 2.11 appears to lie ~25–27 % surfactant blend between 51–52 °C.

2.7 Microemulsions with technical-grade non-ionic surfactants

Sottman et al. discuss some differences when using technical-grade non-ionic surfactants for phase studies, relevant to this study as Biosoft EC-600 (commercial $C_{12}E_7$) is used [15]. Despite having a large distribution of ethoxylate head groups, there are studies with formulations using technical-grade surfactants showing the surfactant blends can be treated as a single (pseudo) component [20][21].

Sottman illustrates a comparative study made by Jakobs et al. for a system of H_2O-noctane-$C_{12}E_6$ and the technical equivalent DA-6 to see what effect a technical grade surfactant has on phase behaviour [13]. The phase boundaries of the system containing the technical-grade surfactant were distorted at low mass fraction of surfactant. The technical grade surfactant also solubilised n-octane slightly more efficiently than pure $C_{12}E_6$.

The distortion of phase boundaries is due to the broad distribution of the ethoxylation degree of DA-6 and resulting different monomeric solubilities of every specific homologue in water and oil. The lower ethoxylated, more hydrophobic homologues of the surfactant DA-6 tend to dissolve in the oil-excess, oil-swollen micelles or bicontinuous oil-rich domains. The remaining surfactant mixture in the amphiphilic film is more hydrophilic than the base surfactant. Decreasing the surfactant mass fraction gives a higher proportion of the DA-6 dissolved in the non-polar phases, rather than residing at the micellar interfaces and so becomes more hydrophilic. At higher temperatures and lower surfactant concentrations, there is a large distortion of the phase boundaries with lower surfactant concentration. Sottman goes onto describe the distortion in terms of mean curvature of the amphiphilic film. As the surfactant mass fraction decreases, the fraction of large head groups in the film increases, making the amphiphilic film more curved around the oil. Sottman suggests the phase behaviour also depends on the composition of the amphiphilic film.

Conclusion

The phase behaviour of the commercial surfactant $C_{12}E_7$ used in formulations for oil recovery has been determined. The commercial surfactant does show differences from idealised schematics of pure $C_{12}E_7$. To make a coherent comparison, data for the same system with pure $C_{12}E_7$ would need to be taken. The phase studies have validated the use of the commercial surfactant Biosoft EC-600 as a representative of $C_{12}E_7$ and gives insight to the phase behaviour expected for later kinetic experiments.

It would be interesting to conduct further phase studies with pure $C_{12}E_7$ as a comparison to the experiments conducted in our study. The cost of pure $C_{12}E_7$ is ~ £400/ 10 ml (Anatrace), the phase studies in the project used significantly more than 10 ml of surfactant, to use pure $C_{12}E_7$ for comparative phase studies would incur a great cost.

The estimation for the size of swollen micelles has allowed me to make calculations on micelle kinetics during the stopped-flow experiments, which was extended to the surfactant package and cyclohexane microemulsions. Further experiments could also include a study into size of swollen limonene microemulsions using a Small Angle X-ray Scattering method to validate the calculations made.

References

[1] M. J. Rosen, A. W. Cohen, M. Dahanayake, and X. Y. Hua, “Relationship of structure to properties in surfactants. 10. Surface and thermodynamic properties of 2-dodecyloxypoly(ethenoxyethanol)s, C12H25(OC2H4)x OH, in aqueous solution,” *Journal of Physical Chemistry*, vol. 86, no. 4, pp. 541–545, 1982, doi: 10.1021/j100393a025.

[2] A. Czajka, G. Hazell, and J. Eastoe, “Surfactants at the Design Limit,” *Langmuir*, vol. 31, no. 30, pp. 8205–8217, 2015, doi: 10.1021/acs.langmuir.5b00336.

[3] A. Patist, S. S. Bhagwat, K. W. Penfield, P. Aikens, and D. O. Shah, “On the measurement of critical micelle concentrations of pure and technical-grade non-ionic surfactants,” *Journal Surfactants Detergents*, vol. 3, no. 1, pp. 53–58, Jan. 2000, doi: 10.1007/S11743-000-0113-4.

[4] I. M. Hauner, A. Deblais, J. K. Beattie, H. Kellay, and D. Bonn, “The Dynamic Surface Tension of Water,” *Journal. Phys. Chem. Lett*, vol. 8, p. 2022, 2017, doi: 10.1021/acs.jpclett.7b00267.

[5] M. Dreja, W. Pyckhout-Hintzen, H. Mays, and B. Tieke, “Cationic Gemini Surfactants with Oligo(oxyethylene) Spacer Groups and Their Use in the Polymerization of Styrene in Ternary Microemulsion,” *Langmuir*, vol. 15, no. 2, pp. 391–399, 1999, doi: 10.1021/LA981354V/ASSET/IMAGES/LARGE/LA981354VF00007.JPEG.

[6] M. J. Rosen, *Surfactants And Interfacial Phenomena*, vol. 6. 2004. doi: 10.1002/0471670561.

[7] F. Testard and T. Zemb, “Compréhension de la solubilisation par utilisation des principes d’auto-association des tensioactifs à partir des contraintes géometriques,” *Comptes Rendus - Geoscience*, vol. 334, no. 9, pp. 649–663, 2002, doi: 10.1016/S1631-0713(02)01803-5.

[8] T. Sottmann, K. Kluge, R. Strey, J. Reimer, and O. Söderman, “General patterns of the phase behavior of mixtures of H2O, alkanes, alkyl glucosides, and cosurfactants,” *Langmuir*, vol. 18, no. 8, pp. 3058–3067, 2002, doi: 10.1021/la011665x.

[9] R. Strey and M. Kahlweit, “Microstructure of microemulsions,” *New Trends in Colloid Science*, pp. 193–193, 2007, doi: 10.1007/3-798-50724-4_95.

[10] R. Strey, “Microemulsion microstructure and interfacial curvature,” *Colloid Polym Sci*, vol. 272, no. 8, pp. 1005–1019, 1994, doi: 10.1007/BF00658900.

[11] B. M. Kahlweit and R. Strey, “Phase Behavior of Ternary Systems of the Type H2O-Oil-Non-ionic amphiphile,” *Angew. Chem. Int. Ed.*, vol. 24, no. 2, pp. 654–668, 1985, doi: 10.1002/anie.198506541.

[12] T. Sottmann and R. Strey, “Ultralow interfacial tensions in water-n-alkane-surfactant systems,” *Journal of Chemical Physics*, vol. 106, no. 20, pp. 8606–8615, 1997, doi: 10.1063/1.473916.

[13] T. S. and R. S. B.Jakobs, “Efficiency boosting with amphiphilic block copolymers - a new approach to microemulsion formulation,” *Tenside Surfactants Detergents*, vol. 37, no. 6, pp. 357–365, 2000.

[14] M. Kahlweit, R. Strey, and D. Haase, “Phase behavior of multicomponent systems water-oil-amphiphile-electrolyte. 3,” *Journal of Physical Chemistry*, vol. 89, no. 1, pp. 163–171, 1985, doi: 10.1021/j100247a034.

[15] T. Sottmann and C. Stubenrauch, “Phase Behaviour, Interfacial Tension and Microstructure of Microemulsions,” *Microemulsions: Background, New Concepts, Applications, Perspectives*. pp. 1–47, 2009. doi: 10.1002/9781444305524.ch1.

[16] S. Burauer, T. Sachert, T. Sottmann, and R. Strey, “On microemulsion phase behavior and the monomeric solubility of surfactant,” *Physical Chemistry Chemical Physics*, vol. 1, no. 18, pp. 4299–4306, 1999, doi: 10.1039/a903542g.

[17] M. Kahlweit, R. Strey, and G. Busse, “Microemulsions: A qualitative thermodynamic approach,” *Journal of Physical Chemistry®*, vol. 94, no. 10, pp. 3881–3894, 1990, doi: 10.1039/c2jm30552f.

[18] M. Kahlweit and R. Strey, “Phase Behavior of Ternary Systems of the Type H2O?Oil?Non-ionic Amphiphile (Microemulsions),” *Angewandte Chemie International Edition in English*, vol. 24, no. 8, pp. 654–668, Aug. 1985, doi: 10.1002/ANIE.198506541.

[19] L. Arleth and J. S. Pedersen, “Droplet polydispersity and shape fluctuations in AOT [bis(2-ethylhexyl)sulfosuccinate sodium salt] microemulsions studied by contrast variation small-angle neutron scattering,” *Phys Rev E Stat Phys Plasmas Fluids Relat Interdiscip Topics*, vol. 63, no. 6, pp. 1–18, 2001, doi: 10.1103/PhysRevE.63.061406.

[20] T. Sottmann, M. Lade, M. Stolz, and R. Schomäcker, “Phase behavior of non-ionic microemulsions prepared from technical-grade surfactants,” *Tenside, surfactants, detergents*, vol. 39, no. 1, pp. 20–28, 2002.

[21] H. Kunieda and N. Ishikawa, “Evaluation of the hydrophile-lipophile balance (HLB) of non-ionic surfactants. II. Commercial-surfactant systems,” *Journal Colloid Interface Sci*, vol. 107, no. 1, pp. 122–128, 1985, doi: https://doi.org/10.1016/0021-9797(85)90155-9.

Chapter 3 Micelle exchange kinetics setup and theory

Micellar dynamics have been extensively studied using a stopped-flow fluorescence technique [1]–[6]. When considering the exchange processes in micellar systems, there are usually two well-separated processes: one relaxation process that occurs on a microsecond timescale and a slower process, which can vary from a millisecond timescale to seconds [4]. As discussed in §1.1.3 the slower process often occurs via micelle fusion.

Micelles can collide and merge to form ‘super-micelles’ via a fusion mechanism, The micelles can exchange contents before then returning to ‘proper micelles’ through successive monomer loss via the Becker-Döring mechanism, or by fission back into two micelles. Oil can be solubilised by empty micelles fusing with a surfactant-covered oil-water interface and then budding off again as a microemulsion droplet containing oil. The fusion process between micelles gives an indication of the kinetics of the fusion process with an oil drop or oil film, relevant for oil recovery. Stopped-flow fluorescence measurements were taken to observe the rate of equilibration of contents, related to the rate of transient dimer formation. Using a suitably insoluble fluorescent probe, we can ensure the exchange process occurs via micelle fusion.

The stopped-flow technique can be summarised as follows. Drive syringes rapidly force two reaction solutions through a mixing chamber into an observation cell. The flow is then stopped, and the reaction is monitored using a spectroscopic probe as a function of time. The reaction solutions in our case are swollen micelles doped with a suitable fluorescent probe. The exchange of contents can be observed through fluorescence dequenching or FRET.

3.1 Factors considered for experiment

There are several factors which needed to be carefully thought through for successful micelle collisions and at a rate which is observable. Our microemulsions are formulated at a high concentration and so a suitable dilution of our microemulsions was needed to maintain clear stable microemulsions at a concentration where kinetics was on a measurable timescale. The stopped-flow spectrometer can take acquisitions with a minimum integration time of 8 ms. Consequently, the conditions must be selected so that the kinetics take place on a timescale that is longer than 8 ms. In addition to this, the instrument has an associated ‘deadtime’ with acquisitions taken of 10 ms. The ‘deadtime’ is the time taken for the solutions to get from the syringes to the cell for observation. The ‘deadtime’ can limit the timescale at the fast end and frequency of spectral acquisition. To negate the ‘deadtime’ the acquisition is started before the experiment and continues after the experiment has finished The kinetics become slower the lower the concentration, but a limit is set by the CMC and also by the concentration of the fluorophore and the sensitivity of the detection system.

The choice of fluorescent dye also needed to be carefully considered. The fluorescent probe needs to have low solubility in water to solubilise preferentially in our swollen micelles. Pyrene is often used for stopped-flow fluorescent measurements, its solubility in water is $7x10^{-7}$ M and it readily dissolves in the hydrophobic core of the microemulsion micelles; therefore pyrene was initially chosen for our study. Pyrene is a polycyclic aromatic hydrocarbon with four benzene rings.

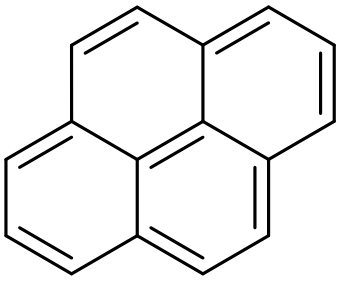

Figure 3.1: Chemical structure of pyrene molecule.

Monomeric pyrene fluorescence is characterised by the vibronic bands in the region of 375–410 nm (figure 3.2). The ratio of the intensities of the first I_1 and third I_3 vibronic bands is related to the polarity of the local pyrene environment, therefore will be

sensitive to the local environment. The observed spectrum confirms that the pyrene fluorescence arises from pyrene molecules in a non-polar environment (the micellar core) and not from free molecules in solution. A comparative assessment was made with spectra taken for pyrene dissolved in water, a fluorescence spectrum of pyrene in water can be found in figure 5, Appendix B. A pyrene molecule can absorb a photon and be excited to its S1 state. Excited pyrene monomers may associate with a ground state pyrene monomer to give a broad excimer emission band at 450–480 nm (figure 3.2). The ratio of the monomer bands to this broad excimer band is a measure of the average number of pyrene molecules per micelle. When a transient dimer is formed, pyrene molecules will be shared between the two daughter micelles. If a pyrene labelled micellar solution mixes with an unlabeled micellar solution, the average number of pyrene molecules per micelle will decrease. Monitoring the monomer to excimer ratio over time can therefore, in principle, be used to measure the kinetics of formation of transient dimers.

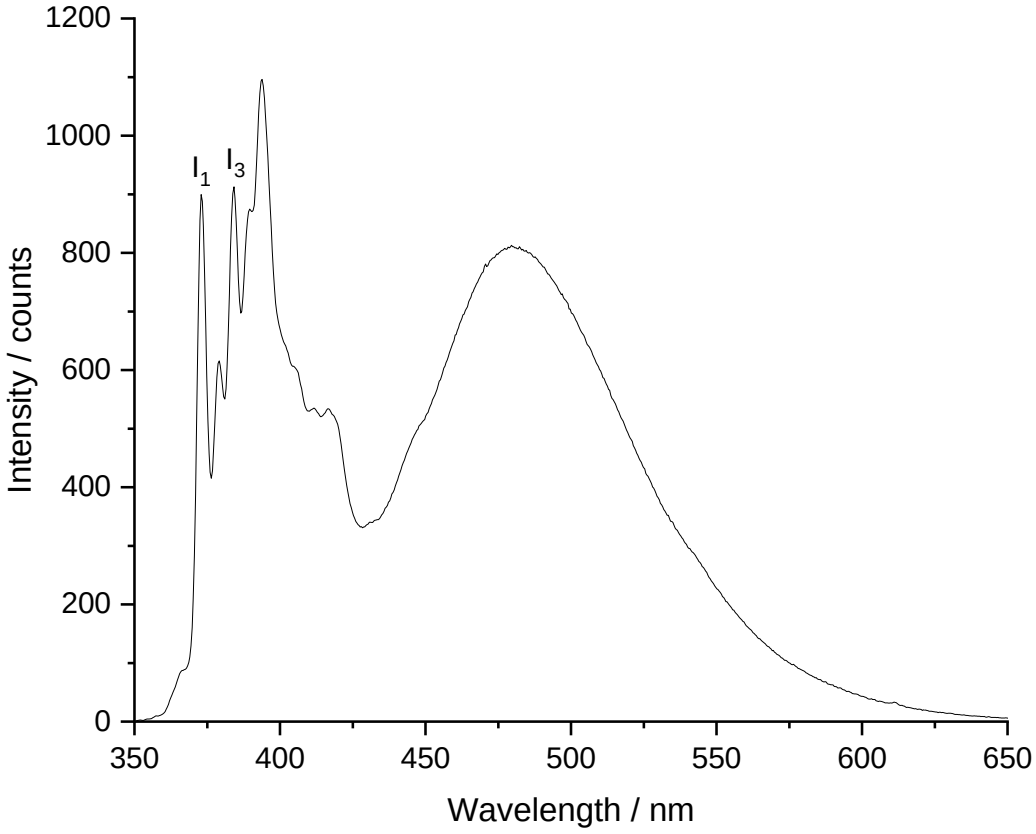

Figure 3.2: Pyrene fluorescence spectra for 0.078 mM pyrene in 11 mM Surfactant package. Excitation wavelength 337 nm.

To estimate the fraction of micelles occupied by pyrene molecules a Poisson distribution was used [7], [8]

$$\frac{M_n}{M} = \frac{(\bar{n})^n \, e^{-\bar{n}}}{n!} \tag{3.1}$$

where M_n is the concentration of micelles containing *n* pyrene molecules. $\bar{n}$ is the average number of pyrene molecules per micelle and *M* the total micelle concentration.

In using a Poisson distribution, I assume that all the micelles have the same aggregation number, *N*, and that *N* is independent of the number of pyrene molecules in the micelles, that the total micelle concentration remains constant, and that the probability of a pyrene molecule being found in a micelle is independent of whether or not there are other pyrene molecules in the micelle i.e. the ground state pyrene molecules do not interact.

$\bar{n}$ can be calculated through a knowledge of the micellar concentration and pyrene concentration using equation 3.2.

$$\bar{n} = \frac{c}{M} \tag{3.2}$$

where *c* is the pyrene concentration. The micellar concentration can be calculated using the relationship of aggregation number and the critical micelle concentration as seen in equation 3.3.

$$N = \frac{[C_{12}E_7] - CMC}{M} \tag{3.3}$$

N is different for pure $C_{12}E_7$ in water [9] and for limonene microemulsions, calculated to be 595. $[C_{12}E_7]$ is the total surfactant concentration in the system and the CMC is taken from the literature [9]. The micellar concentration, average number of pyrene molecules per micelle and aggregation number for the case of limonene microemulsions and $C_{12}E_7$ in water are given in table 3.1. From $\bar{n}$, the concentration of micelles containing one pyrene molecule M_1 can be calculated using equation 3.1. From this, the concentration of micelles containing two or more pyrene molecules $M_{>1}$ can also be calculated by subtracting the case of zero pyrene molecules and 1 pyrene molecule from the total micellar concentration. The micellar concentration for a given population of pyrene molecules is shown in table 3.1.

Table 3.1: *N, M,* $\bar{n}$, M_0, M_1 and $M_{>1}$ for 11 mM limonene microemulsion and $C_{12}E_7$ in water at a given pyrene concentration of 0.073 mM. *N* for $C_{12}E_7$ in water was taken from the literature [10].

	N	*M* / mM	$\bar{n}$	M_0 / mM	M_1 / mM	$M_{>1}$ / mM
$C_{12}E_7$ in water	64	0.17	0.43	0.11	0.048	0.012
limonene microemulsion	595	0.02	3.65	0.0005	0.002	0.018

Using the results in table 3.2, the ratio of monomer to excimer emission can be determined using the relationship $M_1/M_{>1}$. After a mixing run, the micellar solution filled with pyrene is mixed with an equal concentration of unlabelled micelles, effectively reducing $\bar{n}$ by half. Therefore, M_n needs to be recalculated after dilution with unlabelled micelles using the same method as used for the results in table 3.1. Table 3.2 gives the ratio of monomer to excimer emission before and after an experimental run for $C_{12}E_7$ in water and limonene microemulsion. The difference in the monomer to excimer emission ratio before and after dilution with water shows the sensitivity to the exchange kinetics.

Table 3.2: Equilibrium monomer to excimer ratio for 11 mM limonene microemulsion and $C_{12}E_7$ in water with 0.073 mM pyrene before and after dilution with an equal volume of unlabelled solution.

	$M_1/M_{>1}$	After dilution $M_1/M_{>1}$
$C_{12}E_7$ in water	4	2.63
limonene microemulsion	0.11	0.54

3.2 Experimental setup

3.2.1 Stopped-flow instrumentation

Pyrene fluorescence spectra are acquired with a QE65000 Spectrometer (Ocean optics) capable of fast integration times (≥8 ms) with a high sensitivity. The grating is tuned to detect light in the range 350–700 nm, suitable for measuring pyrene fluorescence in micelles. The excitation wavelength is set to 337 nm from a Xe-Ar lamp monochromated with a 2-mm slit width. Figure 3.3 shows a schematic of the stopped-flow device.

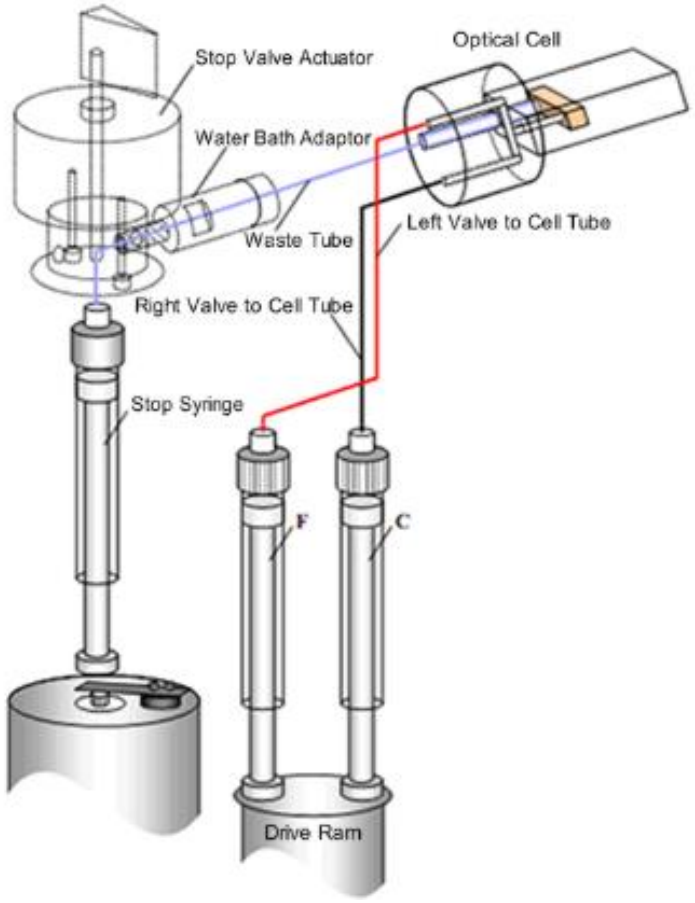

Figure 3.3: Schematic of sample handling unit stopped-flow device. Schematic taken from photophysics operating manual with permission [11] . Details of permission can be found at the end of the thesis in permission table.

Each drive syringe is filled first with the microemulsion containing pyrene and driven through a T-mixer into the 20-μL quartz optical cell using a pneumatic drive ram, the pressure of which is kept at 4 bar using a constant stream of nitrogen. After a number of drives to ensure the cell is filled with swollen micelles containing pyrene, drive syringe C is replaced with the microemulsion system without pyrene present. 1:1 mixing is then achieved by driving these two syringes together and the change in fluorescence is recorded using the QE65000 spectrometer. Particular care must be taken when loading the samples into the drive syringes to avoid the formation of air bubbles, which can scatter the excitation light into the optical fibre.

3.2.2 Solution preparation

A stock solution of pyrene dissolved in ethanol is made, then a sample of the pyrene dissolved in ethanol is extracted into a clean volumetric flask and ethanol is evaporated under a stream of nitrogen to leave a thin film of pyrene in the flask.

A microemulsion stock was prepared using the method discussed in section 2.1. As our microemulsions are formulated well above the CMC, the concentration of micelles is quite high. It could prove difficult to observe a transient dimer forming due to a high number of collisions taking place and so diluting the mixture with MilliQ water is required prior to the addition to the thin film of pyrene. The microemulsion can then be added to the flask to make up the solution. A stirrer bar was added, and the solution was left to stir vigorously for at least 12 hours, or until no solid pyrene was visible. The solution was also covered whilst stirring to avoid any photobleaching effects.

For comparative studies, a limonene-free 'surfactant package' was also formulated using the same mass ratios for $C_{12}E_7$, IPA and pure water.

The concentration of pyrene, *c,* was changed for each sample to give an absorbance, *A*, of 0.5, calculated using the Beer-Lambert Law:

$$A = \varepsilon c L \tag{3.4}$$

where ε is the molar extinction coefficient, and *L* is the path length of light in the cell. An absorbance of 0.5 was chosen to avoid absorbing all the incident light at the front wall of the cell which would result in a very weak fluorescence signal.

3.3 Results and discussion

3.3.1 Initial trials

Initial trials were conducted to give a comparison between a surfactant package and our swollen micelles. Figures 3.4 and 3.5 show a high-speed acquisition taken for 11 mM $C_{12}E_7$ swollen micelles in our microemulsion system and 11 mM $C_{12}E_7$ micelles in water, respectively, at equilibrium. A separate fluorescence spectrum of pyrene in water can be found in appendix B (figure 5) as a comparison to figures 3.4 and 3.5 and help determine if the signal was coming from free pyrene in the bulk.

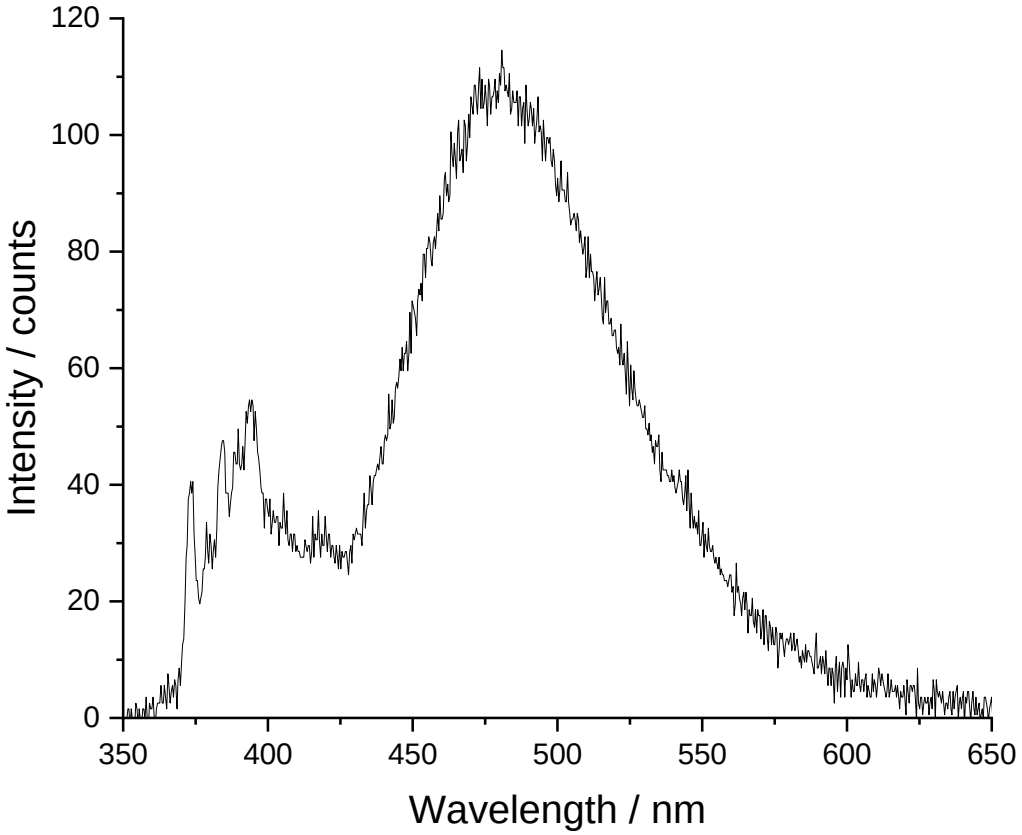

Figure 3.4: Limonene microemulsion, $C_{12}E_7$ 11 mM, pyrene 0.073 mM, integration time 10 ms, excitation wavelength 337 nm.

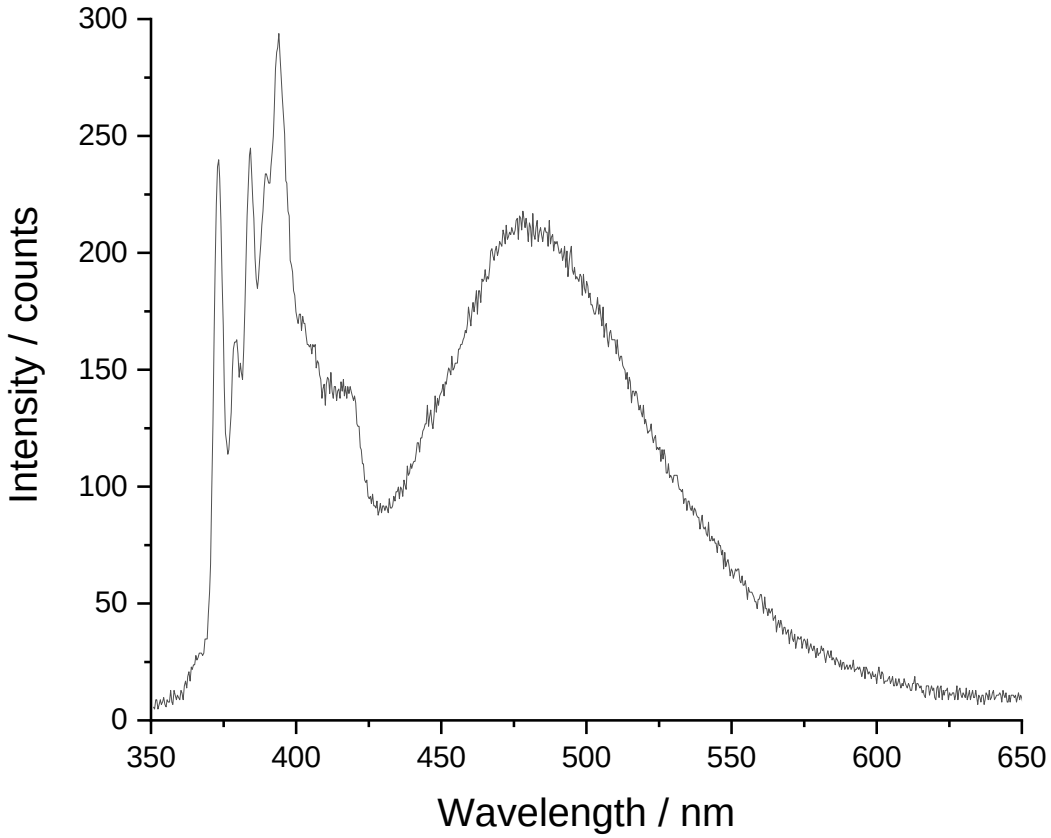

Figure 3.5: Surfactant package, $C_{12}E_7$ 11 mM, pyrene 0.073 mM, integration time 10 ms, excitation wavelength is 337 nm.

The relative intensities of the monomeric bands and broad excimer peak in figure 3.4 shows dominance in the excimer peak. The dominance of the excimer peak in figure 3.4 indicates the majority of the micelles in a limonene microemulsion system are populated by 2 or more pyrene molecules. In contrast, the relative intensities of the monomer and excimer peaks in figure 3.5 show a much more even distribution of monomer and excimer peaks. Referring to table 3.2, figures 3.4 and 3.5 follows the distribution of micelles populated by pyrene calculated using a Poisson distribution, the $M_1/M_{>1}$ is greater for $C_{12}E_7$ in water than limonene. The comparison of monomer and excimer peak intensities in figures 3.4 and 3.5 show that limonene is affecting the ratio of pyrene monomers and excimers formed, which is a consequence of the larger micelles in a microemulsion. The solubility of pyrene in water is low so pyrene will be present either in micelles or excess limonene. With limonene microemulsions, there will be fewer micelles present in the system, therefore the same number of pyrene molecules are distributed amongst fewer micelles, thus increasing the number of excimers formed.

The overall peak intensities for the surfactant package are higher than for limonene microemulsions. The same concentration of pyrene and surfactant is used for both experiments, with the position of the probe and light source remaining constant. Both solutions are clear, so the difference is not due to scattering. I conclude that the quantum yield for fluorescence of pyrene is lower in a limonene environment than in a surfactant micelle.

3.3.2 Micelle exchange experiments

The pyrene fluorescence spectra from a 11 mM surfactant package and limonene microemulsion at equilibrium (figures 3.4 and 3.5) have enough signal to attempt dilution mixing experiments with the same conditions. Therefore 1:1 mixing experiments were conducted to observe the fusion of micelles. A syringe containing pyrene-filled micelles and a syringe containing empty micelles were pneumatically pushed simultaneously into the cell at a volume ratio of 1:1. These 1:1 mixing experiments were undertaken for micelles in water and limonene microemulsions with a $C_{12}E_7$ concentration of 11 mM, and pyrene concentration of 0.073 mM, as in the equilibrium experiments in §3.3.1. The high-speed acquisition function was used with a 10 ms integration time for each scan taken and a total run time of 10 s, i.e each scan seen in a time series takes 10 ms to be acquired and depicted with a different colour. High-speed acquisitions have a small time delay after triggering, therefore acquisitions were triggered before the empty micelles were introduced into the cell, allowing initial mixing to be observed.

Figure 3.6 shows the 1:1 mixing experiment for the limonene microemulsions. Figure 3.7 shows the 1:1 mixing experiment for the surfactant package. The acquisition conditions and colour scheme for individual scans are the same for figures 3.6 and 3.7. The colour scheme is explained in the figure caption for figure 3.6.

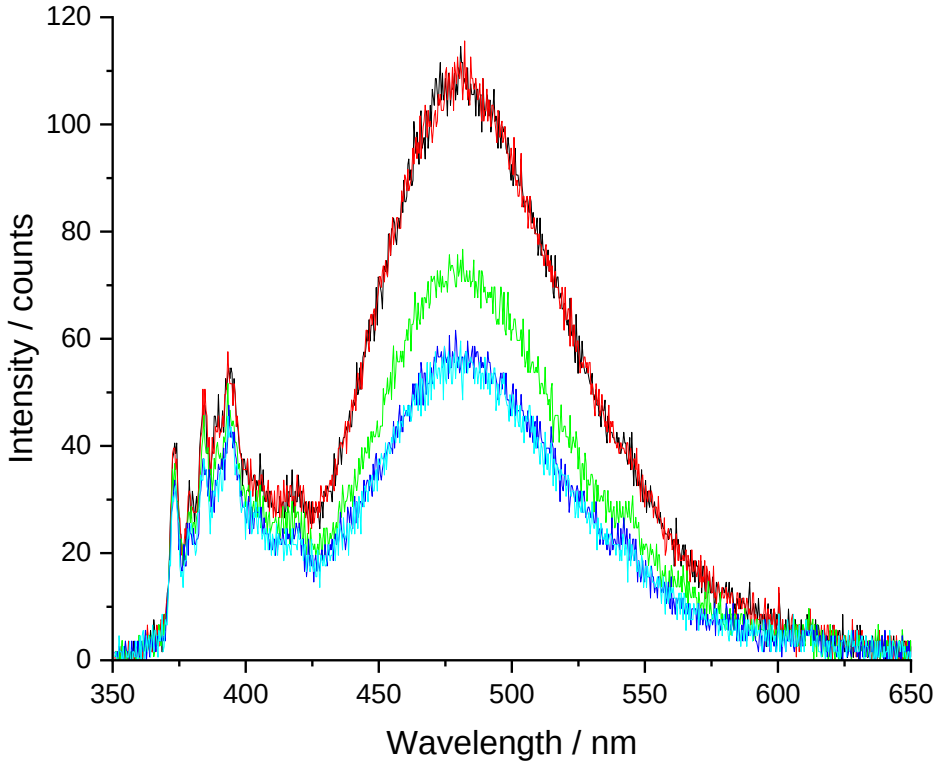

Figure 3.6: Limonene microemulsions 1:1 mixing, $C_{12}E_7$ 11 mM, pyrene 0.073 mM, integration time 10 ms. Run time of 10 seconds. Excitation wavelength is 337 nm. The black scan indicates an initial scan of pyrene-filled micelles before mixing with empty micelles. The red scan indicates the microemulsion still in equilibrium one scan before mixing. The light green scan is directly after the red scan and indicates the initial mixing point. The mixing time (>8 ms) is shorter than the minimum acquisition time of a spectrum (8 ms), mixing has occurred during this scan, so this trace is a composite of spectra before and after mixing. The dark blue scan is the fourth scan which is overlapping with the final scan (light blue) of the experiment.

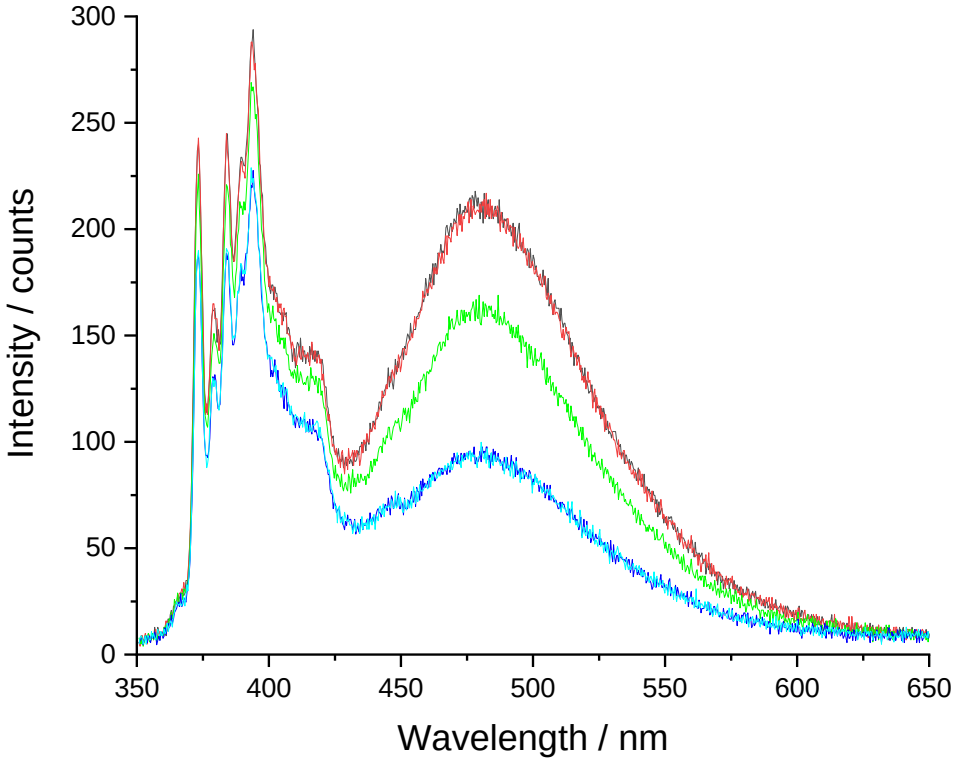

Figure 3.7: Surfactant package 1:1 mixing, $C_{12}E_7$ 11 mM, pyrene 0.073 mM, integration time 10 ms. Run time of 10 seconds. Excitation wavelength is 337 nm.

Figures 3.6 and 3.7 show a similar trend. When the empty micelles are introduced the intensity of the excimer peak reduced significantly, whereas the monomer peak reduces in intensity to a much lesser extent. The behaviour of the excimer peak is as expected, with more empty micelles being introduced, there can be an exchange of pyrene from micelles containing two or more pyrene molecules into the empty micelles. There is a decrease in the total amount of fluorescence as the concentration of pyrene has halved and so the amount of absorbed light decreases.

Figures 3.6 and 3.7 both show that exchange of pyrene between labelled and empty micelles is fast on the timescale of the acquisition time. For surfactant and limonene, the first and last measurements after mixing are indistinguishable, showing exchange is occurring too quickly to measure by stopped flow mixing.

3.3.3 Diffusion calculation

As the exchange process seems to be occurring at such a fast rate, it is useful to determine how fast the micelles are moving in the system and give an estimate to the collision rate of the micelles in the system. Calculation of the diffusion coefficient of a microemulsion droplet and the diffusion-controlled reaction rate for two microemulsion droplets colliding into each other could go some way to explaining whether we are capable of observing the rate of micelle fusion.

It is possible to determine the diffusion coefficient of a microemulsion droplet using the Stokes-Einstein equation shown in equation 3.5 assuming the droplet is spherical.

$$D = \frac{k_B T}{6\pi\eta r} \tag{3.5}$$

k_B is Boltzmann constant, T is temperature, η is the viscosity of the medium (water) taken from the literature [12] and r is the radius of our microemulsion droplet calculated in §2.3.

$$\mathrm{D} = \frac{1.38\ x\ 10^{-23} m^2 kg\ s^{-2} K^{-1} \times 298K}{6\times\pi\times 0.897\times 10^{-3} kg\ m^{-1}\ s^{-1} \times 5.2\times 10^{-9} m}$$

$$\mathrm{D} = 4.7 \text{ x } 10^{-11} \text{ m}^2 \text{ s}^{-1} \tag{3.6}$$

The diffusion-controlled reaction rate can be determined for two microemulsion droplets colliding into each other using a Smoluchowski model [13]. It is assumed that both droplets are spherical, the droplets are in a state of flux and so both diffusing, and finally the reaction is fully diffusion controlled. With these considered, equation 3.7 can be derived.

$$k_D = 4\pi(D_A + D_B)RN_A \quad (3.7)$$

D_A and D_B are the diffusion coefficients for each droplet. R is the critical radius which is equal to the sum of both droplet radii. N_A is Avogadro's number. By substituting the diffusion coefficient in equation 3.6 and also using the calculated radius of our microemulsion droplets, we can get an estimate k_D of 7.4 x 10^6 m^3 mol^{-1} s^{-1}. For a micelle concentration of ~0.1 mM (assuming ~10^2 surfactant molecules per micelle) the average time between collisions is ~ 1 μs. Even if only 1 in 1000 collisions led to the formation of a transient dimer and the exchange of micellar contents, the solution would equilibrate on the millisecond timescale.

3.3.4 Attempts to slow collision rate

As these experiments are currently running at the fastest integration times possible for the spectrometer, it is necessary to lower collision rates to observe transient dimer formation. One possible solution would be to lower the number of micelles in the system by reducing surfactant concentration. The micelles will have further to diffuse to transfer pyrene molecules.

Another alternative would be to introduce repulsive forces to slow collision rates using charged surfactants such as sodium dodecyl sulphate (SDS). If the number of micelles is known in the system, then an appropriate amount of SDS added would charge some of the micelles enough to create repulsive forces between the micelles and thus slowing the rate at which collisions occur.

Reducing the concentration

The number of micelles was lowered by reducing the surfactant concentration to 2 mM. Figure 3.8 shows the 1:1 mixing experiment for limonene microemulsions at 2 mM $C_{12}E_7$ concentration.

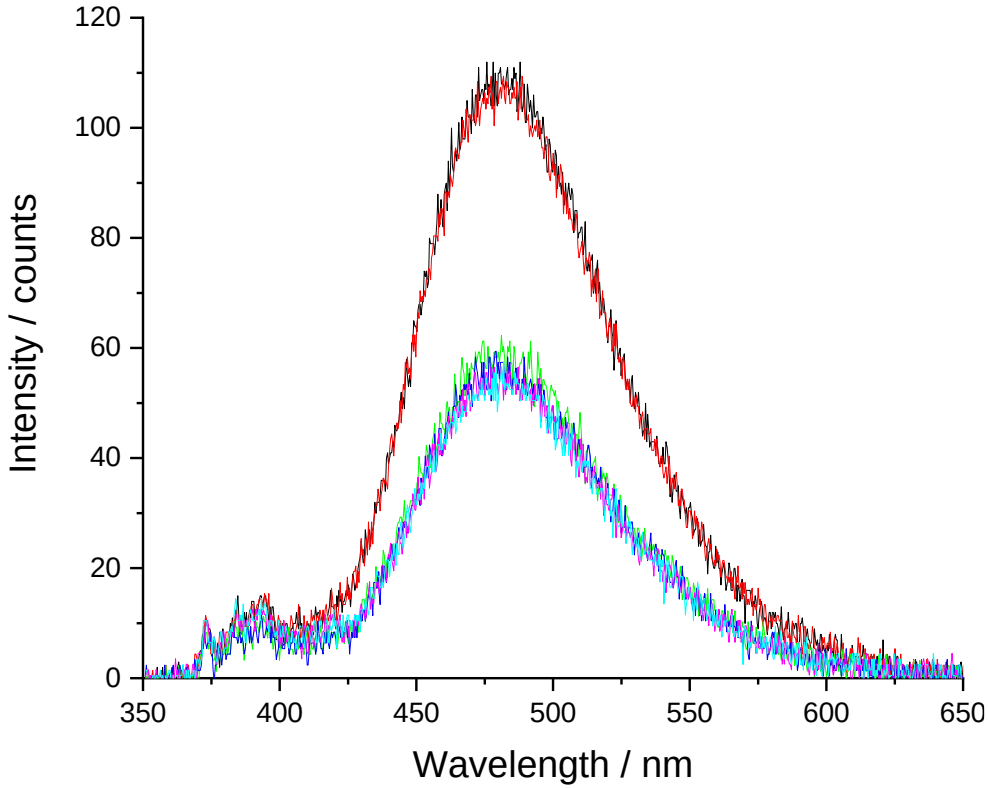

Figure 3.8: Limonene microemulsions 1:1 mixing, $C_{12}E_7$ 2 mM, pyrene 0.073 mM, integration time 10ms. Run time of 10 seconds. Excitation wavelength is 337 nm. The black line indicates an initial scan before mixing, the red scan indicates the micelles still in equilibrium one scan before mixing. The light green scan is directly after the red scan and indicates the initial mixing point; it is likely that mixing occurred at the beginning of this acquisition. The dark blue scan is the following scan, the pink scan follows the dark blue scan which is overlapping with the final cyan scan of the experiment.

The collisions at 2 mM surfactant concentration suggest the exchange kinetics are complete within 20 ms of mixing the two solutions as evidenced by the spectral overlap of the pink scan and cyan scan. The surfactant concentration was reduced further to 0.8 mM, still well above the CMC and a replicant of industrial working conditions. To do this successfully I had to adjust the pyrene concentration from 0.073 mM to 0.024 mM. At 0.073 mM, only a broad excimer peak was observed with the monomer peak barely distinguishable. There are far fewer micelles available to hold pyrene molecules, meaning a greater number of excimers (arising from 2 or more pyrene molecules in a given micelle). However, when the pyrene concentration is lowered too much there is not enough signal to give an observable spectrum. Therefore, after a number of trials I found a pyrene concentration of 0.024 mM gave satisfactory results.

Figure 3.9 shows 1:1 mixing experiment for limonene microemulsions at 0.8 mM $C_{12}E_7$ concentration. Figure 3.10 shows 1:1 mixing experiment for $C_{12}E_7$ in water at 0.8 mM $C_{12}E_7$ concentration.

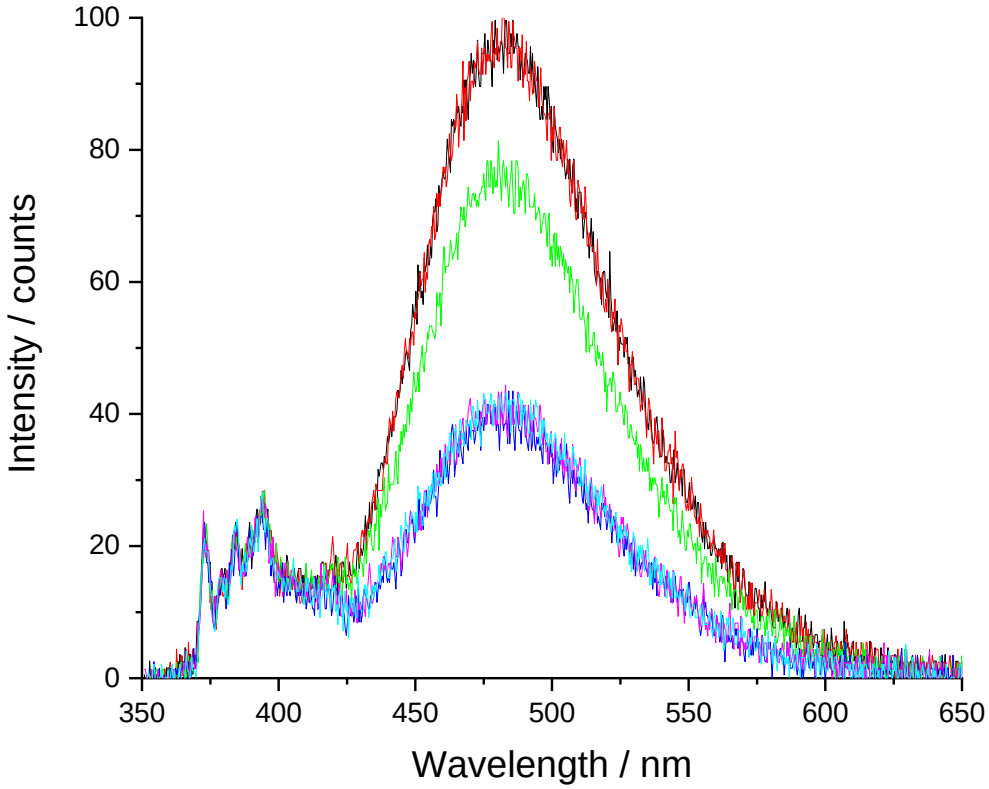

Figure 3.9: Limonene microemulsions 1:1 mixing, $C_{12}E_7$ 0.8 mM, pyrene 0.024 mM, integration time 10ms. Run time of 10 seconds. Excitation wavelength is 337 nm. For colour scheme see figure 3.8.

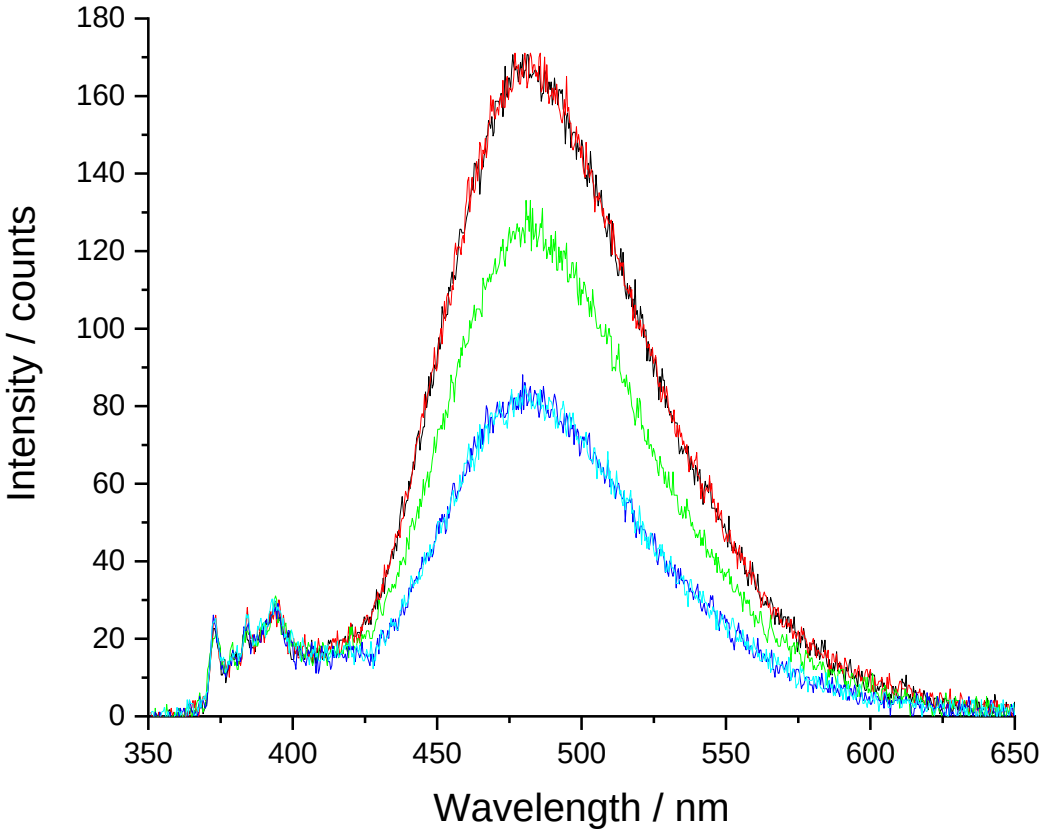

Figure 3.10: Surfactant package 1:1 mixing, $C_{12}E_7$ 0.8 mM, pyrene 0.024 mM, integration time 10 ms. Run time of 10 seconds. Excitation wavelength is 337 nm. For colour scheme see figure 3.8.

Figures 3.9 and 3.10 show that reducing the concentration of the surfactant has not slowed the exchange kinetics by a discernible amount. The exchange after initial mixing equilibrates within 20 ms for limonene microemulsions due to an overlap of the pink scan and cyan scan. For the surfactant package exchange equilibrates within 10 ms as indicated by the overlap of the dark blue and cyan scan in figure 3.10.

It is interesting, when comparing figures 3.9 and 3.10, that there is a greater intensity in signal for $C_{12}E_7$ in water and also what appears to be a greater fraction of excimers (in contrast to Figures 3.6 and 3.7). From a qualitative view, it seems that the monomer intensity for figures 3.9 and 3.10 remains the same, but the excimer intensity has increased by around 50%. However, the blue and cyan curves are still the same, so reducing the surfactant concentration has not slowed the collision rate down to an extent in which it can be observed on the 10 ms timescale.

Introducing repulsive forces

Reducing the surfactant concentration did not slow the collision rate down effectively enough to be observed at 10 ms. I introduced repulsive forces by charging the micelles at lower surfactant concentration (0.8 mM) to observe the micelle fusion process. Yan et al. studied the adsorption kinetics of non-ionic micellar solutions using an overflowing cylinder experiment [14]. Yan et al. found the addition of small amounts of charged surfactants, less than 10% of the total surfactant concentration, dramatically reduced the rate of adsorption of $C_{16}E_8$ in micellar solution. When ionic surfactants were present, only uncharged micelles adsorbed to the air-water interface. Following this example, the introduction of charged micelles into our system may slow the micelle fusion process enough to observe their kinetics.

Figure 3.11 shows 1:1 mixing experiment for limonene microemulsions at 0.8 mM $C_{12}E_7$ and 5% SDS (as a fraction of the concentration of $C_{12}E_7$). Charged swollen micelles filled with pyrene are pneumatically mixed with charged swollen micelles without pyrene at a ratio of 1:1. The colour scheme for mixing is the same as shown from previous figures, see figure 3.8 caption for a description of the colour scheme. Figure 3.12 shows 1:1 mixing experiment for $C_{12}E_7$ in water at 0.8 mM $C_{12}E_7$ concentration and 5% SDS.

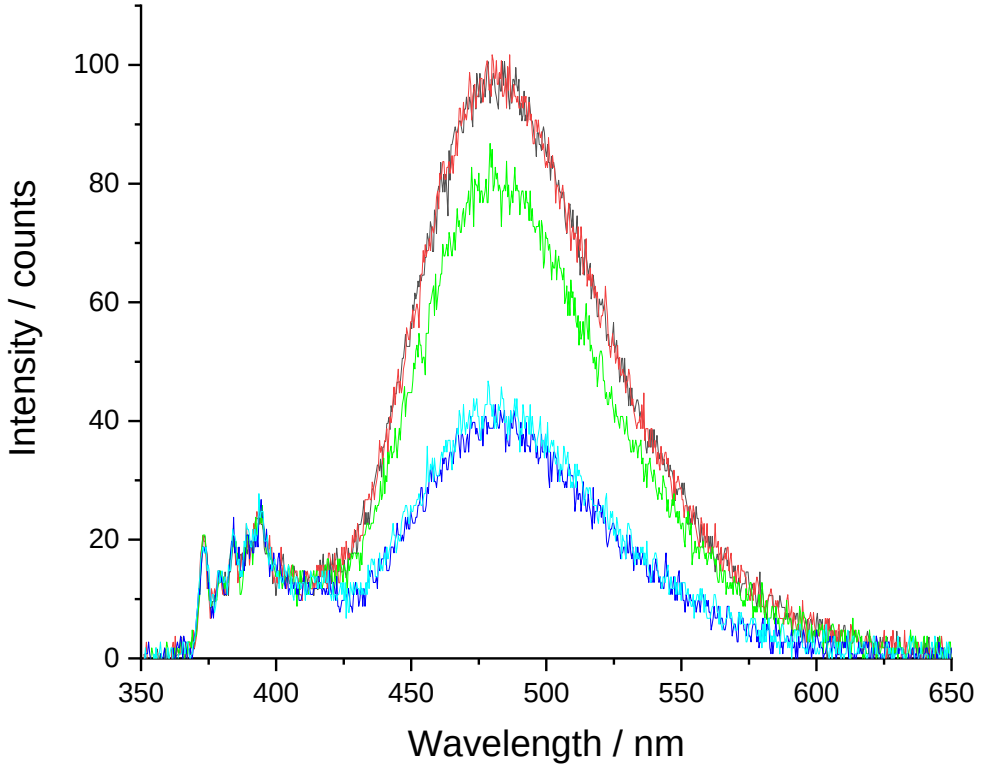

Figure 3.11: Limonene microemulsions in microemulsion system with 5% SDS 1:1 mixing, $C_{12}E_7$ 0.8 mM, pyrene 0.024 mM, integration time 10 ms. Run time of 10 seconds. Excitation wavelength is 337 nm.

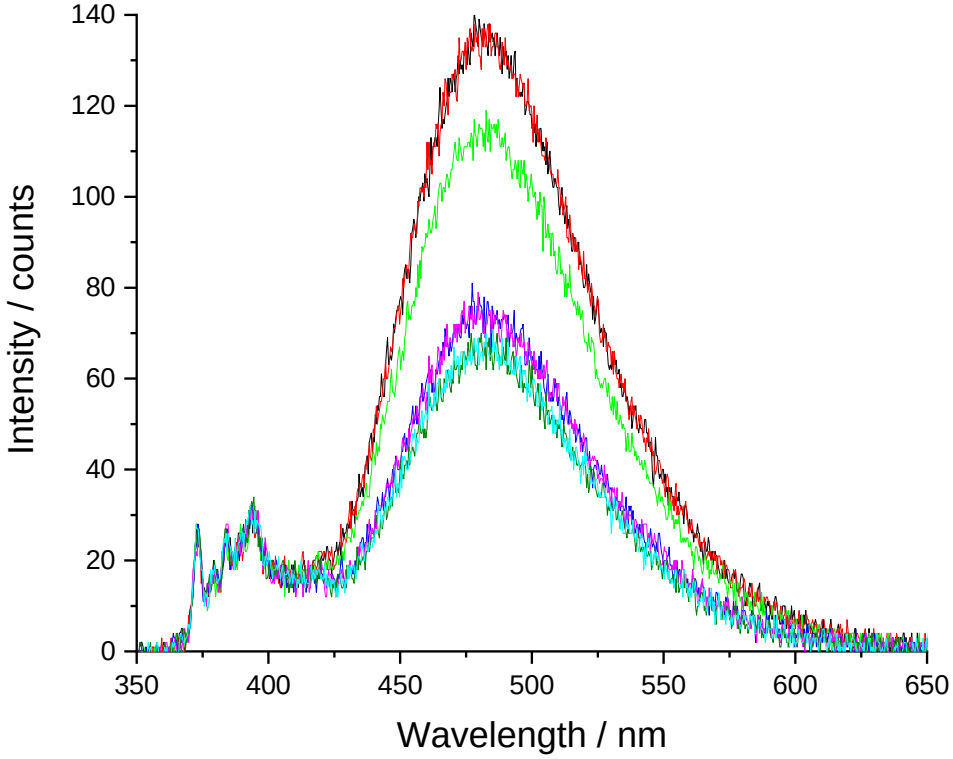

Figure 3.12: Surfactant package 1:1 mixing with 5% SDS, $C_{12}E_7$ 0.8 mM, pyrene 0.024 mM, integration time 10 ms, run time of 10 seconds, excitation wavelength is 337 nm. The black line indicates an initial scan before mixing, the red scan indicates the micelles still in equilibrium one scan before mixing. The light green scan is directly after the red scan and indicates the initial mixing point. The dark blue is the following scan, which is overlapping with the fourth pink scan, the dark green scan follows the pink scan and is overlapping with the final cyan scan.

Figures 3.11 and 3.12 show a similar trend. Both show mixing occurring on a timescale smaller than 10 ms, mixing occurs during the light green scan and is finished before the following dark blue scan. Figure 3.12 appears to show a slower relaxation process occurring from the subsequent overlapping dark blue and light blue scans in the presence of SDS. Despite successfully conducting experiments at lower $C_{12}E_7$ concentrations with SDS, it is not clear what processes are involved, however the evidence does seem to indicate there are more processes occurring than simply exchange of contents at short timescales (<10 ms).

A comparative study was undertaken to determine what affect a change in micro viscosity may have on the micelle exchange and the role played by limonene. Hexane was chosen as a suitable solvent to test; hexane is a common fraction found in petroleum and has a lower viscosity to limonene.

The same method to formulate a hexane microemulsion was used as previously with limonene, keeping the same ratios of water/IPA/$C_{12}E_7$/oil. A clear stable microemulsion was formed after gentle mixing. The same dilution method was used as for limonene microemulsions. Trials using a surfactant concentration of 11, 2 and 0.8 mM were used, with pyrene concentration adjusted accordingly. The hexane mixing experiments gave similar results as the limonene and micelles in water experiments. Results of the hexane mixing experiments for 11 mM and 0.8 mM $C_{12}E_7$ can be found in appendix B.

These pyrene mixing experiments led to further questions about the processes occurring that could be giving these fast exchange rates. One possibility was that exchange of pyrene between micelles was occurring not through micelle fusion but by diffusion of pyrene molecules through the aqueous phase. Although pyrene is a very hydrophobic molecule (comprising four fused benzene rings, Figure 3.1) it does have a small solubility in water. As for micelle collisions above, the Smoluchowski model can be used to calculate the diffusion-controlled rate for a pyrene molecule entering a micelle [15]. Equation 3.7 can be used, where D_A and D_B are now the diffusion coefficients of a micelle and pyrene in water, respectively. The micelle diffusion coefficient was calculated previously §3.3.3 and the diffusion coefficient for pyrene in water is taken from the literature [16] . The diffusion-controlled rate for a pyrene molecule entering a micelle k_D was calculated as 6×10^7 m^3 s^{-1} mol^{-1}. At equilibrium,

the rate of pyrene molecules entering and exiting the micelles is equal. To obtain an upper limit on this rate, we can use the solubility limit of pyrene in water as a concentration of pyrene molecules in the bulk. The literature value of the solubility of pyrene in water is 0.135 mg/L [17], yielding a concentration of pyrene in water is 6.7 x 10^{-7} M. With this value, and using k_D, the rate of entry and exit of pyrene molecules in micelles at equilibrium (k_p) is given in equation 3.8.

$$k_p = 2.83 \times 10^4\ s^{-1} \tag{3.8}$$

This gives a time scale for pyrene molecules entering and exiting micelles of 3.5 x 10^{-5} s, less than one tenth of a millisecond, based on a purely diffusion model. This is an obvious cause for concern as the changes in intensity in the previous experiments could be attributed to pyrene molecules simply entering and exiting micelles from the bulk. Even if the pyrene concentration were one hundredth of the saturation concentration, we would have difficulty observing exchange kinetics. The pyrene concentration is of the order of ~1% of the surfactant concentration in the micelles (to get good sensitivity to the monomer/excimer ratio) and pyrene does not mix ideally with the hydrocarbon chains of $C_{12}E_7$ or limonene, so the bulk pyrene concentration will be >1% of the saturation value.

Attempts were made to reduce the surfactant concentration whilst charging the micelles to see some observable kinetics without success. If equilibration of pyrene (which is uncharged) occurs via diffusion of pyrene molecules through the aqueous phase, then charging the micelles would have no effect on the kinetics. Therefore, it was necessary to find a fluorescent probe that is much less soluble in water to prevent the probe molecule moving through bulk solution as readily as the case for pyrene. The probe we chose is a fluorescently labelled lipid, lissamine rhodamine B sulfonyl ammonium salt, 18:1 Liss Rhod PE (figure 3.13). The rhodamine probe has a higher molar mass (1301.71 $gmol^{-1}$) and is virtually insoluble in water (too low to measure) due to the two long hydrocarbon chains on the lipid. Exchange of the probe by diffusion through the bulk solution will therefore occur much more slowly.

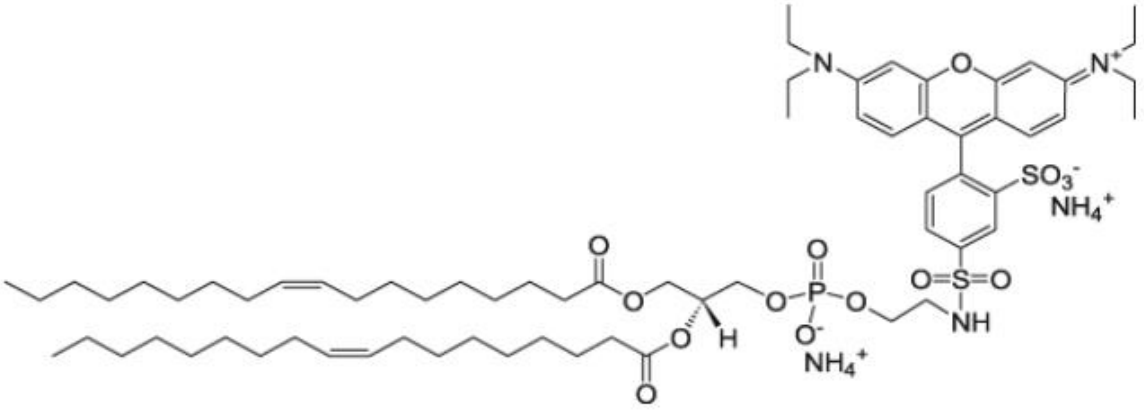

Figure 3.13: Molecular structure of 18:1 Liss Rhod PE. Product name: 1,2-dioleoyl-sn-glycero-3-phosphoethanolamine-N-(lissamine rhodamine B sulfonyl) (ammonium salt).

Mixing experiments using 18:1 Liss Rhod PE were conducted using the same method as with the pyrene probe. The concentration of 18:1 Liss Rhod PE was kept at ≤1% of $C_{12}E_7$ molar concentration for mixing experiments to avoid inner filter effects and to ensure the probe did not change the mechanical properties of the micelles. Inner filter effects are a common issue for fluorescence spectroscopy, which usually arises when there is a high concentration of the fluorescent chromophore. The excitation beam is attenuated by the sample so only the front of the sample fluoresces, not allowing light to travel through the whole of the sample [18].

It was hoped that interactions between fluorophores might change the shape of the emission curve or that the dye may self-quench, so that dilution would increase the intensity of fluorescence if mixing occurred. However, there were no changes to the peak shape on dilution of the dye and the overall signal decreased due to the lower dye concentration. It was not possible to infer any information on the exchange of contents between micelles. The results from the 18:1 Lissamine Rhod-PE mixing experiments can be found in appendix B.

18:1 Lissamine Rhod-PE has been used by Arenas et al. in combination with another fluorescently labelled lipid (NBD-PE) to observe fast collisional lipid transfer using Förster resonance energy transfer (FRET) in a stopped-flow experiment [19]. One syringe was labelled with both probes and mixed with empty lipid particles. The lipid concentrations ranged from 40–0.5 mM and the probe concentrations were ≤1% molar concentration of the lipid.

The structure of NBD-PE is given in figure 3.14 below. As with Lissamine Rhod-PE, the two long acyl chains lead to very low bulk solubility, so solubilisation will primarily occur in the micelle rather than the aqueous bulk phase.

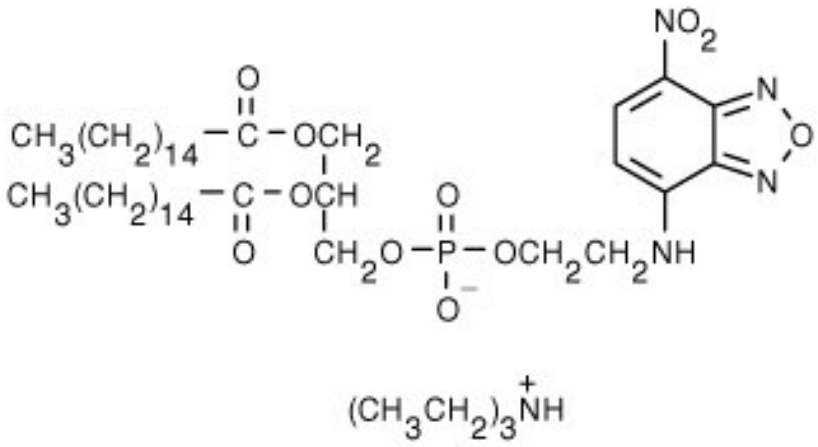

Figure 3.14: Molecular structure of N-(7-nitrobenz-2-oxa-1,3-diazol-4-yl)-1,2-dihexadecanoyl-sn-glycero-3-phosphoethanolamine, triethylammonium salt (NBD-PE), molecular mass 956.25.

I therefore decided to use the FRET stopped-flow technique described by Arenas et al. to study micelle fusion. The theory of FRET will be discussed in section 3.4 and the experimental set up in 3.4.1.

3.4 Förster Resonance Energy Transfer

Förster (or Fluorescence) Resonance Energy Transfer (FRET) involves the interaction between the excited states of two dye molecules, in which excitation energy is transferred from a donor molecule to an acceptor molecule. A common FRET pair used is NBD-PE and 18:1 Liss Rhod PE (Rh-PE), which are used for our studies.

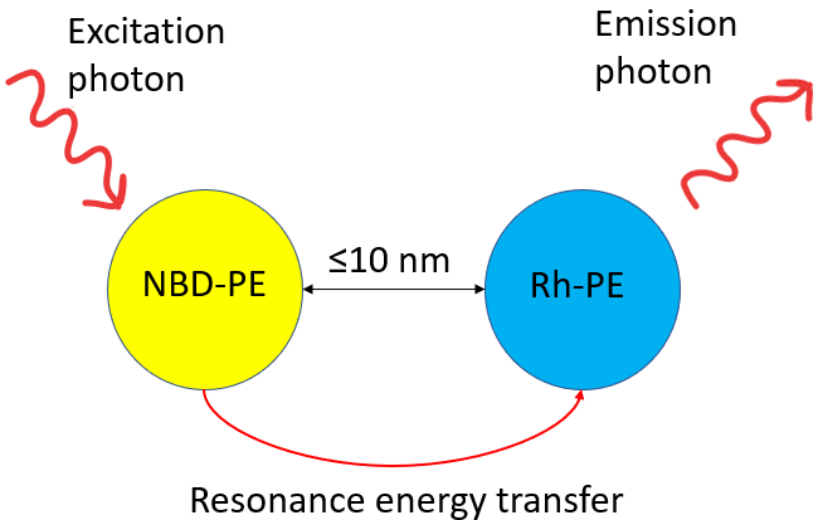

Figure 3.15: Schematic of successful FRET, using NBD-PE as the donor molecule and Rh-PE as the acceptor molecule.

FRET is a distance-dependent interaction between the electronic excited states of two dye molecules. Efficiency of FRET is dependent on the inverse 6^{th} power of the intermolecular separation. Three conditions need to be satisfied for a successful FRET experiment.

1. Donor and acceptor molecules must be in close proximity to one another. (Usually 10–100 Å).
2. Absorption spectrum of acceptor must overlap the emission spectrum of the donor.
3. Donor and acceptor transition dipole orientations must be approximately parallel.

Additionally, acceptor concentration cannot be too high, or it will absorb all the donor emission and fluoresce, even when it is not close to the donor.

If donor and acceptor probes are in different micelles, they will be too far apart for FRET. If the fusion of two micelles leads to acceptor and donor being in the same micelle (typical diameter <3 nm, microemulsion diameter estimated to be 10 nm) they will be in close enough proximity for FRET to occur, increasing the acceptor emission and reducing the donor emission.

For our experiments, the donor probe was chosen to be NBD-PE and the acceptor probe Rh-PE. There are two reasons for choosing these two probes: firstly, both Rh-PE and NBD-PE are sufficiently hydrophobic to dissolve preferentially in the micelles over the bulk aqueous solution. Secondly, the emission spectra of NBD-PE and

absorbance spectra of Rh-PE have a good degree of overlap as can be seen in figure 3.16.

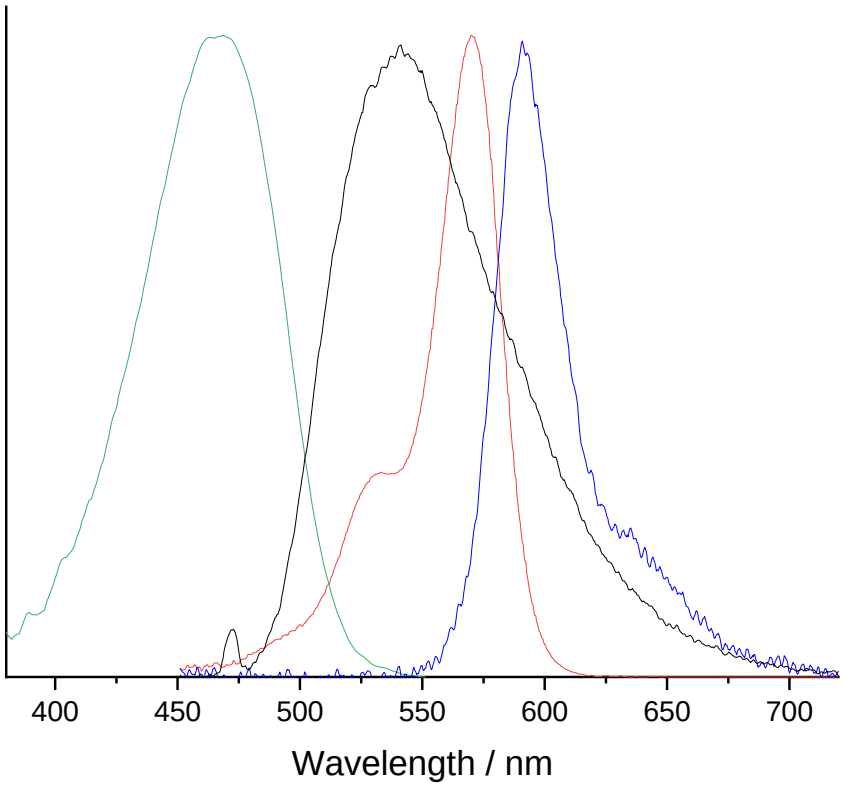

Figure 3.16: Spectral overlap and FRET of Rh-PE and NBD-PE. The green line is NBD-PE excitation spectrum, the black line is NBD-PE emission, the red line is Rh-PE excitation, the blue line is the Rh-PE emission.

By measuring the change in the intensity ratio of donor/acceptor emission following mixing in a stopped flow device, it is possible to quantify the exchange of contents and the kinetics of mixing.

3.4.1 Experimental setup for FRET experiments

The experimental setup for the FRET experiments is similar to previous pyrene kinetic experiments using the stopped-flow system described in §3.2.1. Syringe A is filled with the micellar solution containing the donor probe. Syringe B is filled with the micellar solution containing the acceptor probe (Rh-PE). Syringe A and syringe B are pneumatically mixed at a 1:1 ratio using the stopped-flow device and the change in NBD-PE to Rh-PE emission intensity ratio over time indicates the rate of FRET exchange. The concentration of NBD-PE is kept at 1% by mole of surfactant and Rh-PE at 0.5% by mole of surfactant to give a good peak ratio and avoid changing the mechanical properties of our micelles. An illustration for syringe A and syringe B with the resulting mixture can be seen in figure 3.17.

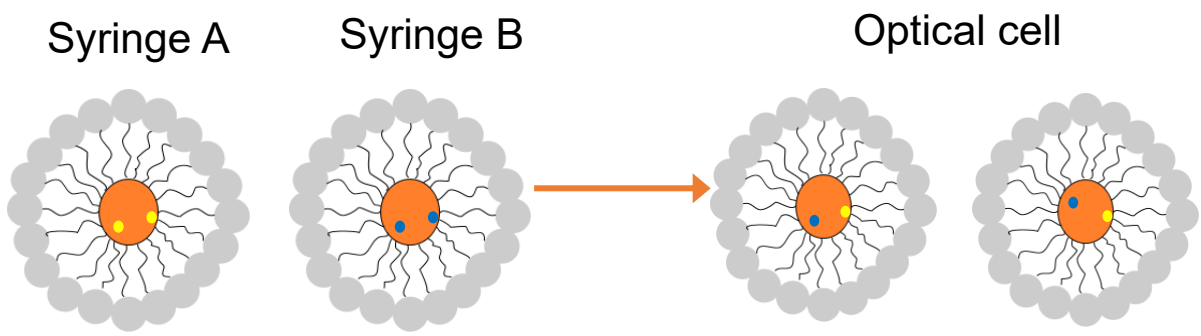

Figure 3.17: Illustration of micelles inside syringes A and B. The final state is a representation of the micelles in the optical cell after equilibration of contents. The yellow dots indicate NBD-PE dye molecules, the blue dots indicate Rh-PE dye molecules.

A new method was designed to make stock solutions of Rh-PE and NBD-PE in micelles. Stock solutions for 1% NBD-PE and 0.5% Rh-PE by mole of $C_{12}E_7$ are made for 20 mM microemulsion systems in separate 30-mL capped amber sample bottles fitted with a PTFE/silicon septum. These solutions can then be diluted with water to lower concentrations for experimental runs. 1 mL (Hamilton, Gastight bevel tip) 250 µL and 100 µL (SGE, fixed bevel) glass syringes are used when transferring the dye solutions in order to reduce evaporation loss. A detailed overview of the preparation method for the 20 mM microemulsion stock solutions is shown below.

Stock procedure for microemulsion filled with Rh-PE and NBD-PE

To make a 20 mM microemulsion stock with 0.5% Rh-PE by mole of $C_{12}E_7$.

1. Take 2 mL of the Rh-PE (received as 5 x 2 mL solutions dissolved in chloroform 1 mg/mL from AvantiPolarlipids) and syringe into a 30 ml amber sample bottle. Add 0.15 g $C_{12}E_7$, $C_{12}E_7$ is heated to the liquid phase and added using a syringe drop wise on an accurate mass balance ensuring $C_{12}E_7$ is fully dissolved in solution.
2. Evaporate off chloroform under a steady stream of nitrogen in a water bath at 30 ˚C to a thin waxy film ensuring any trace chloroform is fully evaporated, the amber bottle is then enclosed with a PTFE/silicon septum.
3. Add 0.15 g IPA, 0.1 g limonene using glass syringes to the thin waxy film.
4. Sonicate in a bath sonicator for 15 minutes.
5. Add 0.26 g MilliQ water using a glass syringe to generate the original microemulsion concentration.
6. Sonicate in a bath sonicator for 15 minutes.
7. Dilute to 15.36 mL of solution with water to give 20 mM solution. The known volume of water needed for the dilution is converted to mass using literature density values to allow the use of an accurate mass balance. The water is then transferred to the amber bottle using a glass syringe.
8. Sonicate in a bath sonicator for 15 minutes.

To make a 20 mM microemulsion stock with 1% NBD-PE by mole of $C_{12}E_7$. NBD-PE is received as powder from ThermoFisher. Dissolve in chloroform to make up a 10 mg/ 10 mL solution in a 30-mL capped amber bottle fitted with a PTFE/silicon septum.

1. Take 2 mL of the NBD-PE dissolved in chloroform (received as 10 mg powder from AvantiPolarlipids, concentration of NBD-PE in chloroform 10 mg/ 10 mL) and syringe into a 30 ml amber sample bottle fitted with a PTFE/silicon septum. Add 0.1 g $C_{12}E_7$, $C_{12}E_7$ is heated to the liquid phase and added using a syringe drop wise on an accurate mass balance ensuring $C_{12}E_7$ is fully dissolved in solution.
2. Evaporate off chloroform under a steady stream of nitrogen in a water bath at 30 $^{\circ}$C to a thin waxy film ensuring any trace chloroform is fully evaporated, the amber bottle is then enclosed with a PTFE/silicon septum.
3. Add 0.1 g IPA, 0.07 g Limonene using separate glass syringes to the thin waxy film.
4. Sonicate in a bath sonicator for 15 minutes.
5. Add 0.18 g MilliQ water using a glass syringe.
6. Sonicate in a bath sonicator for 15 minutes.
7. Dilute to 10.46 mL of solution with water to give 20 mM solution. The known volume of water needed for the dilution is converted to mass using literature density values to allow the use of an accurate mass balance. The water is then transferred to the amber bottle using a glass syringe.
8. Sonicate in a bath sonicator for 15 minutes.

3.5 Leak issues

After fitting a circulating water bath to the stopped-flow rig there were noticeable stability issues when conducting experiments. It was first thought there may be an issue with a batch of stock solutions made, however the same results were found with previously successful solutions. The nature of the instability suggested there may be a slow leak in the system. A pressure hold experiment was conducted and confirmed there was a leak. An image taken of the stopped flow mixing unit can be seen in figure 3.18 below. Figure 3.18 highlights the suspected components that could contribute to the leak.

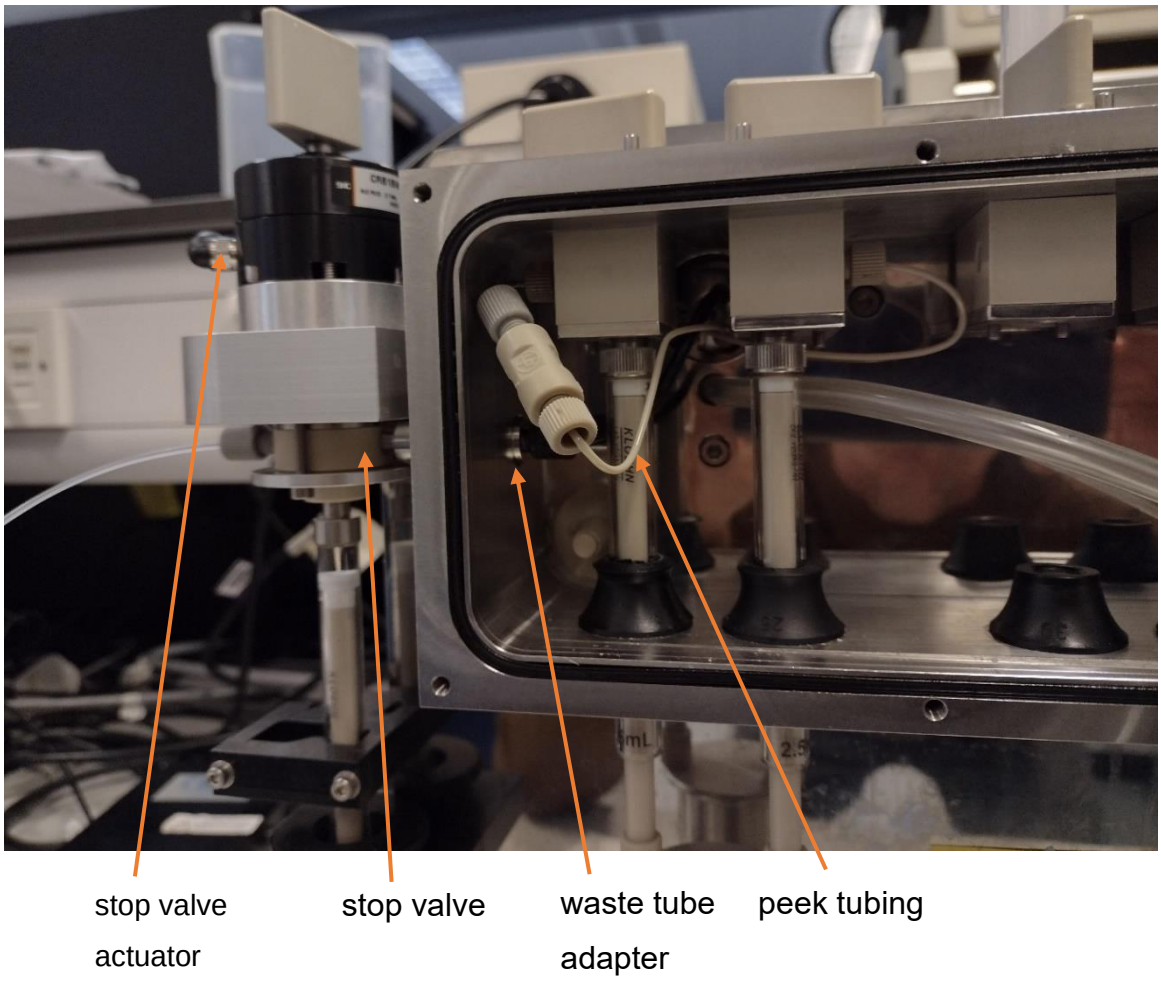

Figure 3.18: Image taken of the stopped-flow setup with water bath housing window removed. Location of the key elements for leak issues detailed.

Two potential causes of the leak were identified, the first being damage to the peek tubing from the drive syringe into the optical cell. The water bath uses a continuous flow of water to give thermostatic control of the system. The flow of water had forced the peek tubing against the drive syringe housing unit, which over time had caused a small perforation of the peek tubing. The peek tubing was replaced and held into place away from the drive syringe housing unit for future experiments.

The stop valve controls the flow from the optical cell to the stop syringe and from the stop syringe to the waste collection beaker. The stop valve was not clearing from the closed and open position correctly. It is important the stop valve is not connected to the waste tube adapter too tightly (finger tight is recommended) as it does not allow the stop valve to fully open or close. It appears the stop valve had tightened on the waste tube adapter over time to such a degree part of the stop valve had broken inside. Replacing the stop valve and connecting the valve loosely to the waste tube adapter resolved this issue. After taking the stop valve off from the auto assembly unit, there was also noticeable damage on one of the pneumatic tubing connectors. The damage to the pneumatic tubing was unlikely to be causing a leak issue but could have been contributing to the stop valve not fully opening or closing and so was also replaced.

3.6 Photobleaching and drifting tests

I undertook trials to account for drifting and also photobleaching for both dyes. Separate microemulsion systems of NBD-PE and Rh-PE were left in the optical cell for an extended period. First, the shutter from the monochromator was closed to determine if there was any local drift or relaxation processes occurring. A separate set of tests were undertaken whereby the shutter was kept open to test for possible photobleaching. For the Rh-PE tests, the excitation wavelength is moved from 468 nm to 560 nm whilst measuring the emission spectra of pure Rh-PE. For the shutter closed tests, there is a negligible change in intensity. For the shutter open tests, after 10 minutes there is a noticeable drop in intensity for both dyes. Rh-PE has an overall intensity drop of 1.7% over 10 minutes with an average drop of 0.17% / minute. NBD-PE has an overall intensity drop of 1.9% over 10 minutes and an average drop of 0.19% / minute.

An experiment was devised to determine if any dye molecules remained on the side walls of the flow cell from previous runs. MilliQ water was driven through the cell numerous times after filling the optical cell with 5 mM NBD-PE micellar solution. The acquisition time was increased to 5 seconds as it was expected that very few dye molecules would still be present in the cell after being driven through with water. Figure 3.19a shows the result of the first drive. The black spectrum indicates NBD-PE in the cell before water is pushed through. The green spectrum was acquired after 10 seconds and the blue spectrum 1 minute after the drive with water. Figure 3.19(b) expands the vertical scale so that the weak spectra after displacing the dye solution are more clearly visible.

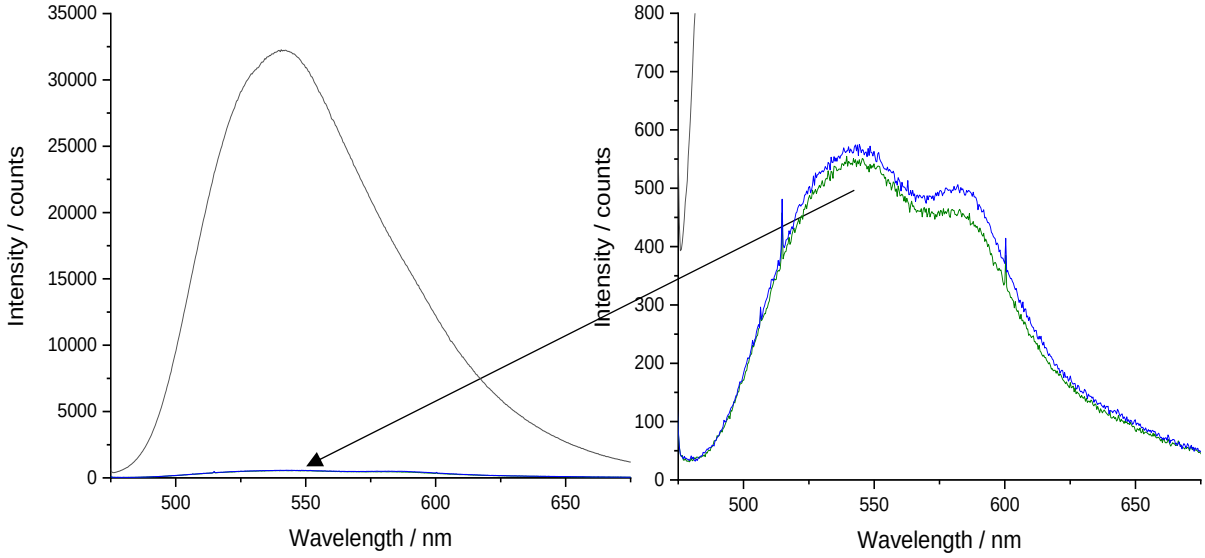

Figure 3.19 a: First water drive. Initial cell contents 5 mM NBD-PE microemulsion. 5 s integration time. Excitation wavelength 468 nm.

Figure 3.19b: Enhanced region of interest from figure 3.19a.

Figure 3.20 is the result of a subsequent drive through with water after the first drive from figure 3.19a and 3.19b. The light blue spectrum is 10 seconds after displacing the contents of the cell water and the orange spectrum after 10 minutes.

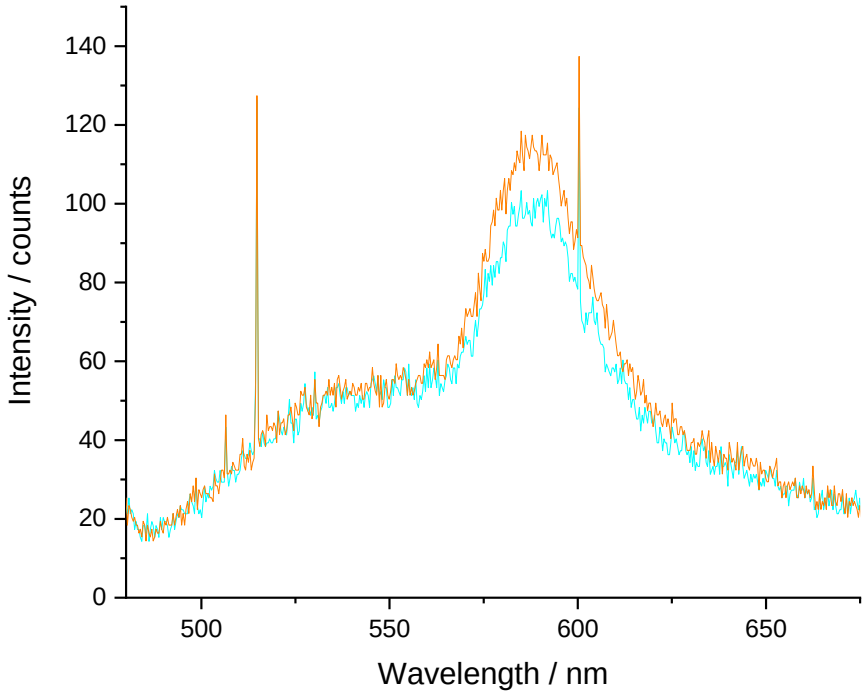

Figure 3.20 : Second water drive. Initial cell contents 5 mM NBD-PE microemulsion. 5 s integration time. Excitation wavelength 468 nm.

Figures 3.19a, 3.19b and 3.20 show that there are still some NBD-PE and RH-PE dye molecules left on the cell walls that give a FRET signal. The FRET signal from the cell walls can only be seen when the bulk NBD signal is low enough and the acquisition time is greatly increased. This signal can be removed with a thorough wash using a mixture of water and IPA between runs, for this run the cell was not thoroughly cleaned through. After one drive of water there remains ~1–2% of signal which falls to <1% after a subsequent drive. The wall signal present in figure 3.20 is only 0.4% of the bulk signal and should not be a cause for concern for experiments taken.

Conclusion

The micelle fusion experimental setup using a stopped-flow fluorescence technique has been discussed in detail. Experiments using a pyrene dilution experiment were unsuccessful despite efforts to adjust the experimental conditions. The need for less soluble fluorescent probes was evident from the pyrene mixing experiments and diffusion calculations.

The introduction of fluorescently labelled lipids addressed the solubility issues found for pyrene experiments. The requirements for a successful FRET exchange for our studies and the combination of FRET with a stopped-flow technique have been discussed. Challenges found during experimentation for the FRET studies, results of which will be discussed in later chapters, have also been noted. Chapter 4 will discuss the initial results for our FRET stopped-flow experiments and the tools used to analyse the FRET exchange data quantitatively.

References

[1] S. Takaramoto, Y. Nakasone, K. Sadakane, S. Maruta, and M. Terazima, 'Time-resolved detection of SDS-induced conformational changes in α-synuclein by a micro-stopped-flow system', *RSC Adv*, vol. 11, no. 2, pp. 1086–1097, Jan. 2021, doi: 10.1039/D0RA09614H.

[2] J. Zhang, S. Chen, Z. Zhu, and S. Liu, 'Stopped-flow kinetic studies of the formation and disintegration of polyion complex micelles in aqueous solution', *Physical Chemistry Chemical Physics*, vol. 16, no. 1, pp. 117–127, Nov. 2013, doi: 10.1039/C3CP53608D.

[3] L. Piñeiro, M. Novo, and W. Al-Soufi, 'Fluorescence emission of pyrene in surfactant solutions', *Adv Colloid Interface Sci*, vol. 215, pp. 1–12, Jan. 2015, doi: 10.1016/J.CIS.2014.10.010.

[4] Y. Rharbi and M. A. Winnik, 'Solute exchange between surfactant micelles by micelle fragmentation and fusion', *Adv Colloid Interface Sci*, vol. 89–90, pp. 25–46, Jan. 2001, doi: 10.1016/S0001-8686(00)00054-3.

[5] M. Hilczer, A. v. Barzykin, and M. Tachiya, 'Theory of the stopped-flow method for studying micelle exchange kinetics', *Langmuir*, vol. 17, no. 14, pp. 4196–4201, Jul. 2001, doi: 10.1021/LA001285W/ASSET/IMAGES/MEDIUM/LA001285WE00035.GIF.

[6] I. M. Griffiths, C. J. W. Breward, D. M. Colegate, P. J. Dellar, P. D. Howell, and C. D. Bain, 'A new pathway for the re-equilibration of micellar surfactant solutions', *Soft Matter*, vol. 9, no. 3, pp. 853–863, 2013, doi: 10.1039/c2sm27154k.

[7] P. P. Infelta and M. Grätzel, 'Statistics of solubilizate distribution and its application to pyrene fluorescence in micellar systems. A concise kinetic model,' *Journal Chem Phys*, vol. 70, no. 1, pp. 179–186, 1979, doi: 10.1063/1.437218.

[8] R. C. Dorrance and T. F. Hunter, 'Absorption and emission studies of solubilization in micelles. Part 2.—Determination of aggregation numbers and solubilisate diffusion in cationic micelles', *Journal of the Chemical Society, Faraday Transactions 1: Physical Chemistry in Condensed Phases*, vol. 70, no. 0, pp. 1572–1580, 1974.

[9] M. J. Rosen, *Surfactants and interfacial phenomena*, vol. 40. 1989. doi: 10.1016/0166-6622(89)80030-7.

[10] J. B. Jeong, S. R. Yang, and J. D. Kim, 'Micellar aggregation and structure of dodecyl heptaethoxylates (C12E7) with different oxyethylene distributions in aqueous media', *Langmuir*, vol. 18, no. 23, pp. 8749–8755, 2002, doi: 10.1021/la011836y.

[11] S. Flow and S. March, 'User Manual SX20 Stopped Flow Spectrometer', no. March. p. 24, 2012.

[12] R. A. Clará, A. C. G. Marigliano, and H. N. Sólimo, 'Density, viscosity, and refractive index in the range (283.15 to 353.15) K and vapor pressure of α-pinene, d-limonene, (±)-linalool, and citral over the pressure range 1.0 kPa atmospheric pressure', *J Chem Eng Data*, vol. 54, no. 3, pp. 1087–1090, Mar. 2009, doi: 10.1021/JE8007414/SUPPL_FILE/JE8007414_SI_001.PDF.

[13] J. Steinfeld, J. Francisco, and W. Hase, 'Reactions in Solution', in *Chemical Kinetics and Dynamics*, 1989, pp. 163–164.

[14] C. Yan, A. Angus-Smyth, and C. D. Bain, 'Adsorption kinetics of non-ionic surfactants in micellar solutions: effects of added charge', *Faraday Discuss*, vol. 160, no. 0, pp. 45–61, Jan. 2013, doi: 10.1039/C2FD20118F.

[15] K. Laidler, *Chemical Kinetics*, Third. HarperCollinsPublishers, Inc., 1987.

[16] K. E. Gustafson and R. M. Dickhut, 'Molecular Diffusivity of Polycyclic Aromatic Hydrocarbons in Aqueous Solution', *Journal. Chem. Eng. Data*, vol. 39, pp. 281–285, 1994, Accessed: Dec. 18, 2022. [Online]. Available: https://pubs.acs.org/sharingguidelines

[17] GSI environmental, 'GSI Chemical Database'.

[18] S. Kumar Panigrahi and A. Kumar Mishra, 'Inner filter effect in fluorescence spectroscopy: As a problem and as a solution', *Journal of Photochemistry and Photobiology C: Photochemistry Reviews*, vol. 41, p. 100318, Dec. 2019, doi: 10.1016/J.JPHOTOCHEMREV.2019.100318.

[19] R. Cuevas Arenas *et al.*, 'Fast Collisional Lipid Transfer among Polymer-Bounded Nanodiscs', *Sci Rep*, vol. 7, no. April, pp. 1–8, 2017, doi: 10.1038/srep45875.

Chapter 4 Quantitative methods used for Förster Resonance Energy Transfer (FRET)

4.1 Qualitative view of FRET experimental data and need for quantitative analysis

Chapter 3 describes experiments to use FRET to measure exchange between micelles, an example of which can be seen in figure 4.1. Spectra were acquired every 20 ms; a selection of these spectra have been chosen to show the progression of FRET. The peak at 480–565 nm arises from emission from the donor probe NBD-PE, the peak at 565–700 nm arises from emission from the acceptor probe Rh-PE. There is a shoulder peak on the emission spectra of Rh-PE between 630–666 nm indicative of Rh-PE emission, which is not present in the spectrum of NBD-PE alone. The minimum around 570 nm arises from absorption of the NBD-PE emission by Rh-PE molecules in different micelles from the emitter and corresponds to the wavelength of the maximum in absorption spectrum of Rh-PE (see Figure 4.2). A gradual decrease in NBD-PE emission and increase in Rh-PE emission occurs over time as the micelles exchange their contents and conditions for FRET are met. Note the presence of an isosbestic point at 575 nm, which indicates that the spectra arise from the conversion of one ‘species’ into a second ‘species’ that is from NBD-PE emission to FRET. The absence of an isosbestic point indicates that there is some other process happening as well, which could include factors such as photobleaching or creaming (both of which reduce the number of fluorophores in the path of the excitation light).

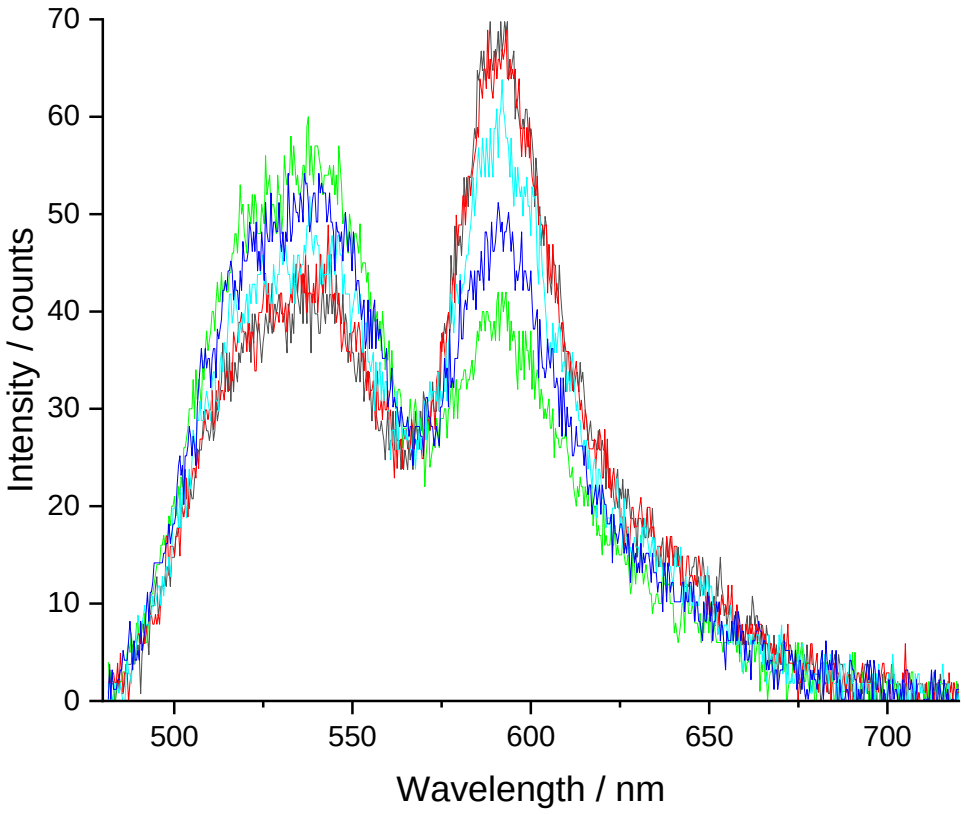

Figure 4.1: Unrefined FRET data for 2 mM limonene microemulsions at 25 °C. Excitation wavelength 468 nm. Integration time 20 ms. Black line is t_0 (the final spectrum before mixing), light green line is 40 ms, dark blue line is 5 s, cyan line is 15 s, red line is 30 s.

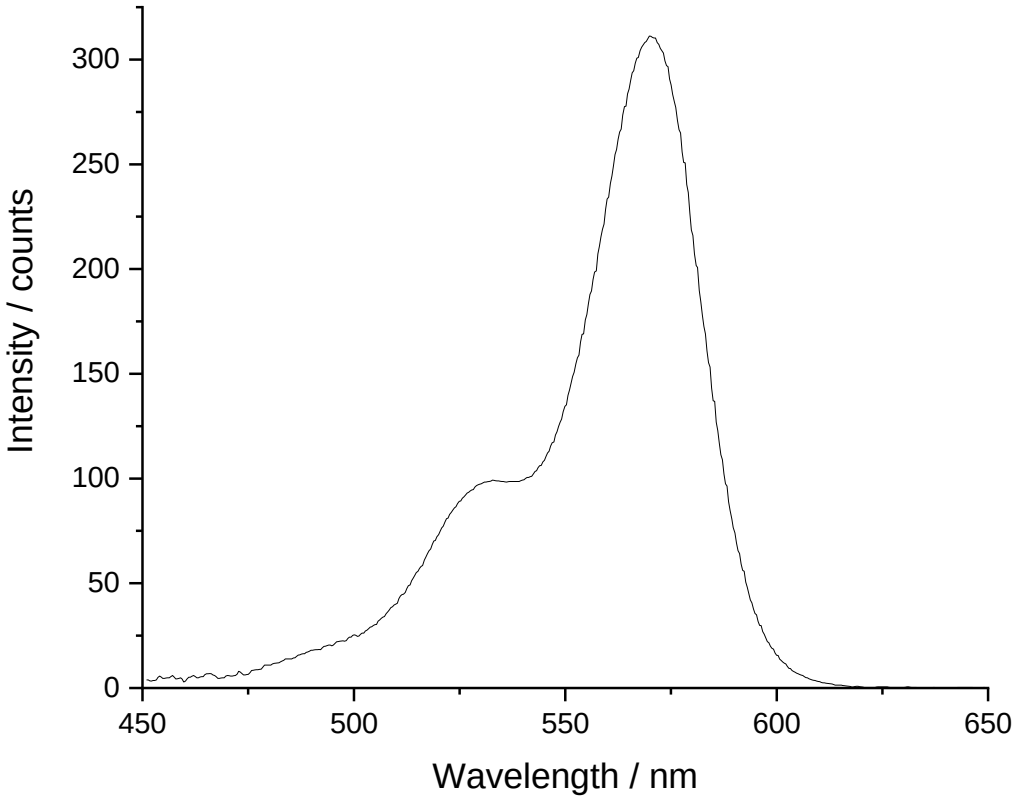

Figure 4.2: Rh-PE emission spectra. Excitation wavelength 560 nm, integration time 20 ms.

FRET is much slower than the diffusion-controlled process observed with pyrene mixing experiments and enables the observation of the exchange of contents during micelle fusion.

Although these data give a good qualitative description for micelle exchange, a quantitative description of the exchange is needed to derive meaningful kinetic data.

Factor analysis is a term used for methods that deconvolute and impart meaning to spectra based on Principal Component Analysis (PCA). PCA is often used in chemometrics, as it is a powerful technique for producing abstract orthogonal components and reducing the noise in a series of spectra. Factor analysis has been used for many kinetic studies, with a number of variations of factor analysis depending on the need. Carvalho et al. combine kinetic equations and iterative target transformation factor analysis to resolve spectroscopic data and monitor a reaction [1]. Zhao et al. used factor analysis to derive a kinetic profile of absorptive components in an autocatalytic reaction between potassium permanganate and hydrogen peroxide [2]. Amrhein et al. discuss the use of target factor analysis to determine the number of independent reactions and their stoichiometries without knowledge of their reaction kinetics [3]. Amrhein notes the importance of data pre-treatment for successful analysis. Factor analysis is used in different subject areas as well as reaction kinetics to deconvolute and analyse complex data [4]–[6]. Davies et al. used target factor analysis to identify full spectral profiles in complex mass spectrometry data [4]. Factor analysis was able to distinguish between overlapping signals to identify different volatiles in heated tobacco biomass. Goretzko gives an overview on the use of exploratory factor analysis for psychological research [6]. Factor analysis was also used by Sakib et al. to assess the severity of COVID-19 fears in Bangladesh [5].

Factor analysis can be used to analyse the Förster Resonance Energy Transfer for my micellar system, I use a particular area of factor analysis known as Target Factor Analysis (TFA). Target factor analysis can reduce noise, determine which factor is contributing most to the spectra and quantify the rate of exchange in the stopped flow FRET kinetic data.

4.2 Target Factor Analysis (TFA)

Target factor analysis consists of two main steps, principal component analysis (PCA) and ‘rotation’. Malinowski pioneered the theory of factor analysis in the context of a chemist [7]–[9]. The matlab code I have used for factor analysis (see appendix C) has been modified from a previous group member, David Woods, and Malinowski’s original code to suit my experimental data [7], [10]. Target factor analysis is closely related to principal component analysis, with an additional step where TFA attempts to represent the results using physically realistic spectra rather than abstract mathematical components. As my objective is to determine the kinetics of the reaction the coordinate rotation and decomposition of the spectra into abstract factors is not of immediate concern. Figure 4.3 gives a summary of the key steps involved in factor analysis for my FRET kinetic experimental data.

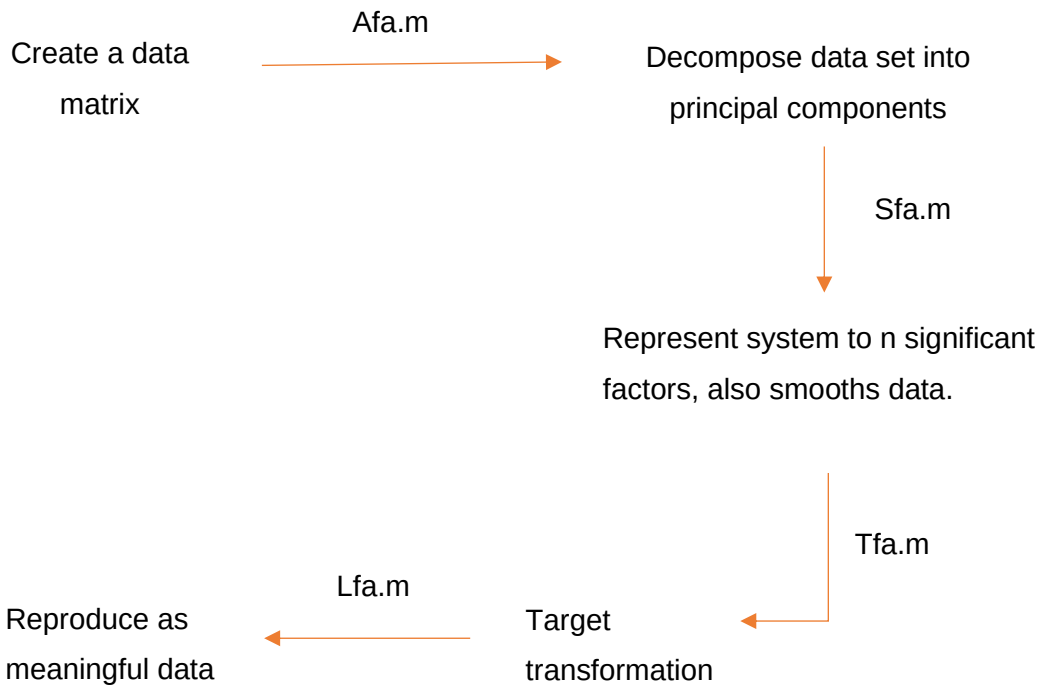

Figure 4.3: Flow illustration of the factor analysis process for FRET kinetic spectra. Afa.m, Sfa.m, Tfa.m and Lfa.m are the Matlab scripts used for each step of the process.

The matlab scripts in figure 4.3, with their definitions are listed below,

- Afa.m – abstract factor analysis – Calculates abstract factors from the data matrix.
- Sfa.m – significant factor analysis – A program designed to help determine the number of significant factors in a matrix.
- Tfa.m – target factor analysis – Designed to target test suspected factors, compress the factors, and provide rotation required for analysis.
- Lfa.m – loading factor analysis – Calculates factor loadings and errors in the loadings.

The first step in both TFA and PCA is to decompose the data set, D, using the abstract analysis script. The data set D containing *c* spectra*,* each spectra *c* is made up of a number of points *r*. The Afa.m, script decomposes the data matrix into its principal components to give,

$$\mathrm{D} = \mathrm{RC} \tag{4.1}$$

where *R* (size $r \times s$) and *C* (size $s \times c$) are abstract row and column matrices. The component *s* for each case corresponds to the number of eigenvectors that are used to make up the data. The matrices *R* and *C* do not correspond to any real spectra. To generate R and C, singular value decomposition (SVD) is used,

$$\mathrm{D} = \mathrm{U}\Sigma\mathrm{V}^{\mathrm{T}} \tag{4.2}$$

U and *V* are orthonormal matrices, holding the information about the column and row space of the data matrix *D*. Σ is a diagonal matrix of singular values and ^{T} is the transpose of the matrix. This follows onto a definition for the row space as,

$$\mathrm{R} = \mathrm{U}\Sigma \tag{4.3}$$

with a definition of the column space as,

$$\mathrm{C} = \mathrm{V}^{\mathrm{T}} \tag{4.4}$$

In SVD, the first column of *U* and row of *V* contain as much meaningful data as possible contributing to the data matrix *D*. Therefore, a linear combination of the first column of *U* and first row of *V* is the first abstract component. Subsequent rows and columns containing the information on data are used to give the remaining number of abstract components, after this the remaining factors are treated as noise.

The compressed versions of R and C can be used to give a refined version of the data, without the noise. The Afa.m and Sfa.m code is used for this step and will output the number of significant factors for the data set. It is important to choose the correct number of significant abstract factors for the data set. If too many significant factors are chosen, there will be an unnecessary level of noise treated as real data; if too few significant factors are chosen it can lead to a loss of real data from the dataset. An example of a significant factor investigation for my experimental data can be found in §4.3.3.

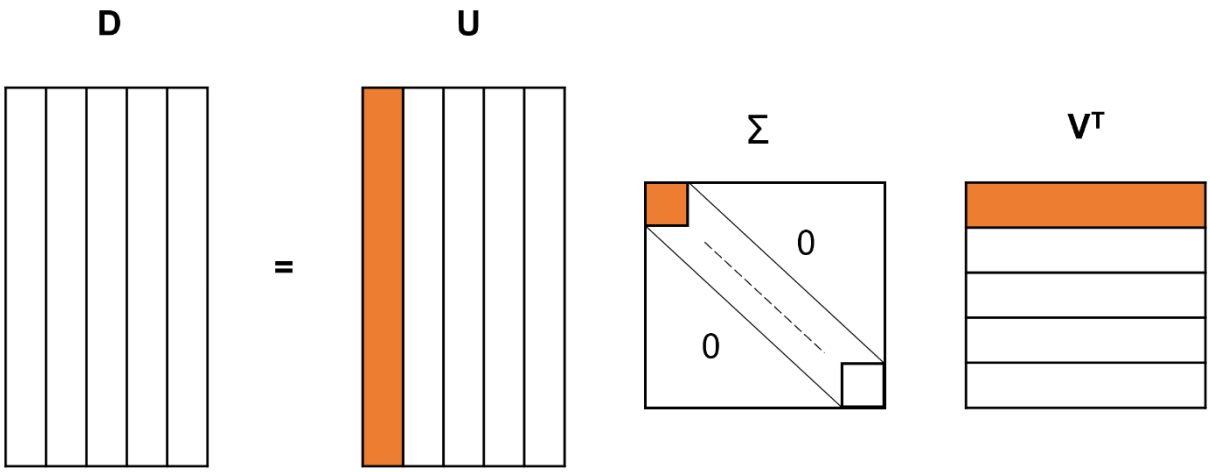

Figure 4.4: Schematic of the singular value decomposition step. The highlighted column in U, the highlighted row in V^T and the highlighted value in Σ combine to give the first abstract factor.

The next step is a coordinate rotation of the compressed data to give a set of realistic spectra with their component weights using the Tfa.m script. Target factor analysis uses a transformation matrix (*T*), containing the initial abstract factors.

The transformation of the abstract factors into weighted real spectra is as follows,

$$\begin{aligned} \mathrm{D} &= (\mathrm{RT})(\mathrm{T}^{-1}\mathrm{C}) \\ &= \mathrm{X}_{\mathrm{real}}\mathrm{Y}_{\mathrm{real}} \end{aligned} \tag{4.5}$$

The transformation matrix is calculated using a least-squares method,

$$\hat{x}_l = \mathrm{Rt_l} \tag{4.6}$$

where $\hat{x}_l$ is the predicted vector and t_l *t*he associated transformation vector. The Tfa.m code generates a t_l to give a $\hat{x}_l$ that most closely matches the test vector *(*x_l), from which *T* can be determined.

The rotation is given boundaries using a set of target spectra, x_l. Suitable target spectra can differ depending on the nature of the experiment. Malinowski has produced a function named the SPOIL function to give the suitability of the targets. The SPOIL function is derived from the relationship of the error in the refined spectrum (REP) and the error in the target spectrum (RET), the SPOIL value of the *ith* component is given by,

$$SPOIL_i = \frac{RET_i}{REP_j} \tag{4.7}$$

Malinowski defines three classes of target spectrum. Target spectra with a SPOIL value less than three are appropriate, if the value is between three and six, they are also acceptable, however a target spectrum with a value more than six does not qualify as a suitable target. The SPOIL function is built into my code to give feedback on the target spectra for each experimental run.

Once the target transformation has occurred, the Lfa.m script is used to calculate the loadings associated with each target factor. The loadings for each factor can be thought of as the relative contribution of the target factor within the original set of spectra. For a kinetic experiment where the loadings will change over time, loadings associated with a target factor will either increase or decrease, depending on whether the component is increasing or decreasing in relation to the target factor. The terms loadings and weightings can often be interchanged for loading factor analysis and are for this thesis.

4.3 Use of Target Factor Analysis for kinetic data

I used Target Factor analysis to determine the kinetics of FRET associated with micelle fusion. This section applies the theory in §4.2 specifically for my stopped flow FRET data. I have used the case of 2 mM limonene microemulsion FRET at 25 °C as an example. Each step described in figure 4.3 is discussed below.

4.3.1 Pre-processing data

The data must be pre-processed before using factor analysis. To negate trigger dead time as described in section 3.2, the acquisition is started before the experiment and continues after the experiment has finished. It is important to remove the pre-mixing data taken for factor analysis.

The wavelength region of interest must be determined to ensure erroneous peaks are not considered for analysis. Quite often during experimental runs there is a significant amount of scattered excitation light detected from the spectrometer. An example of the scattered light peak can be seen in figure 4.5. The scattering peak may vary over the course of an experiment. A wavelength range between 485 nm and 720 nm was used for factor analysis of all of my mixing data to exclude the scattering peak. By removing the scattering peak any unwanted noise associated with scattering peak is removed. Keeping the wavelength range tight to the emission spectra of NBD-PE and Rh-PE also minimises additional noise being generated from areas of the spectra which do not contribute any information about the kinetics of the experiment.

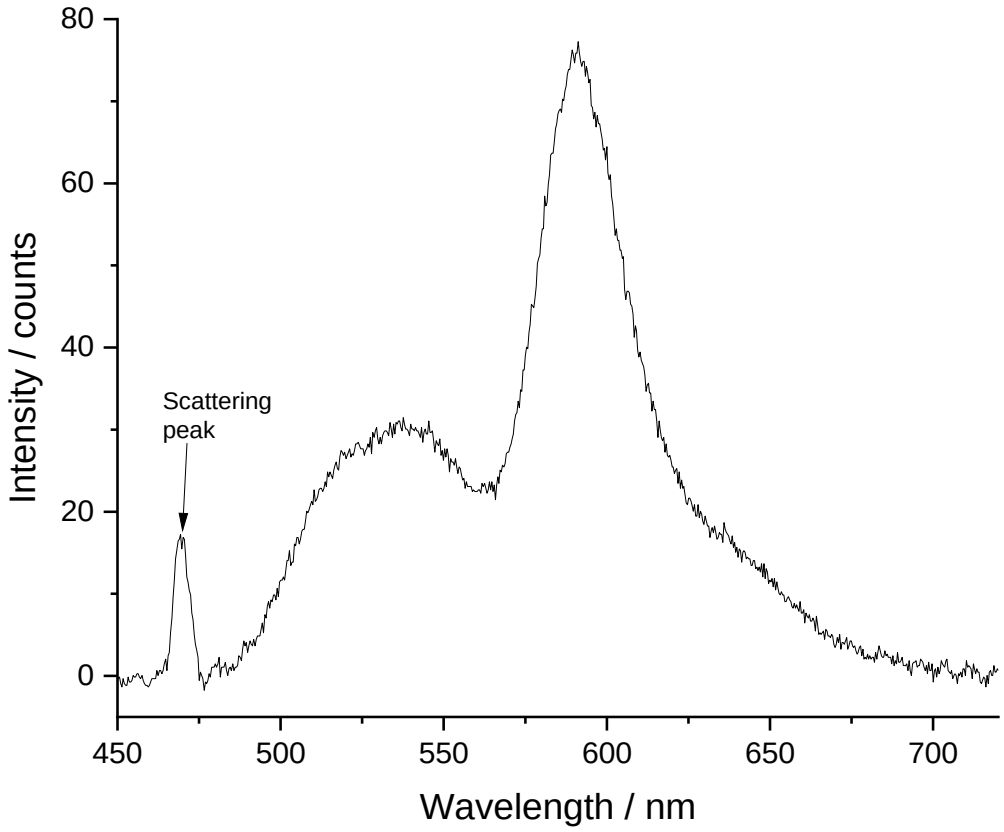

Figure 4.5: Example of a FRET limonene experiment after completion, excitation wavelength 468 nm, integration time 20 ms.

The effect of scattering in the optical cell was a source for much consideration as it had the potential to affect the kinetic results. Tests were undertaken to determine if there was a correlation between the intensity of the scattering and fluorescence peaks, which was found not to be the case. However, when progressing with experiments using a crude oil mimic (discussed in chapter 8) the baseline began to skew, which seemed to originate from the scattering peak. If the skew from the baseline affects the NBD-PE and Rh-PE emission peaks, the relative intensity of each peak used for the loading factor analysis would misrepresent the kinetic reaction. Therefore, it was necessary to investigate if this baseline skew would affect the kinetic results. The scattering peak would also cause a tail to be visible ~490 nm, for the baseline correction tests, the region was cut off at 490 nm to avoid this tail being present for the analysis.

Figure 4.6 shows a single refined scan at the end of a typical result from the FRET crude-oil-mimic mixing experiment. Comparison with Figure 4.5 shows the elevated baseline at short wavelengths. Figure 4.7 is the same scan after a baseline correction, the baseline correction was made through a linear baseline subtraction between 490

nm and 720 nm, 490 nm was chosen as the first feasible wavelength to use before the scattering peak influenced fluorescence and 720 nm is typically where no fluorescence is observed. Note there is a slight decrease in the Rh-PE peak intensity from figure 4.6 to figure 4.7, and a large decrease in the NBD-PE peak intensity.

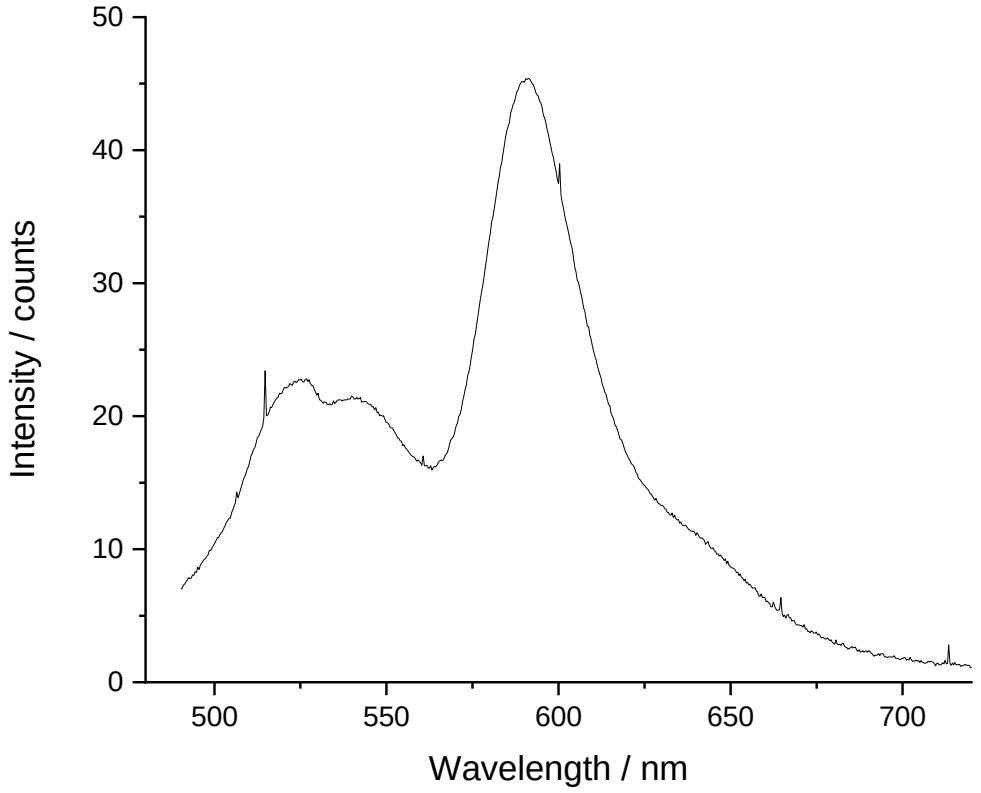

Figure 4.6: Single scan at the end of a FRET run. 10 mM squalane emulsion with NBD mixed with 2 mM limonene swollen micelles filled with Rh-PE. Excitation wavelength 468 nm, integration time 200 ms.

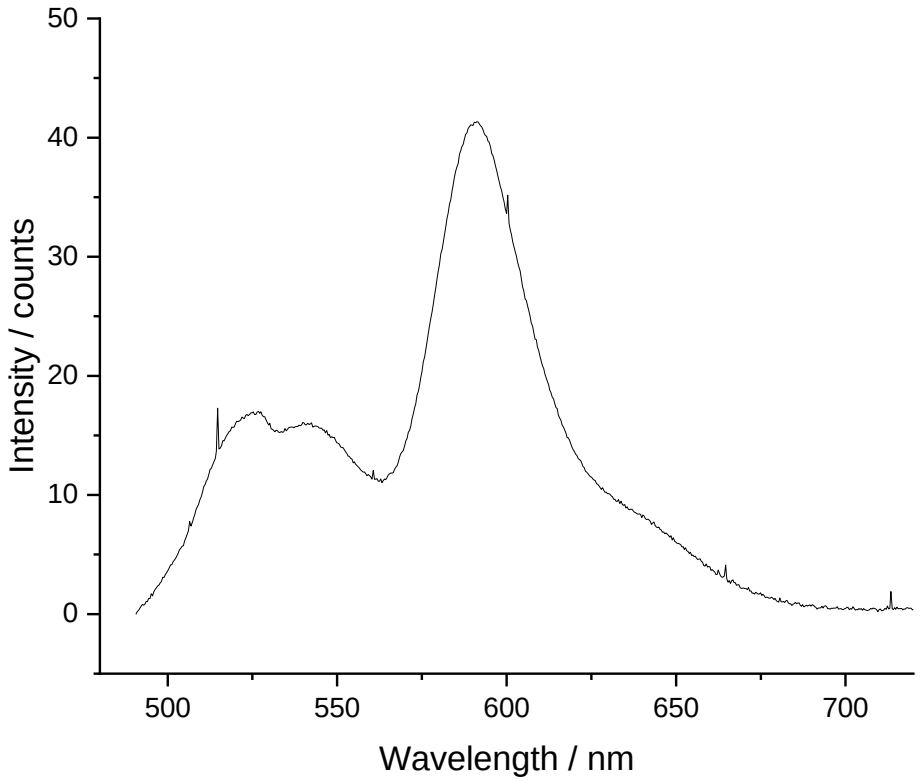

Figure 4.7: Single scan at the end of a FRET run after a baseline correction. 10 mM squalane emulsion with NBD mixed with 2 mM limonene microemulsion filled with Rh-PE. Excitation wavelength 468 nm, integration time 200 ms.

The baseline treatment shown in figure 4.7 was applied to all scans in the same mixing run. The new ‘baseline corrected’ set of scans were then analysed using factor analysis to obtain kinetic data. Figure 4.8 shows a comparison for the loading results of the original ‘skewed’ mixing data and the ‘baseline corrected’ data.

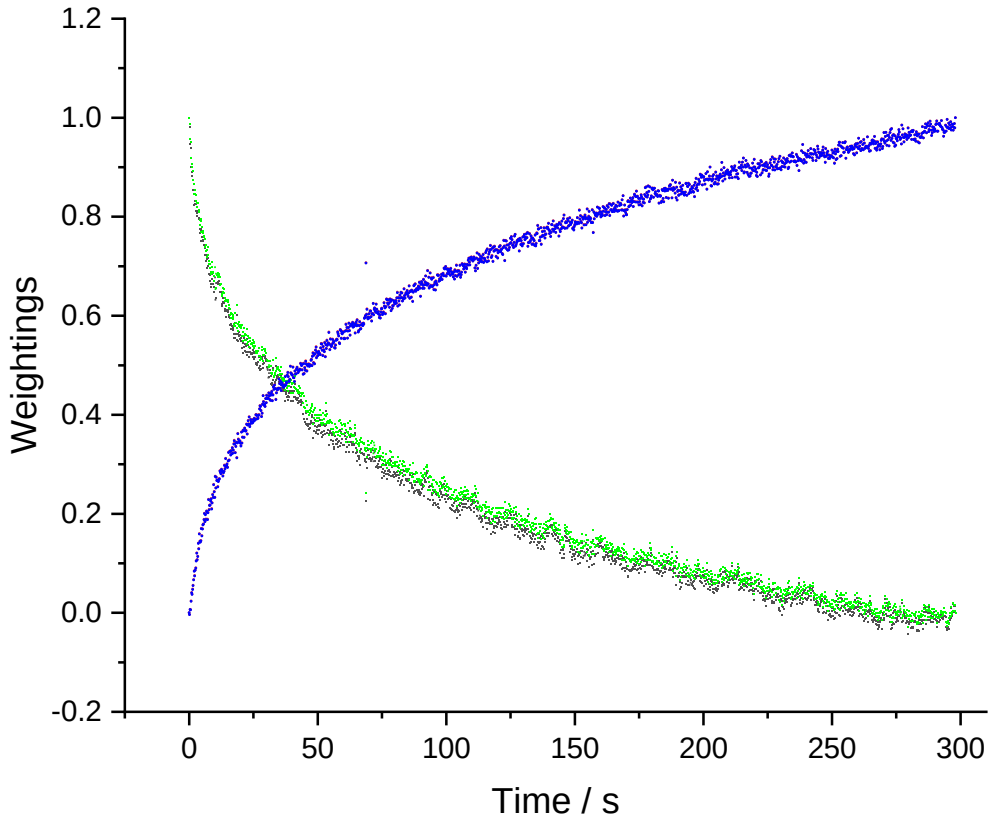

Figure 4.8: Loading data for 10 mM squalane emulsion with NBD mixed with 2 mM limonene microemulsion filled with Rh. The black points represent the NBD emission from the 'skewed' data, the green points represent the NBD emission from the 'corrected' data, the red points represent the Rh emission from the 'skewed' data, the blue points represent the Rh emission from the 'corrected' data.

The results in figure 4.8 show that the baseline skew does not materially affect the kinetic results from the FRET data. Further investigation with other experiments gave the same result as found in figure 8. As a result, we can safely assume that the skew in the baseline resulting from the scattering peak does not affect the overall kinetic results. Baseline correction for the skewed peaks therefore does not need to be considered for this particular piece of work.

4.3.2 Compressing the data set

After pre-processing the data, a data matrix is constructed for one experimental run. The data matrix is compressed and refined using SVD in the Afa.m script. Figure 4.9 shows the result of refining the data using SVD for a single scan in an experimental run, with a comparison of the refined scan and the initial unrefined scan. For this example, the number of significant factors was kept to two and total number of spectra in the data set was 2900. This example shows how much the data quality can be improved by exclusion of the noise contained in the principal components that do not contain significant information.

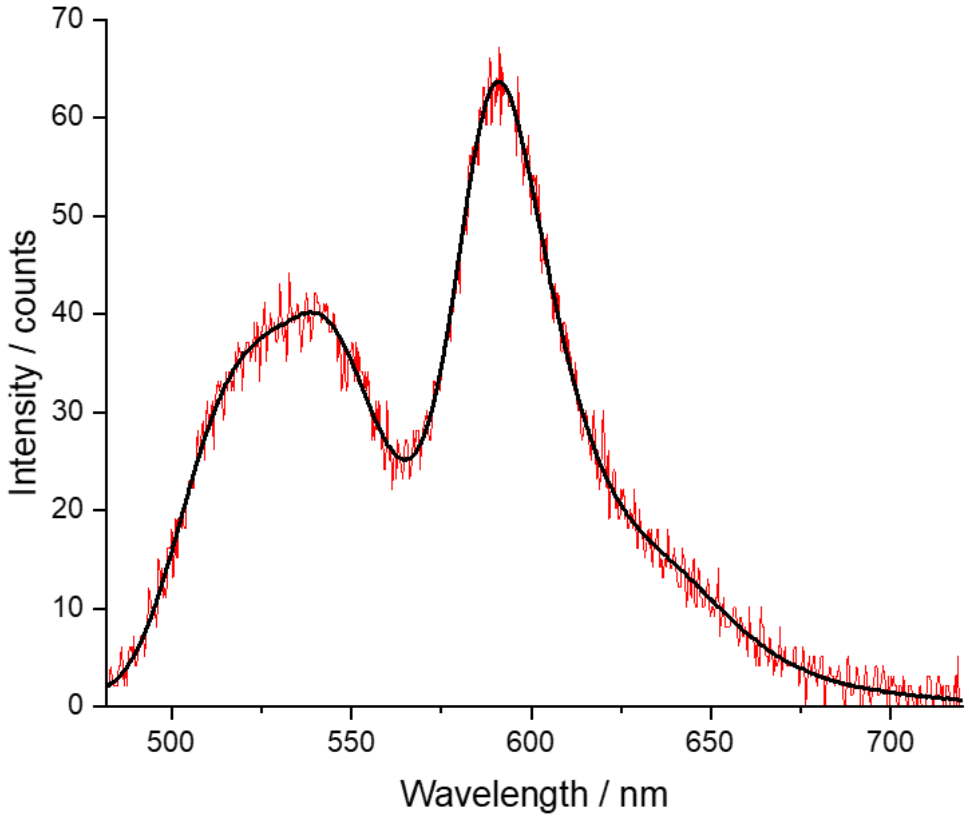

Figure 4.9: 2 mM limonene microemulsion FRET run, excitation wavelength 468 nm, integration time 20 ms. Black line indicates a refined mixing spectrum of the unrefined mixing spectrum (red line).

4.3.3 Significant factor investigation

The Sfa.m script is used to investigate a suitable number of factors for the compression of the data. For my kinetic FRET experiments, two significant factors were found to be most suitable. An example of the significant factor investigation has been detailed below.

The experimental data taken for this investigation was an experimental run for limonene microemulsion FRET run at 25 °C. The Sfa.m code was adapted to explore the number of factors that best represent a mixing run. Figure 4.10 shows a scree plot, which plots the singular value against the number of principal components chosen. I chose to plot the contributions from the first 10 factors from the FRET data.

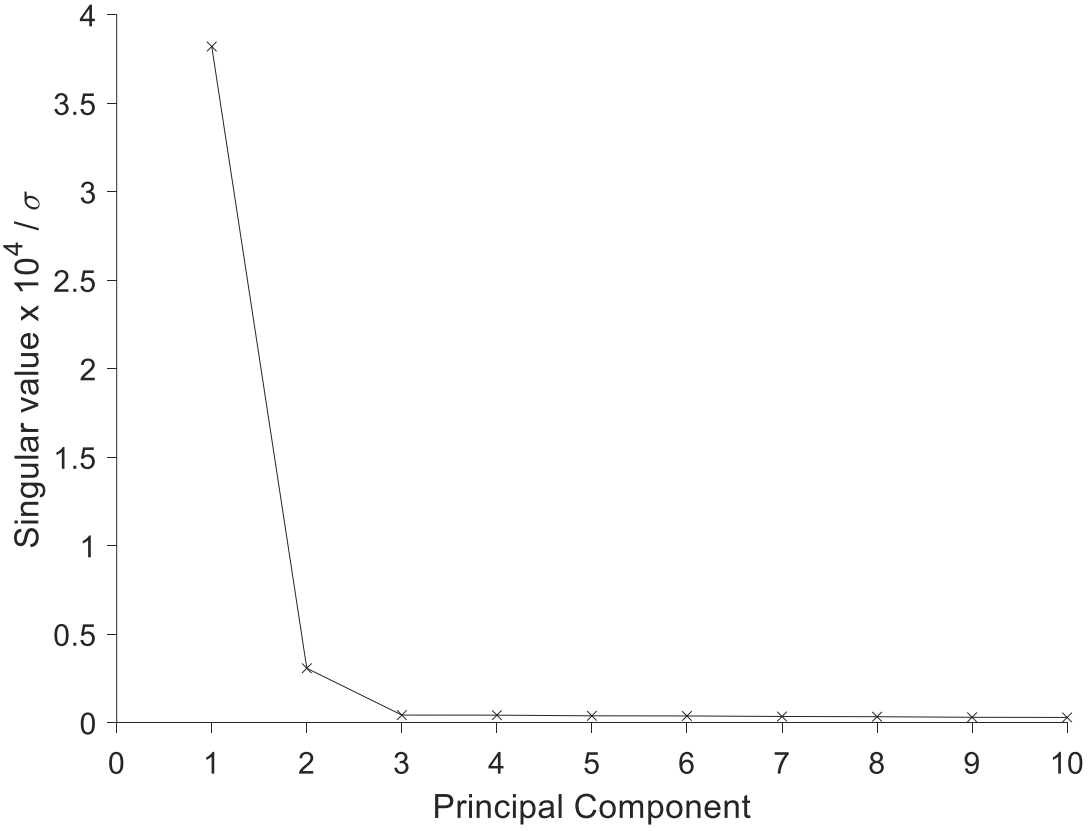

Figure 4.10: Scree plot of significant factors vs their singular value from an experimental run of 2 mM limonene microemulsion FRET at 25 °C

Figure 4.10 indicates the majority of the information lies in the first component. There is a large drop off in intensity to the second component but still a significant singular value. From the second to third component the singular value of components decreases to close to zero. After the third component there is no change in the singular value. I tested the first three factors to see what each factor would produce.

Figure 4.11 is the first factor, containing the majority of the spectral information and looks like the sum of the NBD-PE and Rh-PE spectra Figure 4.12 is the second factor and is orthogonal to the first component; note that the NBD-PE and Rh-PE peaks appear with opposite signs. The NBD-PE spectrum (after absorption by Rh-PE in the cell) is generated from a sum of the first two factors while the Rh-PE spectrum is generated from a difference between the factors. Figure 4.13 is the third factor and shows what seems to be a waveform. Figure 4.13 suggests that there is interference between reflections from two parallel surfaces somewhere in the optical path. However, there is no information relevant to the experiment that can be extracted from the third factor and for the purpose of this study it can be treated in the same way as noise and excluded from the refined spectra.

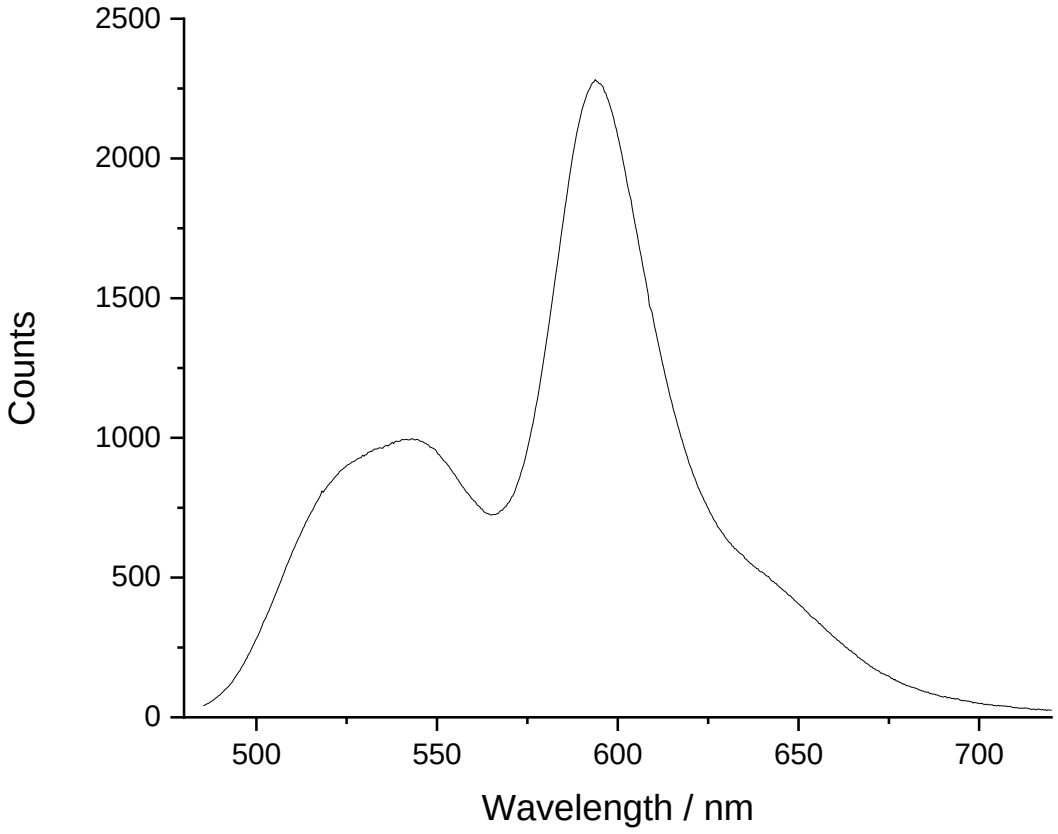

Figure 4.11: 1st factor from an experimental run of 2 mM limonene microemulsion FRET at 25 °C.

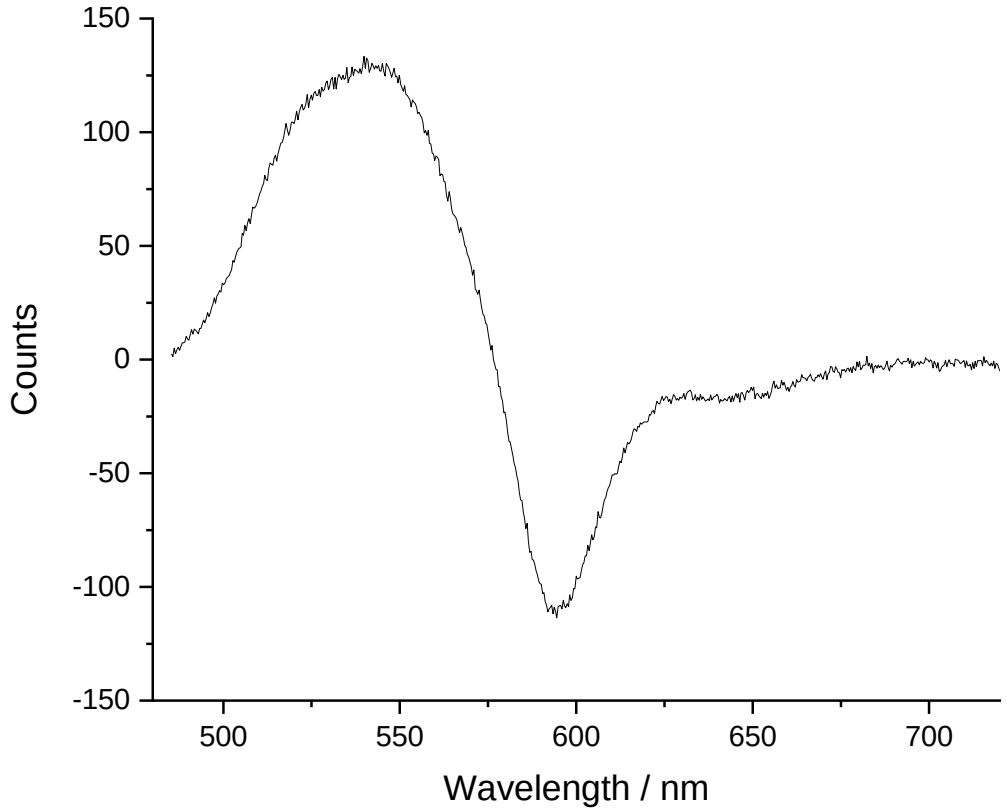

Figure 4.12: 2nd factor from an experimental run of 2 mM limonene microemulsion FRET at 25 °C.

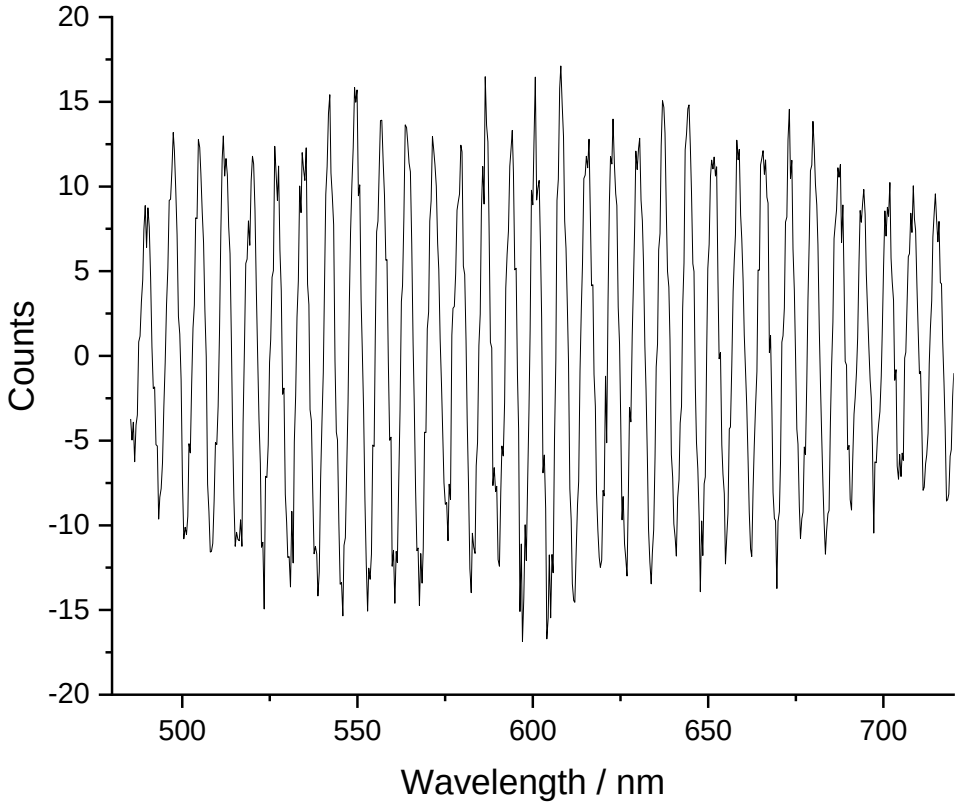

Figure 4.13: 3rd factor from an experimental run of 2 mM limonene microemulsion FRET at 25 °C.

From the significant factor investigation, it is clear two factors best represent the data for each experimental run of limonene microemulsion FRET. A similar case is found for all of our FRET data, from solvent changes to the emulsion mixing experiments.

4.3.4 Target Transformation

The next step is a coordinate rotation to extract the refined spectra corresponding to the micelles filled with NBD-PE and micelles filled with rhodamine and their component weights in each of the kinetic spectra. To perform this rotation a pair of target spectra are required that approximate to our t_0 and 'end point'. Figure 4.14 gives an example of a typical pair of target spectra used for the transformation. Note that these spectra do not represent the NBD-PE and Rh-PE spectra themselves. At the beginning of the run (after mixing but before any FRET has taken place) the spectrum represents NBD-PE emission after passing through a solution containing Rh-PE, which absorbs part of the NBD-PE emission (as noted in §4.1). However, the first spectrum recorded after mixing already includes some FRET if the kinetics are not very slow on the acquisition timescale. The final spectrum is a combination of NBD-PE emission (after Rh-PE absorption in the cell) plus the Rh-PE emission from FRET, the final spectrum does not need to be the equilibrium spectrum as first-order kinetics is observed. The fact that these spectra do not represent the 'pure' NBD-PE and Rh-PE spectra makes no difference to the kinetic parameters derived subsequently.

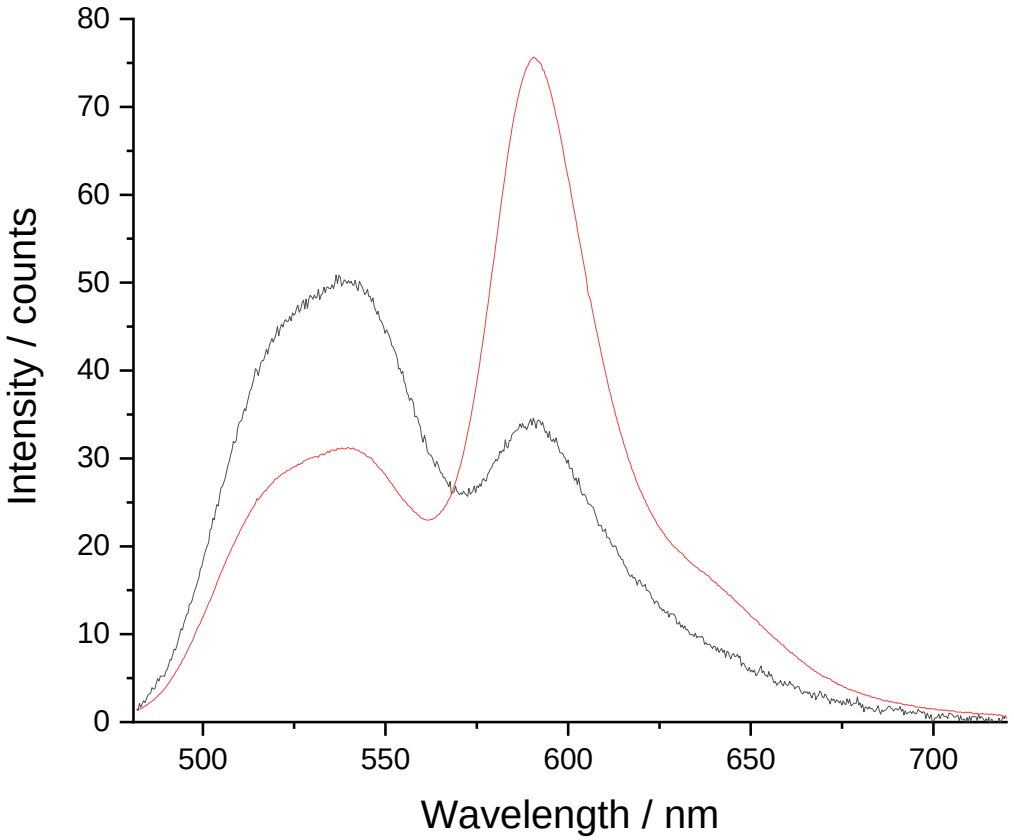

Figure 4.14: Target spectra used from refined data set of 2 mM limonene microemulsion FRET data.

There are a few systematic errors that can occur when using TFA, particularly when choosing suitable target spectra. If the target spectra do not give representative peaks for t_0 and the 'end point', the reproduced data can give misleading weighting data. The targets should also be suitably different to each other in order for the TFA to distinguish between each factor. A number of different target spectra were trialled for our mixing data before deciding on a representative t_0 and 'end point' as the target sets. The choice of the target spectra whilst impacting the weightings, does not affect the kinetic parameters derived from the weightings.

4.3.5 Loading factor analysis

The final step is to use the Lfa.m code to attribute loadings or weightings to the progression of FRET to the target factors chosen. The weightings themselves have no chemical meaning, thus need to be converted to something meaningful. We can use the weightings to calculate the rate constants of exchange from the change in weightings over time for each probe. Figure 4.15 is a plot of weightings from t_0 and the 'end point' over time in a single FRET run. For simplicity, when considering loading data and rate kinetics, t_0 target is described as NBD-PE (black data points) and the end point target is described as Rh-PE (red data points). A simple exponential decay function can be fit to give the rate of decay of NBD-PE and Rh-PE and to derive the rate of FRET between the micelles and are also shown as solid lines in figure 4.15. The equation for the exponential decay function for NBD-PE and Rh-PE are as follows,

$$\begin{aligned} NBD\ rate \quad & y(t) = ae^{(-kt_1)} \\ Rh\ rate \quad & y(t) = 1 - ae^{(-kt_1)} \end{aligned} \tag{4.8}$$

The weightings of the NBD-PE and Rh-PE components are fit separately to give two k values. The two k values should agree with each other within given error. By taking individual k values for NBD-PE and Rh-PE, the two k values could be used an indicator of whether there was an error in processing of the data or other effects at play in the experiment itself. This complements the use of the isosbestic point to check whether or not a simple FRET process is being observed.

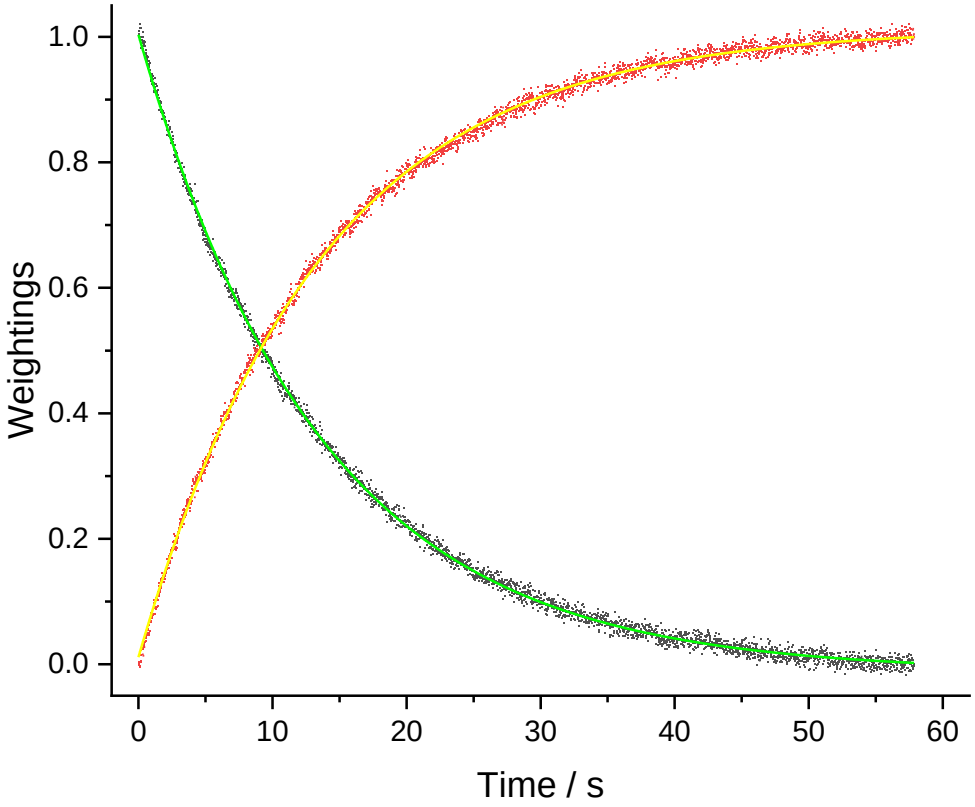

Figure 4.15: Weighting results from a 2 mM limonene microemulsion FRET run at 25 °C. The NBD-PE weightings are represented by black data points with a solid green line fit, the Rh-PE weightings are represented by red data points with a solid yellow fit.

To determine if the single parameter model was suitable, first a visual inspection of the fit was taken. If the fit using the single exponential decay was good, then the single parameter model was seen as a potentially valid model. If a double exponential decay was a better fit, then this indicated the single parameter model was not valid. Each curve fitting would provide errors on the exponent as well as its value. A total of 9 runs are used for a particular set of solutions to provide an average k value for each probe and experimental run. From this a standard mean error could be calculated from the k values. If the error in k values lied within one another for each probe, this gave further justification for a single parameter model. If k values did not agree with each other then it would indicate there were further influences on the spectra not captured by the single parameter model. The first experimental run would give results for the mixing and loading data that were inconsistent with subsequent runs, therefore the first run of each set of solutions was discarded for analysis.

The reproducibility of the loading data and curve fitting can be seen in figure 4.16 with the weightings of three experimental runs for a 2 mM limonene FRET experiment at 25 °C.

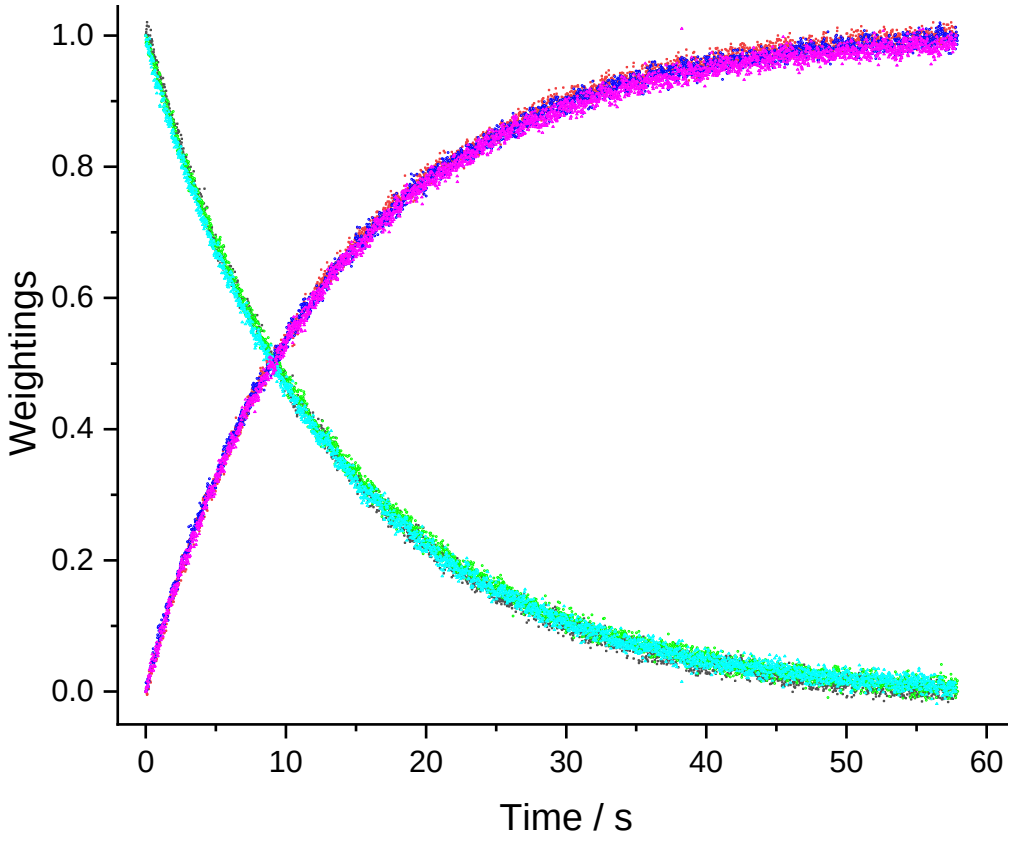

Figure 4.16 : Weighting results of three experimental runs from a 2 mM limonene microemulsion FRET at 25 °C. Run 1 is denoted by black markers for NBD-PE and red markers for Rh-PE. Run 2 is denoted by green markers for NBD-PE and dark blue markers for Rh-PE. Run 3 is denoted by cyan markers for NBD-PE and pink markers for Rh-PE.

The observed rate constants taken for the three experimental runs in figure 4.16 can be seen in table 4.1.

Table 4.1: Observed rate constants from the exponential decay fitting with their individual errors, of experimental runs shown in figure 4.16.

Experimental run	k_{obs} / s^{-1}	
	NBD-PE	Rh-PE
Run 1	0.099 ± 0.0001	0.094 ± 0.0001
Run 2	0.096 ± 0.0002	0.096 ± 0.0001
Run 3	0.099 ± 0.0002	0.094 ± 0.0001

The weightings shown in figure 4.16 give satisfactory reproducibility. The standard error between each run for NBD-PE and Rh-PE is calculated to be 0.08 and 0.06 respectively. Run 1 and 3 are within twice the standard error of each other for NBD-PE and Rh-PE, however run 2 does not, showing some variance between runs. It is necessary to take multiple repeats to mitigate the variance between each run. When

considering NBD-PE compared with Rh-PE, they do not agree within 2σ. The discrepancy between each run and individual probes points to some possible sources of uncertainty in each individual run. The use of an average observed rate constant for each probe over 9 runs lowered the overall uncertainty in the experiments, as can be seen in the results in the later chapters.

4.3.6 Relating observed rate constants to underlying molecular processes

Experimentally, we observe that FRET signal for mixing of microemulsions or surfactants follows a first-order growth (for Rh-PE emission) and decay (for NBD-PE emission), with the same rate constant for both processes. It is useful to relate the observed first-order rate constant, k_{obs}, to the kinetics of the underlying molecular processes.

The total concentration of micelles after mixing = [M]. Immediately after mixing, [M]/2 of those micelles came from the NBD-PE containing solution and [M]/2 from the Rh-PE containing solution. The FRET emission from the Rh-PE dye molecules can be dealt with first. This Rh-PE emission can be displayed as the following,

$$I(t) = I(\infty)(1 - e^{-k_{obs}t}) \tag{4.9}$$

The intensity of the FRET emission from the Rh-PE dye depends on the probability, $P(t)$, that an Rh-PE fluorophore is in the same micelle as an NBD-PE fluorophore, thus we can write,

$$P(t) = P(\infty)(1 - e^{-k_{obs}t}) \tag{4.10}$$

Initially, there are no micelles containing both Rh-PE and NBD-PE, so $P(0) = 0$. The rate of change of P is

$$\frac{dP}{dt} = P_{\infty} k_{obs} e^{-k_{obst}t} \tag{4.11}$$

The initial rate

$$\left.\frac{dP}{dt}\right|_{t=0} = P_{\infty} k_{obs} \tag{4.12}$$

The first step is to consider the distribution of NBD-PE over the [M]/2 micelles from the NBD-PE containing solution. Let the average number of NBD-PE molecules per micelle initially be $\bar{n}_{NBD}$. After the system has equilibrated, the average number of NBD-PE per micelle will be $\bar{n}_{NBD}/2$, as there are an equal number of micelles mixing from each syringe.

Assuming a Poisson distribution of dye molecules, the initial probability that a micelle is empty (n_{NBD}=0) is

$$P(n_{NBD}=0, t=0) = e^{-\bar{n}_{NBD}} \tag{4.13}$$

and the final probability is

$$P(n_{NBD}=0, t=\infty) = e^{-\bar{n}_{NBD}/2} \tag{4.14}$$

The initial probability (after mixing but before any fusion occurs) that an Rh-PE fluorophore is in a micelle with an NBD-PE fluorophore is zero. The final probability is

$$P(n_{NBD}\neq 0, t=\infty) = \left(1-e^{-\bar{n}_{NBD}/2}\right) \tag{4.15}$$

Thus $P(\infty)$ in eq. 4.10 is equal to $\left(1-e^{-\bar{n}_{NBD}/2}\right)$ (4.16)

Assuming exchange of fluorophores between micelles occurs just through micelle fusion. The second-order rate constant for collisions between micelles will be k_2 and the probability of formation of transient dimer in a collision be δ. We assume that if a transient dimer forms and then breaks down again into two micelles, any fluorophores in the transient dimer are randomly distributed between the two micelles.

Now we look to calculate the initial rate in equation 4.12. The rate of collision of a micelle containing Rh-PE with a micelle from the NBD-PE containing syringe is k_2[M]/2. The rate of collisions leading to randomisation of the contents of the micelles is δ k_2[M]/2. The question is how many of these collisions lead to Rh-PE and NBD-PE being in the same micelle?

Let us consider the limit of low dye concentrations, $\bar{n}$<<1, which is a good approximation at least for the surfactant package. Then if we linearise the exponential in equation 4.13 to give,

$$P(n_{NBD}=1)=\bar{n}_{NBD} \tag{4.17}$$

where we have neglected any micelles with n_{NBD}>1 due to the low concentration of dyes. Similarly, we assume that the micelles in the solution containing Rh-PE contain either zero or one Rh-PE molecule. If we fuse a micelle containing one NBD-PE molecule and one Rh-PE molecule, then the probability of both molecules ending up in the same micelle after fission of the transient dimer is 0.5. Therefore (using equation 4.12), the initial rate at which an Rh-PE molecule enters into an NBD-PE containing micelle is

$$\left.\frac{dP}{dt}\right|_{t=0}=\delta k_2\frac{[M]}{2}\times\bar{n}_{NBD}\times\frac{1}{2}=P_\infty k_{obs} \tag{4.18}$$

Now, in the limit $\bar{n}<<1$, equation 4.15 give us,

$$P_\infty=\bar{n}_{NBD}/2 \tag{4.19}$$

and thus equation 4.17 can be rearranged to,

$$k_{obs}=\delta k_2\frac{[M]}{2} \tag{4.20}$$

One can repeat the analysis for the decay of the fluorescence of NBD-PE and obtain the same equation for k_{obs}, consistent with the physical requirement that the same rate constant is obtained for both processes.

We have assumed here that $\bar{n}_{NBD}<<1$. It is straightforward to calculate k_{obs} in the other limit $\bar{n}_{NBD}>>1$. In this case, every collision of an Rh-PE containing micelle with a micelle from the NBD-containing syringe will lead to FRET, so equation 4.18 becomes

$$\left.\frac{dP}{dt}\right|_{t=0}=\delta k_2\frac{[M]}{2}=P_\infty k_{obs} \tag{4.21}$$

However, P_∞ in this case is 1 (since every micelle at equilibrium will contain at least one NBD fluorophore) and we obtain the same equation 4.20 for k_{obs}.

While a calculation of the rate for intermediate value of $\bar{n}$ is more complicated, since one has to consider the Poisson distribution of dye populations, it is reasonable to assume that equation 4.20 holds for all $\bar{n}$.

Conclusion

The use of factor analysis as a quantitative tool for complex data has been discussed. The processes involved in target factor analysis to quantitively analyse data has been discussed theoretically. The use of TFA for my studies has also been discussed using a limonene microemulsion FRET run example to describe the process in more detail. The reproducibility of the quantitative analysis used to obtain k values has been shown with a 3-run exemplar in the form of a stacked LFA spectra and comparison of tabulated k values. Using TFA as a quantitative tool for my FRET experiments has enabled me to extract rates for micelle exchange and deconvolute the raw data. TFA has been used to analyse the data in chapters 5, 6, 7 and 8 in the same way as has been discussed in this chapter.

A mechanistic argument to relate the observed rate constants for micelle fusion to underlying molecular processes has been undertaken for micelle interaction. For the studies introducing charge and a crude oil mimic (chapters 7 and 8) this derivation would need to account for the additional processes occurring and should be subject to further study.

References

[1] A. R. Carvalho, J. Wattoom, L. Zhu, and R. G. Brereton, “Combined kinetics and iterative target transformation factor analysis for spectroscopic monitoring of reactions,” *Analyst*, vol. 131, no. 1, pp. 90–97, 2006, doi: 10.1039/B510875F.

[2] Y. Li, Y. Zhao, and Z. Zhu, “Kinetic Investigation of the Autocatalytic Reaction between Potassium Permanganate and Hydrogen Peroxide with Soft-modeling Methods,” *Analytical Sciences*, vol. 27, no. 1, pp. 37–41, Jan. 2011, doi: 10.2116/ANALSCI.27.37.

[3] M. Amrhein, B. Srinivasan, and D. Bonvin, “Target factor analysis of reaction data: use of data pre-treatment and reaction-invariant relationships,” *Chemical Engineering Science*, vol. 54, no. 5, pp. 579–591, Mar. 1999, doi: 10.1016/S0009-2509(98)00270-X.

[4] A. Davies, J. T. Grant Nicol, C. Liu, J. Tetteh, and K. McAdam, “Identification of volatiles from heated tobacco biomass using direct thermogravimetric analysis—Mass spectrometry and target factor analysis,” *Thermochimica Acta*, vol. 668, pp. 132–141, Oct. 2018, doi: 10.1016/J.TCA.2018.08.007.

[5] N. Sakib *et al.*, “Psychometric Validation of the Bangla Fear of COVID-19 Scale: Confirmatory Factor Analysis and Rasch Analysis,” *International Journal of Mental Health and Addiction*, pp. 1–12, May 2020, doi: 10.1007/S11469-020-00289-X/TABLES/4.

[6] D. Goretzko, T. T. H. Pham, and M. Bühner, “Exploratory factor analysis: Current use, methodological developments and recommendations for good practice,” *Current Psychology 2019 40:7*, vol. 40, no. 7, pp. 3510–3521, May 2019, doi: 10.1007/S12144-019-00300-2.

[7] E. R. Malinowski, “Factor Analysis in Chemistry,” 1980.

[8] M. McCue and E. R. Malinowski, “Target factor analysis of infrared spectra of multicomponent mixtures,” *Analytica Chimica Acta*, vol. 133, no. 2, pp. 125–136, May 1981, doi: 10.1016/S0003-2670(01)93488-9.

[9] M. McCue and E. R. Malinowski, “Target factor analysis of infrared spectra of multicomponent mixtures,” *Analytica Chimica Acta*, vol. 133, no. 2, pp. 125–136, May 1981, doi: 10.1016/S0003-2670(01)93488-9.

[10] D. A. Woods, “Dynamics of Surfactant Adsorption at Solid – Liquid Interfaces,” no. November, 2011, [Online]. Available: http://etheses.dur.ac.uk/3277/

Chapter 5 Temperature effects on micelle exchange using stopped-flow FRET experiment

A detailed description of the experimental set up for stopped-flow FRET can be found in section 3.4.1.

The phase behaviour of a microemulsion is affected by changes in temperature. The droplet size distribution of a microemulsion affects the stability of the microemulsion and is related to the penetration power of the microemulsion into the porous rock media [1]. A change in temperature will change the particle size distribution of the microemulsion droplets (through a change in the area per surfactant molecule at the micelle-water interface) and increase the diffusion rate of droplets. With an increase of diffusion rates and change in droplet size, the rate of micelle exchange will change when the temperature of the system changes. A study of the rate of micelle exchange with a change in temperature could give further insight to the efficacy of micelle penetration in rock pores under different well conditions. The probability of micelle overcoming the activation barrier for fusion to occur during a collision is also temperature dependant, this could be the dominant effect for a micelle fusion process.

A thermostatic circulating water bath was installed on the stopped-flow rig, allowing water to surround the mixing syringes and the optical cell. Temperature controlled mixing was conducted and quantitatively analysed at 0.5 mM, 2 mM and 5 mM for both the microemulsion and surfactant package at 15 °C, 25 °C and 35 °C. Flotek use a surfactant concentration of 0.8 mM in their microemulsion package for enhanced oil recovery. By using a concentration range between 0.5 mM and 5 mM there can also be a useful concentration comparison alongside a temperature change for micelle exchange. Data for the 2 mM solution are shown in Figures 5.1–5.6 below.

To ensure the samples reach the desired temperature, the phase tubes are immersed in the water bath after preparation for at least five minutes. The samples are then transferred to the mixing syringes surrounded by the thermostatic water bath.

For all cases in figures 5.1–5.6, the cell was filled with the results of the previous (identical) FRET run. The black “equilibrium” line (t_0) is the spectrum taken immediately

before the freshly mixed solutions are introduced into the cell. For micelles that exchange rapidly (such as those discussed in this chapter), this spectrum will be of an equilibrium solution. All time stamps given for an individual run is with respect to t_0. Since the mixing time (>8 ms) is shorter than the minimum acquisition time of a spectrum (8 ms), the first spectrum after t_0 contains a mixture of the spectrum of the old (equilibrium) solution and the new freshly mixed solution. Since the detector and the stopped flow device are not synchronised, mixing occurs at an arbitrary time during the first spectrum. While this first spectrum could be useful for determining the exact point of mixing, the analysis of first-order kinetic data does not require an absolute time after mixing. Consequently, this first spectrum is excluded from the plots below.

We cannot assume that the mixed solutions reach equilibrium in the time between successive runs (typically a few mins). Therefore, the spectrum at t_0 might not represent the equilibrium end-point. To determine whether the mixing process has reached equilibrium we compare the final scan against a separate 'expected end point'. The 'expected end point' for each case was made by mixing the surfactant with 0.5% NBD-PE and 0.25% Rh-PE by mole of the surfactant before dispersing in water. The expected end point assumes complete 1:1 mixing of micelles has taken place.

The general trend for each experiment follows the theory previously stated: as the excitation energy is transferred from the NBD-PE to Rh-PE, the NBD-PE emission intensity decreases, and the Rh-PE emission intensity increases. There is an additional complexity in the spectra from the overlap of the Rh-PE absorption spectrum and NBD-PE emission spectrum; however, provided that the Rh-PE concentration does not change with time, the absorption of NBD emission by Rh-PE in different micelles (i.e. not FRET) and its subsequent emission as Rh-PE fluorescence does not affect the kinetics of the exchange process deduced by TFA.

Figures 5.1–5.6 showing the unrefined and refined mixing experiments contain isosbestic points. An isosbestic point implies a process involving just two species, in which one species is converted into another (in this case NBD fluorescence and NBD-Rh FRET). The absence of an isosbestic point implies that there is a third species contributing to the spectra or that there are additional factors affecting the intensity of the fluorescence (e.g. creaming, scattering, changes in quantum yield). The

appearance or absence of an isosbestic point is a useful tool to determine whether there are additional processes other than FRET occurring.

5.1 Limonene microemulsion stopped-flow FRET experiments

Micelle exchange data for 2 mM limonene microemulsions at 15 °C, 25 °C and 35 °C is shown in figures 5.1a, 5.1b, 5.2a, 5.2b, 5.3a and 5.3b, respectively. In each case, Panel a shows the raw data and Panel b the refined data after reconstructing the spectra from only the significant components. The refined spectra make it much easier to identify isosbestic points and the shoulder around 650 nm that is characteristic of Rh-PE emission. Each figure selects scans specifically to show the progression of FRET over time. In each case the t_0 spectrum (immediately before mixing) is in black and the final spectrum in the run is in red.

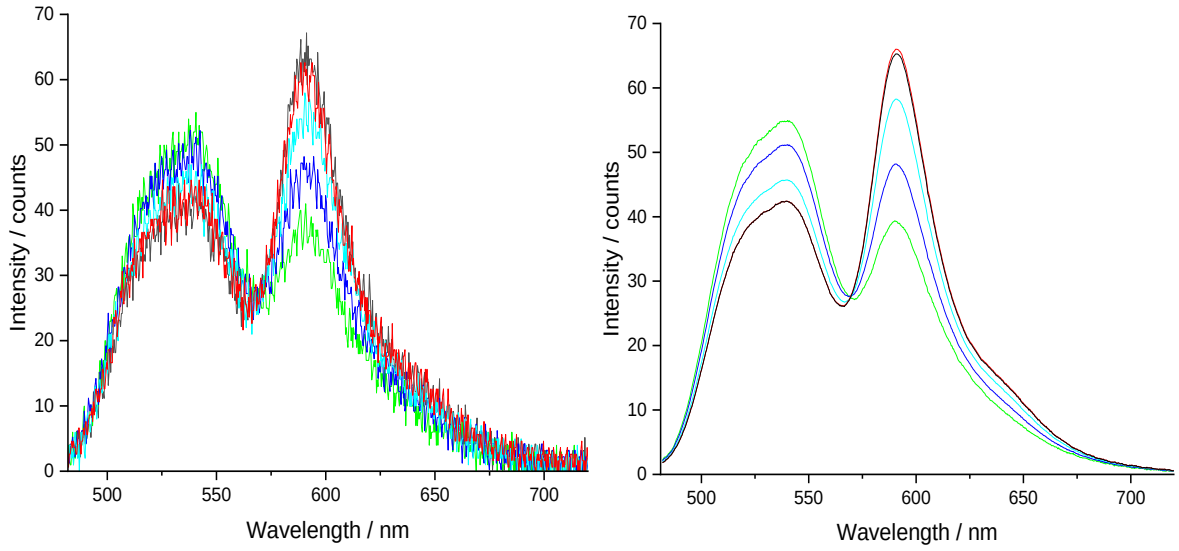

Figures 5.1a and 5.1b: 15 °C mixing data for 2 mM limonene microemulsions. Excitation wavelength 468 nm. Integration time 20 ms. Black line is t_0, light green line is 40 ms, dark blue line is 10 s, cyan line is 30 s, red line is 1 min.

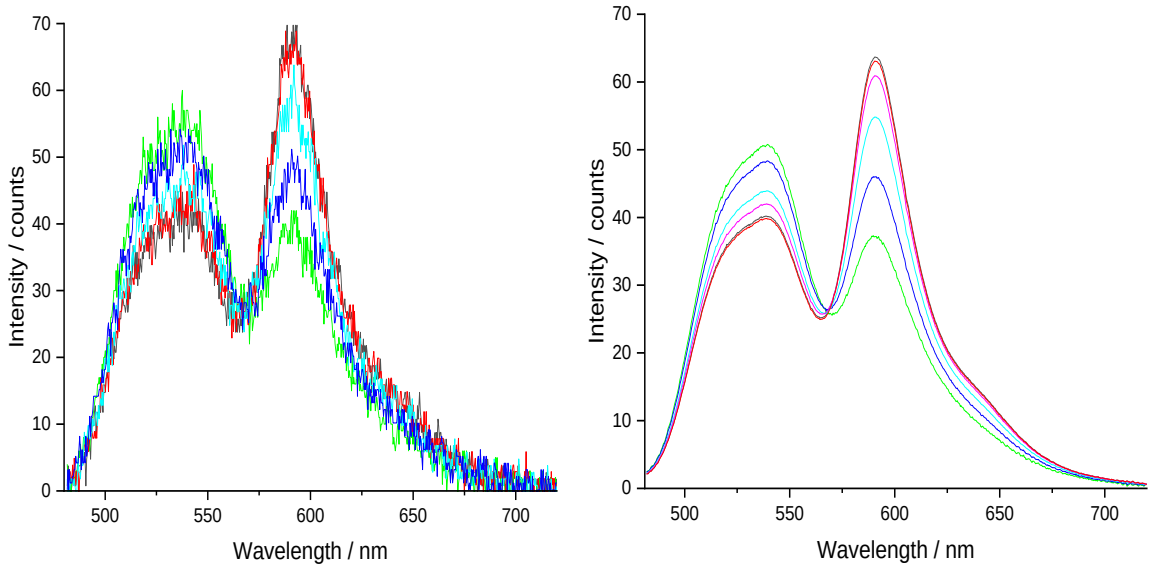

(a) (b)

Figures 5.2a and 5.2b: 25 °C mixing data for 2 mM limonene microemulsions. Excitation wavelength 468 nm. Integration time 20 ms. Black line is t_0, light green line is 40 ms, dark blue line is 5 s, cyan line is 15 s, red line is 30 seconds.

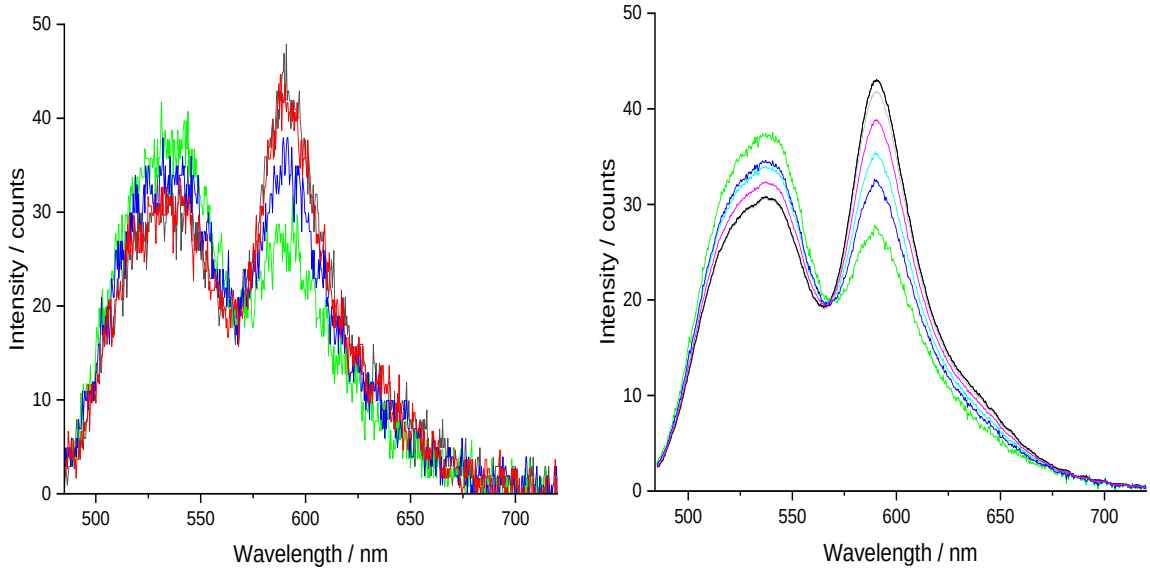

(a) (b)

Figures 5.3a and 5.3b: 35 °C mixing data for 2 mM limonene microemulsions. Excitation wavelength 468 nm. Integration time 20 ms. Black line is t_0, light green line is 40 ms, dark blue line is 1 s, red line is 5 seconds.

A qualitative inspection of figures 5.1–5.3 shows that as temperature increases, the rate of FRET increases. The FRET lifetime at 15 °C occurs on the timescale of 60 s, at 25 °C on the timescale of 30 s and at 35 °C on the timescale of 5 s. As the concentration is fixed, we can assume the increase in FRET is not a result of more probes being in close enough proximity to each other for FRET and therefore the result of another effect. The fish tail results (§2.6) establishes that the limonene microemulsions remain in the Winsor IV region as the temperature is changed between 15 °C and 35 °C at fixed concentration. Observation of the bulk system before and after mixing did not suggest a phase change or any effects such as sedimentation or creaming. An isosbestic point is observed for each temperature and concentration suggesting one kinetic pathway.

5.2 Surfactant package stopped-flow FRET experiments

A comparative study using empty micelles (i.e. no limonene) with stopped-flow FRET experiments at 15 °C, 25 °C and 35 °C has been undertaken at 0.5 mM, 2 mM and 5 mM. As with the limonene microemulsion experiments, the FRET data for 2 mM surfactant package at 15 °C, 25 °C and 35 °C is shown in figures 5.4a, 5.4b, 5.5a, 5.5b, 5.6a and 5.6b. As with limonene, in each case, panel a shows the raw data and panel b the refined data after reconstructing the spectra from only the significant components. Each figure selects scans specifically to show the progression of FRET over time. In each case the t_0 spectrum (immediately before mixing) is in black and the final spectrum in the run is in red. Note that there are fewer spectra in each kinetic run for the surfactant package than for the microemulsion, so the noise reduction in the refined spectra is less than in Figures 5.1–5.3.

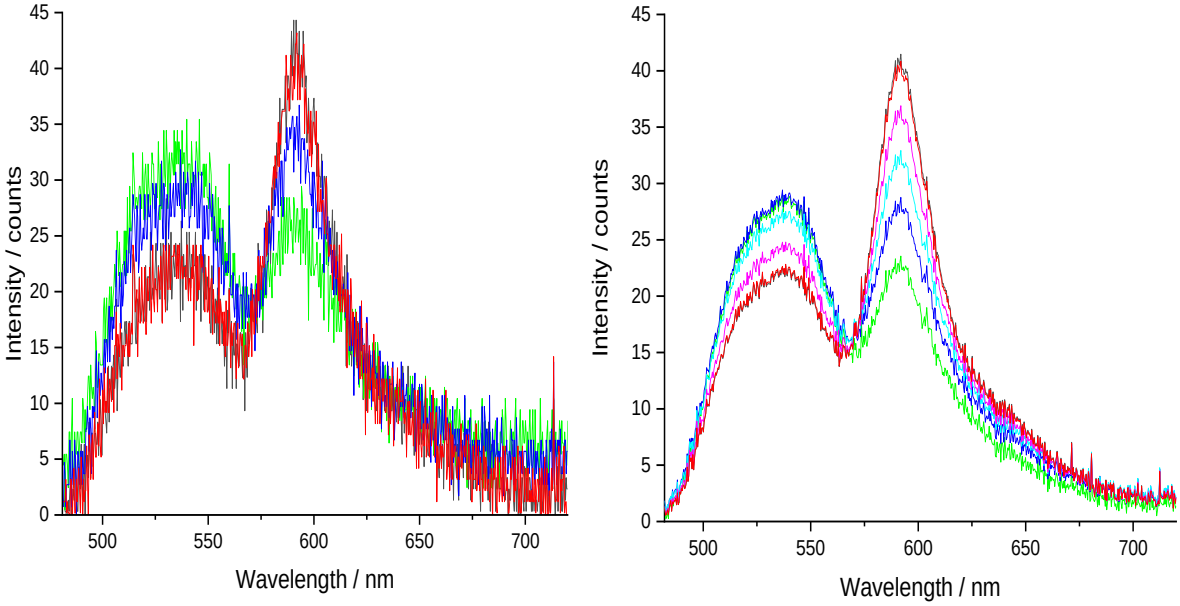

Figure 5.4a and 5.4b: 15 °C FRET data for 2 mM surfactant package. Excitation wavelength 468 nm. Integration time 20 ms. Black line is t_0, light green line is 40 ms, dark blue line is 1 s and red line is 5 s.

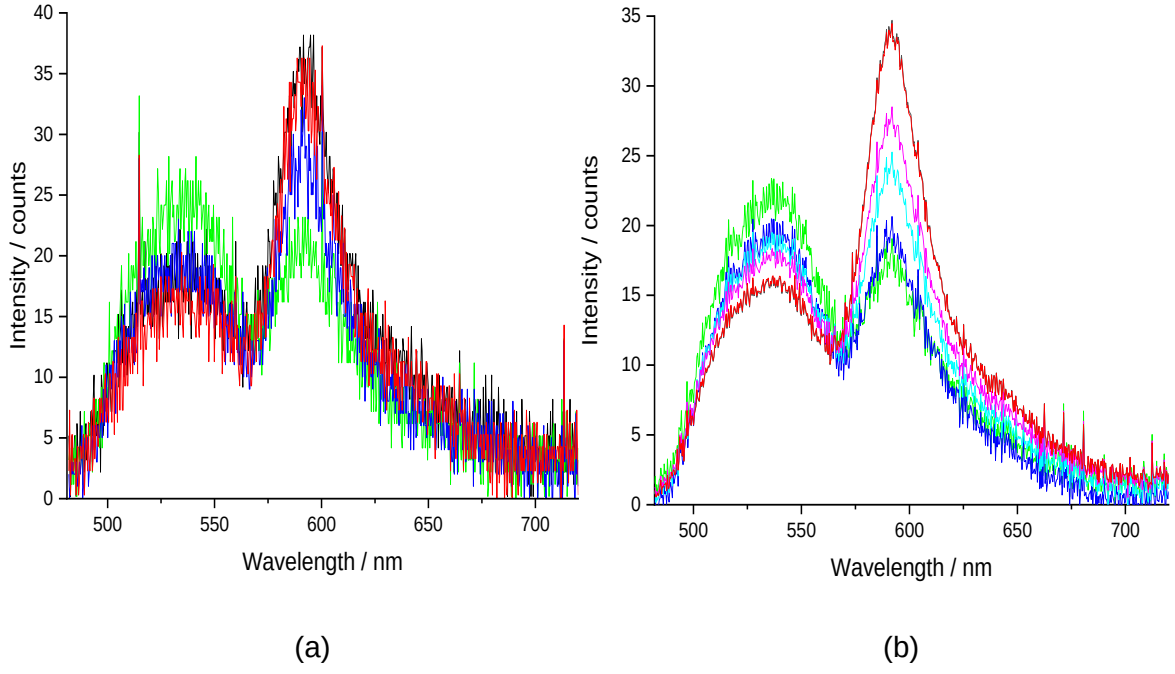

Figures 5.5a and 5.5b: 25 °C FRET data for 2 mM surfactant package. Excitation wavelength 468 nm. Integration time 20 ms. Black line is t_0, light green line is 40 ms, dark blue line is 260 ms and red line is 1 s.

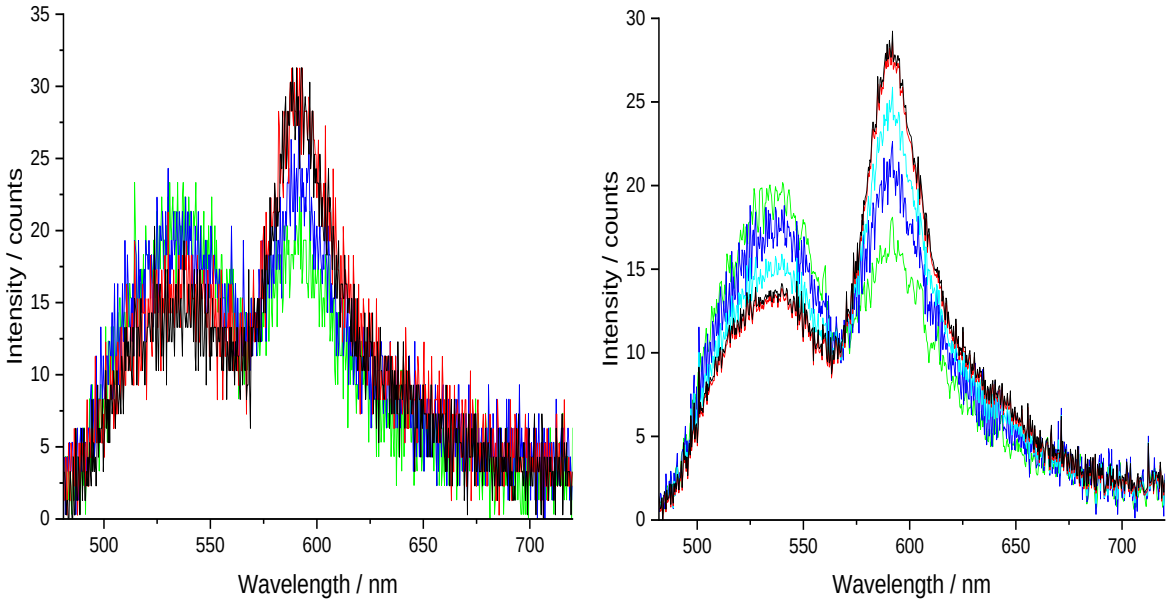

(a) (b)

Figures 5.6a and 5.6b: 35 °C FRET data for 2 mM surfactant package. Excitation wavelength 468 nm. Integration time 20 ms. Black line is t_0, light green line is 40 ms, dark blue line is 80 ms, red line is 140 ms.

The surfactant package shows the same relationship of temperature with FRET when the concentration is fixed. The time required for exchange to be complete, as revealed by the FRET kinetics, decreased from 5 s at 15 °C to 1 s at 35 °C and 140 ms at 35 °C. The surfactant package undergoes FRET on a much faster timescale than limonene microemulsions for the case of 2 mM $C_{12}E_7$. Despite being noisier, the refined spectra for each concentration and temperature show an isosbestic point present, indicating one kinetic pathway. Quantitative analysis of the data will give a definitive comparison of kinetic FRET for the surfactant package and limonene microemulsion with varying temperature and concentration of surfactant.

5.3 Quantitative treatment of FRET data

Each mixing run was analysed using target factor analysis to calculate observed rate constants for FRET with respect to the two components which I label NBD-PE (at the beginning of the experiment) and Rh-PE (at the end), though each component contains contributions from both fluorophores. Figures 5.7 and 5.8 are examples of the loading factor analysis results for a single FRET experiment of limonene microemulsions and surfactant package, respectively. The surfactant concentration for each example is 2 mM at 25 °C and shows the progression of FRET in a more succinct manner.

Figures 5.7 and 5.8 show a smooth progression of FRET between the NBD-PE and Rh-PE probes and were fitted with a single exponential decay. An observed rate constant for each fluorescent probe was determined. A comparison of the observed rate constant for NBD-PE and Rh-PE gives more information on the possible contributions giving rise to FRET between the micelles. The single exponential decay fit suggests that there was only one kinetic pathway contributing to FRET, which I propose is due to micelle fusion and fission. Figure 5.7 shows FRET is complete after ~55 seconds for limonene microemulsions, figure 5.8 shows FRET is complete after ~2 seconds for the surfactant package. Figures 5.7 and 5.8 gives further evidence of faster FRET kinetics for the surfactant package than limonene microemulsions.

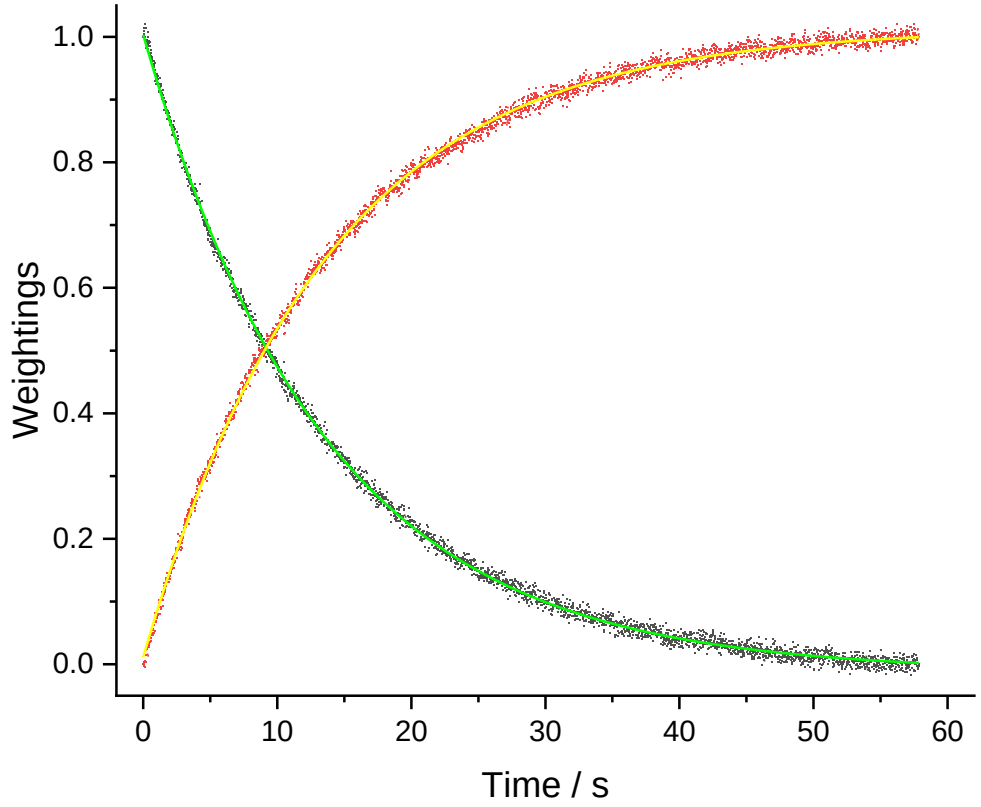

Figure 5.7: Loading result for FRET of 2 mM limonene microemulsion 25 °C. The NBD-PE weightings are represented by black data points with a solid green line fit, the Rh-PE weightings are represented by red data points with a solid yellow fit.

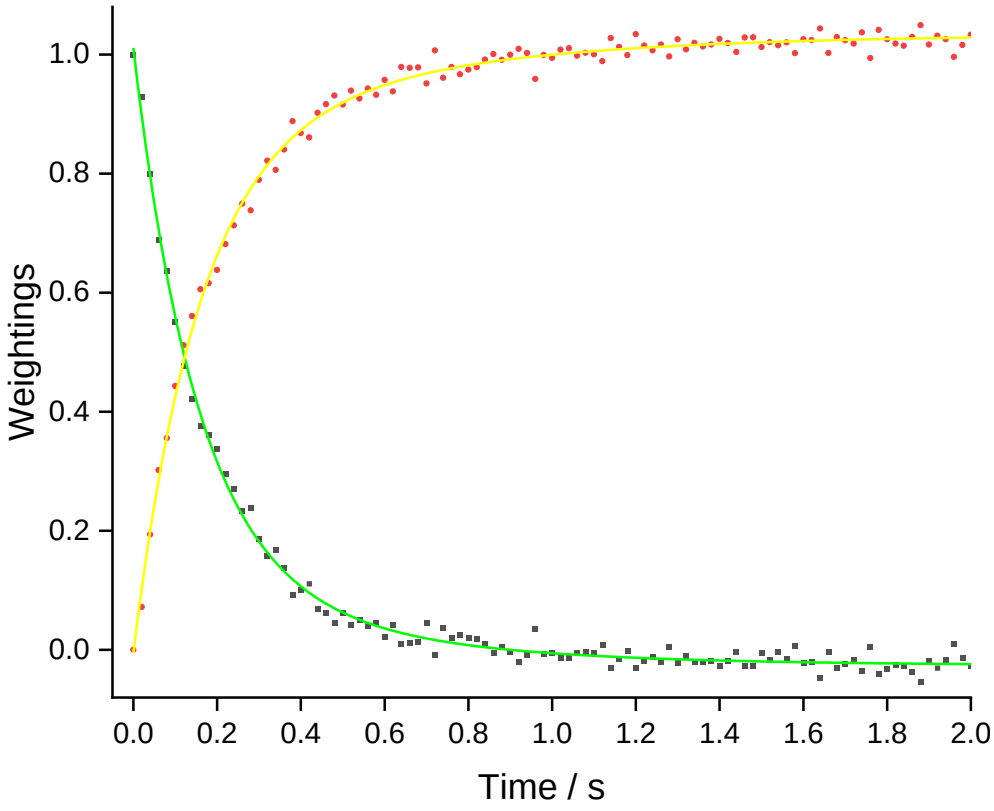

Figure 5.8: Loading result for FRET of 2 mM surfactant package 25 °C. The NBD-PE weightings are represented by black data points with a solid green line fit, the Rh-PE weightings are represented by red data points with a solid yellow fit.

Figures 5.9 and 5.10 plot the observed rate constants for NBD-PE and Rh-PE at each concentration and temperature for limonene microemulsions and surfactant package respectively. The observed rate constants calculated are an average of 8 experimental runs for each concentration and temperature. The error bars have been removed from the plots to avoid confusion when reading the data points; table 5.1 reports the observed rate constants for both the limonene microemulsions and surfactant package with their calculated errors. The observed rate constants determined from the NBD-PE and Rh-PE components agree within error for both limonene microemulsions and surfactant package in all cases. When the observed rate constants for NBD-PE and Rh-PE for a particular case correspond to each other within error, we can infer the change in weightings used to calculate the observed rate constant were solely attributed to FRET. Linear fits for both NBD-PE and Rh-PE kinetics have been taken for each temperature interval. The linear fits have been forced through an origin (0,0): as the micelle concentration tends to zero, the collision rate also tends to zero. It should be noted the small monomer concentration is being neglected for figures 5.9 and 5.10.

If the linear fits in figures 5.9 and 5.10 show a good fit with the data points, they would indicate simple second-order kinetics, where exchange proceeds through collisions between micelles. Figure 5.9 shows that limonene microemulsion exchange does not follow simple second-order kinetics and thus not purely through collisions. Figure 5.10 shows that at low surfactant concentration the surfactant package does follow second-order kinetics. At higher temperature the fit is not as good a fit for the surfactant package.

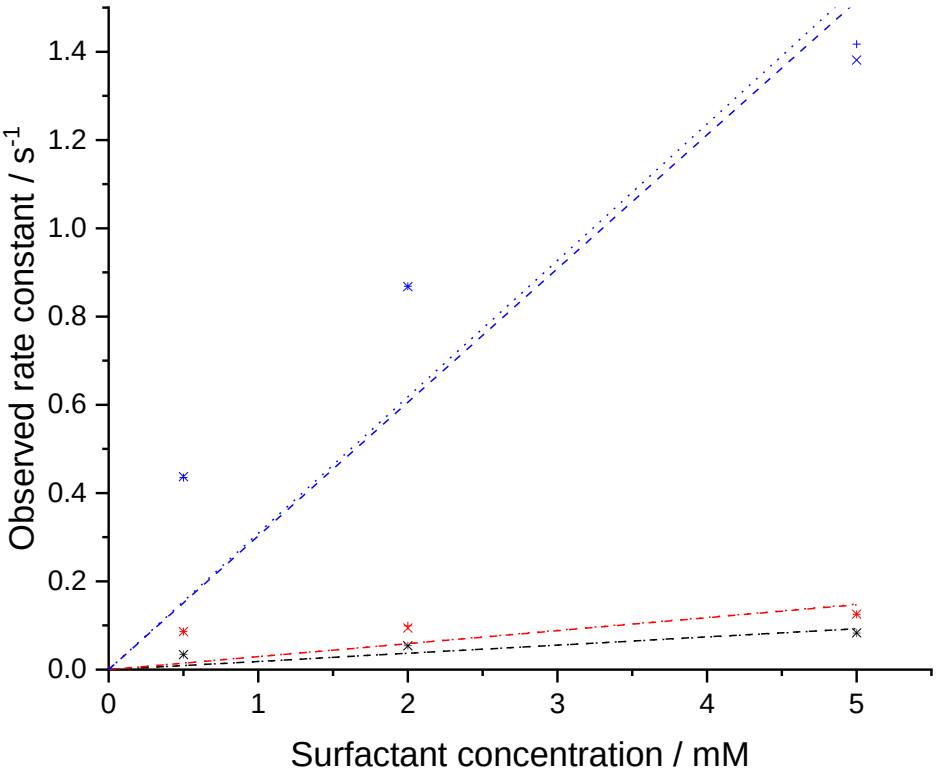

Figure 5.9: Plot of surfactant concentration vs observed rate constant for FRET of limonene microemulsions at 0.5 mM, 2 mM, and 5 mM and three different temperatures of 15 °C (black), 25 °C (red) and 35 °C (blue). The + symbol and dotted line linear fit corresponds to the NBD-PE kinetics. The x symbol and dashed line linear fit corresponds to Rh-PE kinetics.

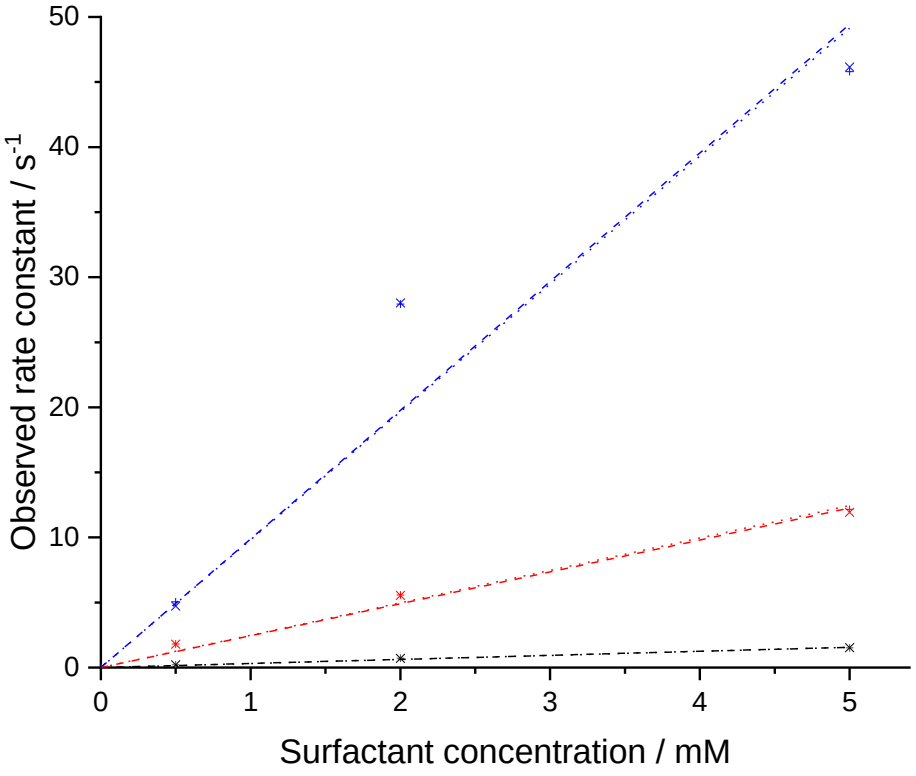

Figure 5.10: Plot of surfactant concentration vs observed rate constant for FRET of surfactant package at 0.5 mM, 2 mM, and 5 mM and three different temperatures of 15 °C (black), 25 °C (red) and 35 °C (blue). The + symbol and dotted line linear fit corresponds to the NBD-PE kinetics. The x symbol and dashed line linear fit corresponds to Rh-PE kinetics.

Table 5.1: Observed rate constants for limonene microemulsions and surfactant package FRET experiments at all temperature and concentration ranges. A propagation of errors was undertaken for the standard error in the mean value.

Limonene microemulsion						
Surfactant concentration / mM	k_{obs} at 15 °C / s^{-1}		k_{obs} at 25 °C / s^{-1}		k_{obs} at 35 °C / s^{-1}	
	NBD-PE	Rh-PE	NBD-PE	Rh-PE	NBD-PE	Rh-PE
0.5	0.034 ± 0.001	0.034 ± 0.001	0.036 ± 0.002	0.086 ± 0.001	0.44 ± 0.01	0.44 ± 0.01
2	0.054 ± 0.001	0.054 ± 0.001	0.099 ± 0.003	0.094 ± 0.004	0.87 ± 0.01	0.87 ± 0.01
5	0.083 ± 0.008	0.083 ± 0.007	0.125 ± 0.001	0.126 ± 0.001	1.41 ± 0.06	1.38 ± 0.07
Surfactant package						
Surfactant concentration / mM	k_{obs} at 15 °C / s^{-1}		k_{obs} at 25 °C / s^{-1}		k_{obs} at 35 °C / s^{-1}	
	NBD-PE	Rh-PE	NBD-PE	Rh-PE	NBD-PE	Rh-PE
0.5	0.209 ± 0.016	0.209 ± 0.017	1.81 ± 0.07	1.80 ± 0.07	5.1 ± 0.6	4.7 ± 0.5
2	0.715 ± 0.010	0.714 ± 0.008	5.57 ± 0.12	5.54 ± 0.16	28 ± 1	28 ± 1
5	1.52 ± 0.03	1.52 ± 0.02	12.2 ± 0.2	11.9 ± 0.2	46 ± 3.0	46 ± 3

It should be noted from table 5.1 the error in the k_{obs} for the 5 mM surfactant package data at 35 °C is high. As the surfactant package FRET occurs on a much shorter timescale for 5 mM runs at 35 °C than limonene microemulsions there was a greater degree of variability between each run. Figure 5.11 shows the loading results for a single run at 5 mM 35 °C, FRET occurs over a very short timescale, meaning there are fewer data points to fit and less certainty with the fit. The spectrometer is taking acquisitions at the fastest acquisition time possible (8 ms) for these runs. The limits of the spectrometer is contributing to the variability in the kinetic data and is something we cannot improve upon without significant experimental changes.

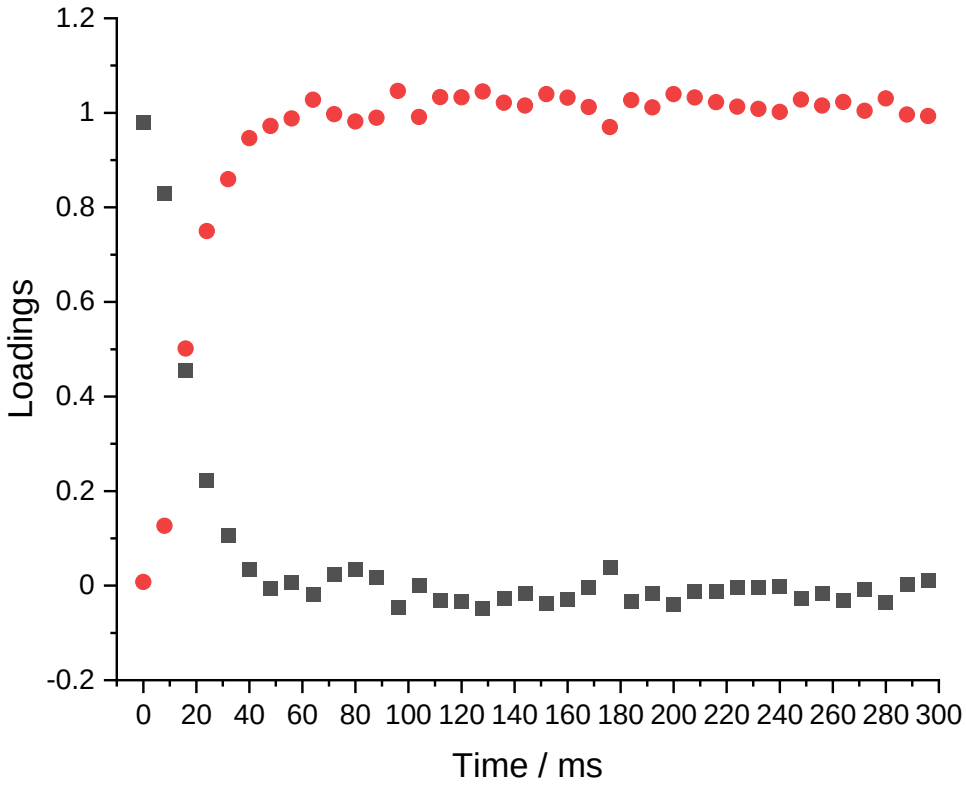

Figure 5.11: Loading results from 5 mM cyclohexane FRET experiment at 35 °C. The red dots shows the progression of Rh-PE FRET, the black squares shows the progression of NBD-PE FRET.

5.3.1 Activation energy of micelle exchange

From the rate constants presented, if the rate-limiting step is the formation of transient dimers, the transient dimer formation could be an activated process showing Arrhenius kinetics in which an activation energy can be extracted. Figures 5.12 and 5.13 show the Arrhenius plot for limonene microemulsion and surfactant package.

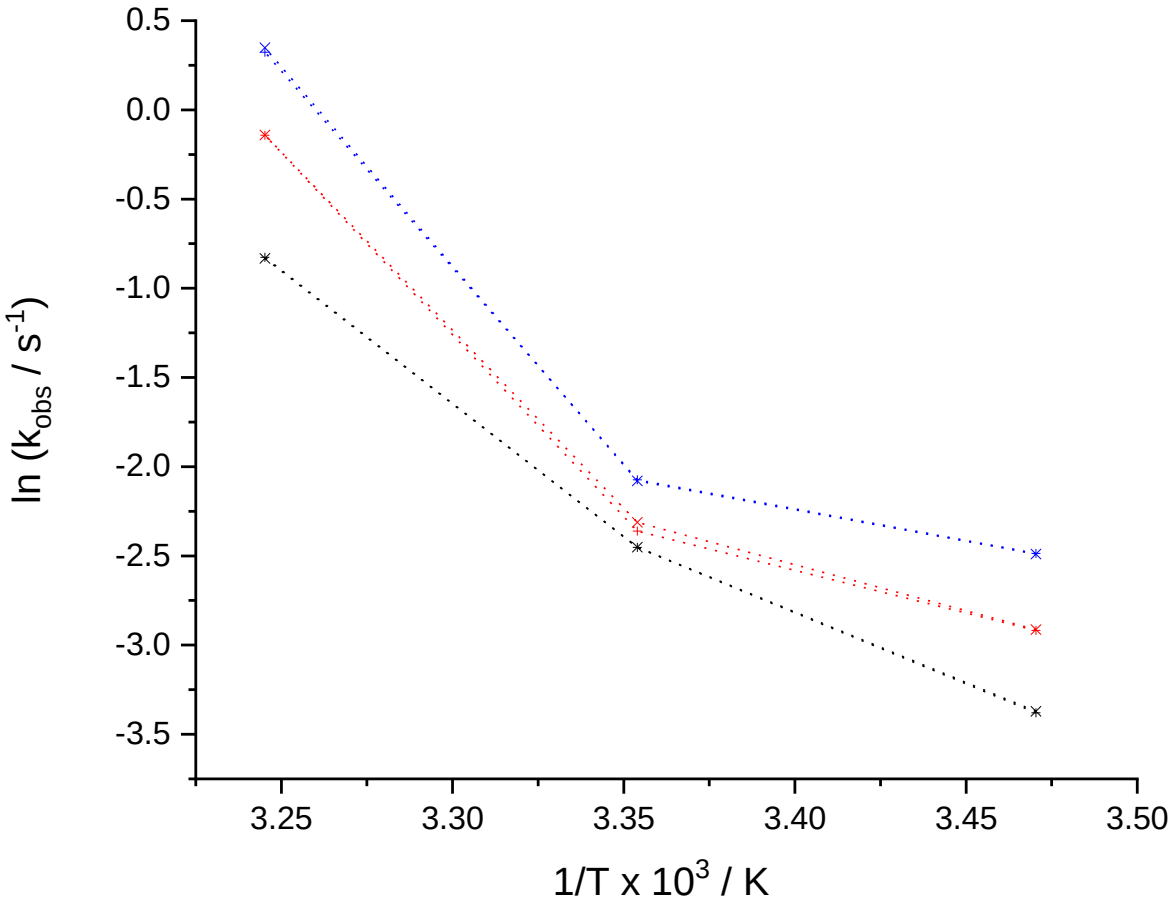

Figure 5.12: Arrhenius plot from observed rate constants of limonene microemulsions at three different concentrations of 0.5 mM (black), 2 mM (red) and 5 mM (blue). The + symbol corresponds to the NBD-PE kinetics and the x symbol corresponds to Rh-PE kinetics.

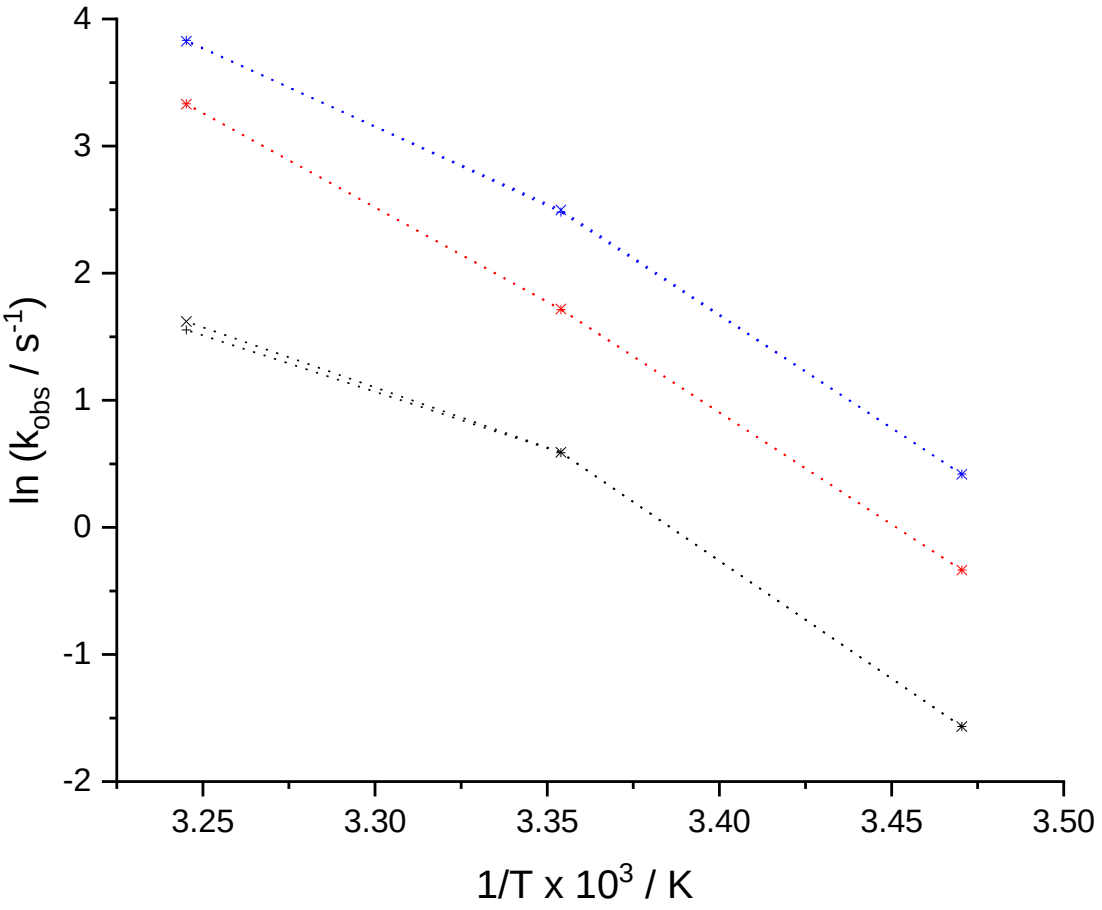

Figure 5.13: Arrhenius plot from observed rate constants of surfactant package at three different concentrations of 0.5 mM (black), 2 mM (red) and 5 mM (blue). The + symbol corresponds to the NBD-PE kinetics and the x symbol corresponds to Rh-PE kinetics.

It is clear the Arrhenius plots in figures 5.12 and 5.13 are not linear as would be anticipated. This could indicate for micelle fusion, the rate-limiting step changes with temperature. A more rigorous experiment including a greater number of data points would help to elucidate the non-linearity in the Arrhenius plots. A more detailed discussion can be found in §5.4. The slope of each line can be used using the Arrhenius equation (equation 5.1) to obtain the activation energy at each concentration.

$$k = Ae^{-Ea/RT}$$

$$\ln k = lnA - \frac{Ea}{RT} \qquad (5.1)$$

An average of activation energy for the three concentrations can be used to determine an overall activation energy for NBD-PE and Rh-PE for the limonene microemulsion

and surfactant package case. The average activation energies and corresponding interaction energy per molecule for NBD-PE and Rh-PE for the limonene microemulsion and surfactant package are in table 5.2. The interaction energy per molecule relates the total energy contribution to the interaction between the micelles. The interaction energy can be related to a micelle fusion mechanism as being the difference in energy between the transient dimer (or super micelle) and the sum of the two micelles.

Table 5.2: Activation energies and interactive energies per molecule of NBD-PE and Rh-PE for limonene microemulsion and surfactant package FRET.

	NBD-PE Ea /kJ mol^{-1}	Rh-PE Ea / kJ mol^{-1}	NBD-PE interaction energy / J	Rh-PE Interaction energy / J
Limonene microemulsion	100	100	1.66×10^{-19}	1.66×10^{-19}
Surfactant package	127	126	2.11×10^{-19}	2.09×10^{-19}

Figures 5.12 and 5.13 show micelle exchange kinetics from the FRET experiments do not follow simple Arrhenius kinetics and there are many factors which affect the observed rate constants such as change in overall micelle size. The activation energies given can show the effect that water viscosity may be having on the observed rate constants (the diffusion coefficient is inversely proportional to the viscosity). Figure 5.14 shows the Arrhenius plot for the viscosity of water for T= 0–40 °C. The water viscosity was taken from Huber et al. [2].

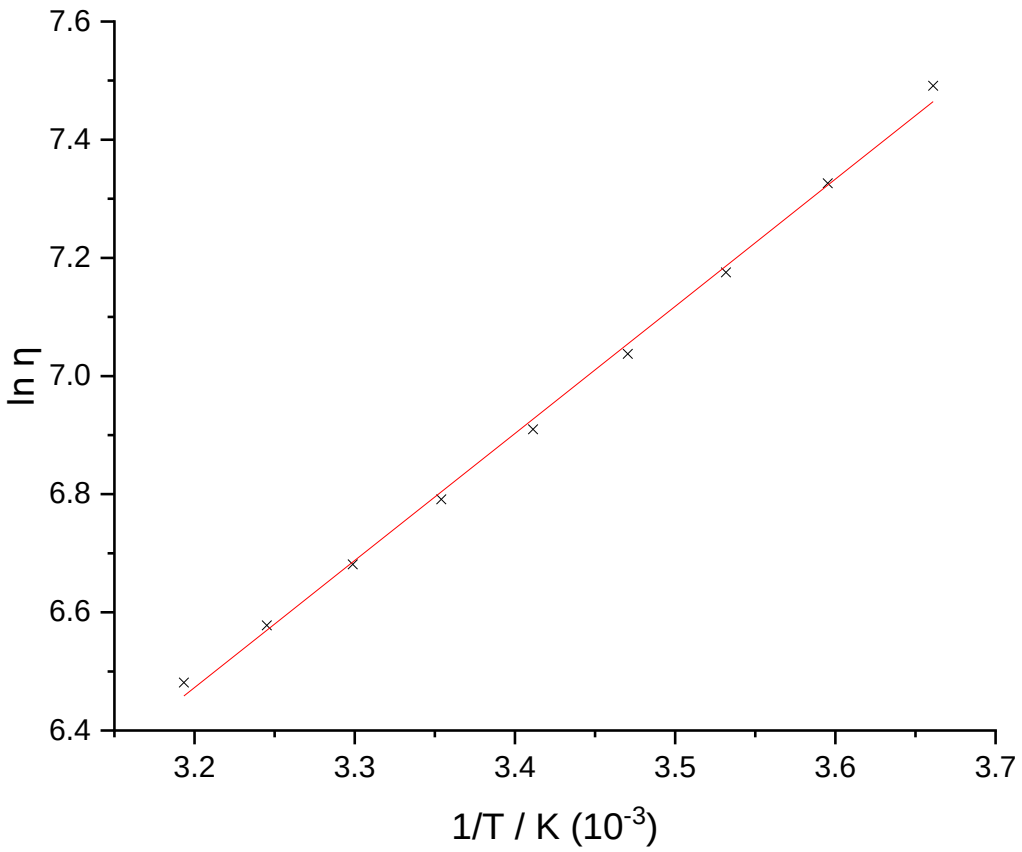

Figure 5.14: Arrhenius plot for the viscosity of water. The data points are represented with a black cross and linear fit with a solid red line.

Adapting equation 5.1 to be used with the viscosity of water, the activation energy was calculated to be 17.9 kJ mol^{-1}. The activation energy for water is nearly an order of magnitude lower than activation energies, showing the acceleration in the exchange rate with temperature is not just due to the increased diffusion rate at higher temperatures.

5.3.2 Diffusion controlled rate constant vs observed rate constant

The observed rate constant has been shown to not follow a simple kinetic pathway. There is also a large disparity between the surfactant package and limonene microemulsion rate constants. By calculating the diffusion-controlled rate constant for micelle exchange for the limonene microemulsion and surfactant package it can be

determined whether the difference in observed rate is purely down to diffusion-controlled collisions.

In §2.2 I was able to use the relationship of surface area to volume ratio of a sphere to calculate the core volume of our limonene microemulsion droplets and surfactant package micelles using equation 5.1. This was taken a step further in §3.3.3 to determine the diffusion-controlled collision rate for limonene microemulsion droplets. The same calculation was used for surfactant package in the absence of limonene. In §4.3.6 the kinetics of the underlying molecular processes were discussed to give the expression for the second-order rate constant k_2 of micelle fusion,

$$k_{obs} = \delta k_2 \frac{[M]}{2} \tag{5.2}$$

The relationship between the observed rate constant and diffusion-controlled reaction rate can be used to estimate δ, from which k_2 can be calculated and is given in table 5.3. Table 5.3 shows a comparison of the diffusion-controlled collision rate of limonene microemulsion droplets and surfactant package with the observed rate constants from FRET for a 2 mM surfactant concentration at 25 °C.

Table 5.3: Comparison of diffusion controlled reaction rate and observed micelle exchange rate constants for limonene microemulsion and surfactant package micelles at 2 mM and 25 °C.

	Diffusion controlled reaction rate /10^4 s^{-1}	Observed rate constant NBD-PE / s^{-1}	Observed rate constant Rh-PE / s^{-1}	δ / 10^{-3}	k_2 / 10^7 s^{-1} mol^{-1} dm^3
Limonene microemulsion	2.39	0.099	0.094	0.004	2.4
Surfactant package	21.92	5.57	5.54	0.025	22

The diffusion-controlled reaction rate is 2 orders of magnitude greater for limonene microemulsion and 1 order of magnitude greater for surfactant package than the observed rate constant for FRET. The results in table 5.3 suggests that the faster kinetics for the surfactant package are not purely due to the number of possible

collisions. The calculation of k_2 shows there is another factor influencing the likelihood that each collision will lead to a fusion mechanism.

When introducing a change in concentration, solvent or temperature the barrier of exchange may be overcome more readily, going someway to explaining the FRET kinetics observed.

5.4 Discussion of FRET data

There are three key observations made from the FRET data given in §5.2 and 5.3. The first observation is that the surfactant package undergoes FRET at least 10 times faster than limonene microemulsion and considerably more for many cases. The second observation is when the temperature is increased FRET increases for both limonene microemulsions and surfactant package. The third observation is when the concentration is increased, FRET increases for both limonene microemulsions and surfactant package.

An understanding of the exchange process taking place can help to explain the three key observations made. For the exchange process, two mechanisms could be at play, the first is the exit and re-entry of solutes, in this case limonene or fluorescent probes from one micelle to another. Zana et al. studied the kinetics of pyrene excimer formation in non-ionic surfactant molecules close to the cloud point [3]. Zana found that the exit and re-entry of pyrene molecules competed with a micelle fusion mechanism. This exit and re-entry may occur with limonene molecules for the case of limonene microemulsions but would not affect the FRET rate increase as the fluorescent probes will remain fixed within the micelle core. If the exit and re-entry mechanism occurred for the fluorescent probes, the rate would be independent of the micellar concentration, which was not found to be the case. The more likely mechanism, which has been discussed previously, is the micelle fusion and formation of super micelles via transient dimer formation. For super micelle formation there is a barrier of exchange which must be overcome. The barrier to exchange for our limonene microemulsion and surfactant package can be estimated from the observed activation energies given in table 5.2 minus the contribution from viscosity of water

(calculated to be 17.9 kJ mol^{-1}). The barrier to exchange for 2 mM limonene microemulsions and surfactant package at 25 °C roughly equates to 82.1 kJ mol^{-1} and 109.1 kJ mol^{-1} respectively Winnick and Rharbi studied the kinetics of fusion and fragmentation for the non-ionic surfactant triton X-100 using stopped-flow fluorescence with a pyrene derivative [4]. Winnick and Rharbi found the measured rate of micelle exchange to be 5000 times slower than the diffusion-controlled reaction rate leading to 1 collision in 5000 resulting in exchange via fusion. Comparing my data in table 5.3, 1 collision in 40 000 for surfactant package and 1 collision in 240 000 for limonene microemulsion leads to fusion limonene microemulsion collisions are much less likely to lead to fusion than for the surfactant package case despite a lower barrier to exchange.

The calculation of k_2 shows when considering the likelihood a collision leads to fusion, exchange for the surfactant package is 10 times faster than for limonene microemulsions. When considering the case of limonene microemulsions and our surfactant package which can be referred to as empty micelles, the observed rate constant for the surfactant package has a faster exchange rate at all temperatures and micelle concentration. A simple explanation for this observation could be due to the swelling of the micelles from limonene increasing the distance of acceptor and donor dye molecules, lowering the probability of FRET and thus slower exchange kinetics. The number of dye molecules per micelle could have an effect on the kinetics of micelle exchange. Further experiments changing the relative dye concentrations, with a model to predict the change in different statistical distribution would be useful for future studies.

Another contribution to the contrast in FRET could be due to the barrier in diffusion of the solvent inside the micelle core. The comparison in 5.3.2 does however demonstrate that higher frequency of collisions does not define the observed rate of FRET between micelles. The nature of the oil inside the micelle could also play a significant role in the rate of FRET, which is explored further in chapter 6.

5.4.1 Temperature effects on FRET

As the temperature is increased for both the limonene microemulsions and surfactant package the rate of FRET increases as shown qualitatively in figures 5.1–5.6. Figures 5.9 and 5.10 confirms this result when isolating each concentration measured. The

quantitative analysis confirms the sharper jump in kinetic exchange from 25–35 °C than 15–25 °C observed from the qualitative results.

There are several contributions to the barrier of exchange via transient dimer formation. The activation energy associated with the formation of a ‘super micelle’ acts as a barrier to micelle exchange. As the temperature increases, there is an increase in the thermal energy of the micelles. With an increased thermal energy, it is easier for micelles to overcome the energy barrier to fusion. The Arrhenius plots in section 5.3.1 show the dependence on exchange kinetics with temperature. This dependence does not show a completely linear trend when moving through the temperature range, which could be in part due to the contributions to the barrier of exchange.

A higher activation energy would usually give a slower reaction (greater energy barrier to fusion), however despite the surfactant package having a higher activation energy than limonene, the observed rate constant and k_2 is greater for the surfactant package. This could mean the pre-exponential factor is different for the surfactant package and limonene microemulsion for micelle fusion. The pre-exponential factor in solution may follow transition-state theory, whereby two micelles potential energy reaches a maximum to the activated product or in our case a transient dimer. For FRET to be successful, the dipoles must satisfy the correct orientation and fluorescent pair needs to be close enough to exchange. The pre-exponential factor for FRET in the micelles may change with temperature as a result of success of FRET conditions being satisfied, therefore giving some understanding to the non-linearity in figures 5.12 and 5.13. The activation energies for both the limonene microemulsion and surfactant package are an order of magnitude higher than for the viscosity of water. As shown with the subtraction of viscosity contribution for the surfactant package and limonene microemulsion, the viscosity contribution is negligible. The activation energy for viscosity and diffusion coefficient are dependent on temperature, however as the temperature range is small (only 20 K) this will be a negligible effect.

The greater dependence on temperature shown for surfactant package could also mean the preferred curvature of $C_{12}E_7$ micelles for the surfactant package decreases further as temperature increases, causing a flattening of the micelle surface. Experiments in §2.4 show that as temperature increases, the oil solubility (given from the oil solubilisation ratio) increases for the limonene microemulsion making fusion

easier. The studies in §2.4 also shows that the limonene microemulsion is not at the oil solubility limit, making the micelles more curved than desired. The increased curvature will strain the interface making fusion easier. As the surfactant package has no solubilised oil, the decrease in preferred curvature could allow the micelles to fuse more readily in the surfactant package than the limonene microemulsion case.

The nonlinearity in the Arrhenius plots for limonene microemulsions and surfactant package could be due to an external factor we are not yet able to explain with the data available, such as a change in morphology of the micelles when increasing temperature.

5.4.2 Concentration changes

As the concentration of $C_{12}E_7$ is increased, the exchange rate increases. There are more micelles in the system, resulting in a greater number of collisions and a higher probability that a donor dye molecule is in close enough proximity to an acceptor dye molecule for FRET.

Conclusion

The FRET experiments have given some interesting results and developed our understanding of the FRET process within micelles. With the known relationship between FRET and changes in temperature or concentration of surfactant, formulators are better able to tune their microemulsions for different conditions in oil wells.

The surfactant concentration has a significant effect on the rate of FRET for both limonene microemulsions and surfactant package. Temperature effects also have a complex effect on the rate of FRET; however, the quantitative analysis show the kinetic pathway for FRET is influenced by a number of factors. From the comparison of limonene microemulsions and surfactant package, the type of solvent used can play a significant role in micelle exchange.

The comparison of temperature, concentration and solvent give insights into what influences the efficacy of micellar solution in oil recovery. If a change in solvent significantly effects FRET it can provide further insight into the mechanism of oil recovery.

References

[1] A. Bera, T. Kumar, K. Ojha, and A. Mandal, “Screening of microemulsion properties for application in enhanced oil recovery,” 2013, doi: 10.1016/j.fuel.2013.12.051.

[2] M. L. Huber *et al.*, “New International Formulation for the Viscosity of H 2 O,” 2009, doi: 10.1063/1.3088050.

[3] R. Zana and C. Weill, “Effect of temperature on the aggregation behaviour of non-ionic surfactants in aqueous solutions,” *Journal de Physique Lettres*, vol. 46, no. 20, pp. 953–960, Oct. 1985, doi: 10.1051/JPHYSLET:019850046020095300.

[4] Y. Rharbi, M. A. Winnik, and K. G. Hahn, “Kinetics of fusion and fragmentation non-ionic micelles: Triton X-100,” *Langmuir*, vol. 15, no. 14, pp. 4697–4700, Jul. 1999, doi: 10.1021/LA990064R/ASSET/IMAGES/LARGE/LA990064RF2.JPEG.

[5] P. Kroll, J. Benke, S. Enders, C. Brandenbusch, and G. Sadowski, “Influence of Temperature and Concentration on the Self-Assembly of Non-ionic CiEj Surfactants: A Light Scattering Study,” *ACS Omega*, vol. 7, no. 8, pp. 7057–7065, Mar. 2022, doi: 10.1021/ACSOMEGA.1C06766/SUPPL_FILE/AO1C06766_SI_001.PDF.

Chapter 6 Solvent effects on micelle exchange using stopped-flow FRET experiment

A number of hydrocarbons types such as alkanes, alkenes and aromatic hydrocarbons have been used as microemulsions, and their phase behaviour studied [1]–[3]. Whilst there have been plenty of studies on relation of efficacy of microemulsion oil recovery with factors such as surfactant type, concentration, salinity and viscosity of microemulsions [4]–[8] there has not been a great deal of study on the effects of the oil in microemulsions with relation to the efficacy of oil recovery. Zhang et al. studied the relative efficacy of limonene in comparison with other oils in a microemulsion system for oil removal. Zhang et al. found all microemulsion formulations had a higher removal efficiency when compared to a surfactant package. Limonene based microemulsions performed best at low concentration compared with xylene-based microemulsions. This is one of few studies dedicated to the effects of the oil component in microemulsion enhanced oil recovery [9]. By studying the micellar exchange kinetics of limonene microemulsion with other known microemulsion forming oils, we could determine whether exchange kinetics are correlated with the effectiveness of the microemulsion for asphaltene removal [9], [10].

For this study, two alternative solvents were chosen, cyclohexane and methyl laurate. The justification for each chosen solvent can be found in the forthcoming sections within this chapter. A table of the physical parameters for each solvent can be found in table 6.1 below. The equivalent alkane carbon number (EACN) could unfortunately not be found for methyl laurate.

Table 6.1: Comparison of the physical parameters for limonene, cyclohexane and methyl laurate.

	Molecular weight / $gmol^{-1}$	Viscosity at 293 K / mPa.s	Surface tension	EACN
Limonene	136.24	0.93 [11]	28.5 [14]	1.8 [16]
Cyclohexane	84.16	1.01 [12]	25.0 [15]	2.1 [16]
Methyl laurate	214.35	3.12 [13]	29.6 [15]	--

6.1 Cyclohexane microemulsion FRET experiments

Cyclohexane was chosen as an alternative solvent to compare with limonene due to the similarity of their equivalent alkane carbon number (EACN), with limonene having an EACN of 1.8 and cyclohexane 2.1 [16]. The EACN is a dimensionless number which relates an oils ability to modify the sponteneous curvature of an interfacial film. In practical terms, an oil's EACN number gives the hydrophobicity or 'oilyness' of the oil used. The EACN can be derived by either using a titration method experimentally or predicted using mathematical modelling and machine learning [16]. By choosing an oil with a similar EACN value as limonene, the properties of the microemulsions at equilibrium should be similar. The microemulsion formula was the same, with cyclohexane being a direct replacement of limonene by weight. Stock solutions of cyclohexane microemulsion were also made with 1% NBD-PE by mole of $C_{12}E_7$ and 0.5% Rh-PE by mole of $C_{12}E_7$ in the same way as limonene microemulsions.

The purity of cyclohexane was examined using ^{1}H NMR, which showed no significant impurity peaks (appendix D).

For ease of comparison, the refined FRET spectra for 2 mM limonene microemulsions as shown in chapter 5 are reproduced in Figure 6.1. Recall that the FRET causes a decrease in the NBD-PE peak at 500–560 nm and an increase in the Rh-PE peak between 560–680 nm.

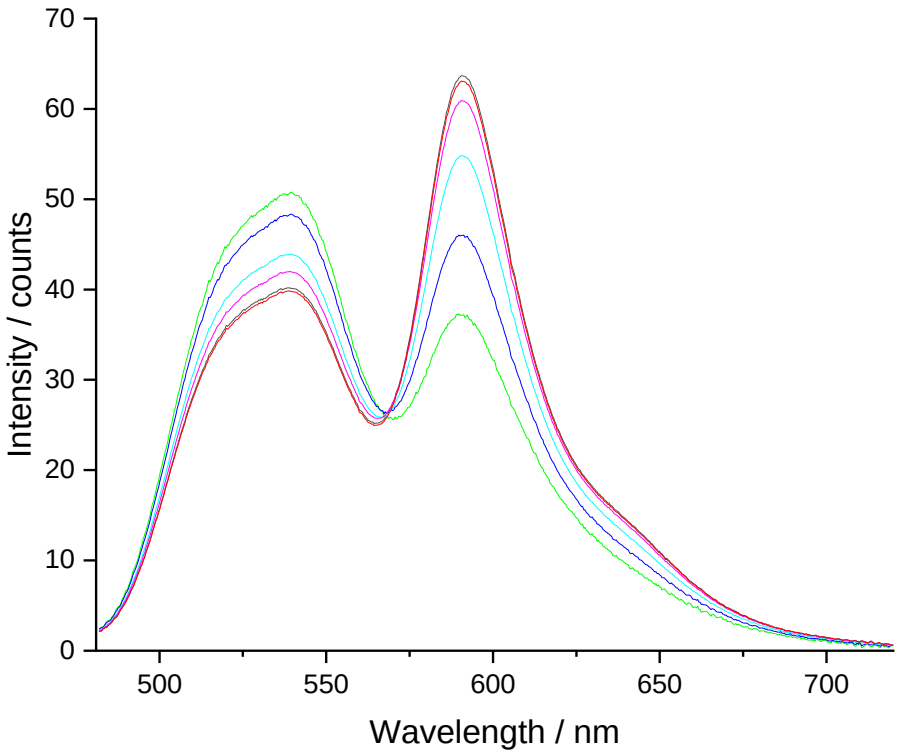

Figure 6.1: Refined spectra for 25 °C FRET data for 2 mM limonene microemulsions. Excitation wavelength 468 nm. Integration time 20 ms. Black line is t_0, light green line is 40 ms, dark blue line is 5 s, cyan line is 15 s, pink line is 25 s and red line is 30 seconds.

FRET experiments were undertaken at 0.5 mM, 2 mM and 5 mM surfactant concentration at 15 °C, 25 °C and 35 °C for cyclohexane microemulsions. Figures 6.2–6.4 show examples of the refined data for cyclohexane microemulsion FRET experiments at 2 mM for 15 °C, 25 °C and 35 °C.

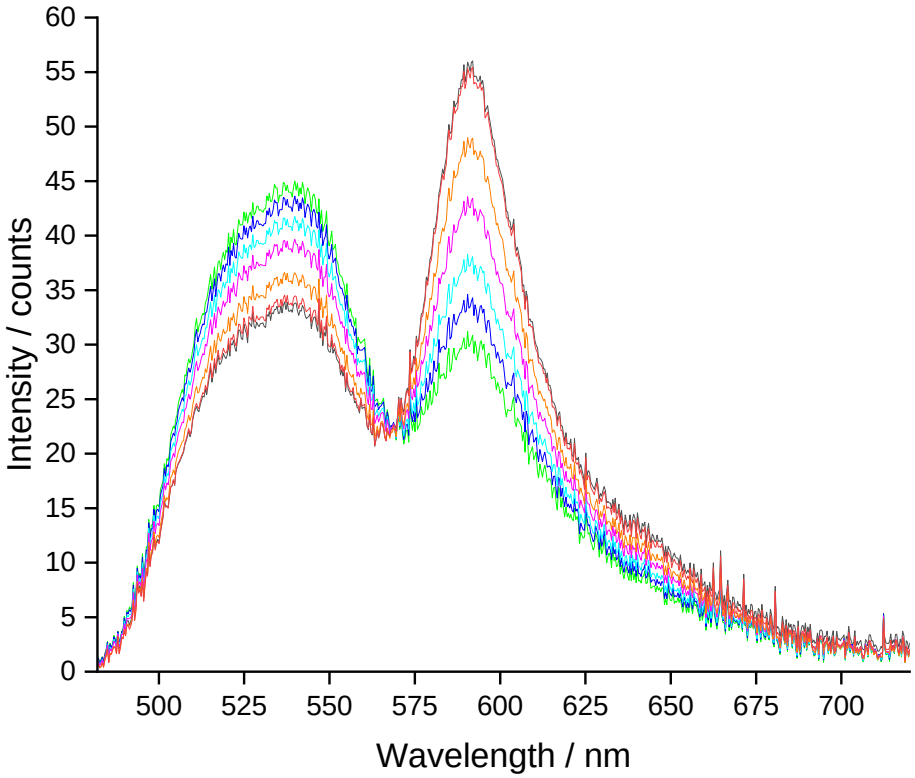

Figure 6.2: Refined spectra for 2 mM cyclohexane microemulsion FRET experiment at 15 ˚C. NBD-PE 1% by mole of $C_{12}E_7$, Rh-PE 0.5% by mole of $C_{12}E_7$. Acquisition time 20 ms. Black line indicates the solution at equilibrium before mixing, the green line is after 40 ms, the dark blue line after 260 ms, the cyan line is after 500 ms, pink line is 1 s, orange line is 2 s and red line after 5 seconds.

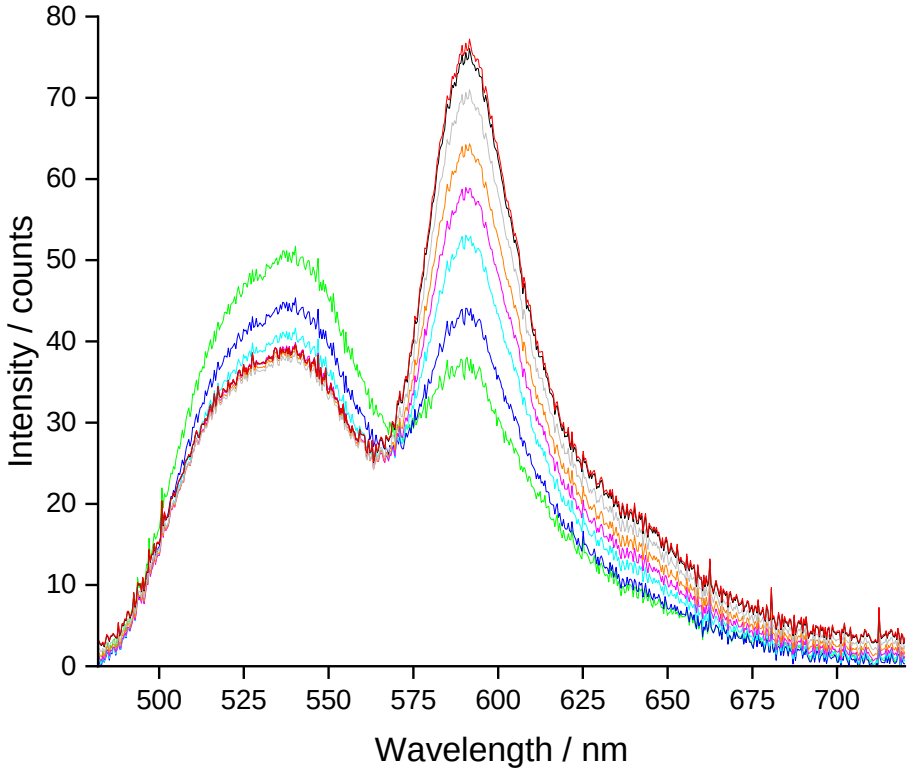

Figure 6.3: Refined spectra for 2 mM cyclohexane microemulsion FRET experiment at 25 ˚C. NBD-PE 1% by mole of $C_{12}E_7$, Rh-PE 0.5% by mole of $C_{12}E_7$. Acquisition time 20 ms. Black line indicates the solution at equilibrium before mixing, the green line is after 40 ms, the dark blue line after 240 ms, the cyan line is after 500 ms, pink line is 750 ms, orange line is 1 s, grey line is 1.5 s and red line after 3 seconds.

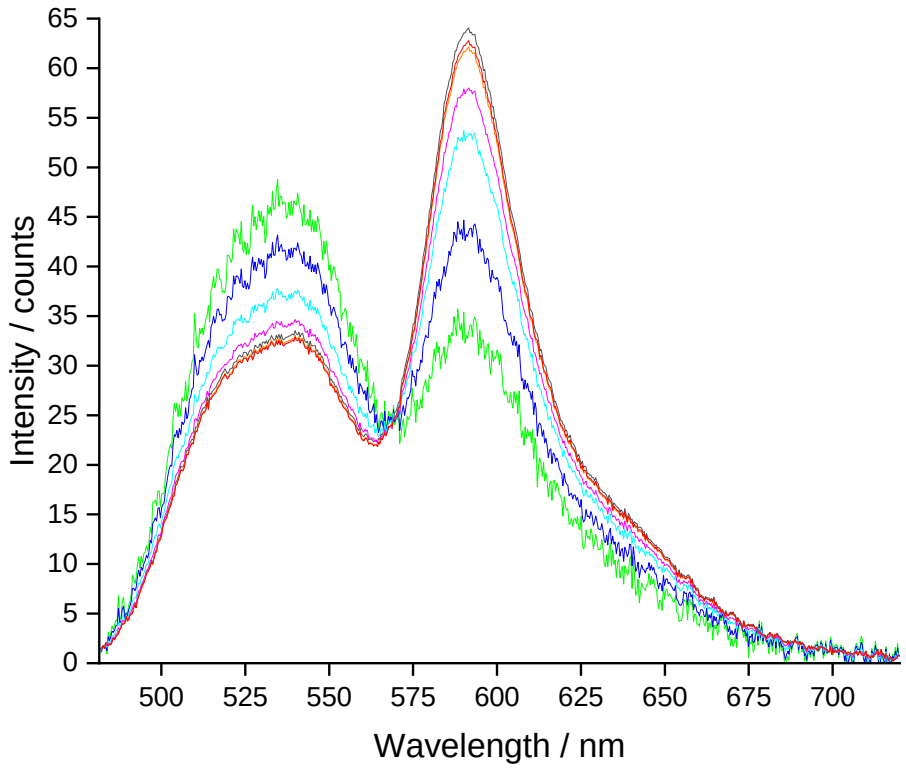

Figure 6.4: Refined spectra for 2 mM cyclohexane microemulsion FRET experiment at 35 ˚C. NBD-PE 1% by mole of $C_{12}E_7$, Rh-PE 0.5% by mole of $C_{12}E_7$. Acquisition time 20 ms. Black line indicates the solution at equilibrium before mixing, the green line is after 40 ms, the dark blue line after 60 ms, the cyan line is after 80 ms, pink line is 100 ms, orange line is 200 ms, and red line after 500 ms.

It should be noted from figure 6.4 for 40 ms and 60 ms scans the smoothing from the quantitative analysis is not consistent with the rest of the spectra. This is strange behaviour, which is found for each run. The SPOIL function returned a satisfactory result. Referring to §4.3.3 it appears there may have been more interference in the cell which corrected after 60 ms.

6.2 Quantitative treatment of cyclohexane FRET data

As with the case for limonene microemulsions and surfactant package data, the FRET data for cyclohexane was quantitively analysed using target factor analysis to obtain rate constants for FRET. Figure 6.5 shows the loading factor analysis for a single FRET experiment of cyclohexane microemulsions at 2 mM surfactant concentration and 25 °C.

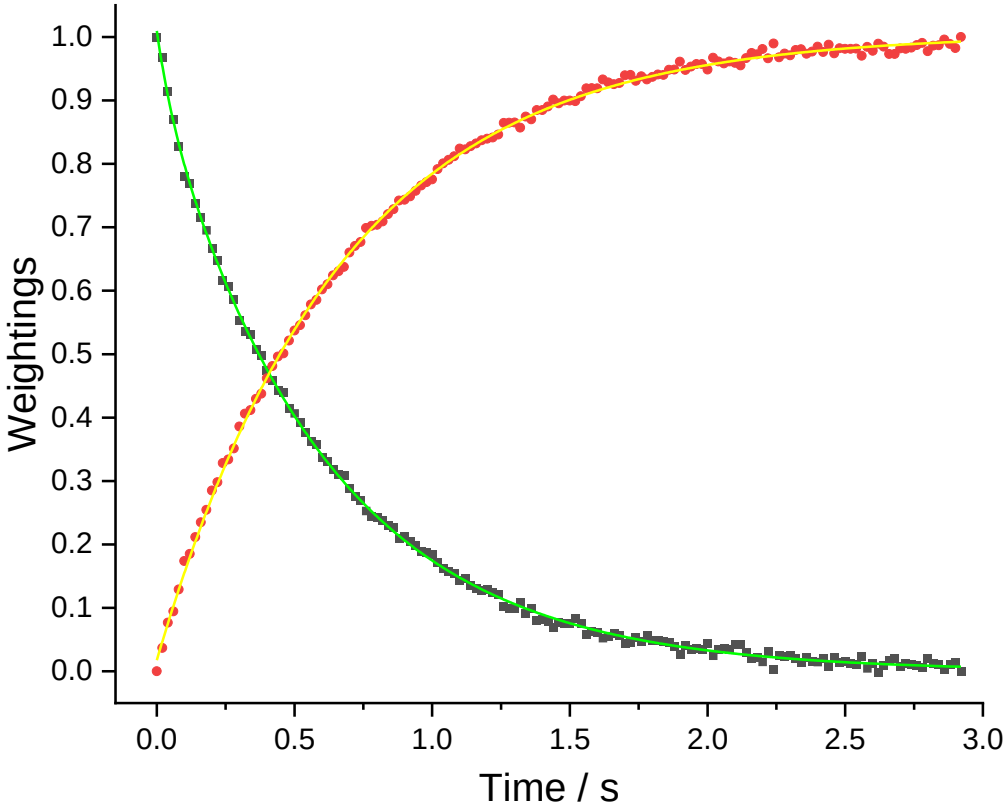

Figure 6.5: 25 °C loading data for 2 mM cyclohexane FRET. The black squares indicate NBD-PE loadings with the green line indicating the decay fit, the red circles indicate Rh-PE loadings with the yellow line indicating the decay fit.

The cyclohexane results indicate successful FRET, which fit a single exponential decay much like with limonene and surfactant package. The rate constants calculated from the loading results for each concentration and temperature value have been plotted in figure 6.6 below. The observed rate constants calculated are an average of 8 experimental runs for each concentration and temperature. The error bars have been omitted from the figure to avoid confusion when reading the data points, but are tabulated in Table 6.1.

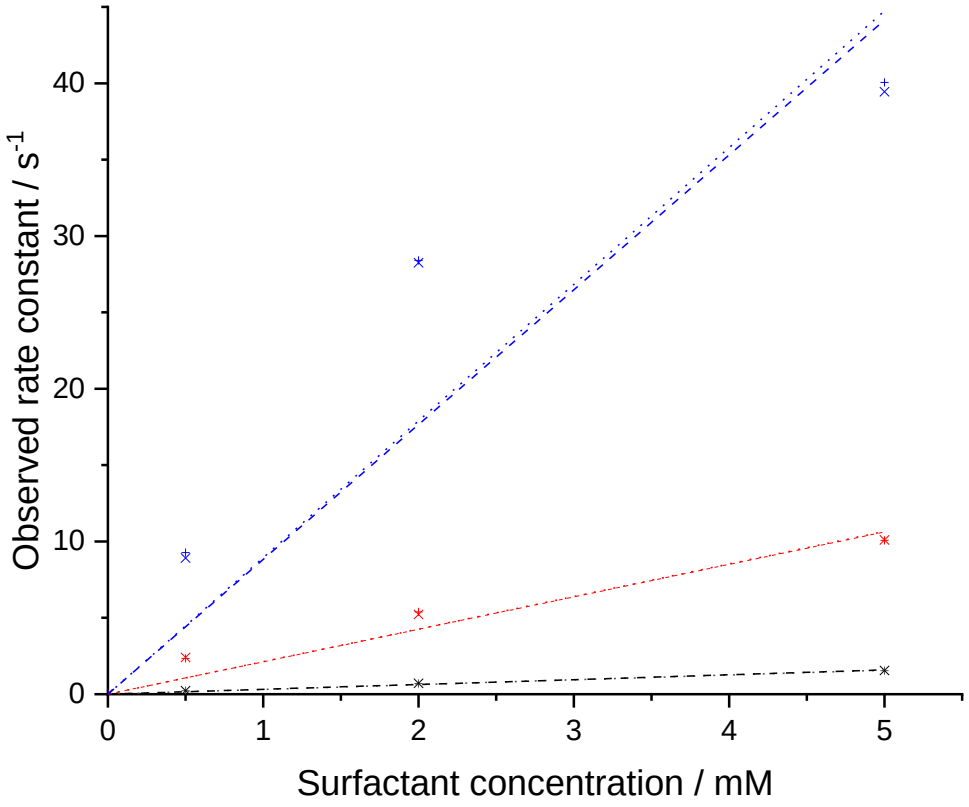

Figure 6.6: Plot of surfactant concentration vs observed rate constant for FRET of cyclohexane microemulsions at 0.5 mM, 2 mM, and 5 mM and three different temperatures of 15 °C (black), 25 °C (red) and 35 °C (blue). The + symbol and dotted line linear fit corresponds to the NBD-PE kinetics. The x symbol and dashed line linear fit corresponds to Rh-PE kinetics.

The linear fits for each temperature in figure 6.6 show that the observed rate constant at low temperatures do follow simple second-order kinetics, but as the temperature increases there are other contributions to the observed rate constant than just collisions between micelles.

Table 6.1 gives the data points plotted in figure 6.6 with their respective error. Much like with limonene microemulsions and surfactant package results, if NBD-PE and Rh-PE display the same rate constant for a particular case within error, then we can assume micelle exchange is the sole contributor to the observed rate constant. The limonene microemulsion results from chapter 5 have also been included to compare the exchange rate of the two solvents.

Table 6.2: Observed rate constants for cyclohexane microemulsions and limonene microemulsions FRET experiments at all temperature and concentration ranges with given errors.

Cyclohexane microemulsion						
Surfactant concentration / mM	k_{obs} at 15 °C / s^{-1}		k_{obs} at 25 °C / s^{-1}		k_{obs} at 35 °C / s^{-1}	
	NBD-PE	Rh-PE	NBD-PE	Rh-PE	NBD-PE	Rh-PE
0.5	0.227 ± 0.003	0.228 ± 0.003	2.3 ± 0.2	2.4 ± 0.3	9.3 ± 0.2	8.9 ± 0.1
2	0.703 ± 0.003	0.709 ± 0.003	5.4 ± 0.2	5.2 ± 0.2	28 ± 1	28 ± 1
5	1.538 ± 0.007	1.551 ± 0.006	10 ± 0.6	10 ± 0.5	40 ± 3	39 ± 3
Limonene microemulsion						
Surfactant concentration / mM	k_{obs} at 15 °C / s^{-1}		k_{obs} at 25 °C / s^{-1}		k_{obs} at 35 °C / s^{-1}	
	NBD-PE	Rh-PE	NBD-PE	Rh-PE	NBD-PE	Rh-PE
0.5	0.034 ± 0.001	0.034 ± 0.001	0.086 ± 0.002	0.086 ± 0.001	0.44 ± 0.01	0.44 ± 0.01
2	0.054 ± 0.001	0.054 ± 0.001	0.099 ± 0.003	0.094 ± 0.004	0.87 ± 0.01	0.87 ± 0.01
5	0.083 ± 0.008	0.083 ± 0.007	0.125 ± 0.001	0.126 ± 0.001	1.41 ± 0.06	1.38 ± 0.07

From the rate constants presented in figure 6.6, the rate limiting step was investigated, much like in chapter 5, assuming Arrhenius kinetics. If the rate-limiting step is the formation of transient dimers and the transient dimer formation is an activated process, then the kinetics can be assumed to be second-order and the resulting Arrhenius plot will show a linear trend.

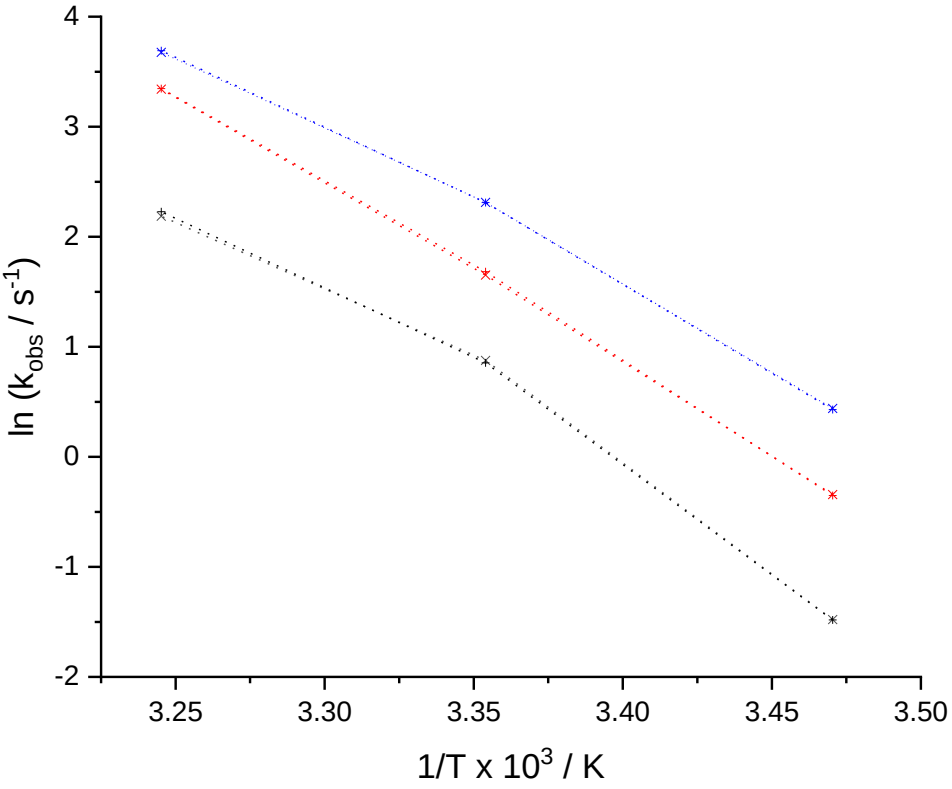

Figure 6.6: Arrhenius plot from observed rate constants of cyclohexane microemulsion at three different concentrations of 0.5 mM (black), 2 mM (red) and 5 mM (green). The + symbol corresponds to the NBD-PE kinetics and the x symbol corresponds to Rh-PE kinetics.

2 mM surfactant concentration shows a largely linear trend, however 0.5 mM and 5 mM surfactant concentration does not. The activation is not constant with temperature at 0.5 and 5 mM and does not show simple second order kinetics. A linear fit was attempted for data shown in figure 6.7 and an activation energy was calculated using the Arrhenius equation below.

$$k = Ae^{-Ea/RT}$$

$$\ln k = lnA - \frac{Ea}{RT} \qquad (6.1)$$

An average of the activation energy for the three concentration was taken to determine the overall activation energies for NBD-PE and Rh-PE with cyclohexane microemulsion micelle exchange. The average activation energies for NBD-PE and

Rh-PE for the cyclohexane microemulsion are tabulated in table 6.3 and agree with each within error. Limonene microemulsion and surfactant package activation energies have also been included as a comparison.

Table 6.3: Activation energies of NBD-PE and Rh-PE for cyclohexane and limonene microemulsion micelle exchange.

	NBD-PE Ea / kJ mol^{-1}	Rh-PE Ea / kJ mol^{-1}
Cyclohexane microemulsion	131	130
Limonene microemulsion	100	100
Surfactant package	127	126

6.3 Discussion of cyclohexane FRET results

For cyclohexane microemulsions, the relationship between the rate of FRET with temperature and concentration is the same as limonene microemulsions: k_{obs} increases with both concentration and temperature. As the surfactant concentration increases the number of micelles also increases, making successful collisions more likely and thus a greater rate of micellar exchange. As the temperature is increased, the thermal energy of the micelles increases, allowing a greater number of micelles to form 'super micelles' and exchange contents. The lower viscosity in water will increase the diffusion coefficient of micelles allowing a greater number of collisions between the micelles.

NBD-PE and Rh-PE observed rate constants agree with each other within error for each value. The isosbestic point remains fixed for each change in condition. These two indicators, along with the single exponential decay fitting suggest that there is only one pathway contributing to the change in FRET.

As discussed in chapter 5 for the surfactant package case, at higher concentration and temperature there are fewer data points to fit for cyclohexane microemulsions due to a faster exchange rate, giving less certainty to the fit than for limonene microemulsions.

When comparing limonene microemulsions with cyclohexane microemulsions, FRET is more than an order of magnitude faster for cyclohexane microemulsions. This could be due to different diffusion coefficient of the micelles for each solvent, leading to either fewer or more collisions. Assuming the microemulsion droplets are spherical, the

diffusion coefficient of microemulsion droplets can be described by the Stokes-Einstein equation. Moving from cyclohexane to limonene the radius of the microemulsion droplet will change. An estimate of the radius of a microemulsion droplet has been calculated for cyclohexane microemulsion droplets, using the same principles used in chapter 2 for limonene microemulsion droplets. The radius of the limonene and cyclohexane microemulsion droplets and their diffusion coefficients are given in table 6.4.

Table 6.4: Radius of microemulsion droplet and diffusion coefficient for limonene and cyclohexane microemulsions. Viscosity of the medium water was taken from the literature [17].

Solvent	Diffusion coefficient / $m^2\ s^{-1}$ x 10^{-11}	Radius of microemulsion droplet / nm
Limonene	4.6	5.2
Cyclohexane	4.4	5.5

The cyclohexane droplets are larger as the density of cyclohexane (0.779 g cm^{-3} [18]) is lower than limonene (0.844 g cm^{-3} [11]). For the same mass ratio, the cyclohexane microemulsion droplets will have a larger radius. The calculation for the size of a cyclohexane droplet and diffusion coefficient can be found in the appendix D. The higher diffusion coefficient of limonene microemulsions would suggest a slightly higher number of collisions. The larger droplets for cyclohexane mean collisions are more likely to occur. The two opposing effects effectively cancel each other out with respect to micellar kinetics. The faster micelle exchange kinetics for cyclohexane microemulsions must be a result of another phenomena.

Unlike limonene microemulsions, there seems to be a sharper increase from 15–25 °C than from 25–35 °C. The Arrhenius plot in figure 6.7 and comparison of the activation energies in table 6.3 show that cyclohexane microemulsion micelle exchange has a greater dependance on temperature than limonene microemulsion. It could be postulated that there is an additional characteristic of limonene microemulsions, for example a difference in morphology, creating an additional barrier to micelle exchange and less dependence on temperature.

6.4 Methyl Laurate microemulsion FRET experiments

To investigate this solvent effect on micelle exchange further, methyl laurate was chosen as an additional solvent for study. Methyl laurate has been studied by Flotek due to its similar phase behaviour and surface tension to limonene microemulsions upon dilution [19].

Methyl laurate microemulsions were prepared in the same way as limonene microemulsions with the weight fraction of limonene replaced by methyl laurate. Figure 6.8 is an example of a FRET experiment with methyl laurate microemulsions.

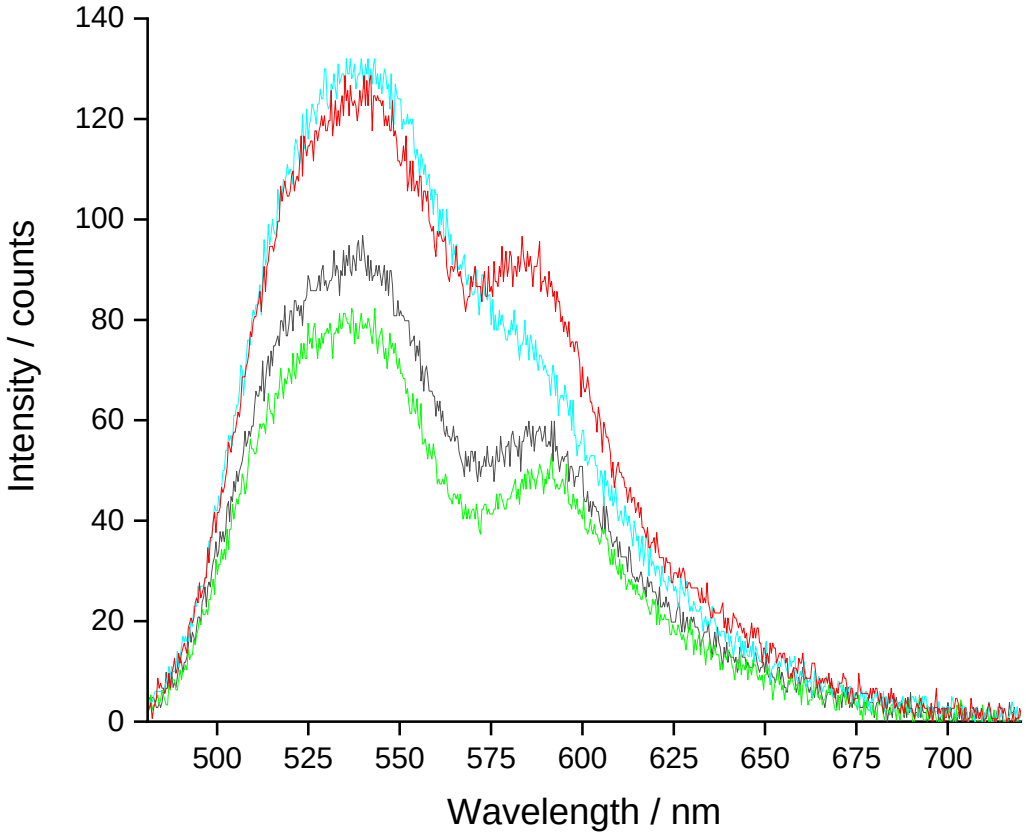

Figure 6.8: 2 mM methyl laurate microemulsion FRET experiment at 25 °C. NBD-PE 1% by mole of $C_{12}E_7$, Rh-PE 0.5% by mole of $C_{12}E_7$. Black line indicates the solution at equilibrium before mixing, the green line is after 20 ms, the cyan line after 1 minute and red line after 30 minutes.

The NBD-PE emission appears to increase over time, contrary to the expected trend for FRET. The Rh-PE peak at long times has the same intensity relative to the NBD peak as it does at short times. At intermediate times, the Rh-PE peaks disappeared (cyan spectrum). The reason for this unexpected behaviour was subsequently diagnosed to a leak in the cell (see §3.5), which led to fresh NBD-PE or Rh-PE solutions replenishing the cell contents on the timescale of the experiment. Nevertheless, the absence of an increase in the Rh-PE peak with time and the

absence of the characteristic shoulder peak between 630–660 nm due to Rh-PE emission for any scan shows that no FRET is occurring even after 30 minutes. The red spectrum at 30 minutes shows the characteristic dip at 575 nm arising from absorption of the NBD-PE emission by Rh-PE in other micelles and the peak seen at 590 nm is just the NBD-PE signal to the long-wavelength side of the Rh-PE absorption.

One possible explanation for the lack of FRET is that hydrolysis of methyl laurate formed lauric acid, which would ionise in dilute solution to give laurate ions. Laurate is a soap and could co-adsorb with $C_{12}E_7$ at the micellar interface, charging the micelles. At low ionic strengths, there would then be a strong double layer repulsion between micelles, inhibiting the formation of transient dimers and thus preventing FRET. If this hypothesis is correct, adding salt to screen the electrical double layer repulsions should cause FRET to be observed again. Figure 6.9 shows FRET experiments with methyl laurate microemulsions in the presence of 100 mM NaCl. The addition of NaCl shows some FRET over a long period of time, with the addition of salt highlighting how slow the exchange is compared with previous oils.

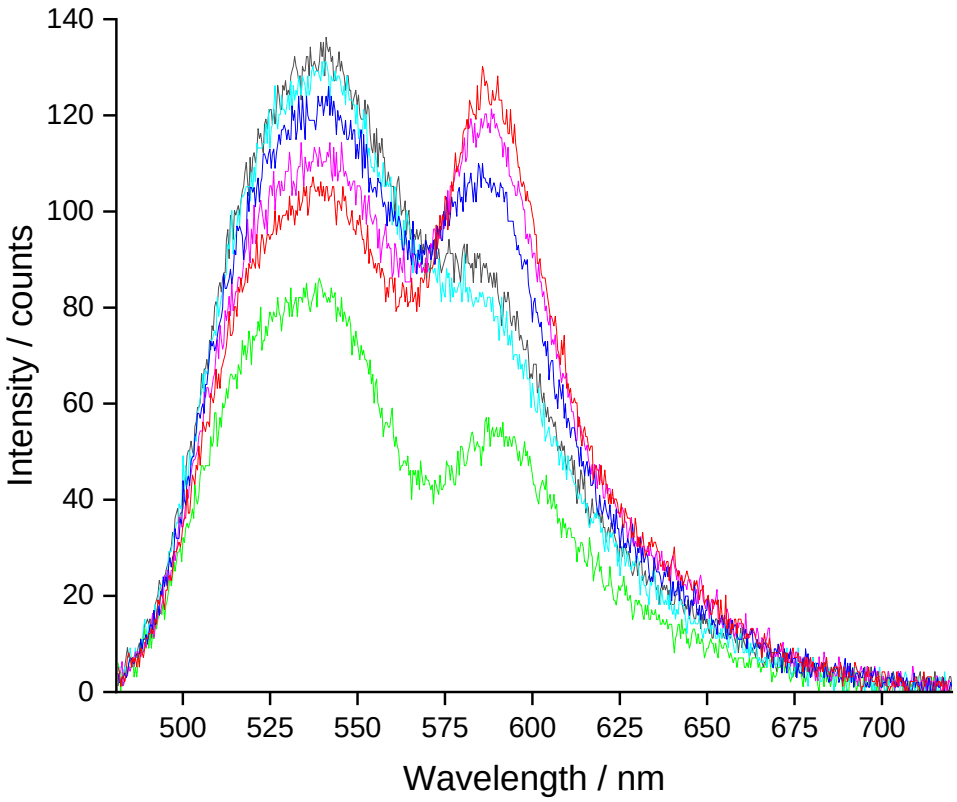

Figure 6.9: 2 mM methyl laurate microemulsion FRET experiment with 100 mM NaCl at 25 °C. NBD-PE 1% and Rh-PE 0.5% by mole of $C_{12}E_7$. Black line indicates solution at equilibrium before mixing, the green line is after 40 ms, the cyan line after 1 min, blue line after 5 mins, pink line after 15 mins and red line after 30 mins.

Figures 6.8 and 6.9 show strange behaviour not seen with previous experiments. The sudden drop in intensity, then increase over time for both probes is surprising. Treating the solution with 100 mM NaCl appears to have some indication of FRET and over a longer period the NBD-PE appears to have displaced the solution. Formation of lauric acid did not appear to be cause for the surprising trends observed or preventing FRET.

The purity of methyl laurate was tested using ^{1}H NMR. The NMR results of methyl laurate showed peaks that could not be assigned to methyl laurate, shown in the appendix D. It was deduced that there was some degree of contamination with the methyl laurate provided. The NMR did not show any formation of lauric acid. It was also thought there was some degree of degredation of methyl laurate occuring over time in the stock solutions.

Fresh stock solutions were made with pure methyl laurate(Sigma-Aldrich, 99.5% purity) verified by ^{1}H NMR. A typical attempt for FRET can be seen in figure 6.10 for the fresh solution.

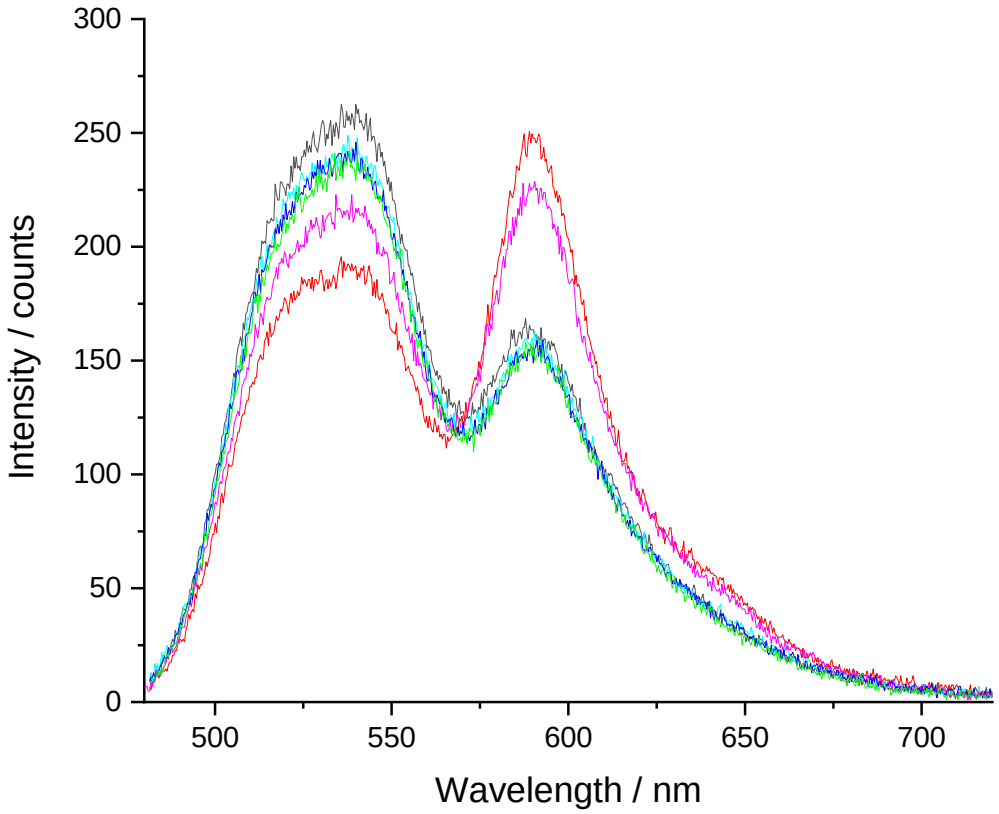

Figure 6.10: 2 mM methyl laurate microemulsion FRET experiment with 100 mM NaCl at 25 °C. Integration time 100 ms. NBD-PE 1% by mole of $C_{12}E_7$, Rh-PE 0.5% by mole of $C_{12}E_7$. Black line indicates solution at equilibrium before mixing, green line is the first scan after mixing at 100 ms, the blue line is after 1 s, the cyan line after 1 minute, the pink line after 30 mins red line after 1 hour.

There does appear to be FRET over a long period of time from the appearance of the shoulder peak at 630–660 nm and change in peak intensities over time. However, the absence of an isosbestic point and the increase in the NBD-PE peak over time indicates that there is still some leakage of solution being replaced by NBD-PE from one of the syringes.

The results in figure 6.10 show for methyl laurate microemulsions there is a barrier to exchange giving much slower FRET kinetics than seen before. The progression of FRET was analysed using factor analysis for the slow kinetics. The best fit was a linear fit for the loading data, suggesting zero order rate kinetics, the observed rate kinetics can be found in table 6.5. It should be noted there are large errors in the fit due to limited data points, the data was not taken continously after 1 minute to mitigate an unreadable sized data file.

Table 6.5: Observed rate constant for 2 mM methyl laurate microemulsion FRET at 25 °C.

Surfactant concentration / mM	NBD-PE k_{obs} / s^{-1}	Rh-PE k_{obs} / s^{-1}
2	2.8×10^{-4}	2.8×10^{-4}

Comparing the results in table 6.5 to the results in table 6.2. The observed rate constant for micelle exchange with methyl laurate microemulsions is ~20 000 times slower than cyclohexane microemulsions and ~400 times slower than limonene microemulsions at 2 mM surfactant concentration and 25 °C. The leak was discovered after the methyl laurate experiments were complete but, given the very slow kinetics, I decided not to repeat the experiments.

Conclusion

The study to change the oil solvent has given some interesting and thought-provoking results. The scale of contrast in the observed kinetics for FRET between a cyclohexane microemulsion and limonene microemulsion is a surprising result, which cannot be explained fully from my current study. The methyl laurate experiments did exhibit very slow exchange kinetics when salt was introduced. The use of salt in a charged micelle study given in chapter 7 was partly inspired by the trials of methyl laurate.

I was successfully able to use the stopped-flow FRET procedure for different microemulsion systems and further studies using this system can be confidently implemented. The role of oil solvent in a microemulsion system should be explored further if as there could be more insightful information gained for oil solvents with differing phase behaviour, either from additional functional groups or relative viscosity.

The comparison of exchange kinetics for different oils has been shown successfully for limonene and cyclohexane. This could be extended for other oils, such as BTEX chemicals to determine if there is any correlation with comparative studies of different oils efficacy for oil removal in microemulsion systems [9], [10]. By comparing other solvents there can be further justification to the choice of limonene over other suitable solvents, the performance of the limonene is comparable with cyclohexane and as limonene is a biodegradable solvent would be a more suitable choice for formulators as we continue to transition to net-zero.

References

[1] H. Liu, P. Zhou, Z. Wu, S. Chen, and C. Ding, “Solubilization Behavior of Organic Mixtures in Optimum Winsor Type III Microemulsion Systems of Sodium Dodecyl Sulfate,” *Journal Surfactants Deterg*, vol. 21, no. 4, pp. 497–507, Jul. 2018, doi: 10.1002/JSDE.12053.

[2] R. Sripriya, K. Muthu Raja, G. Santhosh, M. Chandrasekaran, and M. Noel, “The effect of structure of oil phase, surfactant and co-surfactant on the physicochemical and electrochemical properties of bicontinuous microemulsion,” *Journal Colloid Interface Sci*, vol. 314, no. 2, pp. 712–717, Oct. 2007, doi: 10.1016/J.JCIS.2007.05.080.

[3] T. Zhu *et al.*, “Advances of microemulsion and its applications for improved oil recovery,” *Adv Colloid Interface Sci*, vol. 299, p. 102527, Jan. 2022, doi: 10.1016/J.CIS.2021.102527.

[4] V. C. Santanna, F. D. S. Curbelo, T. N. Castro Dantas, A. A. Dantas Neto, H. S. Albuquerque, and A. I. C. Garnica, “Microemulsion flooding for enhanced oil recovery,” *Journal Pet Sci Eng*, vol. 66, no. 3–4, pp. 117–120, Jun. 2009, doi: 10.1016/J.PETROL.2009.01.009.

[5] A. Bera, T. Kumar, K. Ojha, and A. Mandal, “Screening of microemulsion properties for application in enhanced oil recovery,” 2013, doi: 10.1016/j.fuel.2013.12.051.

[6] H. Yang *et al.*, “Low-Cost, High-Performance Chemicals for Enhanced Oil Recovery,” *Proceedings - SPE Symposium on Improved Oil Recovery*, vol. 2, pp. 1474–1497, Apr. 2010, doi: 10.2118/129978-MS.

[7] J. Mariyate and A. Bera, “A critical review on selection of microemulsions or nanoemulsions for enhanced oil recovery,” *Journal Mol Liq*, vol. 353, p. 118791, May 2022, doi: 10.1016/J.MOLLIQ.2022.118791.

[8] P. Kamranfar and M. Jamialahmadi, “Effect of surfactant micelle shape transition on the microemulsion viscosity and its application in enhanced oil recovery processes,” 2014, doi: 10.1016/j.molliq.2014.07.009.

[9] Z. Zhang, A. Perrard, S. Trabelsi, and S. L. Biswal, “Evaluation of Asphaltene Remediation Using Microemulsion Formulations in a Porous Media Microfluidic Device,” *Energy and Fuels*, vol. 35, no. 14, pp. 11162–11170, Jul. 2021, doi: 10.1021/ACS.ENERGYFUELS.1C00483/SUPPL_FILE/EF1C00483_SI_001.PDF.

[10] H. W. Hernandez, W. Ehlert, and S. Trabelsi, “Removal of crude oil residue from solid surfaces using microemulsions,” *Fuel*, vol. 237, no. July 2018, pp. 398–404, 2019, doi: 10.1016/j.fuel.2018.10.035.

[11] R. A. Clará, A. C. G. Marigliano, and H. N. Sólimo, “Density, viscosity, and refractive index in the range (283.15 to 353.15) K and vapor pressure of α-pinene, d-limonene, (±)-linalool, and citral over the pressure range 1.0 kPa atmospheric pressure,” Journal Chem Eng Data, vol. 54, no. 3, pp. 1087–1090, Mar. 2009, doi: 10.1021/JE8007414.

[12] “Dynamic Viscosity of Cyclohexane from Dortmund Data Bank.” http://www.ddbst.com/en/EED/PCP/VIS_C50.php (accessed Sep. 22, 2023).

[13] P. Wu, L. Zhang, S. Zhao, C. Wang, Y. Guo, and W. Fang, “Density and Viscosity of the Ternary System Pinane + n-Dodecane + Methyl Laurate and Corresponding Binary Systems at T = 293.15−333.15 K,” Cite This: J. Chem. Eng. Data, vol. 66, pp. 2706–2716, 2021, doi: 10.1021/acs.jced.1c00057.

[14] K. A. Lewis, J. Tzilivakis, D. J. Warner, and A. Green, “An international database for pesticide risk assessments and management,” Human and Ecological Risk Assessment, vol. 22, no. 4, pp. 1050–1064, May 2016, doi: 10.1080/10807039.2015.1133242.

[15] D. Instruments GmbH, “Surface tension values of some common test liquids for surface energy analysis”, Accessed: Sep. 22, 2023. [Online]. Available: www.dataphysics-instruments.com

[16] L. Delforce *et al.*, “Fast Prediction of the Equivalent Alkane Carbon Number Using Graph Machines and Neural Networks,” vol. 7, pp. 38869–38881, 2022, doi: 10.1021/acsomega.2c04592.

[17] J. Kestin, M. Sokolov, and W. A. Wakeham, “Viscosity of liquid water in the range −8 °C to 150 °C,” *J Phys Chem Ref Data*, vol. 7, p. 941, 1978, doi: 10.1063/1.555581.

[18] “Cyclohexane | C6H12 - PubChem.” https://pubchem.ncbi.nlm.nih.gov/compound/Cyclohexane (accessed Dec. 04, 2022).

[19] “US Patent for Diluted microemulsions with low surface tensions Patent (Patent # 11,180,690 issued November 23, 2021) - Justia Patents Search.” https://patents.justia.com/patent/11180690 (accessed Oct. 14, 2022).

Chapter 7 Effect of charge on micelle fusion kinetics

The effectiveness of surfactant flooding in mobilising oil and altering wettability can be affected by the salinity in the water or presence of salt in the shale formations. Surfactant adsorption, phase trapping and precipitation on the rock surface can lead to significant surfactant loss in enhanced oil recovery [1]. For a rock surface with a negative surface charge such as sandstone, controlling the charge of the micellar system would minimise adsorption to the surface and increase the efficacy of oil recovery. The salinity in water can influence the adsorption of the surfactant to the surface and stability of micellar formulation. ShamsiJazeyi, Verduzco and Hiraska found the presence of salt, in this case sodium polyacrylate, can reduce the adsorption of charged micelles on various rock formations [2]. By introducing charge to my limonene microemulsion system and subsequently adding salt, the effect of charge on micellar kinetic exchange can be studied and compared to the efficacy of surfactant systems in oil recovery.

Solvent effects and changes in temperature were shown to have significant effects on the kinetics of micelle fusion for non-ionic surfactants in micellar solution. Chapter 3 discussed the possibility of introducing repulsive forces between micelles by incorporating a small proportion of an ionic surfactant to slow down the fast exchange processes occurring when using pyrene as a fluorescent probe. The introduction of repulsive forces was ineffective since exchange occurred via diffusion of pyrene through the bulk solution, a process which is unaffected by the charge on the micelles. Addition of salt screens the electrical double layer repulsions between charged micelles. In Chapter 6, I suspected that microemulsions of methyl laurate might be changed due to lauric acid impurities and investigated the effect of adding salt on the kinetics of the FRET experiments. In this chapter I take a system that exhibits fast exchange kinetics due to micelle fusion/fission and explore the effect on the kinetics of adding charge to the micelles.

Colegate and Bain found non-ionic surfactants adsorb to the surface of a liquid jet at a diffusion-controlled rate [3]. Colegate and Bain were able to switch off micellar

adsorption through the incorporation of small amounts of ionic surfactant into the micelle and then switched micellar adsorption back on again through the addition of salt. Another study by Yan and Bain shows the adsorption kinetics of non-ionic micellar systems are sensitive to the introduction of charge in a similar way to Colegate and Bain [4]. By using surfactants with very low CMC's, Bain and Yan were able to gain insights into the mechanism of adsorption from a purely micellar perspective. The classic model for micelle growth and dissolution involves sequential monomer addition and loss, described by the Becker-Döring equations [5]. Aniansson and Wall took this a step further for small perturbations from equilibrium, with two well-separated relaxation times [6]. The first fast relaxation is associated with the exchange of monomers between micelles and is largely diffusion-controlled. The slow relaxation involves the complete breakdown of micelles into monomers. Bain and Yan propose an alternative mechanism for micelle breakdown whereby micelles fuse together followed by monomer loss.

By selectively adding charge to the micelles, Yan and Bain were able to discriminate between possible adsorption mechanisms. Bain and Yan found that adding small amounts of an ionic surfactant, the rate of adsorption for non-ionic surfactant reduces dramatically. Adding low concentrations of salt (a few millimolar) reversed the repulsive screening from ionic surfactants and allowed the charged micelles to adsorb without breaking down into monomers. Bain and Yan modelled the charge distribution as a Poisson distribution. Their model shows that the kinetics were consistent with only uncharged micelles adsorbing. Using Bain and Yan's results as a basis, I investigated how charging micelles may affect micelle fusion for limonene microemulsions. Y. He et al. discuss the adsorption and desorption energy barriers for macroscopic interfaces of surfactant solutions [7]. Y. He suggests that the introduction of repulsive forces leads to strong deviations in adsorption, with other barriers less easy to identify such as diffusion-controlled mechanisms. Addition of sufficiently small amounts of ionic surfactant does not affect the structure of our limonene microemulsions. Any significant changes in exchange kinetics of limonene microemulsions with charged micelles compared to previous studies can thus be ascribed to the electrostatic barrier introduced via addition of charge to the micelles. Varying the amounts of ionic surfactant added to the system allows us to look at the effect of varying the charge on the kinetics of micelle exchange.

7.1 Experimental details of charged micelle study

To charge micelles for my limonene microemulsion system I used sodium dodecyl sulphate (SDS) at three different concentrations of SDS, of 1, 2 and 5% of the total surfactant concentration. I attempted to reverse the repulsive shielding of SDS through the additions of millimolar concentrations of salt, following the example of Yan and Bain.

7.1.1 Distribution of SDS in micellar system

To understand the screening effect of SDS on my limonene microemulsions, it was necessary to calculate the distribution of SDS molecules between the bulk and micelles. Danov et al. studied the equilibrium between micelles and monomers in solutions of mixed surfactant systems [8]. Their study considered a number of models to describe the micelle-monomer equilibria for ionic surfactants and their mixtures based on charge and aggregation number. The most appropriate model for their study was a phase separation model, using chemical equilibrium relationships and supplemented by mechanical and mass balance equations. One key element of their study was to use the concept of Ninham and Mitchell on micelle interfacial tension for ionic-non-ionic mixtures [9]. The concept states that the repulsive electrostatic headgroup region is nullified by the attractive cohesive forces in the tail groups and the hydrophobic effect. The balance of the attractive and repulsive components implies the micelles are effectively in a tension free state with forces in equilibrium. Ninham and Mitchell give mathematical justification for this with their experimental studies on SDS micelles [9]. The jellium model is also used to calculate micelle charge [10], [11]. The jellium model describes the distribution of micelles as uniform with an average micellar concentration, the electric potential obeys a Poisson distribution of charge. Danov et al. show that the micelle formation of a mixture of surfactants follows the regular solution theory. For mixed micellar systems, a defining parameter of the system is the interaction parameter β, between non-ionic and ionic surfactants. The interaction parameter quantifies the level of interaction between a mixture of components, such as $C_{12}E_7$ and SDS. Sierra and Svensson studied the interaction of

mixed surfactant systems [12]. Sierra and Svensson found SDS monomers have a negative interaction parameter with non-ionic surfactants as did the study by Danov et al. [8], [12]. A negative interaction parameter indicates relatively favourable interaction between SDS monomers and non-ionic surfactants. The non-ionic head groups will shield the repulsion between the negative head groups in the micelle, creating a net interaction between the two types of molecules. Sierra and Svensson suggested at low surfactant concentration, SDS monomers would effectively be incorporated into the micelles of non-ionic surfactants, causing a decrease in the overall CMC of the surfactant system [12]. Danov et al. measured the effect of adding salt to mixed surfactant systems [8]. They found the presence of salt greatly affects the CMC of SDS. Their results show a CMC of ~1 mM for SDS in the presence of 10 mM NaCl in a mixed micelle system with non-ionic surfactants. The findings from Danov et al. and Sierra and Svensson have been used for this study to estimate the average number of solubilised SDS molecules in our microemulsion system. Using the theory expressed in the jellium model, the SDS molecules and their charge are evenly distributed amongst the micelles via a Poisson distribution.

The chemical potential of SDS monomers in an ideal dilute solution is given as,

$$\mu_{mon} = \mu_{mon}^{\ominus} + RT \ln\left(\frac{c_{mon}}{c_{cmc}}\right) \tag{7.1}$$

where c_{mon} is the monomer concentration, c_{cmc} is the CMC and $\mu_{mon}^{\ominus}$ is the chemical potential at the cmc.

The chemical potential of an SDS molecule in the micelle, assuming regular solution theory is,

$$\mu_{mic} = \mu_{mic}^{\ominus} + RT \ln x_{1,mic} + RT\beta x_{2,mic}^2 \tag{7.2}$$

where $\mu_{mic}^{\ominus}$ is the chemical potential of an SDS molecule in an SDS micelle and is equal to $\mu_{mon}^{\ominus}$ from the definition above. $x_{1,mic}$ is the mole fraction of SDS in the micelle and $x_{2,mic} = 1 - x_{1,mic}$ is the mole fraction of $C_{12}E_7$. β is the interaction parameter (scaled by $k_B T$).

The total SDS concentration in the system is,

$$c_{tot} = c_{mon} + x_{1,mic} c_{C_{12}E_7}(1 + x_{1,mic}) \tag{7.3}$$

where $c_{c_{12}E_7}(1 + x_{1,mic})$ is the total amount of surfactant in the micelles. Given that the monomer concentration of $C_{12}E_7$ is negligible due to its low cmc, we can assume all the $C_{12}E_7$ is in the micelles.

If δ is the percentage of SDS added to the $C_{12}E_7$ in molar terms, then $c_{tot} = \delta c_{c_{12}E_7}$

So (7.3) becomes

$$c_{mon} = \left(\delta - x_{1,mic}(1 + x_{1,mic})\right) c_{c_{12}E_7} \qquad (7.5)$$

At equilibrium, the chemical potential of the SDS in solution and in the micelles is the same. So, equating (7.1) and (7.2), recalling that the standard chemical potentials are equal in the solution and the micelle, and cancelling *RT* from both sides gives

$$\ln\left(\frac{c_{mon}}{c_{cmc}}\right) = \ln x_{1,mic} + \beta x_{2,mic}^2 \qquad (7.6)$$

Substituting c_{mon} from (7.5),

$$ln\left(\frac{\left(\delta - x_{1,mic}(1 + x_{1,mic})\right)c_{c_{12}E_7}}{c_{cmc}}\right) = ln\, x_{1,mic} + \beta(1 - x_{1,mic})^2 \qquad (7.7)$$

The mole fraction of SDS in the micelle as a fraction of the total micellar concentration $x_{1,mic}$ can be calculated by solving equation 7.7 for each value of δ and given in table 7.1. The interaction parameter, taken from literature gave a negative value for interactions between SDS molecules and $C_{12}E_7$ micelles. This indicates the mixing of the two monomers are energetically favourable as has been described earlier. With a synergy for mixing, the SDS molecules are more likely to be solubilised by my micelle system and more likely to create the screening effect seen by Bain and Yan.

Table 7.1: Addition of SDS to 2 mM limonene microemulsions by molar percentage. The c_{cmc} and β taken from the literature respectively [13] [8].

% SDS	δ	$c_{c_{12}E_7}$ / mM	c_{mon} / 10^{-3} mM	c_{cmc} / mM	β	$x_{1,mic}$
5	0.05	2	1.8	0.08	-0.8	0.047
2	0.02	2	0.7	0.08	-0.8	0.019
1	0.01	2	0.4	0.08	-0.8	0.0097

Comparing δ and $x_{1,mic}$ in table 7.1, the majority of the SDS molecules lie in the micelles but not all, if all of the SDS molecules were in the micelles δ and $x_{1,mic}$ would

be equal. Equation 7.8 can be used to calculate the average number of solubilised SDS molecule per micelle,

$$\bar{n} = x_{1,mic} \times \mathrm{N} \tag{7.8}$$

The aggregation number of the microemulsion is calculated to be 595 and the mole fraction of SDS in the micelle is given in table 7.2.

Table 7.2: The average number of solubilised SDS molecules per micelle $\bar{n}$ with its corresponding SDS concentration.

Concentration of SDS by mole of $C_{12}E_7$	Average number solubilised SDS molecules per micelle $\bar{n}$
5%	28
2%	11
1%	6

7.1.2 Materials

A stock of 2 mM limonene microemulsion was made in the same way as described in chapter 4. 5% 2% and 1% (by mole of $C_{12}E_7$) SDS was added to 2 mM limonene microemulsion sample tubes and stirred until dissolved. To treat the charged micelles with salt, samples of known volume of limonene microemulsion and SDS were transferred into a separate sample tube, 10 mM NaCl was added and stirred until dissolved. The stopped-flow FRET setup was the same as described in chapters 3 and 4. Quantitative analysis, as described in chapter 4, was undertaken for the case of 2 mM limonene microemulsions with 2% SDS with NaCl and the case of 1% SDS with and without NaCl.

7.2 Results and discussion of charged micelle study

7.2.1 5% SDS case

Figure 7.1 shows the FRET experiment for 2 mM limonene microemulsions with 5% SDS. There is no evidence of FRET throughout the experiment, moving from the initial black line (t_0) to the red line of 15 minutes. There was a slight decrease in the overall intensity at intermediate times (see dark blue scan after 5 mins), but the ratio of NBD-PE and Rh-PE emission does not change. We conclude that no significant micelle fusion is taking place on the experimental timescale.

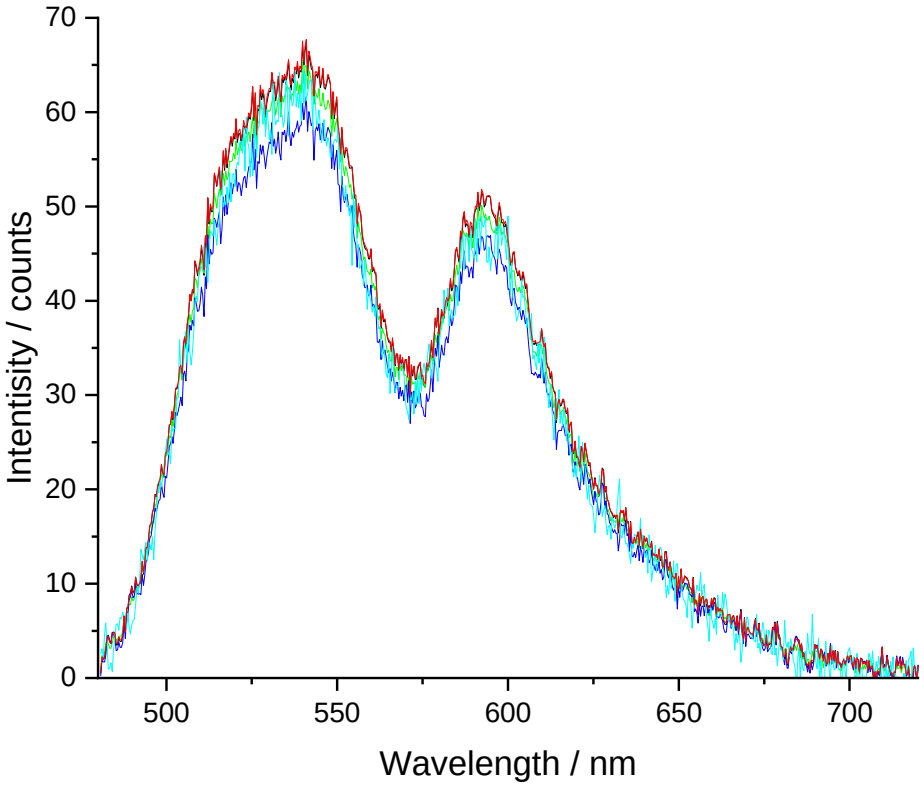

Figure 7.1: FRET data for 2 mM limonene microemulsion with 5% SDS. Excitation wavelength 337 nm, integration time 50 ms. Black line represents t_0, light green line is 1 min, dark blue line is 5 min, cyan line is 10 min and red line is 15 min.

Figure 7.2 shows the same FRET experiment as shown in figure 7.1 with the addition of 10 mM NaCl. Two scans have been shown to give a better insight to the slow kinetics occurring after addition of salt. After leaving the solution in the cell for 15 minutes, there is a slow exchange of NBD-PE with Rh-PE, giving early indications of FRET, but on a much slower timescale than previously seen for limonene microemulsion FRET experiments.

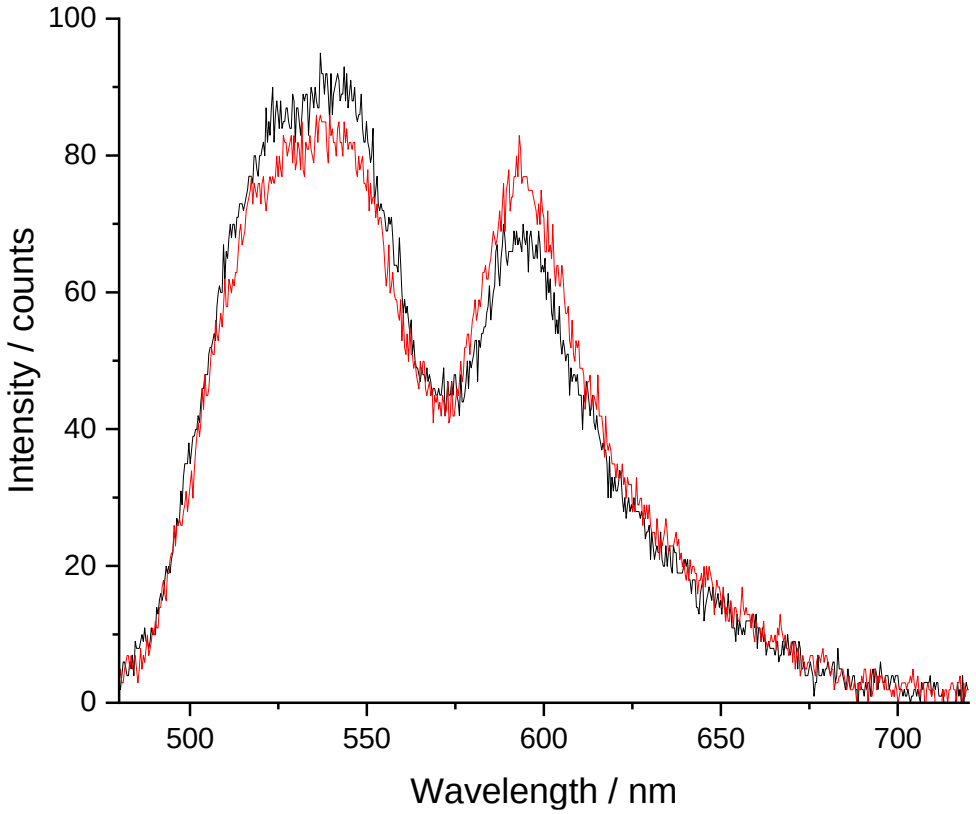

Figure 7.2: FRET data for 2 mM limonene microemulsion with 5% SDS and 10 mM NaCl. Excitation wavelength 337 nm, integration time 50 ms. Black line represents the first scan after mixing 50 ms and red line is 15 min.

When considering the lack of FRET in figure 7.1, using a Poisson distribution, the fraction of uncharged micelles (P_0) can be calculated using the known value of $\bar{n}$. P_0 for the 5% SDS case is calculated to be 6.9 x 10^{-13}, effectively all of the micelles are charged. The charged micelles create a repulsive barrier to micelle fusion. Without micelle fusion the NBD-PE molecules and Rh-PE will not be in the same micelle and so no FRET will occur. The addition of 10 mM NaCl, as seen in figure 7.2, does partially screen the repulsive forces but to a much lesser extent than in the experiments of Yan and Bain, since the microemulsion droplets have a much higher charge than the micelles in their experiments.

7.2.2 2% SDS case

Keeping the limonene microemulsion concentration at 2 mM, 2% SDS was added to the system. The average number of charged SDS molecules per micelle has decreased from 28 solubilised SDS molecules to 11 SDS molecules per micelle, with the fraction of uncharged micelles being 1.2×10^{-5}. Figure 7.3 shows the FRET run for 2 mM limonene microemulsions with 2% SDS.

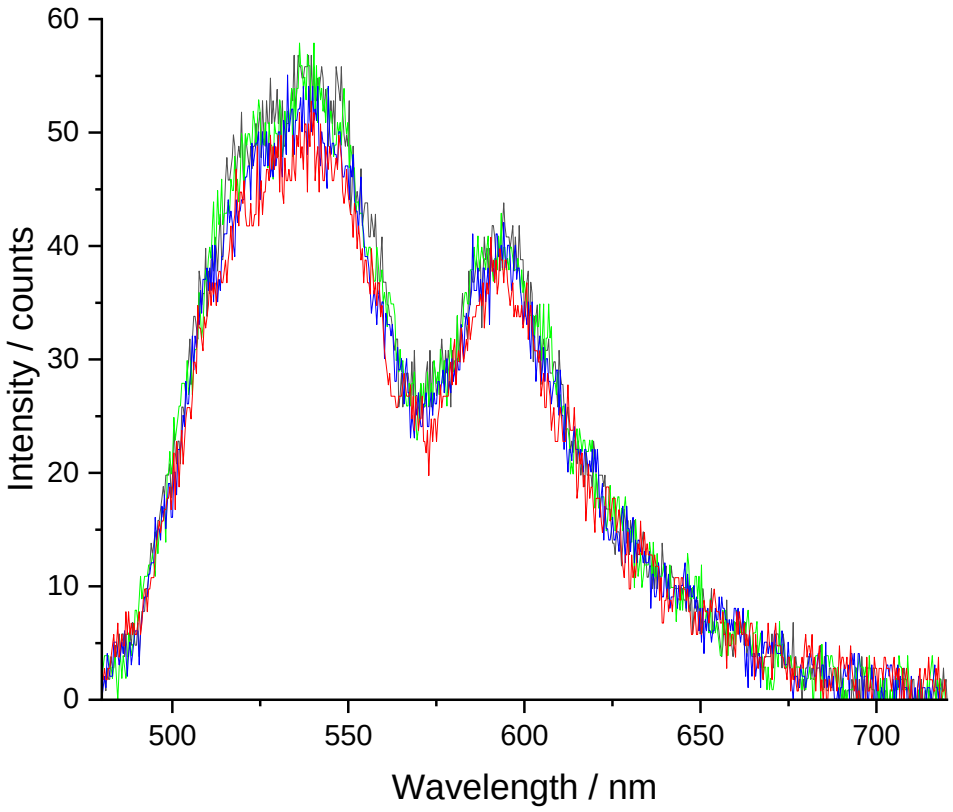

Figure 7.3: FRET data for 2 mM limonene microemulsion with 2% SDS. Excitation wavelength 337 nm, integration time 100 ms. Black line represents t_0, light green line is 1 min, dark blue line is 5 min, and red line is 10 min.

For the case of 2% SDS in the absence of salt no FRET is observed. Figure 7.4 shows the same experiment with 10 mM NaCl added. From inspection of the t_0 (black scan) and scan after 10 minutes (red scan) there has been successful FRET and thus an exchange of contents between the charged micelles. The NaCl in the system has reduced the electrostatic repulsive forces between the micelles, allowing micelle fusion and thus FRET. The timescale for FRET is still much slower than previous limonene FRET experiment with the absence of repulsive forces (see §7.2.4 below for a quantitative analysis).

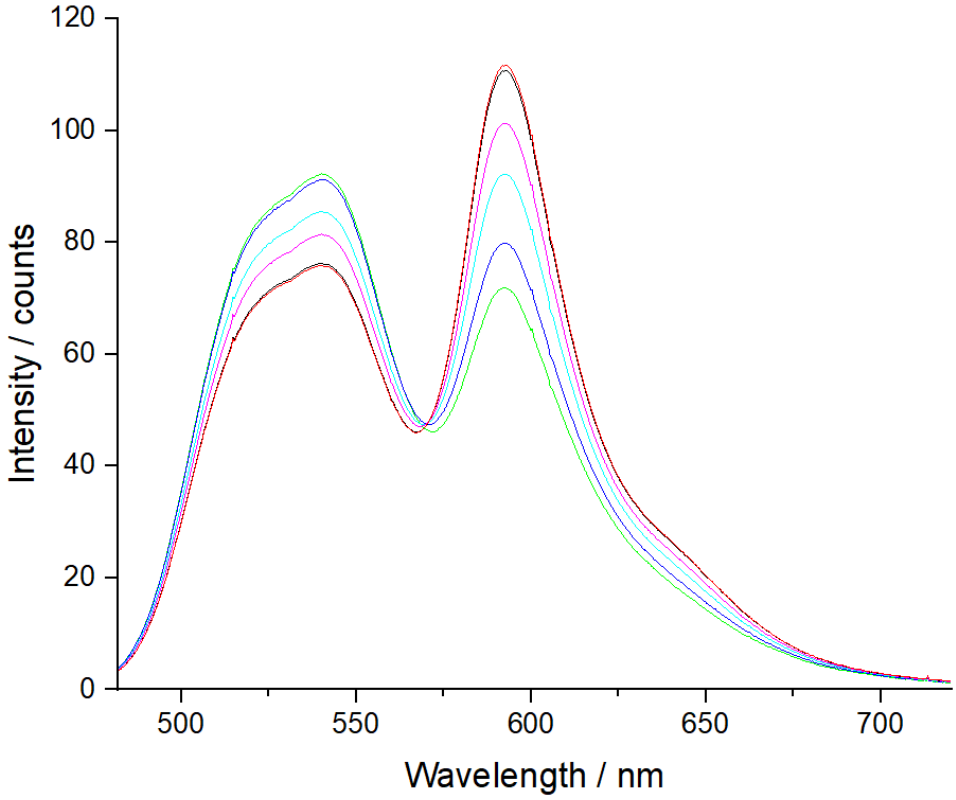

Figure 7.4: FRET data for 2 mM limonene microemulsion with 2% SDS and 10 mM NaCl. Excitation wavelength 337 nm, integration time 100 ms. Black line represents t_0, light green line is 100 ms, dark blue line is 1 min, cyan line is 3 min, 5 min is pink and red line is 10 min.

7.2.3 1% SDS case

SDS concentration was further reduced to a degree where P_0 is 3.1 x 10^{-3}. The case of 1% SDS is shown in the refined spectra in figure 7.5. FRET is observed on a timescale of 10 minutes, For the 1% SDS case, the presence of SDS is still slowing down micelle fusion, however the FRET shows that micelle fusion is occurring. Inspection of figure 7.6, with the addition of 10 mM NaCl, FRET occurs over a much faster timescale and exchange appears to have gone to completion after 15 seconds. The addition of NaCl gives a FRET timescale for limonene microemulsions with SDS similar to limonene microemulsion mixing in the absence of SDS.

In figure 7.5, an isosbestic point appears at ~575 nm, indicating a single kinetic pathway during the FRET experiment for limonene microemulsions with charged micelles. The addition of NaCl in figure 7.6 also shows an isosbestic point at ~575 nm similar to the cases seen for limonene microemulsion FRET in chapter 5.

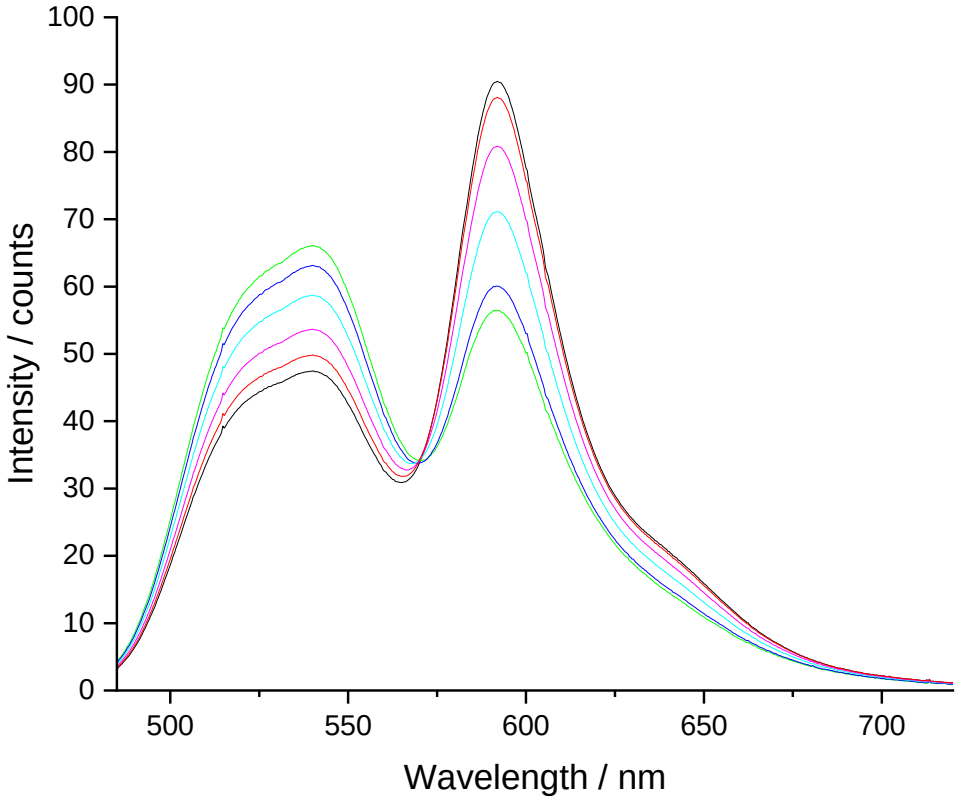

Figure 7.5: Refined FRET data for 2 mM limonene microemulsion with 1% SDS. Excitation wavelength 337 nm, integration time 50 ms. Black line represents t_0, light green line is 100 ms, dark blue line is 1 min, cyan line is 2 min 30 seconds, 5 min is pink and red line is 10 min.

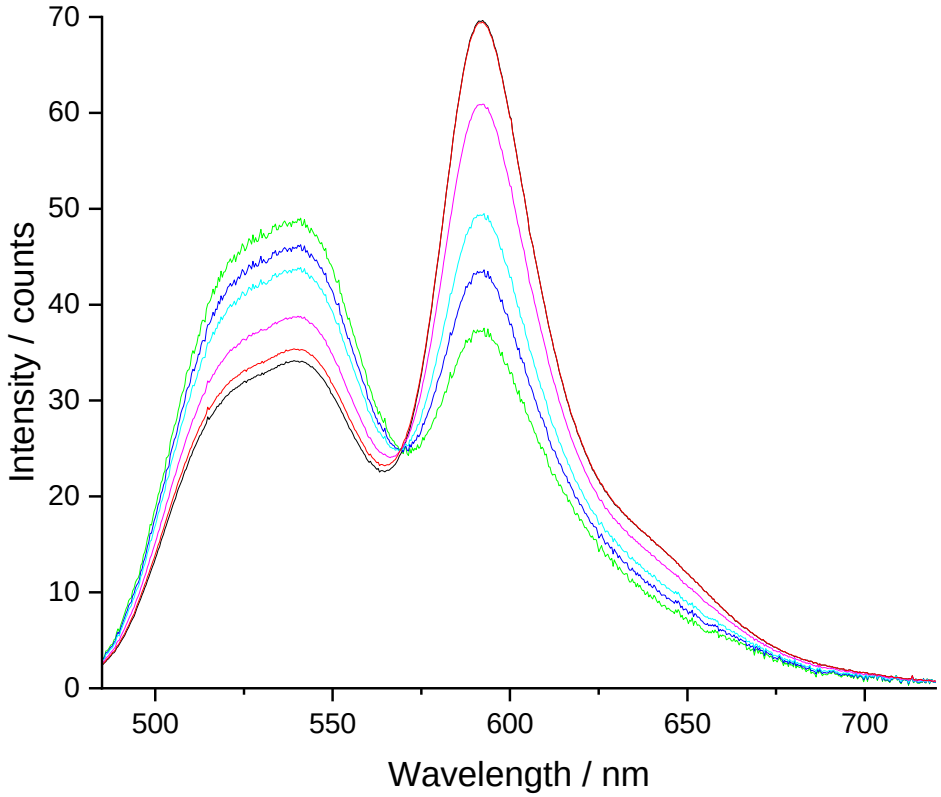

Figure 7.6: Refined FRET data for 2 mM limonene microemulsion with 1% SDS and 10 mM NaCl. Excitation wavelength 337 nm, integration time 50 ms. Black line represents t_0, light green line is 100 ms, dark blue line is 1 s, cyan line is 2 s, pink line is 5 s and red line is 15 s.

7.2.4 Quantitative analysis

After considering each concentration of SDS, I conducted quantitative analysis on the 2% SDS case with the addition of salt and the 1% SDS case with and without the addition of NaCl. The loading data for the case of 2% SDS with the addition of salt can be found in figure 7.7.

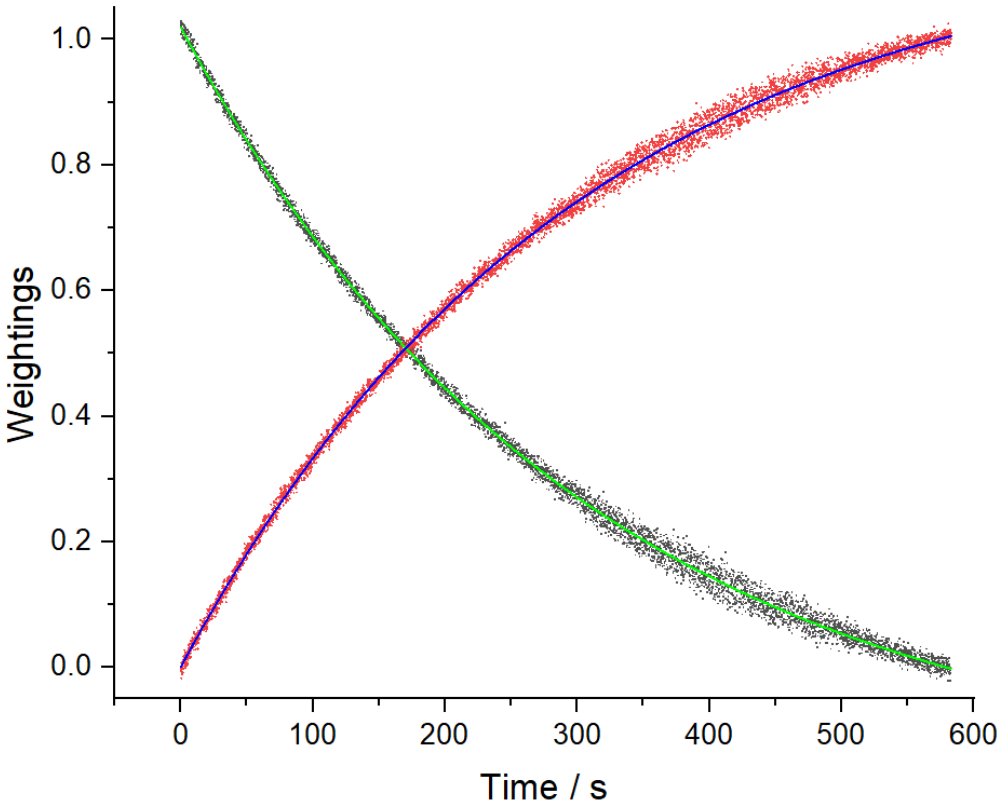

Figure 7.7: Loading data for 2 mM limonene microemulsion FRET with 2% SDS with 10 mM NaCl. The black data points represent NBD-PE weightings with a solid green line fit and red data points represent Rh-PE weightings with a solid blue fit.

The loading data for the case of 2 mM limonene FRET experiments of 1% SDS and 1% SDS with NaCl are shown in figures 7.8 and 7.9 respectively to serve as a comparison of a case with and without the addition of salt.

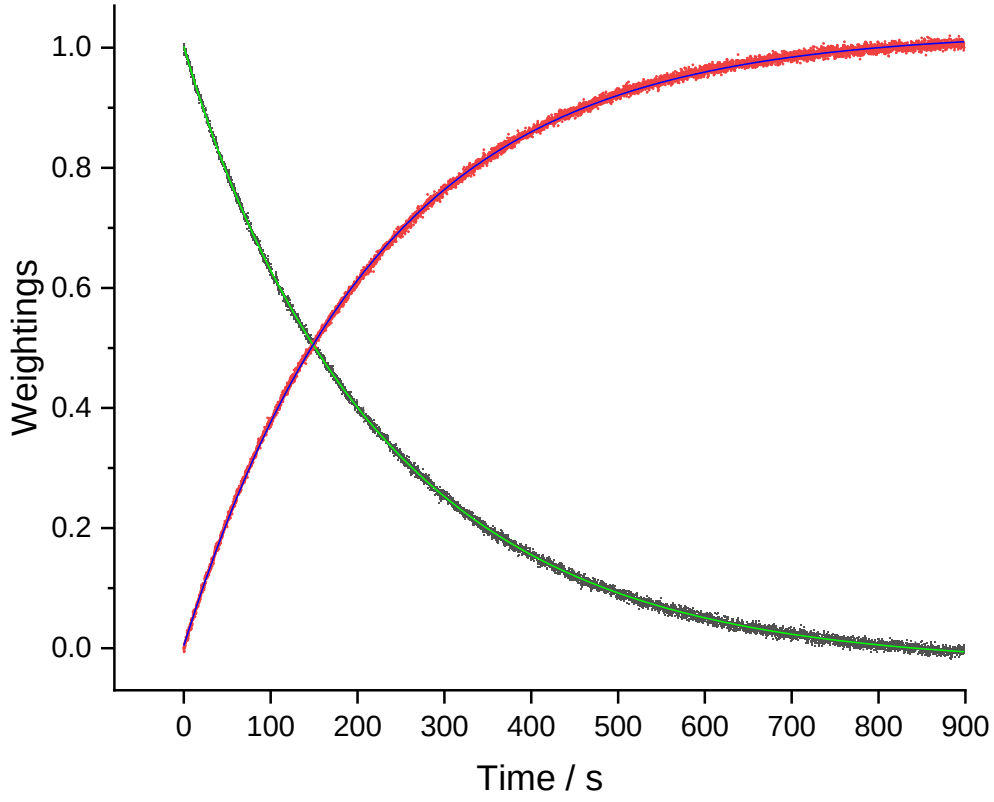

Figure 7.8: Loading data for 2 mM limonene microemulsion FRET with 1% SDS. The black data points represent NBD-PE weightings with a solid green line fit and red data points represent Rh-PE weightings with a solid blue fit.

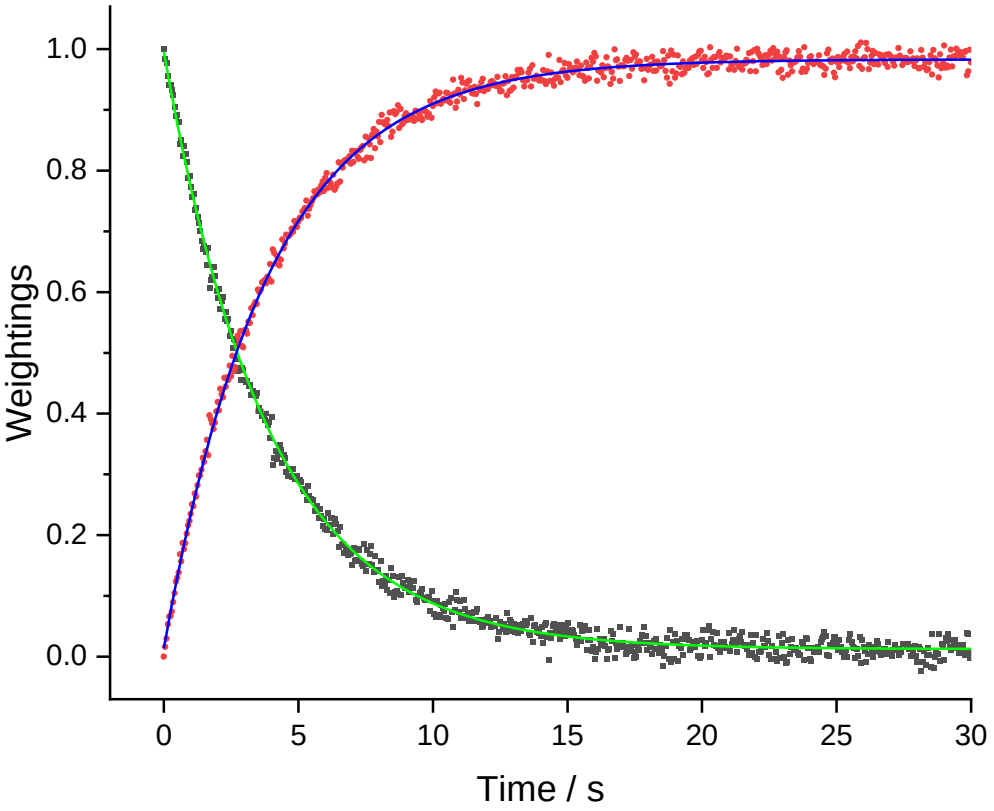

Figure 7.9: Loading data for 2 mM limonene microemulsion FRET with 1% SDS with 10 mM NaCl. The black data points represent NBD-PE weightings with solid green fit, red data points represent Rh-PE weightings with a solid blue fit.

The kinetics in figures, 7.7, 7.8 and 7.9 follows much of what has been observed for limonene microemulsion FRET, as FRET takes place, the emission of NBD-PE decreases and Rh-PE emission increases over time. The loading data for each case was fit with a single exponential decay to give observed rate constants for NBD-PE and Rh-PE. The nature of the exponential decay would indicate only one kinetic pathway contributing to FRET overall for both cases. The observed rate constants for FRET of limonene charged micelles and limonene charged micelles treated with NaCl is given in table 7.3.

Table 7.3: Observed rate constants for 2 mM limonene FRET charged micelle experiments with given errors. The 0% SDS case has been included from the results in chapter 5 for 2 mM limonene microemulsion FRET at 25 °C. * Corresponds to an upper limit for an observed rate constant for 2% SDS based off the change in observed rate constant from the 1% SDS case.

	Observed rate constant / 10^{-2} s^{-1}			
	Limonene microemulsion	Limonene microemulsion	Limonene microemulsion with NaCl	Limonene microemulsion with NaCl
% SDS	NBD-PE	Rh-PE	NBD-PE	Rh-PE
0	9.9 ± 0.3	9.9 ± 0.4	-	-
1	0.45 ± 0.01	0.47 ± 0.01	27.1 ± 0.7	27.2 ± 0.7
2	0.0003*	0.0003*	0.33 ± 0.01	0.33 ± 0.01
5	-	-	-	-

The observed rate constants for NBD-PE and Rh-PE for the limonene charged micelles correspond to each other within two standard deviations. For the case of 1% SDS, the repulsive forces seem to have been effectively ‘switched off’ by NaCl, increasing the observed rate constant by over 60-fold. The fraction of uncharged micelles has been calculated to be 3.1 x 10^{-3}. A further question can be asked, how would the rate of exchange be affected if exchange only occurred when one of the micelles was uncharged. As either micelle can be uncharged for this case, the fraction of uncharged micelles becomes 6.2 x 10^{-3}. The observed rate constant would theoretically be 166 times slower than when the repulsions were fully screened.

When comparing the 0% SDS case with the 1% SDS with NaCl it is surprising to see the observed rate constant is greater for the 1% SDS case. Upon further inspection of

the loading data and refined mixing data it does indicate faster FRET. There could be some charged impurities present in $C_{12}E_7$ which give rise to a repulsion. To prove this, an additional experiment adding salt to the 0% SDS case should be conducted. If there are charged impurities present the addition of salt will speed up the exchange.

The loading data and observed rate constants for the case of charged micelles and charged micelles treated with NaCl show a large dependence of micelle fusion on perturbation of the system. The addition of SDS successfully shows that the introduction of repulsive forces slows the micelle fusion process to a discernible level for limonene microemulsions at 2 mM surfactant concentration. Considering the Poisson distribution of SDS in the micelles, only charged micelles are affected for FRET. When moving to a higher number of populated SDS micelles, the higher the charge of the micelles and therefore the bigger effect the repulsive forces have on micelle fusion. This is evident seeing the slowing of FRET from 1–5% SDS. As the effect of repulsive forces increases with SDS concentration, it is necessary to increase the salt concentration to screen these repulsive forces. A further study to investigate the dependence of micelle fusion on salt concentration and how this relates to a typical oil shale. If an injection has high salinity, the effect of ionic impurities in the shale rock will be masked.

Conclusion

The charged micelle study using the FRET stopped-flow method successfully investigated further condition changes for microemulsion interactions, giving evidence of the versatility of the FRET stopped-flow method when used to study micellar interactions.

The relative coverage of swollen micelles with 5% to 1% SDS shows that the addition of charge has a large effect on micelle fusion. The screening of micelle fusion from repulsive forces can be overcome with a significant concentration of salt. The efficacy of oil recovery can be increased through careful control of charged molecules and salinity.

Further investigations, with higher concentrations of salt and changes in charged micelle concentration would be interesting to give a more definitive study on the effect of charge on the micelle fusion mechanism. This could be related to changes in salinity to the oil reservoir. Salinity changes are known to influence the efficacy of enhanced oil recovery [14], [15], particularly considering surfactant adsorption, using a saline solution may mitigate any repulsive forces found when using charged micelles for oil recovery. If successful, the introduction of a crude oil mimic would give formulators a greater understanding on whether charging micelles would affect the efficacy of oil recovery and give useful information for differing well conditions.

References

[1] A. Fatih Belhaj *et al.*, “The effect of surfactant concentration, salinity, temperature, and pH on surfactant adsorption for chemical enhanced oil recovery: a review,” *Journal Pet Explor Prod Technol*, vol. 10, pp. 125–137, 2020, doi: 10.1007/s13202-019-0685-y.

[2] H. ShamsiJazeyi, R. Verduzco, and G. J. Hirasaki, “Reducing adsorption of anionic surfactant for enhanced oil recovery: Part II. Applied aspects,” *Colloids Surf A Physicochem Eng Asp*, vol. 453, no. 1, pp. 168–175, Jul. 2014, doi: 10.1016/J.COLSURFA.2014.02.021.

[3] D. M. Colegate and C. D. Bain, “Adsorption Kinetics in Micellar Solutions of Non-ionic Surfactants,” 2005, doi: 10.1103/PhysRevLett.95.198302.

[4] C. Yan, A. Angus-Smyth, and C. D. Bain, “Adsorption kinetics of non-ionic surfactants in micellar solutions: effects of added charge,” *Faraday Discuss*, vol. 160, no. 0, pp. 45–61, Jan. 2013, doi: 10.1039/C2FD20118F.

[5] R. Becker and W. Döring, “Kinetische Behandlung der Keimbildung in übersättigten Dämpfen,” *Ann Phys*, vol. 416, no. 8, pp. 719–752, Jan. 1935, doi: 10.1002/ANDP.19354160806.

[6] E. A. G. Aniansson *et al.*, “Theory of the kinetics of micellar equilibria and quantitative interpretation of chemical relaxation studies of micellar solutions of ionic surfactants,” *Journal of Physical Chemistry*, vol. 80, no. 9, pp. 905–922, 1976, doi: 10.1021/j100550a001.

[7] Y. He, P. Yazhgur, A. Salonen, and D. Langevin, “Adsorption–desorption kinetics of surfactants at liquid surfaces,” *Adv Colloid Interface Sci*, vol. 222, pp. 377–384, Aug. 2015, doi: 10.1016/J.CIS.2014.09.002.

[8] K. D. Danov, P. A. Kralchevsky, and K. P. Ananthapadmanabhan, “Micelle–monomer equilibria in solutions of ionic surfactants and in ionic–non-ionic mixtures: A generalized phase separation model,” *Adv Colloid Interface Sci*, vol. 206, pp. 17–45, Apr. 2014, doi: 10.1016/J.CIS.2013.02.001.

[9] D. J. Mitchell and B. W. Ninham, “Electrostatic curvature contributions to interfacial tension of micellar and microemulsion phases,” *Journal of Physical Chemistry*, vol. 87, no. 16, pp. 2996–2998, 1983, doi: 10.1021/J100239A003/ASSET/J100239A003.FP.PNG_V03.

[10] B. Beresford-Smith, D. Y. C. Chan, and D. J. Mitchell, “The electrostatic interaction in colloidal systems with low added electrolyte,” *Journal Colloid Interface Sci*, vol. 105, no. 1, pp. 216–234, May 1985, doi: 10.1016/0021-9797(85)90362-5.4

[11] B. B.-S. And D. Y. C. Chan, “Electrical Double-layer Interactions in Concentrated Colloidal Systems,” *Faraday Discuss. Chem. Sac*, vol. 76, pp. 65–75, 1983.

[12] M. L. Sierra and M. Svensson, “Mixed Micelles Containing Alkylglycosides: Effect of the Chain Length and the Polar Head Group,” *Langmuir*, vol. 15, no. 7, pp. 2301–2306, Mar. 1999, doi: 10.1021/LA9804177.

[13] M. J. Rosen, *Surfactants And Interfacial Phenomena*, vol. 6. 2004. doi: 10.1002/0471670561.

[14] T. Zhang, yiteng Li, C. Li, S. Sun, and Y. Li, “Effect of salinity on oil production: review on low salinity waterflooding mechanisms and exploratory study on pipeline scaling”, doi: 10.2516/ogst/2020045ï.

[15] L. Yan, H. Aslannejad, S. M. Hassanizadeh, and A. Raoof, “Impact of water salinity differential on a crude oil droplet constrained in a capillary: Pore-scale mechanisms,” *Fuel*, vol. 274, p. 117798, Aug. 2020, doi: 10.1016/J.FUEL.2020.117798.

Chapter 8 Stopped-flow FRET experiments of micelles with a crude oil mimic

The stopped-flow FRET kinetic studies presented in previous chapters have investigated the pathways for an exchange of contents between micelles of the same composition i.e. limonene microemulsions exchanging with other limonene microemulsions. These studies provide a good foundation for understanding micellar interactions and suggest that other systems could be studied using the stopped-flow FRET method. This chapter investigates the feasibility of using the stopped-flow FRET method for interactions of micelles with crude oil emulsions. Crude oils are a complex mixture of organic compounds, with an emulsion droplet size much larger than in a microemulsion. Crude oil also contains aromatic compounds which are fluorescent, adding another degree of complexity to the stopped-flow FRET experiment. Therefore, I decided to attempt experiments with a crude oil mimic to determine if the current stopped-flow FRET setup could observe the exchange process between limonene microemulsion droplets and crude oil.

Methyl naphthalene and squalane were identified as possible oil mimics. Methyl naphthalene has the benefit of being neutrally buoyant in water, but it is also sufficiently soluble that there is likely to be exchange of the oil with the micelles through the solution on the experimental timescale, similar to the problem encountered when using pyrene as a fluorescent probe. Consequently, I concentrated on squalane, the structure of squalane can be seen in figure 8.1.

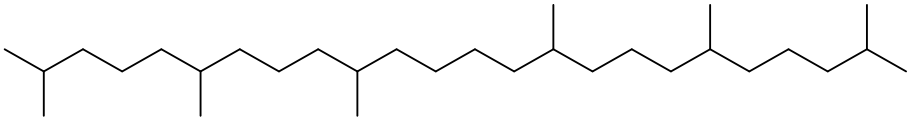

Figure 8.1: Chemical structure of a squalane molecule.

I relied on being able to make a fine enough emulsion that creaming would not be significant during the course of the mixing experiments or in the pump syringes. I monitored the scattering of the incident light at 468 nm during the FRET experiments to see if creaming and/or Ostwald ripening was occurring, both of which would affect the amount of scattered light from the emulsion.

Using an emulsion in the stopped-flow FRET experiment introduces an additional challenge: emulsions tend to be milky white dispersions which scatter light, preventing much of incident light from passing through the flow cell and preventing the fluorescence from reaching the optical fibre used for detection The concentration of squalane had to be carefully considered to maintain a stable emulsion, whilst allowing enough light to pass through the flow cell for measurement.

8.1 Squalane emulsion stock procedure / FRET experimental method

8.1.1 Squalane emulsion stock procedure

A squalane emulsion was made using an ultrasonic horn (sonics, VC505 model with 1/8-inch stepped microtip) for 1 minute keeping the amplitude at 30%. Squalane was kept at 10 mM, with NBD-PE at 1% by mole of $C_{12}E_7$ (2 mM) for the NBD-PE case and 0.5 % Rh-PE by mole of $C_{12}E_7$ for the case of Rh-PE. The solution appeared cloudy and remained cloudy throughout the duration of FRET experiments, without any visible creaming or phase separation.

8.1.2 Squalane emulsion FRET experimental setup

The experimental setup for squalane emulsion FRET experiments is the same as the FRET experiments discussed in previous chapters. Syringe A is filled with the squalane emulsion containing the donor probe (NBD-PE). Syringe B is filled with the micellar solution (with or without limonene) containing the acceptor probe (Rh-PE). Syringe A and syringe B are pneumatically mixed at a 1:1 ratio using the stopped flow device and the change in NBD-PE and Rh-PE emission intensity ratio over time indicates the rate of FRET. The opposing case with syringe A filled with micellar solution containing donor probe (NBD-PE) and squalane emulsion containing the acceptor probe (Rh-PE) was also conducted.

After initial trials, FRET experiments were conducted at room temperature, the excitation wavelength was 468 nm, integration time 200 ms and a total run time of 5 minutes.

The data were analysed as before with target factor analysis using the spectra at the beginning and end of the run as the two target factors. While neither of these spectra represents the case of no exchange or complete exchange, this does not matter for determining the first-order kinetics of exchange.

8.2 Squalane emulsion size distribution

To determine the processes occurring whilst in the flow cell it is useful to determine the size of our emulsions to ensure they are fine enough to prevent creaming, whilst remaining large enough act as a flat surface in relation to limonene microemulsion droplets at a microscopic level. Thus the exchange kinetics will also apply to the interaction of limonene microemulsions with oil in a shale or in a pore, not just an emulsion.

Dynamic light scattering (DLS) is the most common technique used for particle sizing. DLS does have a number of drawbacks to determine the size of our emulsion particles. For DLS measurements, the particle size is measured from changes in light scattering intensity from the Brownian motion of particles. If a sample is polydisperse, the larger particles will scatter light more intensely and dominate the results, not giving an accurate size of the whole sample.

Nanoparticle tracking analysis (NTA) is capable of particle size analysis from around 20–1000 nm. NTA also utilises the light scattering and Brownian motion to obtain the particle size distribution of a sample in liquid suspension. Unlike DLS, NTA does not measure the intensity of scattered light from a bulk sample but observes particle diffusion directly.

The sample is injected using a Hamilton syringe into a sample chamber. The sample chamber is illuminated by a laser beam. Particles in the path of the beam scatter the light and detected by a CMOS (Complementary Metal Oxide Semiconductor) camera. The CMOS camera records the particles and NTA software is able to identify and track individual particles moving under Brownian motion. By tracking the individual trajectory of a particle the NTA software gains information on the mean squared displacement. The mean squared displacement of the particle can be related to the diffusion coefficient D,

$$< x^2 >^{1/2} = 2\left(\frac{Dt}{\pi}\right)^{1/2} \quad (8.1)$$

The rms displacement can then be used to calculate the hydrodynamic radius of the particles from the Stokes-Einstein equation.

$$D = \frac{k_B T}{6\pi\eta_w r_h} \quad (8.2)$$

where r_h is the hydrodynamic radius.

8.2.1 Preparation of emulsion sample

Emulsions were prepared as described in section 8.1 and diluted with 0.1 mM surfactant package solution to the desired concentration range for NTA measurements, between 10^7 and 10^9 particles / ml. Dilution with 0.1 mM surfactant package instead of water keeps the surfactant concentration above the CMC.

8.2.2 Nanoparticle Tracking Analysis (NTA)

NTA measurements were performed with a NanoSight LM14-HS (Malvern Panalytical), equipped with a 405 nm laser. The samples are injected into the sample chamber using luer-lock syringes (Hamilton) until the solution filled the chamber.

Once the sample is loaded into the chamber and laser powered on, it is important to define a suitable region of interest for measurements. There is a visual reference in the instrument known as the ‘thumbprint’ aptly named for its likeness to a thumb shape. The thumbprint is shown in figure 8.2 and can be located manually by adjusting the stage. The best position for capturing images is as close to the thumbprint as possible without interference from the thumbprint region.

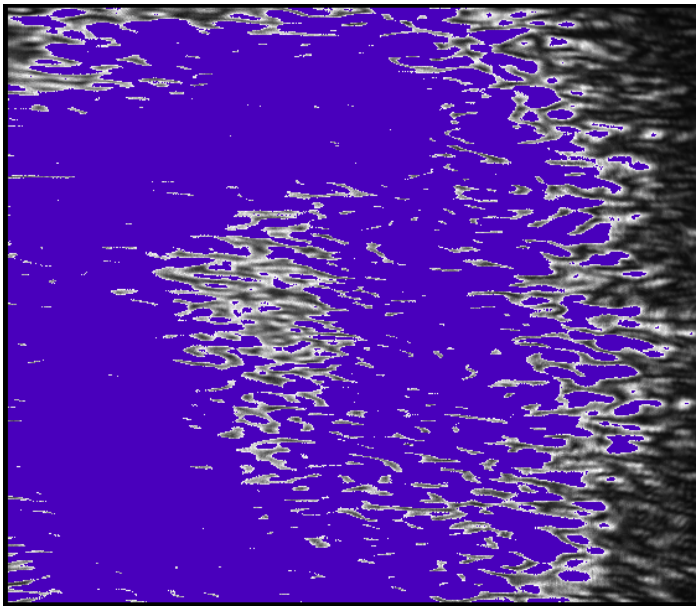

Figure 8.2: Thumbprint region of the sample using the NTA 3.4 software.

Once a region of interest is found away from the thumbprint region, the camera level settings is adjusted so that the image is not saturated with light. Figure 8.3 gives an example of our sample with acceptable levels of light for analysis.

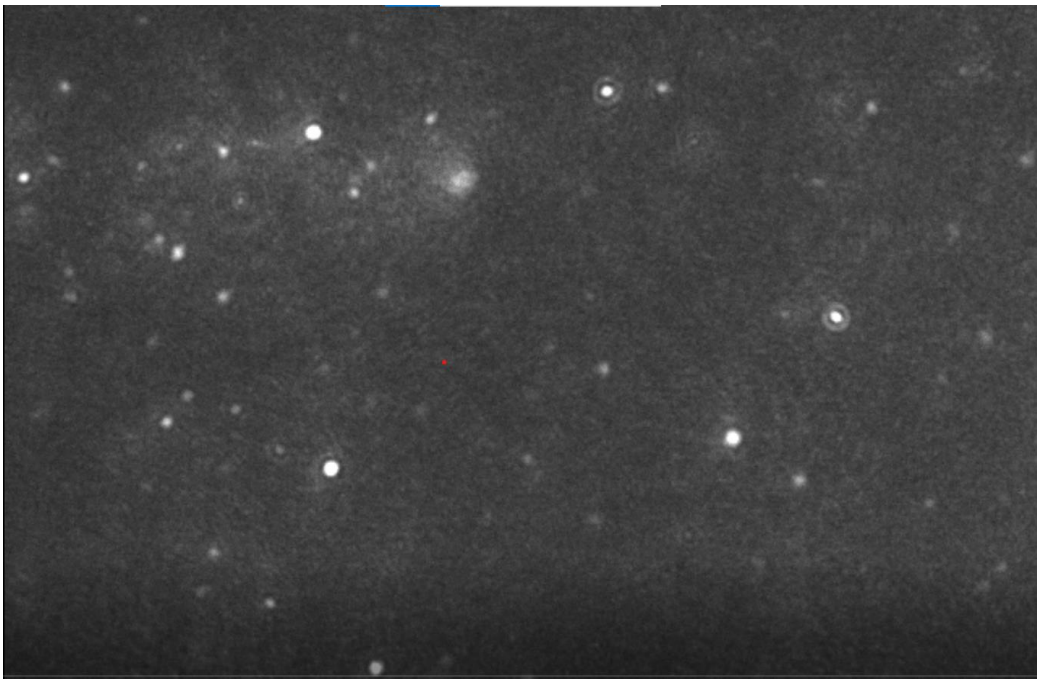

Figure 8.3 : Focussed image of sample used for particle size analysis.

Measurements were performed at room temperature and recorded by the Nanosight software, NTA 3.4. The samples were measured for 60 s with manual screen gain and shutter modes. The mean size of the particles was calculated after 5 consecutive measurements, pushing the sample through the chamber after each measurement.

8.2.3 Results and Discussion

The results for a squalane emulsion diluted 40-fold can be seen in figure 8.3. Of the five individual runs, the mean size of the emulsion particles was determined to be is 213 nm. The concentration was in an acceptable range for analysis. The red, cyan and light green runs show that the emulsion drops are polydisperse with distinct shoulder peaks and additional smaller peaks at larger and smaller size. The observable emulsion droplets have a diameter in the range of 200 nm, which is an order of magnitude larger than the micelles or microemulsion droplets.

These droplets are small enough that creaming will not occur on the experimental timescale for FRET runs. The creaming velocity can be calculated using the Stokes equation,

$$v = \frac{2gr^2(\rho_w - \rho_o)}{9\eta} \tag{8.3}$$

where g is the acceleration due to gravity, r is the radius of the emulsion particle, ρ_w is the density of water, ρ_o is the density of the oil. The creaming velocity was calculated to be 4×10^{-9} ms^{-1}. For a typical run time of 5 minutes a typical emulsion particle would have only travelled ~ 1 μm – much less than the distance it would have diffused due to Brownian motion

The scattered light at 468 nm showed negligible change during the FRET experiments described in §8.3, consistent with an absence of creaming or Ostwald ripening (which coarsens the emulsion and changes its scattering properties).

The difference in size between the emulsion droplets and the micelle or microemulsion droplets means that most of the surfactant in my experiments is in the micelles rather than coating the emulsion droplets. Consequently, the FRET experiments are largely probing the dye composition in the micelles.

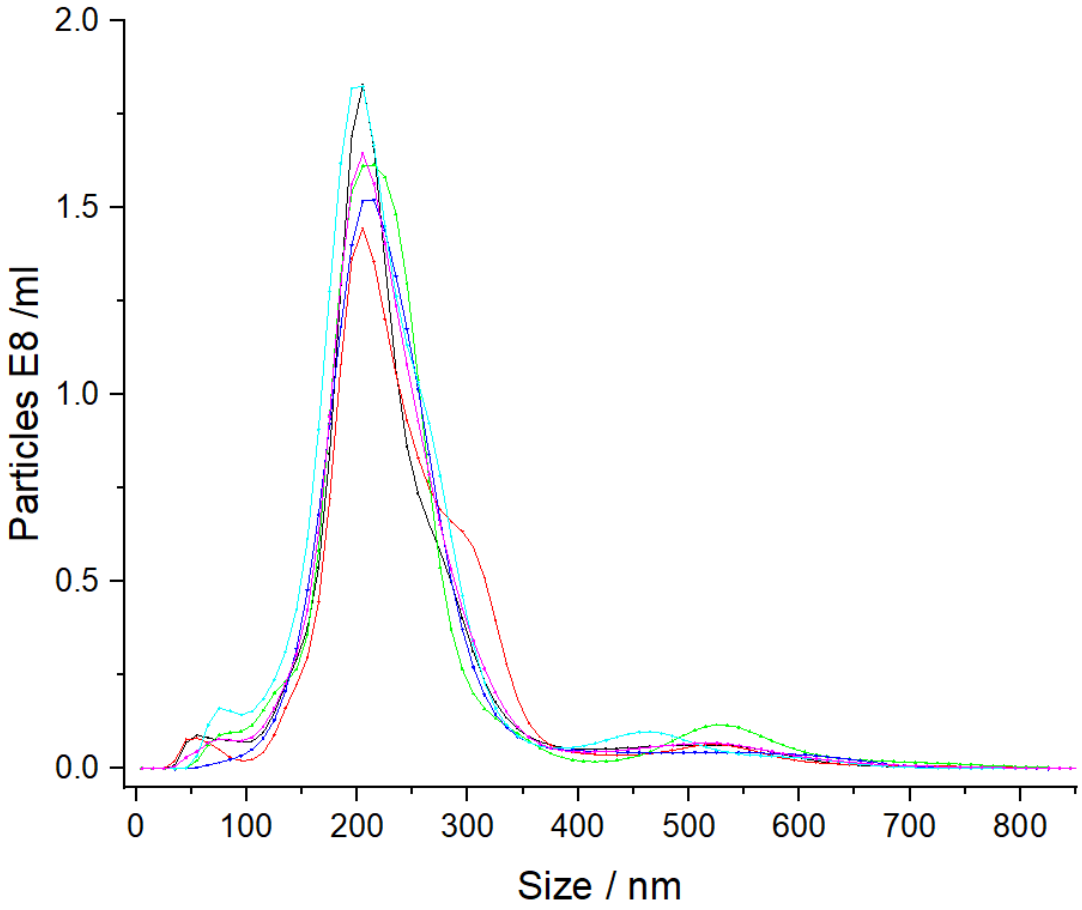

Figure 8.4: Size distribution of 1-40 diluted 10 mM squalane emulsion with 0.1 mM surfactant package.

8.3 Squalane emulsion FRET experiments

8.3.1 Initial trials

Initial trials were conducted for a 10 mM squalane emulsion mixed with 2 mM limonene microemulsion (Figure 8.5). The kinetics are much slower for mixing an emulsion with a microemulsion than for mixing two 2-mM microemulsions, evident from the cyan line at 1 minute showing 60–70% progression for Rh-PE intensity increase, whereas in figure 5.2b in section §5.1 kinetics were complete after 30 seconds.

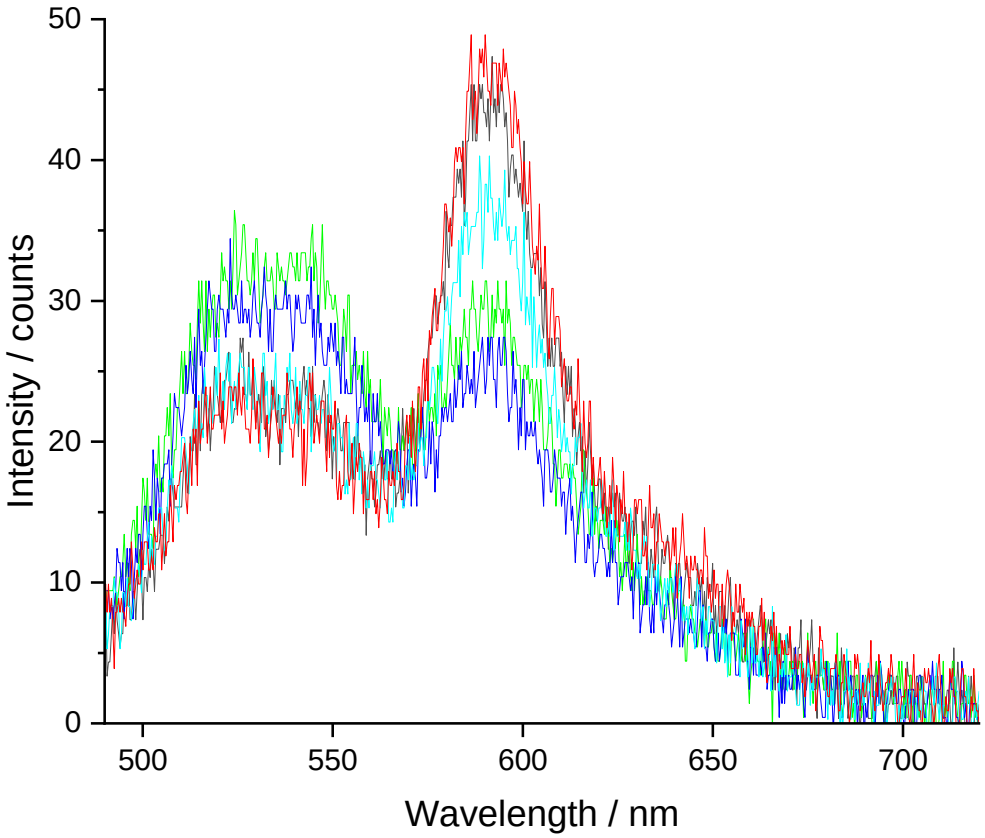

Figure 8.5: FRET experiment for 10 mM squalane emulsion with NBD mixed with 2 mM limonene microemulsion filled with Rh-PE. Black line indicates (t0), light green is 400 ms, dark blue line is 1 s, cyan is 1 min, red is 5 mins.

The data in figure 8.5 is noticeably noisier than experiments with microemulsions and surfactant package interactions previously studied, despite the increase in integration time, due to the scattering of incident light and fluorescence by the emulsion droplets. There is a skew in the baseline arising from additional scattering in the system. Treatment of the skew in the baseline has been discussed in §4.3.1. The skew in the baseline was found not to have an impact on kinetic results.

The incident light scattering as a function of time is shown in figure 8.6. It was important to monitor the change in scattering alongside the FRET. If light scattering changes during the experiment, it will affect the intensity of both the NBD-E and Rh-PE fluorescence. Furthermore, if a change in scattering is due to creaming or Ostwald ripening then the concentration and size distribution will change, which will affect the kinetics.

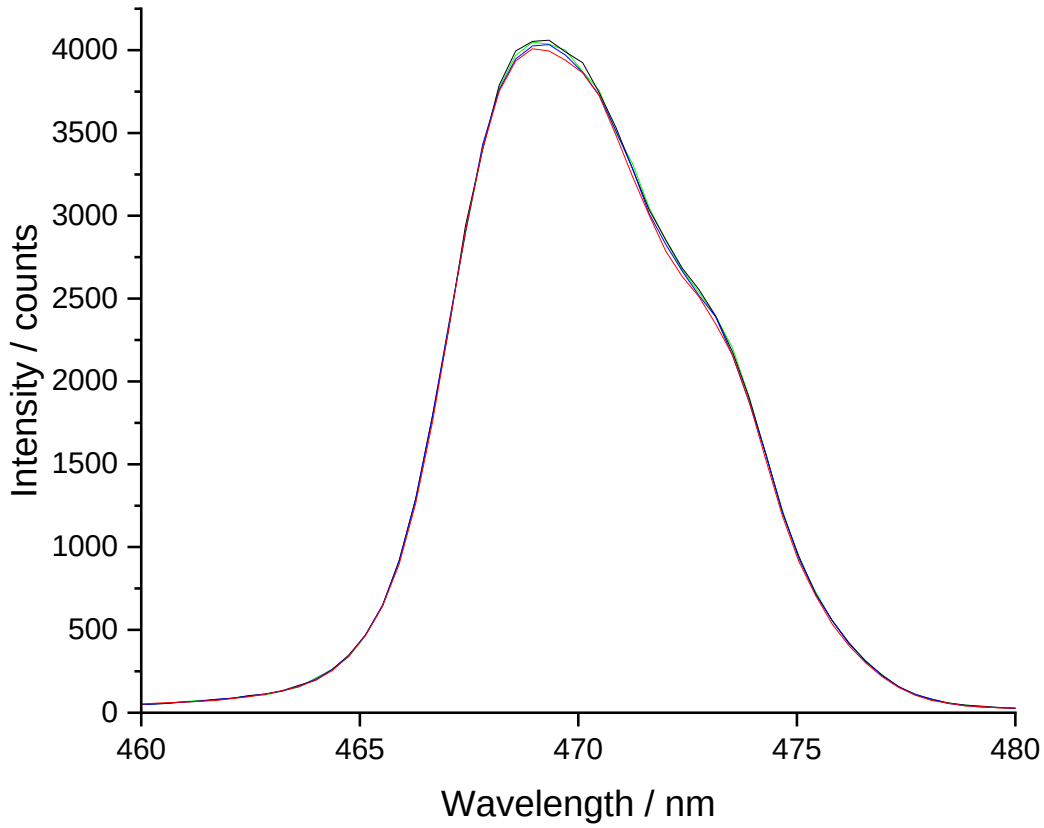

Figure 8.6: Scattering peak range for FRET experiment for 10 mM squalane emulsion with NBD mixed with 2 mM limonene microemulsion filled with Rh-PE. Black line indicates (t_0), light green is 400 ms, dark blue line is 1 s, cyan is 1 min, red is 5 mins.

The scattering peak in figure 8.6 shows negligible change during the FRET experiment from which we infer that the changes in scattering do not affect the detected FRET signal and that creaming/Ostwald ripening is not occurring in the flow cell on the experimental timescale.

8.3.2 FRET from mixture of a squalane emulsion with a limonene microemulsion and surfactant package

After successful initial trials, a set of repeat experiments were conducted for 10-mM squalane emulsion mixed with 2-mM limonene microemulsion. A comparative study was also undertaken using the surfactant package with a squalane concentration of 10 mM and surfactant concentration of 2 mM. The comparison with the surfactant package can be used to determine the role that limonene plays in the exchange of content between micelles and an oil mimic.

For figures 8.7–8.10, the black line (t_0) indicates the signal from a previous experimental run still in the cell. This curve is the last spectrum before mixing occurs. Note that this curve is not necessarily at equilibrium, depending on how long the previous sample has been left in the cell before mixing. All time stamps given for an individual run are with respect to the black spectrum (t_0). Recall that mixing occurs at some random time during the first spectral acquisition after t_0. The mixing of the solutions is fast compared with the data acquisition time. Consequently, the first spectrum is a combination of the spectrum before mixing and the spectrum immediately after mixing. The first spectrum has been removed from figures 8.7–8.10.

The case for the donor NBD-PE incorporated into a squalane emulsion was first tested. Figure 8.7 and 8.8 shows the FRET results for NBD-PE incorporated into a squalane emulsion mixed with limonene microemulsion and surfactant package, respectively, containing Rh-PE. The case for the acceptor Rh-PE incorporated into a squalane emulsion was also tested (Figures 8.9 and 8.10). Figures 8.7–8.10 show the refined spectra from AFA results to suppress the noise present in the raw spectra (e.g. Figure 8.5) so that FRET over time is depicted more clearly. It should be noted there is no isosbestic point in the results shown in figures 8.7–8.10, implying there is not just one component converting into another component, but an additional kinetic pathway present e.g. due to an environment with a different quantum yield. The mixing data in figures 8.7–8.10 show what seems to be spikes in intensity at certain wavelengths for each time stamp. I am confident that these spikes are artefacts. The spikes occur over a fraction of a nm in wavelength, too sharp to be due to fluorescence. The origin of these artefacts was not determined. The interference fringes described in §4.3.3 are also weakly present in these spectra. The shape of the NBD curves for the emulsion experiments are different from previous experiments, with a flattening of the NBD curve. This does not seem to have any bearing on the kinetics but is worth noting. The number of significant factors used to reconstruct the data set was two. A test with three factors reduced the fringes and spikes but the kinetics are unchanged, therefore two factors were kept for this study.

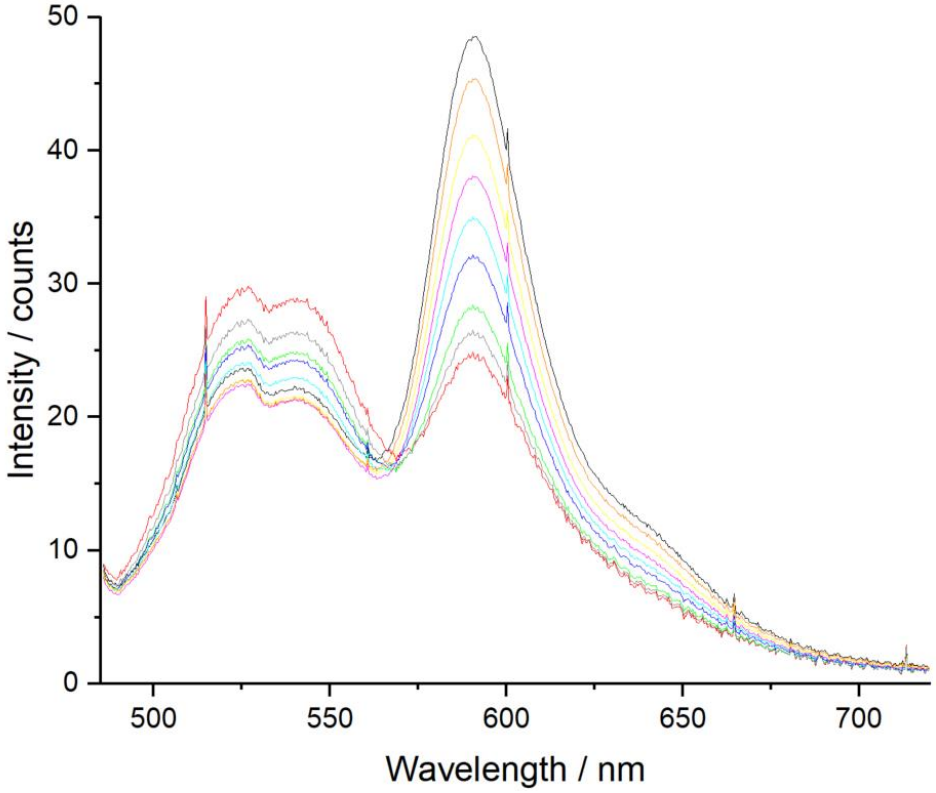

Figure 8.7: Refined mixing data for 10 mM squalane emulsion with NBD-PE mixed with 2 mM limonene-swollen micelles containing Rh-PE. Black line indicates (t_0), red line is 400 ms, grey line is 4 s, light green is 10 s, dark blue line is 30 s, cyan is 1 min, pink is 2 mins, yellow is 3 mins, orange is 5 mins.

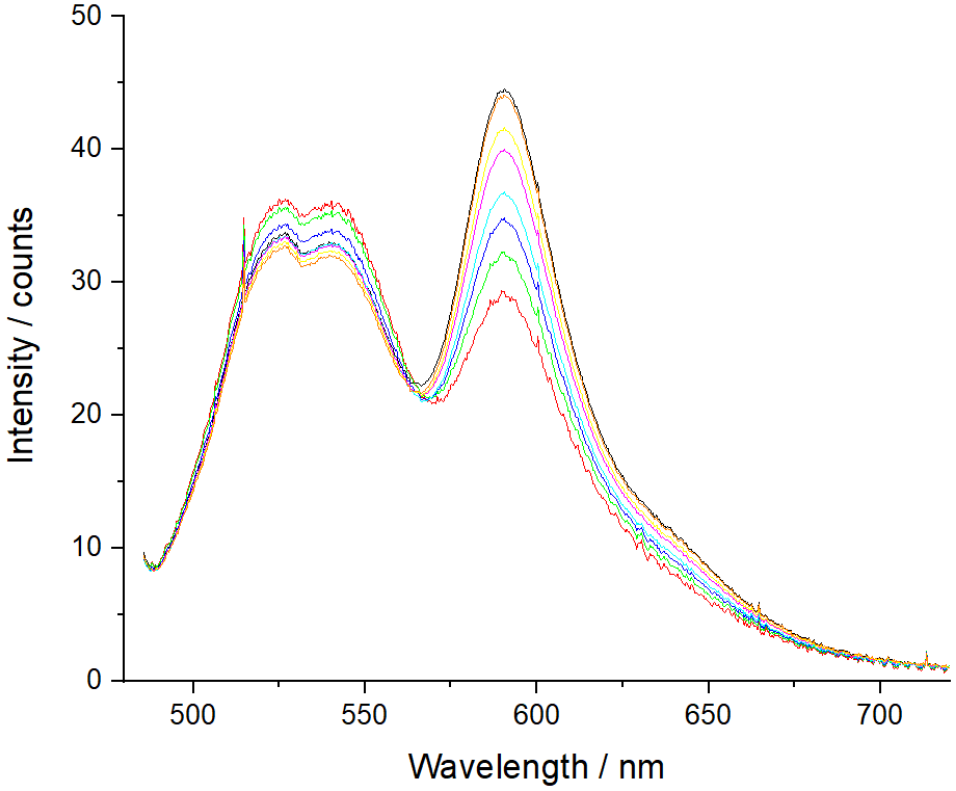

Figure 8.8: Refined mixing data for 10 mM squalane emulsion with NBD-PE mixed with 2 mM surfactant package containing Rh-PE. Black line indicates (t_0), red line is 400 ms, light green is 10 s, dark blue line is 30 s, cyan is 1 min, pink is 2 mins, yellow is 3 mins, orange is 5 mins.

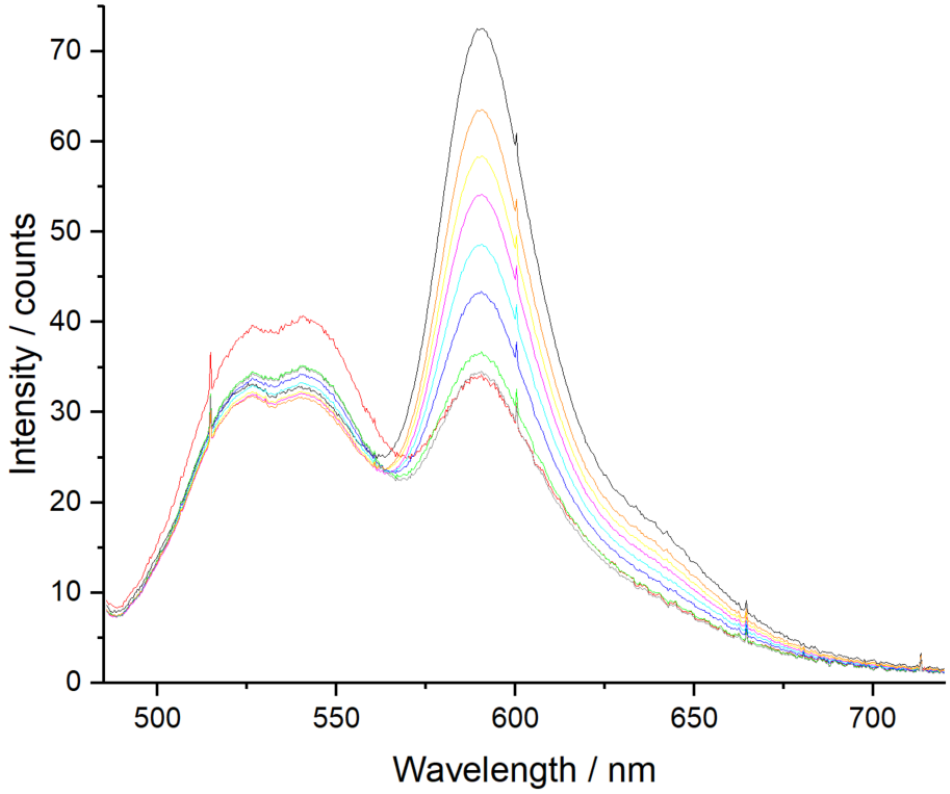

Figure 8.9: Refined mixing data for 10 mM squalane emulsion with Rh-PE mixed with 2 mM limonene microemulsion containing NBD-PE. Black line indicates (t_0), red line is 400 ms, grey line is 4 s, light green is 10 s, dark blue line is 30 s, cyan is 1 min, pink is 2 mins, yellow is 3 mins, orange is 5 mins.

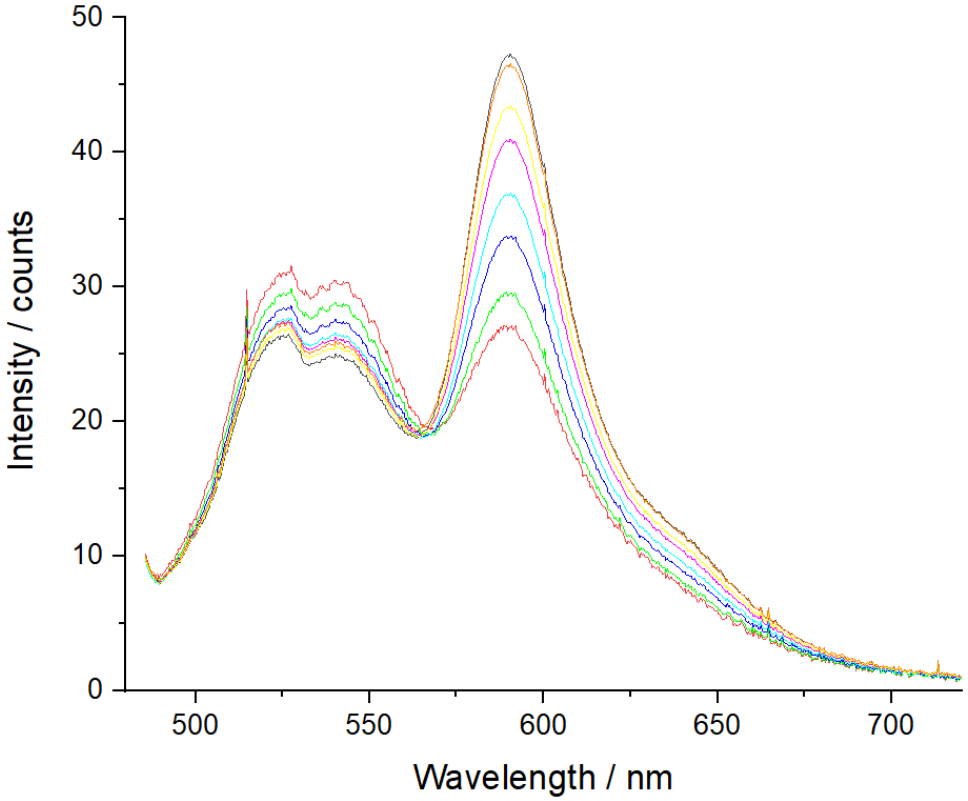

Figure 8.10: Refined mixing data for 10 mM squalane emulsion with Rh-PE mixed with 2 mM surfactant package containing NBD-PE. Black line indicates (t_0), red line is 400 ms, light green is 10 s, dark blue line is 30 s, cyan is 1 min, pink is 2 mins, yellow is 3 mins, orange is 5 mins.

8.3.3 Quantitative results of FRET of squalane emulsion mixing with limonene microemulsion and surfactant package

After a satisfactory set of repeatable runs had been obtained for limonene microemulsion and surfactant package mixing with squalane emulsions, the data were quantitatively analysed using target factor analysis. For quantitative treatment, the slight depression seen in figures 8.7–8.10 at 485 nm resulting from the scattering peak was not included, therefore a cut off from 490 nm was taken.

Figures 8.11 and 8.12 show the LFA results for NBD-PE incorporated into a squalane emulsion mixed with limonene microemulsion and surfactant package, respectively. Figures 8.13 and 8.14 show the LFA results for Rh-PE incorporated into a squalane emulsion mixed with limonene microemulsion and surfactant package, respectively. The LFA results for all experiments best fit a two-phase exponential decay, indicating more than one kinetic pathway during FRET. The fitting equation for the two-phase exponential decay

$$I(t) = A_1 \times e^{-k_1 t} + A_2 \times e^{-k_2 t} + I_0 \qquad (8.4)$$

The observed rate constants k_1 and k_2 are calculated from an average of 8 experimental runs for each probe incorporated in squalane. Table 8.1 gives the observed rate constants for FRET of a squalane emulsion with limonene microemulsion and surfactant package and their calculated errors. The ratio of the pre-exponential factors A_1 *and* A_2 for the squalane mixing experiments are also given along with the micellar exchange results for limonene microemulsions and surfactant package from §5.3.

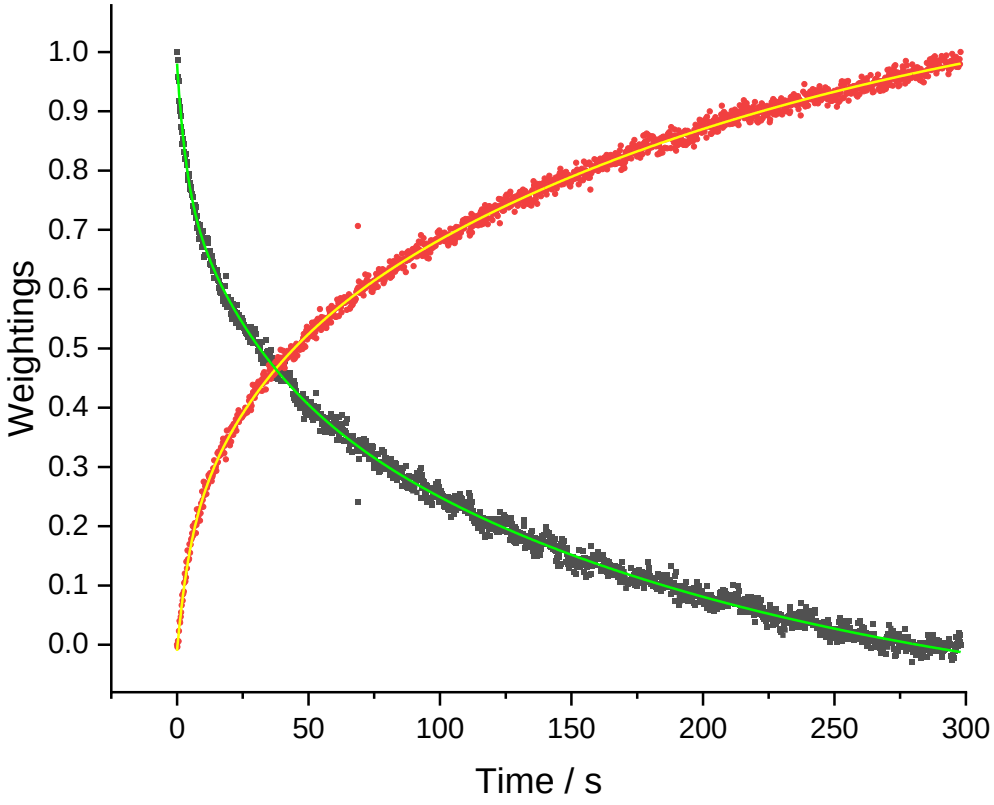

Figure 8.11: Loading data for 10 mM squalane emulsion with NBD-PE mixed with 2 mM limonene microemulsion filled with Rh-PE at 25 °C. The black dots indicate NBD-PE weightings with a solid green line fit, the red dots indicate Rh-PE weightings with a solid yellow line fit.

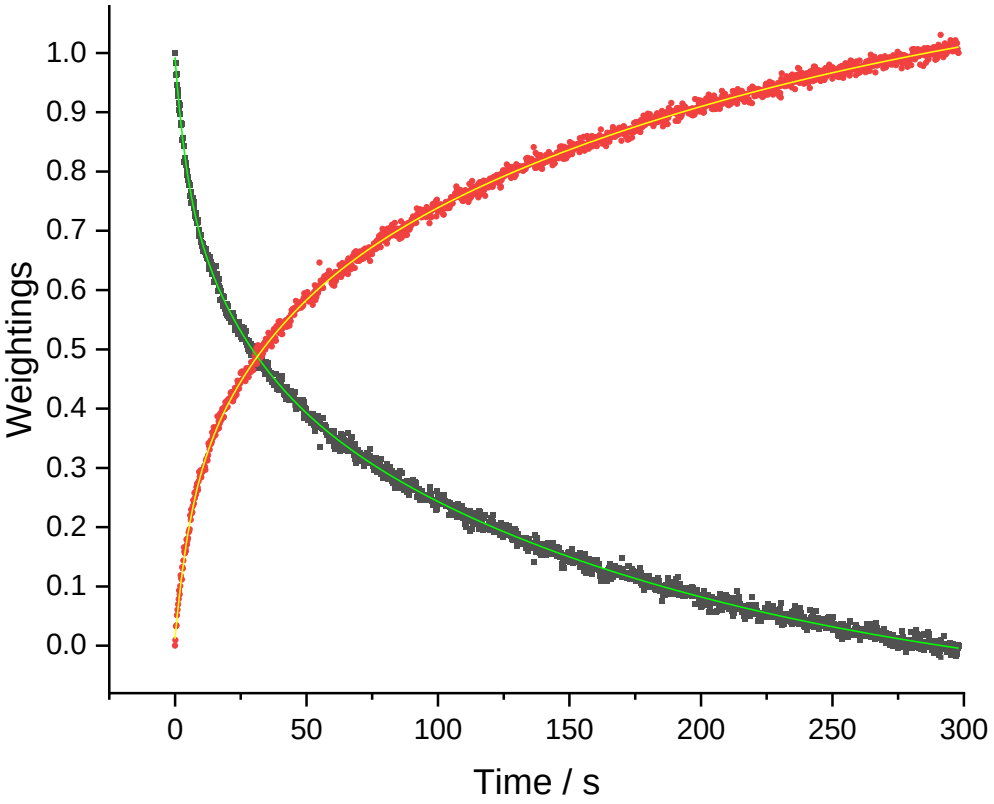

Figure 8.12: Loading data for 10 mM squalane emulsion with NBD-PE mixed with 2 mM surfactant package filled with Rh-PE at 25 °C. The black dots indicate NBD-PE weightings with a solid green line fit, the red dots indicate Rh-PE weightings with a solid yellow line fit.

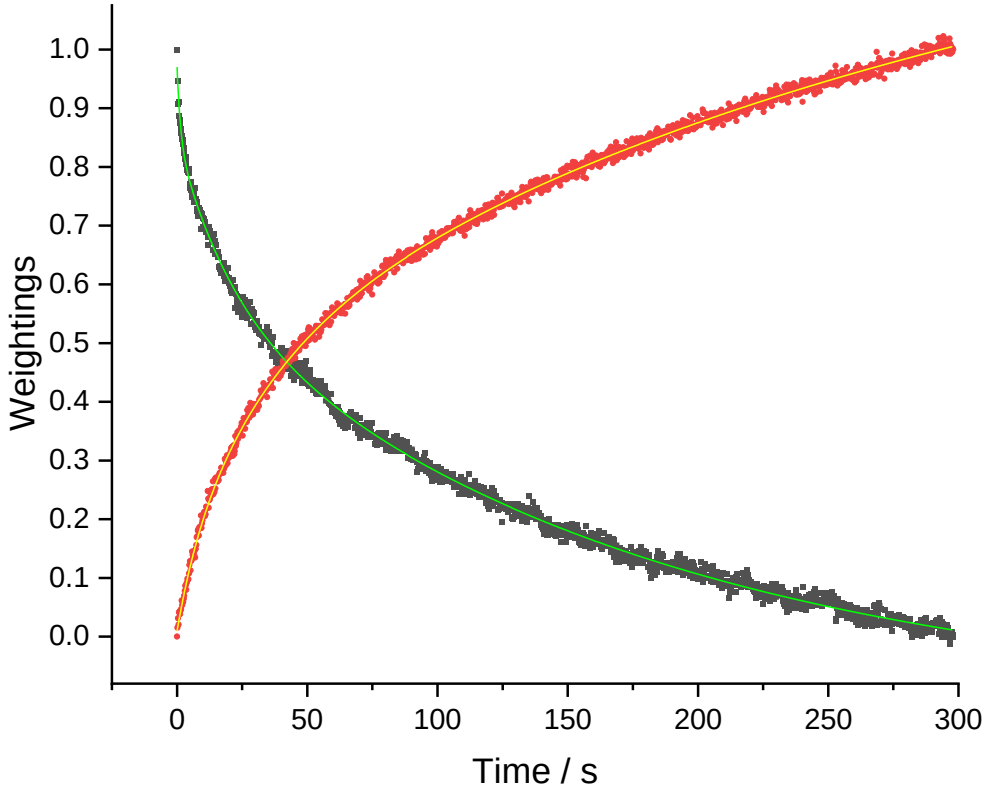

Figure 8.13: Loading data for 10 mM squalane emulsion with Rh-PE mixed with 2 mM limonene microemulsion filled with NBD-PE at 25 °C. The black dots indicate NBD-PE weightings with a solid green line fit, the red dots indicate Rh-PE weightings with a solid yellow line fit.

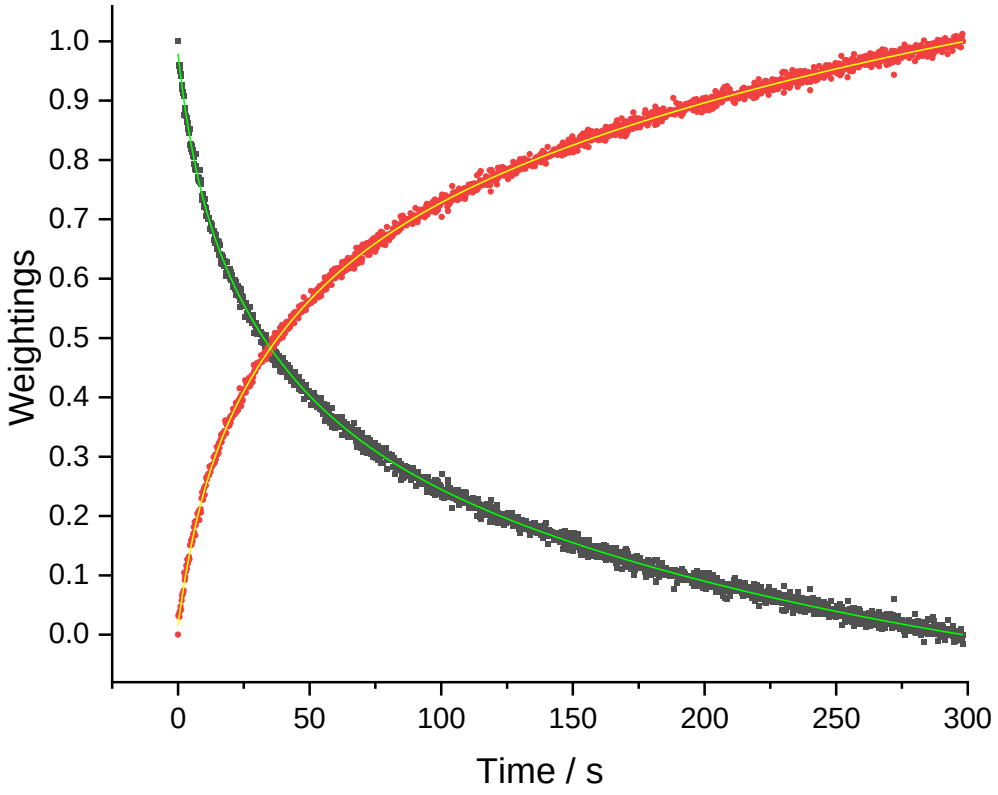

Figure 8.14: Loading data for 10 mM squalane emulsion with Rh-PE mixed with 2 mM surfactant package filled with NBD-PE at 25 °C. The black dots indicate NBD-PE weightings with a solid green line fit, the red dots indicate Rh-PE weightings with a solid yellow line fit.

Table 8.1 : Observed rate constants for FRET experiments of 10 mM squalane emulsions with 2 mM limonene microemulsion and surfactant package at 25 °C with calculated errors. Observed rate constants for micellar exchange in 2 mM limonene microemulsion and surfactant package at 25 °C also given from §5.3.

Limonene microemulsion					
	k_1 / s^{-1}		k_2 / s^{-1}		Pre-exponential factor ratio
	NBD-PE	Rh-PE	NBD-PE	Rh-PE	
NBD-PE in squalane emulsion	0.096 ± 0.005	0.077 ± 0.003	$7.2 \times 10^{-3} \pm 0.2 \times 10^{-3}$	$5.9 \times 10^{-3} \pm 0.2 \times 10^{-3}$	0.55
Rh-PE in squalane emulsion	0.062 ± 0.003	0.047 ± 0.003	$6 \times 10^{-3} \pm 0.1 \times 10^{-3}$	$4.3 \times 10^{-3} \pm 0.1 \times 10^{-3}$	0.56
Surfactant package					
	k_1 / s^{-1}		k_2 / s^{-1}		Pre-exponential factor ratio
	NBD-PE	Rh-PE	NBD-PE	Rh-PE	
NBD-PE in squalane emulsion	0.078 ± 0.001	0.081 ± 0.002	$7.3 \times 10^{-3} \pm 0.1 \times 10^{-3}$	$6.3 \times 10^{-3} \pm 0.1 \times 10^{-3}$	0.62
Rh-PE in squalane emulsion	0.055 ± 0.002	0.052 ± 0.002	$6.9 \times 10^{-3} \pm 0.1 \times 10^{-3}$	$6.1 \times 10^{-3} \pm 0.1 \times 10^{-3}$	0.59
micellar exchange					
	k_{obs} / s^{-1}				-
	NBD-PE		Rh -PE		-
Surfactant package	5.57 ± 0.12		5.54 ± 0.16		-
Limonene microemulsion	0.099 ± 0.003		0.094 ± 0.004		-

8.3.4 Discussion of FRET results

Figures 8.7–8.10 indicate we can successfully observe FRET for squalane emulsions with both empty micelles and micelles swollen with limonene. The evidence of FRET can be seen from the reduction of NBD-PE signal and increase of Rh-PE signal over time along with a signature shoulder peak at ~ 635 nm.

The Loading Factor Analysis (LFA) results from figures 8.11–8.14 show that we can achieve quantitative analysis of the FRET data. From table 8.1 it seems that FRET occurs on a similar timescale for the surfactant package and swollen micelle case. A probable explanation for the similar kinetics is that limonene partitions rapidly between the microemulsion droplets and the emulsion droplet on the timescale of the FRET experiments, through monomer diffusion rather than through collision/fusion of the micelles with the emulsion droplets. Given that the squalane concentration (in molar terms) is five times higher than the limonene concentration, much of the limonene may have dissolved in the squalane droplets by the time that exchange of dyes occurs. There is little evidence for the separate kinetics associated with re-equilibration of the micelle size distribution (but see Figure 8.15 below). Since the squalane is highly insoluble, it does not partition into the micelles through monomer diffusion in the aqueous phase. Consequently, the micelles become depleted in the organic phase and behave more like the surfactant package.

The two-phase exponential decay fit indicates that the kinetic pathway for exchange is more complex with micelles and oil droplets than for simple micelle fusion. First, there are two time constants rather than just one. Second, there is no isosbestic point for the mixing of micelles with emulsions, in contrast to experiments in which micelles were mixed with micelles. The absence of an isosbestic point indicates that there are more than two different ‘spectral components’ i.e. more is happening than just NBD-PE fluorescence being replaced by NBD-PE FRET. It is known that there are various additional pathways that can occur for an exchange of content between micelles[1]–[3]. The exit-entry mechanism for our fluorescent probes as discussed earlier would not be likely as the fluorescent probes are sufficiently insoluble in water. It is unlikely a fission process is occurring due to the stability of the emulsion and microemulsion droplets and collisions are taking place regularly in the system. A fission mechanism

would also not initially exhibit any FRET as our probes are in separate micelles. The absence of an isosbestic point could be a result of the dyes having slightly different emission spectra or absorption spectra or quantum yields depending on which environment the dye is in, i.e., the micelle or the emulsion droplet.

It would be expected the rate constants to be the same for the two components in the fluorescence spectrum (NBD-PE and Rh-PE) and independent of which probe was initially incorporated in each syringe. The Rh-PE *k* values are generally lower than NBD-PE *k* values and do not correspond within experimental error in several cases. The rate of exchange also appears to change depending on which probe is dissolved in the squalane emulsion. The observed rate constants in table 8.1 with Rh-PE in the squalane emulsion are systematically lower. These discrepancies suggest that the actual kinetics are probably more complex than a bi-exponential decay.

The rate constants, k_1, are of the same magnitude as k_{obs} for the limonene microemulsion (table 8.1). This could give some insight into the faster kinetic pathway in the emulsion experiment. If the limonene is solubilising into the squalane droplets we might therefore expect that the k_1 kinetic processes for both experiments would have a similar rate constant to the micellar exchange for the surfactant package itself (found in §5.3). In fact, the rate constant is similar to that of the limonene microemulsion exchange and about two orders of magnitude slower than that of the surfactant package itself. A possible explanation is that some squalane is solubilised in the surfactant micelles, so we are actually looking at collisions between pure surfactant micelles and a squalane 'microemulsion'. Microemulsion collisions have a much lower observed rate constant than pure surfactant observed from previous experiments, and that for methyl laurate the rate of exchange was even slower than for the squalane emulsions. The physical reason could be that the micelles swollen with squalane have a curvature closer to the preferred curvature than surfactant micelles alone. This increases the energy barrier for the change in curvature of the surface needed to former a transient dimer between two micelles. To test this hypothesis, further experiments saturating micelles with squalane and then study the mixing kinetics of these swollen micelles in the two syringes should be undertaken.

To interpret the data in Table 8.1, we first note that the surfactant in the emulsion is in excess and therefore the syringe contains micelles as well as emulsion droplets. To estimate the proportion of surfactant in the emulsion droplets, we assume that all the droplets are spherical and have a radius equal to the mean radius (107 nm). The surface area of each droplet is then $1.4 \times 10^{-13}\,m^2$ and, using the area per molecule of surfactant headgroup ($5.7 \times 10^{-15}\,cm^2$) for $C_{12}E_7$, the number of surfactants required to coat an emulsion drop is 2.5×10^5 molecules. Using the known concentration of oil to make the emulsion and the average size of each emulsion drop from the Nanosight results, the concentration of emulsion drops is 1×10^{12} drops per ml. Combining the number of surfactants required to coat an emulsion drop and the number of emulsion drops gives the amount of surfactant molecules required to emulsify the oil, calculated to be 2.57×10^{17} molecules per ml, which corresponds to a concentration of 0.43 mM. The total surfactant concentration is 2 mM, and therefore the concentration of excess surfactant in the form of free monomers and micelles in the system is 1.57 mM. The cmc of $C_{12}E_7$ is around 0.08mM. Thus, roughly three-quarters of the surfactant (and by implication the dye, assuming it does not preferentially partition into the emulsion or micelles) is in the form of micelles (1.49 mM).

The excess surfactant after coating the emulsion drops that form micelles can contain a fluorescent probe of either NBD-PE or Rh-PE. If we take the case where Rh-PE is incorporated into the emulsion system, the exchange from the Rh-PE from excess micelles with incoming NBD-PE microemulsion gives the fast k_1 observed. The remaining Rh-PE can only give FRET once the incoming NBD-PE containing microemulsion droplets have fused with the emulsion, accounting for the slower k_2 kinetic pathway. Using equation 8.4, the pre exponential factors A_1 and A_2 are associated with the free surfactant in the system and the surfactant emulsifying the squalane oil. The ratio of the pre-exponential factors for squalane emulsion fitting can be seen in table 8.1. The ratio of surfactant in micelles to that emulsion droplets is calculated to be 3.5. The differences between the ratios are quite stark, even when considering the assumptions needed for this comparison, such as uniformity of drop size, which from the Nanosight experiments is known not to be the case. During experimentation, there were some examples that indicated another very rapid initial decay occurring, which fit a 3-phase exponential decay, as can be seen in figure 8.15.

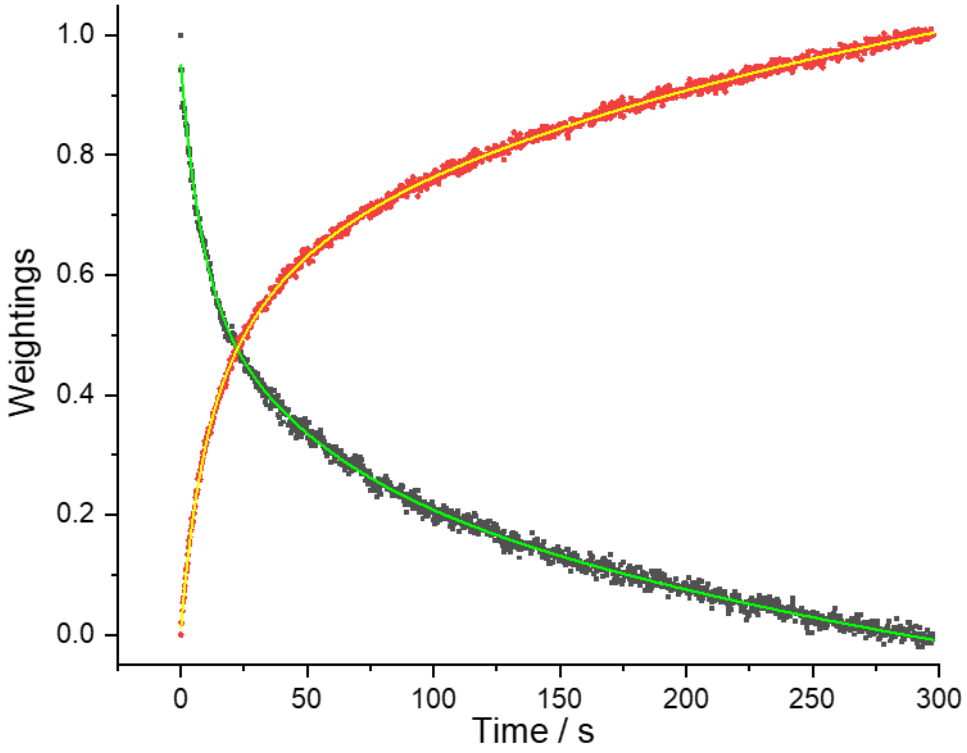

Figure 8.15: Loading data for 10 mM squalane emulsion with NBD-PE mixed with 2 mM limonene swollen micelles filled with Rh-PE at 25 °C using a 3-phase exponential decay fit. The black dots indicate NBD-PE weightings with a solid green line fit, the red dots indicate Rh-PE weightings with a solid yellow line fit.

This rapid initial decay could be associated with limonene dissolving in the squalane droplets. This additional possible pathway could be causing the discrepancy between the ratios of A1:A2 and emulsified surfactant: excess surfactant. Another explanation could be from the dye molecule preferentially solubilising in the droplets compared to micelles.

When considering the k_2 values, associated with collisions of micelles with the emulsion droplets. The probability of collisions leading to an exchange of contents can be calculated, as was discussed for micelle-micelle interactions in §4.3.6. The diffusion-controlled collision rate for limonene microemulsion droplets and emulsion droplets can be calculated as per the method discussed in §3.3.3. The diffusion-controlled collision rate constant *kd* for a squalane emulsion drop colliding with a limonene microemulsion droplet is 1.18×10^8 $m^3\,mol^{-1}\,s^{-1}$, giving a collision rate of 0.1 s^{-1}. The average observed collision rate for the microemulsion experiments was 0.06 s^{-1}. The ratio of the experimental collision rate and the diffusion controlled collision rate, gives the probability that a collision will lead to fusion δ. Therefore the probability

of a collision between the emulsion and microemulsion droplets is 0.058. A comparison of δ values found in §5.3.2 and this case can be seen in table 8.2.

Table 8.2: Comparison of δ for emulsion collisions with microemulsion droplets, surfactant droplet collisions and microemulsion droplet collisions.

	δ
Squalane emulsion-limonene microemulsion	0.058
Limonene microemulsion droplets	4×10^{-6}
Surfactant package	2.5×10^{-5}

The probability of an individual collision leading to fusion is several orders of magnitude higher for the case of an emulsion and microemulsion droplet than both limonene microemulsion and surfactant micelles colliding.

It was earlier inferred the squalane reduces the fusion rate, which brings into question why the second order rate constant is so much higher than the value of k_1. There are two possible explanations for this.

The first is the oil droplet has a very low curvature (radius of curvature ~ 100 nm). If the preferred curvature for the limonene microemulsion droplets is a few nanometres, then there is a lot of bending energy stored in the flat oil-water interface that can be released by the formation of curved structures, such as buds that can then detach to form micelles. If micelle formation is easily achieved, then micelle fusion with the interface must be easy to achieve too, since the two rates are equal at equilibrium.

The second is a discrepancy from the number of encounters at the oil-water interface for a micelle with an oil droplet as opposed to two micelles colliding. When two micelles collide they typically only have one attempt to fuse before they diffuse away again. When a micelle approaches the large, relatively flat surface of an oil droplet it may encounter the interface many times before it diffuses away from the droplet. Each of these encounters can lead to fusion, so the apparent delta value is much greater than the delta value for each encounter. However, as there are much fewer emulsion

droplets, the number of collisions are lower for emulsion-microemulsion than microemulsion-microemulsion, therefore a slower observed rate.

Conclusion

Having successfully demonstrated stopped-flow FRET experiments for the case of squalane emulsions with empty micelles and limonene swollen micelles, I have been able to give a good experimental mimic for micelle exchange with a crude oil droplet. The results have shown two distinct kinetic pathways for FRET, with the possibility of a third mechanism postulated. An explanation to the two distinct kinetic pathways observed has been given, compared with micellar exchange kinetics observed in previous chapters and therefore an exchange of contents for micellar systems with large emulsion droplets. More work should be undertaken to determine if these explanations can be proven experimentally. The ability of the FRET stopped-flow method to observe the exchange kinetics for micelles with a crude oil mimic should allow for continued study with a crude oil derivatives, however much care must be taken to consider the components of the crude oil derivatives.

References

[1] Y. Rharbi and M. A. Winnik, “Solute exchange between surfactant micelles by micelle fragmentation and fusion,” *Advances in Colloid and Interface Science*, vol. 89–90, pp. 25–46, Jan. 2001, doi: 10.1016/S0001-8686(00)00054-3.

[2] I. M. Griffiths, C. J. W. Breward, D. M. Colegate, P. J. Dellar, P. D. Howell, and C. D. Bain, “A new pathway for the re-equilibration of micellar surfactant solutions,” *Soft Matter*, vol. 9, no. 3, pp. 853–863, 2013, doi: 10.1039/c2sm27154k.

[3] I. M. Griffiths, C. D. Bain, C. J. W. Breward, D. M. Colegate, P. D. Howell, and S. L. Waters, “On the predictions and limitations of the Becker-Döring model for reaction kinetics in micellar surfactant solutions,” *Journal of Colloid and Interface Science*, vol. 360, no. 2, pp. 662–671, 2011, doi: 10.1016/j.jcis.2011.04.074.

[4] S. Li, X. Zhang, W. Dong, and W. Wang, “Computer Simulations of Solute Exchange Using Micelles by a Collision-Driven Fusion Process”, doi: 10.1021/la801521b.

[5] R. Pool and P. G. Bolhuis, “Sampling the kinetic pathways of a micelle fusion and fission transition,” *The Journal of Chemical Physics*, vol. 126, no. 24, p. 244703, Jun. 2007, doi: 10.1063/1.2741513.

[6] G. Landazuri, V. V. A. Fernandez, J. F. A. Soltero, and Y. Rharbi, “Length of the Core Forming Block Effect on Fusion and Fission Dynamics at Equilibrium in PEO-PPO-PEO Triblock Copolymer Micelles in the Spherical Regime,” *Macromolecules*, vol. 54, no. 5, pp. 2494–2505, Mar. 2021, doi: 10.1021/ACS.MACROMOL.0C01520/ASSET/IMAGES/LARGE/MA0C01520_0013.JPEG.

Concluding remarks

Throughout this thesis a number of fundamental concepts and techniques were needed to progress the understanding of how limonene microemulsions behave, exchange contents and interact with oil. The experimental story of the thesis can be segmented into three parts; first, determining the phase behaviour of limonene microemulsions with a commercial surfactant. Second, developing a methodology to first observe exchange kinetics of micelles using stopped-flow kinetics and then quantitatively analyse the data. Third, using the knowledge gained from part one, and implementing the technique formed in part two to observe micelle fusion for different micellar environments and eventually the interaction between a mimic crude oil and micelles.

Part one

Understanding the phase behaviour of limonene microemulsions informs the experimental design for part 2 and 3, whilst also helping to explain phenomena seen in parts 2 and 3. The solubilisation capacity experiments with temperature changes was used to give understanding to results found in chapter 5. The spectroscopic and tensiometry data give more detail to the structure and behaviour of the commercial surfactant used and suitability to for phase behaviour experiments. The commercial surfactant allows formulators to use an affordable surfactant to make limonene microemulsions for oil recovery and other uses.

When comparing the ternary phase diagram of the experimental data with the idealised diagrams given, it is clear there are difficulties with the method used for this thesis. The titration method is a classic technique to generate ternary phase diagrams, however, to capture the complexity of a limonene microemulsion system, more experimentation should be undertaken, perhaps using a complementary NMR technique to determine discrete phases observed. The fish tail experimentation does give good reproducibility from the idealised diagram and aligns with published work. The ternary phase diagram was a useful tool to predict the phase behaviour when diluting the system and after a stopped-flow mixing experiment. The fish tail plot also shows the temperature boundaries to maintain a Winsor IV microemulsion at a given

concentration. Future work would include the use of SAXS or SANS to accurately measure the size of the micelles for all cases.

Part two

The stopped-flow kinetic method using pyrene as a fluorescent probe to observe micelle breakdown kinetics has been well observed and supported in the literature. However, as the course of experimentation continued to use the same technique for micelle fusion kinetics, it was clear this method was not sensitive enough. By changing methodology to a stopped-flow FRET method many fruitful experiments were undertaken. One of the greatest strengths of the technique is how robust the technique is for a number of different systems and effective the experiments are in giving data that can be qualitatively inspected. Qualitatively, it is clear when a FRET progression has occurred and a well-defined isosbestic point indicates two different spectral contributions to the experiment.

The challenge was to then use this qualitative data and turn it into something quantitative for formal kinetic analysis. Target Factor Analysis was able to deconvolute the raw data and produce meaningful quantitative data. The ability of TFA to effectively clean the spectra enabled me to keep the surfactant concentration close to industrial concentrations for oil recovery, whilst acquiring data at low timescales. The TFA methodology is also robust when changing the environment, when moving to the emulsion experiments, despite a baseline skew the TFA was able to still obtain reproducible reliable results. The consistency of the NBD-PE and Rh-PE decays is another indicator for a ‘successful’ experiment, the throughout the investigation the kinetics for NBD-PE and Rh-PE for a given system was consistent. Complementing Target Factor Analysis with stopped-flow FRET experimentation provides a powerful tool to understand the kinetics of micelle fusion and to study interactions at other interfaces.

Part three

Testing the stopped-flow FRET kinetic for limonene microemulsion and surfactant package gave some surprising but insightful results. Throughout experimentation, the surfactant package gave faster micelle fusion kinetics than limonene microemulsions. The increase in temperature followed an expected trend, however the rate constant doesn't depend linearly on the concentrations used for this study. The additional comparison of cyclohexane did not give a great deal of insight into the role of oil for fusion kinetics but did provide similar reproducible results as the case for limonene microemulsions and the surfactant package. However, as was evident from the unsuccessful methyl laurate trials, the solvent oil does play an important role in micelle fusion.

The introduction of charge to the micelles created an effective barrier to micelle fusion at appreciable SDS concentration, consistent with theory and published data. The ability to effectively 'switch on' the barrier to fusion using SDS and 'switch off' the barrier using salt can be of use for oil recovery methods, when considering salinity of water in a well and additives in the rock pores.

Moving onto the emulsion case, the absence of an isosbestic point from first inspections clearly indicated there were not two spectral contributions. The quantitative analysis validated this as a two-phase exponential decay was the most suitable fit for the kinetics. The quantitative analysis prompted two definitive plausible mechanisms occurring during the reaction, with a rapid third mechanism also giving possible contribution to the kinetics. The implications of the emulsion experiment show that a crude oil mimic can be used to observe a fusion process between micelles and an oil interface.

The next steps for this project would be to use the stopped-flow FRET experiment would be to use more complex mixtures closer to crude oil. The challenge of using crude oil is twofold, first the oil is black, which would absorb the incident light and inhibit much light from passing through the flow cell. Second, many of the components of crude oil are fluorescent in nature and could interfere with the FRET signal. Using a mixture of asphaltenes and heavy oils would give a more realistic crude oil mimic, whilst avoiding the two mentioned challenges of using real crude oil. The use of a more realistic crude oil mimic gives a better understanding to how the limonene microemulsion would interact with oil in an oil well. If the micelle fusion kinetics can be

attributed to the efficacy of oil well recovery, the stopped-flow FRET technique can then be used to determine the efficacy of oil recovery for a number of different systems. The use of this stopped-flow FRET method coupled with SAXS would be a powerful tool to show the kinetics of micelle fusion and the degree of swelling in the micelles, giving a tangible link to the degree of solubilisation and speed at which the micelles fuse.

Appendix A

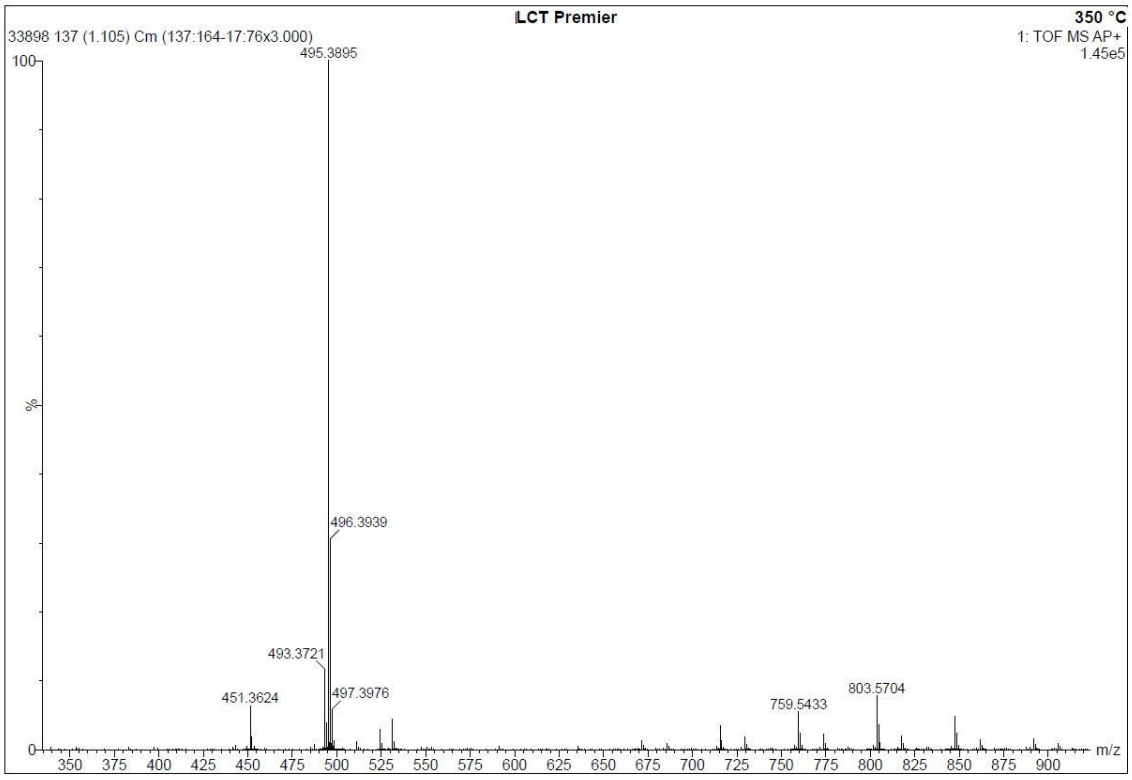

Figure 1: Pure $C_{12}E_7$ Time of Flight Mass Spectrometry.

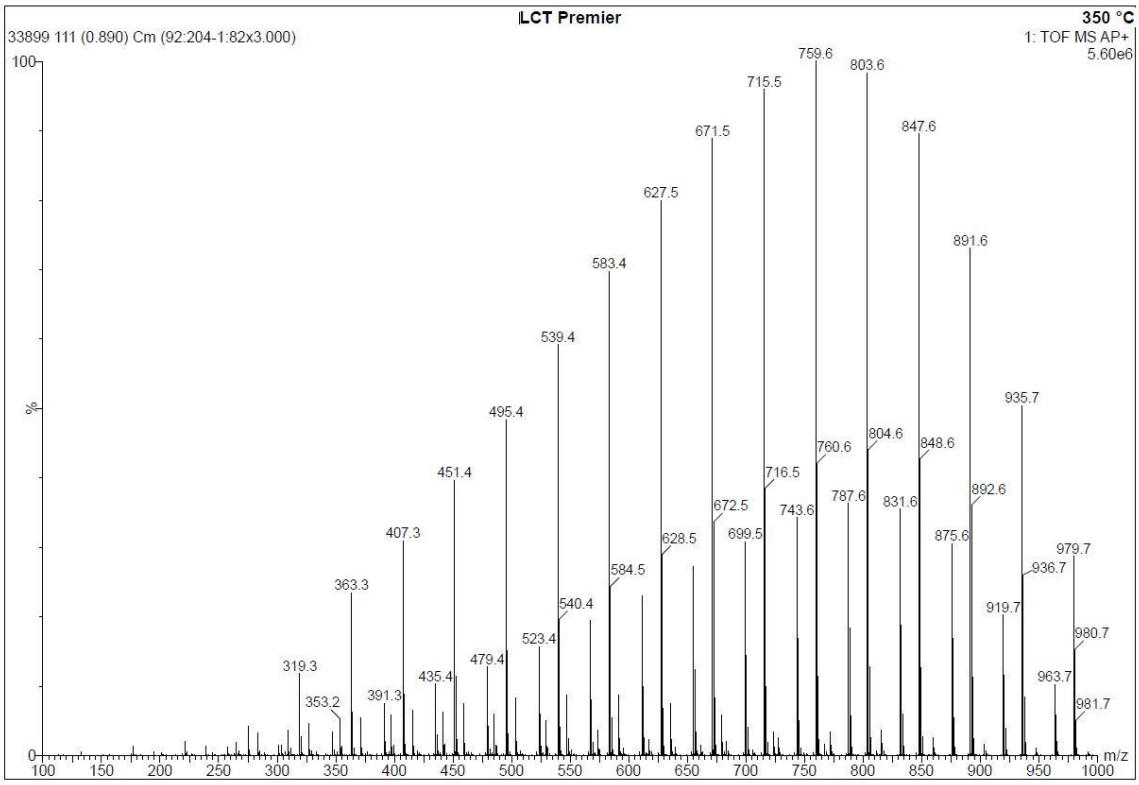

Figure 2: Commercial $C_{12}E_7$ Time of Flight Mass Spectrometry.

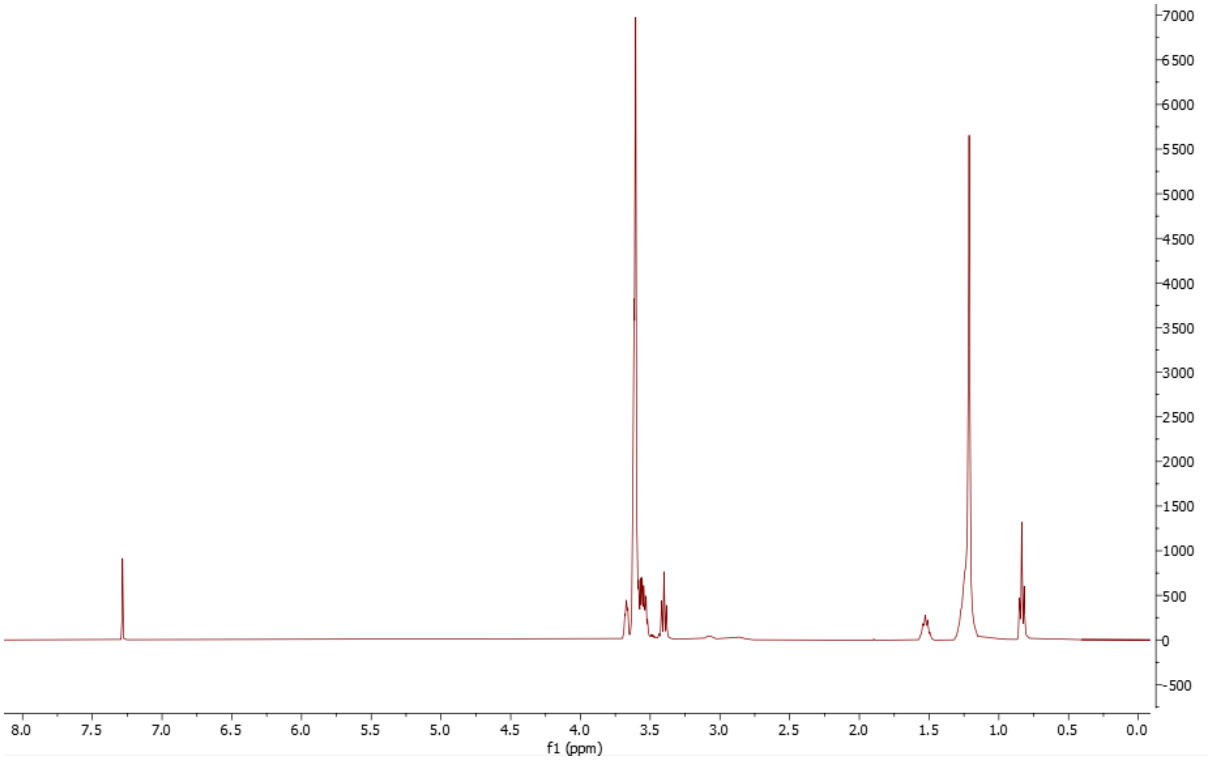

Figure 3: ^{1}H NMR (400MHz, $CDCl_3$) of commercial $C_{12}E_7$. 0.85 (m, 6H), 1.25 (d, J = 5.7 Hz, 15H), 1.55 (t, J = 7.1 Hz, 2H), 2.84 (s, 1H), 3.43 (t, J = 6.9 Hz, 2H), 3.63 (m, 26H), 3.71 (m, 2H).

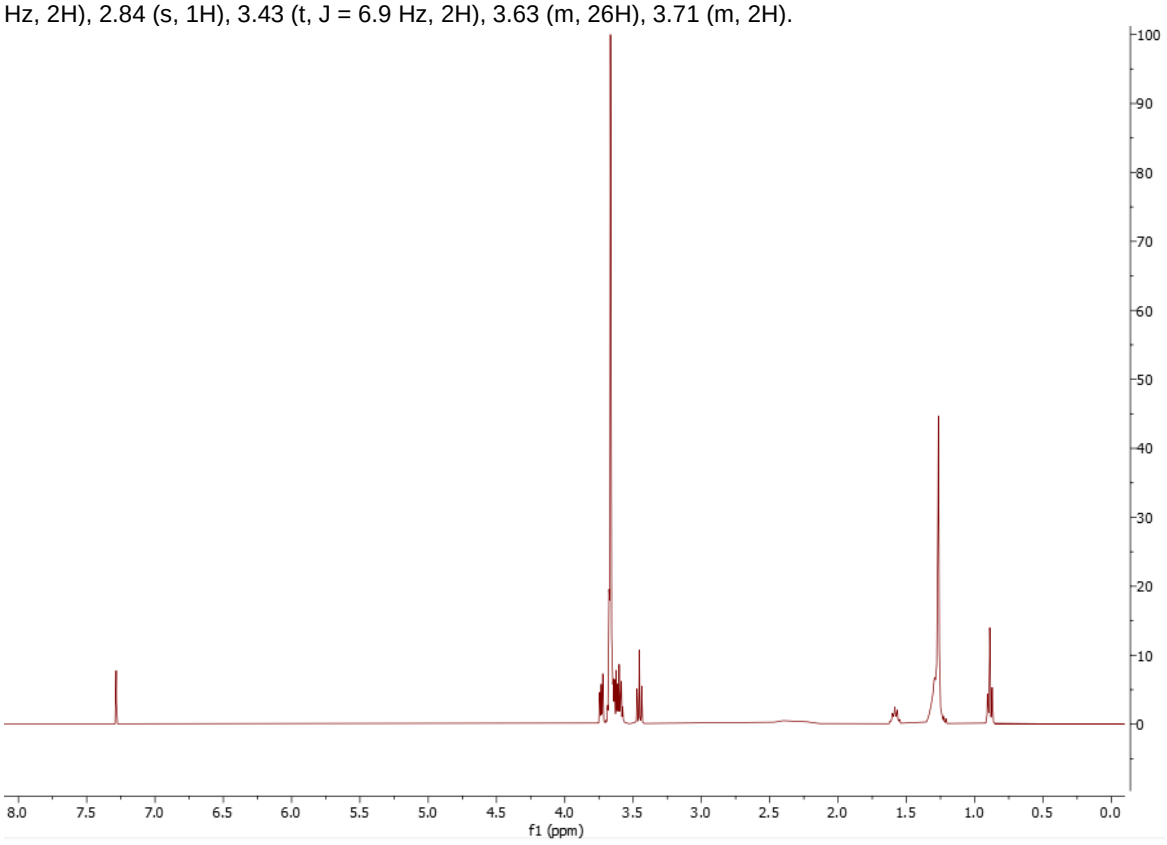

Figure 4: ^{1}H NMR (400MHz, $CDCl_3$) of pure $C_{12}E_7$. 0.85 (m, 6H), 1.25 (d, J = 5.7 Hz, 15H), 1.55 (t, J = 7.1 Hz, 2H), 2.84 (s, 1H), 3.43 (t, J = 6.9 Hz, 2H), 3.63 (m, 26H), 3.71 (m, 2H).

Appendix B

Figure 5 below shows pyrene in water at 0.073 mM concentration. Notice the intensity increase, this is due to a much higher integration time of 1 second due to very low signal levels at 10 and 100 ms.

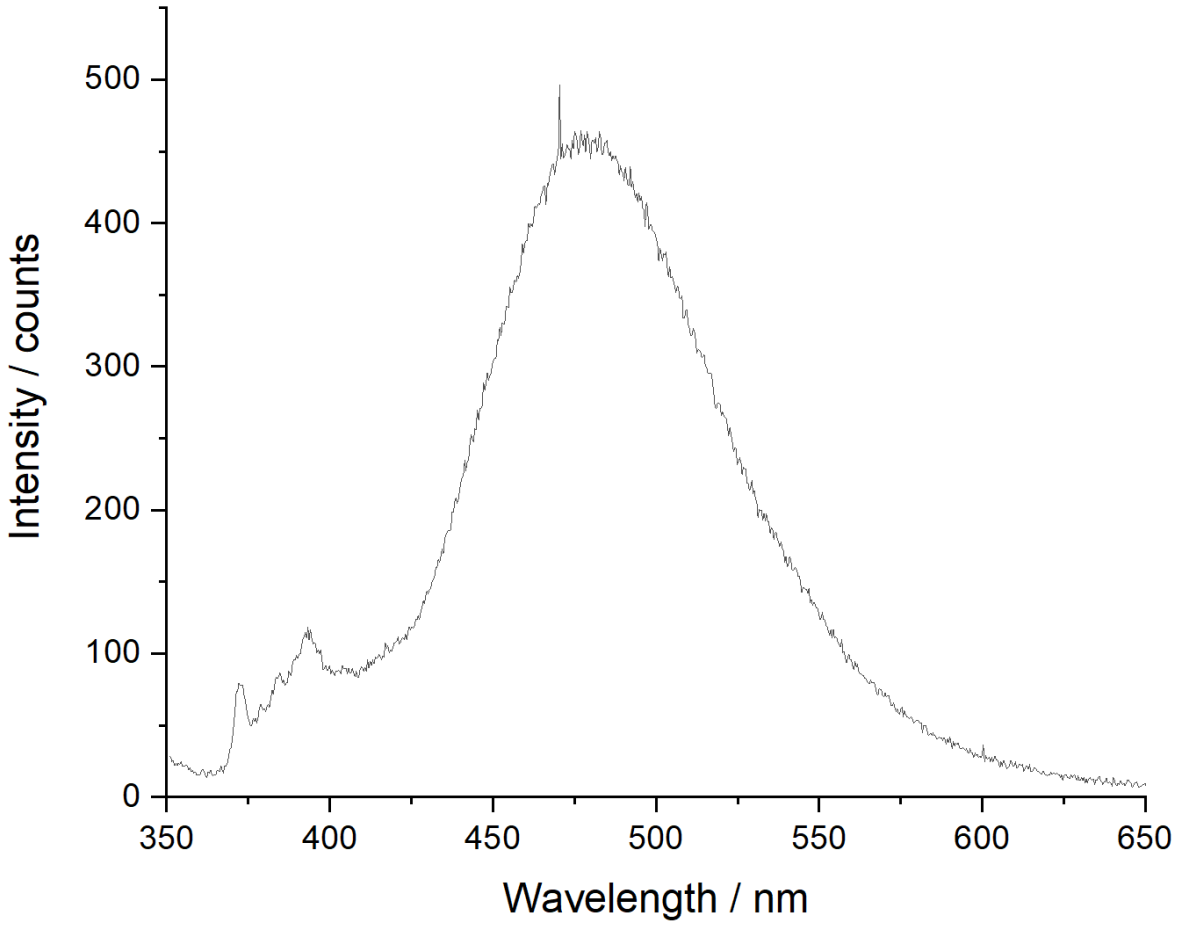

Figure 5: Fluorescence spectra of Pyrene in water 0.073mM, integration time 1 s. Excitation wavelength 337 nm.

Hexane microemulsion mixing experiments

The trend for the hexane microemulsion mixing experiments is the same. The black line indicates an initial scan before mixing, the red scan indicates the micelles still in equilibrium one scan before mixing. The light green scan is directly after the red scan and indicates the initial mixing point. The dark blue is the following scan which

precedes the final dark screen scan, indicating mixing is completed, again on the millisecond timescale.

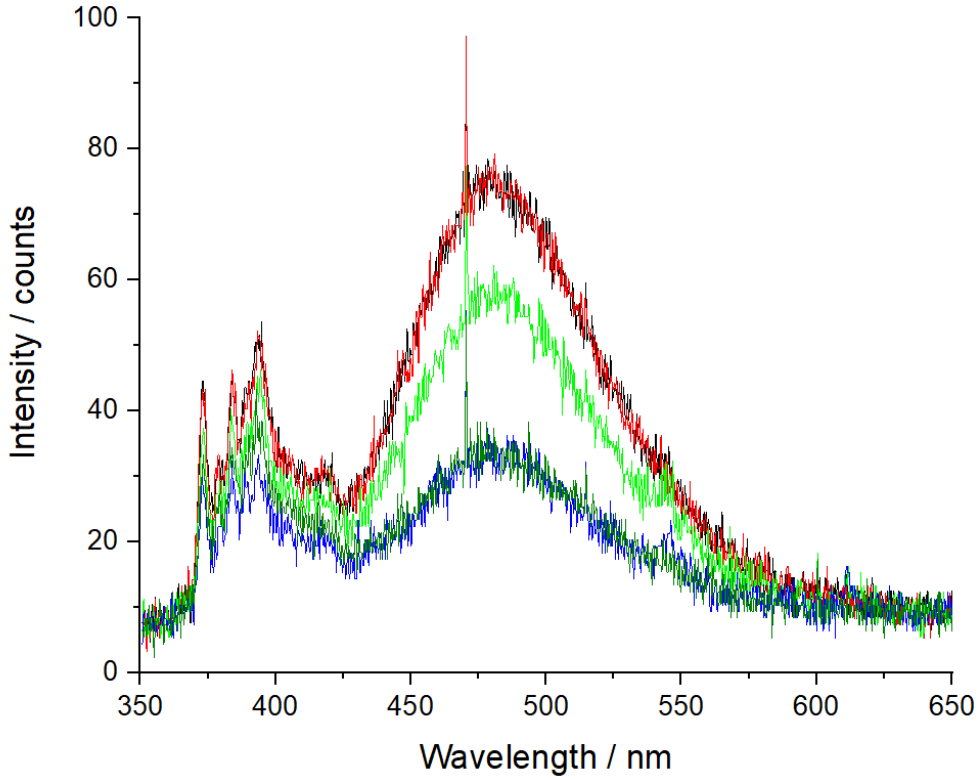

Figure *6*: High speed acquisition of swollen micelles with hexane 1:1 mixing. $C_{12}E_7$ concentration is 11 mM, pyrene concentration is 0.073 mM, integration time 10ms. Run time of 10 seconds. Excitation wavelength of 337 nm.

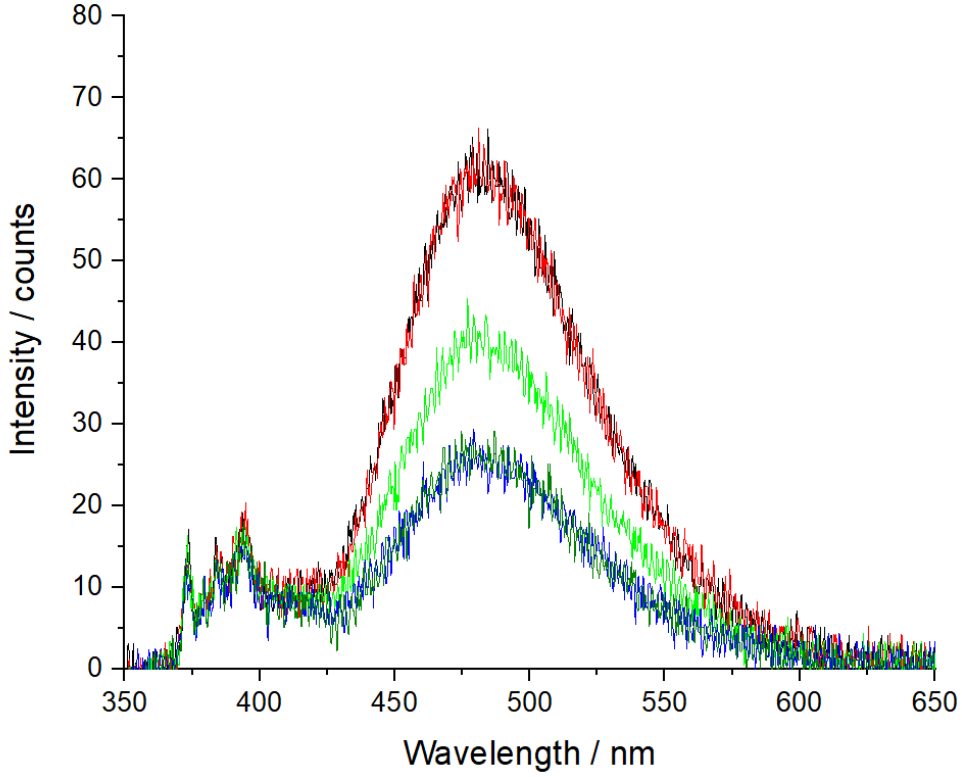

Figure 7: High speed acquisition of swollen micelles with hexane 1:1 mixing. $C_{12}E_7$ concentration is 0.8 mM, pyrene concentration is 0.024 mM, integration time 10ms. Run time of 10 seconds. Excitation wavelength of 337 nm.

18:1 Liss Rhod PE mixing experiments

Figure 3 illustrates the emission spectra of swollen micelles at 0.8 mM $C_{12}E_7$ concentration injected with 18:1 Liss Rhod PE (0.5% molar concentration of $C_{12}E_7$) with an integration time of 100 ms. Figure 4 shows 1:1 mixing experiment for $C_{12}E_7$ in our microemulsion system at 0.8 mM $C_{12}E_7$ concentration and 1%18:1 Liss Rhod PE. Swollen micelles filled with rhodamine are pneumatically mixed with swollen micelles without rhodamine into the cell at a ratio of 1:1. The black line indicates an initial scan before mixing, the red scan indicates the micelles still in equilibrium one scan before mixing. The light green scan is directly after the red scan and indicates the initial mixing point. The dark blue is the following scan which is overlapping with the final dark green scan indicating an end to mixing.

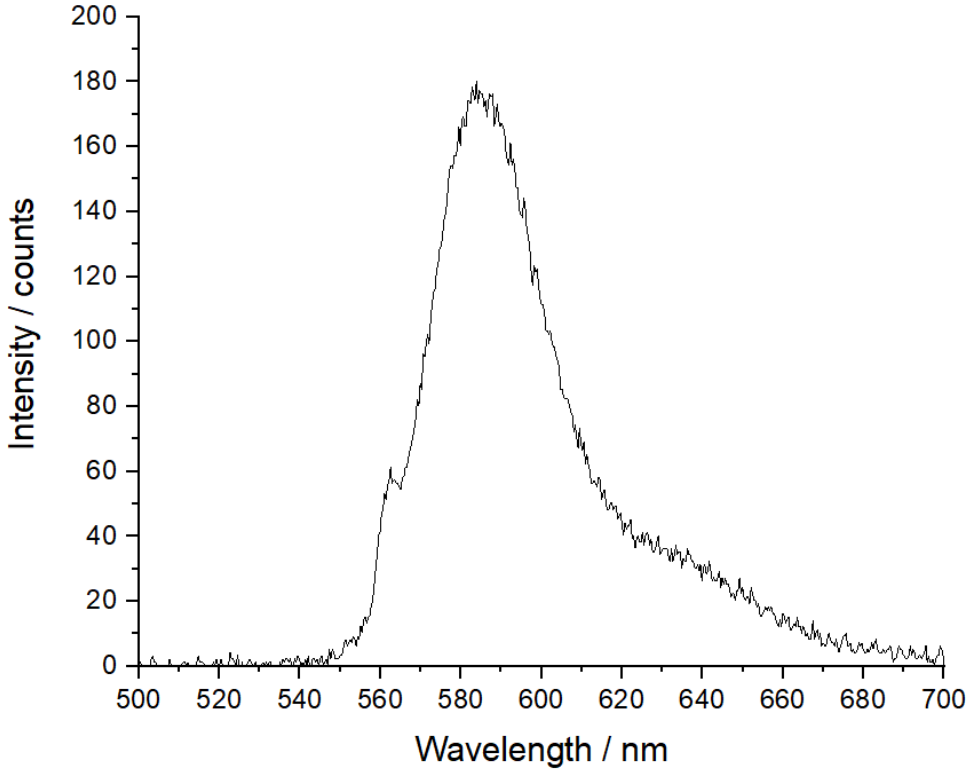

Figure *8*: High speed acquisition of 18:1 Liss Rhod PE in micellar solution at equilibrium. $C_{12}E_7$ 0.8 mM, Rhodamine 0.5%, 100 ms integration time, excitation wavelength 560 nm.

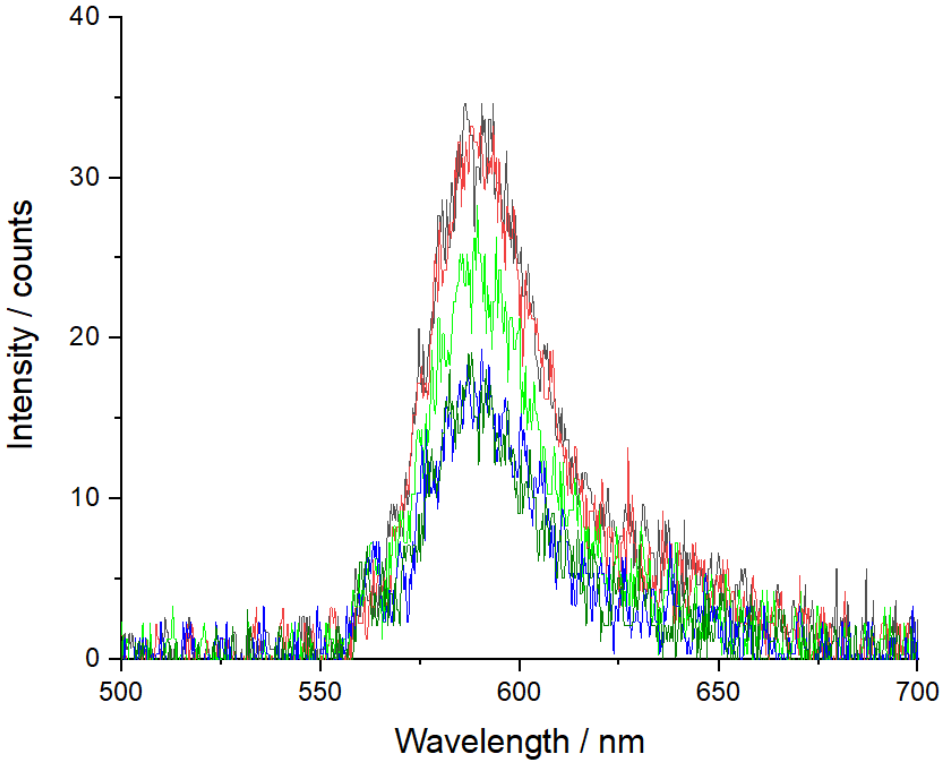

Figure *9*: High speed acquisition of 18:1 Liss Rhod PE 1:1 mixing with empty micelles $C_{12}E_7$ 0.8 mM, Rhodamine 0.5%, 10 ms integration time, run time of 10 seconds, excitation wavelength 560 nm.

Appendix C

I use code which has been adapted from a previous group member, David Woods and from Malinowskis work. The code, with comments can be found below.

Code for quantitative analysis of raw data

```
load ' me_25c_2mm_timed_run4.dat'; % from mixture, kinetics

d= me_25c_2mm_timed_run4;

%time=d(1,2:end);
wavelength = d(2:end,1);
noisydata = d(2:end,2:end);
size_d=size(noisydata);

time=0:10:(size_d(2)-1)*10;  %Dependant on integration time

factors=2; %input from sfa
[r, c, cleanedData] = afa(noisydata, factors);

colormark=['b';'r';'g';'k';'m';'c'];

figure(1)
cla
hold on

for i=1:size_d(2)
    plot(wavelength,noisydata(:,i),['.-' colormark(mod(i-
1,length(colormark))+1)],'Markersize',2,'Linewidth',1)
end

xlabel('Wavelength /nm','Fontsize',12)
ylabel('Intensity','Fontsize',12)
axis tight;
title('Spectra from Mixture')

figure(2)
cla
hold on

for i=1:size_d(2)
    plot(wavelength,cleanedData(:,i),['.-' colormark(mod(i-
1,length(colormark))+1)],'Markersize',1,'Linewidth',1)
end

xlabel('Wavelength /nm','Fontsize',12)
ylabel('Intensity','Fontsize',12)
axis tight;
title('Refined data from AFA')

%% save AFA data
```

```
filename = ['Refined by AFA.txt'];
fp=fopen(filename,'w');
for i=1:size_d(1)
fprintf(fp,'%12.8f\t',wavelength(i))
for j=1:size_d(2)
    fprintf(fp,'%12.8f\t',cleanedData(i,j)); % save file
end
fprintf(fp,'\n');
end
fclose(fp);

%%
spectra = [noisydata(:,3) noisydata(:,end)]; %choose two suitable
spectra from inspection

% plot(wavelength, spectra(:,1),'ro','MarkerSize',3)
% plot(wavelength, spectra(:,2),'ko','MarkerSize',3)
%
%%
figure(3)
cla
sfa(noisydata) % check how many significant factors that sfa tells

%%
factors=2; % input from sfa
xp =tfa(noisydata,factors,spectra); % calculated spectrum for each
component from decomposition of the kinetic measurements
specDifference = spectra - xp;
% rmsSpecDiff = [ rmsSpecDiff, mean(specDifference.^2).' ];

%% save targets
target_spectra=[wavelength xp];
save('Target Spectra.txt','target_spectra','-ascii')

figure(4)
cla
hold on
for i=1:factors
plot(wavelength,spectra(:,i));
plot(wavelength',xp(:,i),'y','LineWidth',1);
end
title('Target spectra (exp) and refined data (TFA)')

figure(5)
cla
hold on
for i=1:factors
plot(wavelength',xp(:,i),'ro','MarkerSize',3); %First mixing target TFA
end

message=[];

for i=1:size_d(2)
    plot(wavelength,cleanedData(:,i),['.-' colormark(mod(i-
1,length(colormark))+1)],'Markersize',1,'Linewidth',1)
    %message=[message; sprintf('t= %2d',i)];
end
%AFA refined data all mixing.
```

```
xlabel('Wavelength /nm','Fontsize',12)

ylabel('Intensity','Fontsize',12)
axis tight;
title('Refined data from TFA (red circles) and AFA (lines)')

loadings = lfa(cleanedData,spectra); % calculated data from kinetic
measurements

l2=[];
for m = 1:size_d(2)
    l2=[l2 lsqnonneg(spectra,cleanedData(:,m))]; % lsqnonneg(matrix,
vector)
end

l3=spectra\cleanedData;

figure(6)
cla
hold on

colormark=['b';'k';'y';'m';'c'];

for i=1:factors
    plot(time,loadings(i,:),['o' colormark(mod(i-
1,length(colormark))+1)],'Markersize',4,'Linewidth',1);
    %plot(time,l2(i,:),'g-','LineWidth',1); %pure matrix divide
    %plot(time,l3(i,:),'r*','LineWidth',1); %least square non-negative
function
end

xlabel('Time /ms');
ylabel('loadings')
title('Kinetics')

%% Save loading
loading_matrix=[time' loadings'];
save('Kinetics Loading.txt','loading_matrix','-ascii')


 figure(7)
 cla
 hold on

 plot(wavelength, noisydata(:,1),'r')
 plot(wavelength, noisydata(:,end),'b')

 c_noisydata=xp*loadings;
plot(wavelength,c_noisydata(:,1),'r','MarkerSize',1);
 plot(wavelength,c_noisydata(:,end),'b','MarkerSize',1);

 xlabel('Wavelength /nm','FontSize',12)
 ylabel('Intensity','FontSize',12)
 axis tight;
 title('Calculated spectra (beginning/end)')
```

Code used for significant factor investigation

```
clear all
load me_25c_2mm_timed_run4.dat; % from mixture i.e. spectrum from kinetic run
d=me_25c_2mm_timed_run4;

wavelength = d(2:end,1);
noisydata = d(2:end,2:end);
size_d=size(noisydata);


%% SVD for the data
sigNo = 654;

[u, s, v] = svd(noisydata, 0);



c = v(:,1:sigNo)';
r = u(:,1:sigNo)*s(1:sigNo,1:sigNo);
cleanedData = r*c;


figure(1)
semilogy(diag(s), 'k' , 'LineWidth',2)
xlabel('Principal Component')
ylabel('Singular value, \sigma')
xlim([0 10])
%set(gca, 'Fontsize', 14)
%% scree plot

figure(2)
plot(diag(s))
xlabel('Principal Component', 'Fontsize', 16)
ylabel('Singular value, \sigma','Fontsize', 16)
set(gca,'box','off');
ax = gca;
ax.FontSize = 16;
set(gca,'TickDir','out');


figure(3)
plot(wavelength,r(:,2))
xlabel('wavelength / nm','Fontsize', 16)
ylabel('Counts','Fontsize', 16)
set(gca,'box','off');
ax = gca;
ax.FontSize = 16;
set(gca,'TickDir','out');
```

Appendix D

^{1}H NMR of cyclohexane

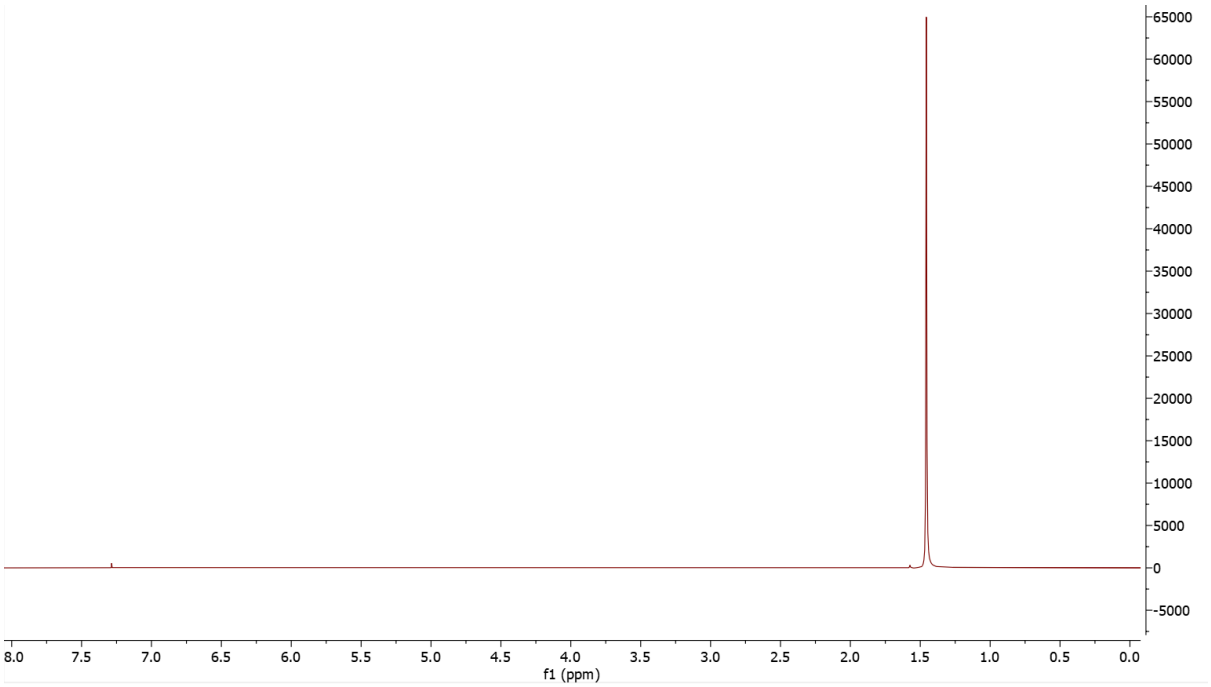

Figure 10: ^{1}H NMR of cyclohexane. No impurities present. δ 1.4 (s, 6H).

Radius of cyclohexane droplet

From §2.2 we can use the same equation to calculate the radius of a cyclohexane microemulsion droplet as a limonene microemulsion droplet.

$$\frac{S}{V} = \frac{3}{R}$$

$$\frac{S}{V} = \frac{A}{V_0 + \left(\nu_l \middle/ \frac{N_s}{N_l}\right)}$$

A = 57 Å^2, or 5.7 x 10^{-15} cm^2, taken from air/water interface measurement from Rosen et al [6].

V_l derivation

Using the density formula, $\rho = \frac{m}{V}$, we can find the volume of one cyclohexane molecule using $V_l = \left(\frac{m}{\rho}\right)$

ρ = 0.779 g/cm^3

m is, $\frac{84.16\ g mol^{-1}}{6.022 \times 10^{23}\ mol}$ = 1.40 x 10^{-22} g

Therefore, $\frac{1.40 \times 10^{-22}\ g}{0.779\ g cm^{-3}} = 1.79 \times 10^{-22}\ cm^3$

V_l = 1.79 x 10^{-22}cm^3

$\frac{N_s}{N_l}$ derivation

Moles of cyclohexane: $\frac{1.5\ g}{84.16\ g mol^{-1}}$ = 1.8 x 10^{-2} mol

Moles of $C_{12}E_7$: $\frac{2.3\ g}{494.71\ g mol^{-1}}$ = 4.65 x 10^{-3} mol

$\frac{4.65 \times 10^{-3}\ mol}{1.8\ \times 10^{-2}\ mol} = 0.26$

$$\frac{N_s}{N_l} = 0.26$$

$$\frac{S}{V} = \frac{5.7 \times 10^{-15}\ cm^2}{3.51 \times 10^{-22}\ cm^3 + (\frac{1.79 \times 10^{-22}\ cm^3}{0.26})}$$

$$\frac{S}{V} = 5.49 \times 10^6\ cm^{-1}$$

Now using equation 4 we can write:

$$R = \frac{3}{(\frac{S}{V})} \qquad R = \frac{3}{5.49 \times 10^6\ cm^{-1}}$$

R = 5.47 x 10^{-7} cm or 5.47 nm

Diffusion coefficient of cyclohexane droplets

$$D = \frac{k_B T}{6\pi n r}$$

$$\mathrm{D} = \frac{1.38\ x\ 10^{-23} m^2 kg\ s^{-2} K^{-1} \times 293K}{6\times\pi\times 0.89\times 10^{-3} kg\ m^{-1}\ s^{-1} \times 5.5\times 10^{-9} m}$$

$$\mathrm{D} = 4.4 \text{ x } 10^{-11}\ \mathrm{m^2\ s^{-1}}$$

^{1}H NMR of methyl laurate

Peak assignments presented, unresolved impurities seen between 3.5 and 4.0 ppm.

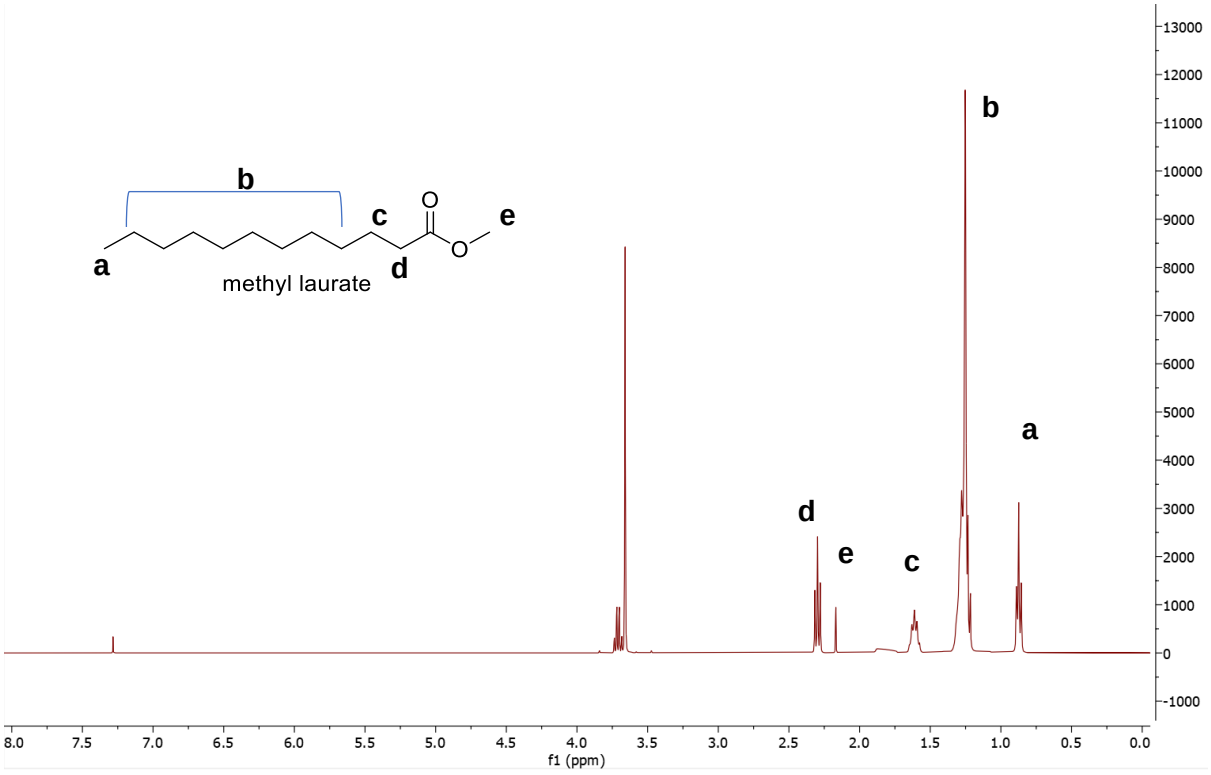

Figure 11: ^{1}H NMR (400 MHz, $CDCl_3$) of methyl laurate with unresolved peaks. δ 0.87 (t, 3H, **a**), 1.26 (m, 16H, **b**) 1.61 (m, 2H, J = 7.1 Hz, **c**), 2.1 (s, 3H, **e**) 2.3 (t, 2H, J = 7.56 Hz, **d**),

^{1}H NMR lauric acid

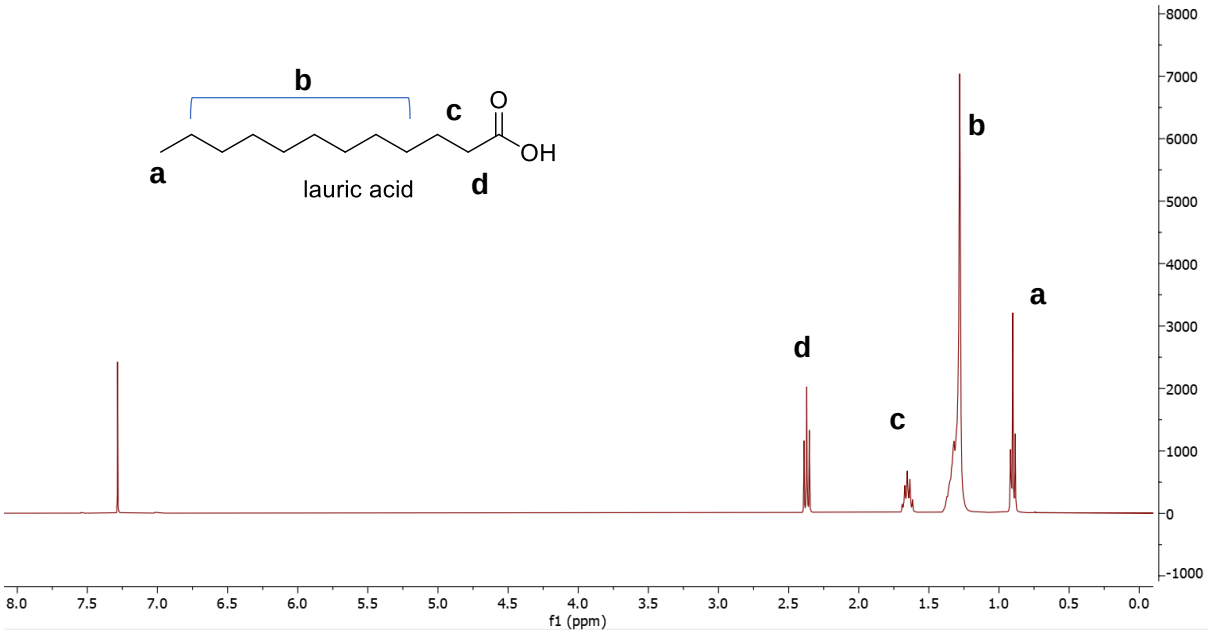

Figure 12: ^{1}H NMR (400 MHz, $CDCl_3$) of lauric acid. 0.9 (t, 3H, **a**), 1.33 (m, 16H, **b**) 1.65 (m, 2H, J = 7.5 Hz, **c**), 2.37 (t, 2H, J = 7.5Hz, **d**),

Permission table for reproduction and redrawing of images

Page	Work in thesis	Source of work	Permission?	Notes
42	Figure 1.4 oil-in-water microemulsion geometry	geometry of oil-in-water and water-in-oil of microemulsion Mitchell, D. John; Ninham, Barry W.	Yes	License agreement: marketplace.copyright.com/rs-ui-web/mp/license/f2694f8b-5b06-4e73-8a87-8e92cec9d5e9/0c536045-68db-4ae5-a2c8-8d30faa88177
77	Figure 3.3 Schematics of stopped-flow system	Photophysics manual: S. Flow and S. March, 'User Manual SX20 Stopped Flow Spectrometer', no. March. p. 24, 2012.	Yes	Written permission via email given.